Electromagnetic fields and interactions in 3D cylindrical structures : modeling and application

Electromagnetic Fields and Interactions in 3D Cylindrical Structures: Modeling and Application

PROEFSCHRIFT

ter verkrijging van de graad van doctor aan de
Technische Universiteit Eindhoven, op gezag van de
rector magnificus, prof.dr.ir. C.J. van Duijn, voor een
commissie aangewezen door het College voor
Promoties in het openbaar te verdedigen
op dinsdag 25 september 2012 om 16.00 uur

door

Koen Joseph Meessen

geboren te Warnsveld

Dit proefschrift is goedgekeurd door de promotor:

prof.dr. E.A. Lomonova MSc

Copromotor:
dr. J.J.H. Paulides MPhil

Summary

**Electromagnetic Fields and Interactions in 3D Cylindrical Structures:
Modeling and Application**

The demand for more efficient and compact actuation systems results in a search for new electromagnetic actuator configurations. To obtain actuators that meet these challenging specifications, accurate modeling of the electromagnetic fields is often a prerequisite. To date, analytical modeling techniques are widely used to predict electromagnetic fields in classical rotary and linear machines represented in two dimensional coordinate systems. One specific technique that is used to analyze and design electromagnetic devices is based on Fourier series to describe sources and the resulting magnetic fields. This thesis presents the extension of this analytical modeling technique to predict the 3D field distribution in cylindrical actuator configurations in a fast and accurate manner.

The presented 3D harmonic modeling technique can be used to describe electromagnetic fields due to presence of permanent magnets in regular and irregular shaped 3D cylindrical structures. It can be applied to current-free cylindrical problems exhibiting periodicity or a soft-magnetic boundary in the axial direction. The cylindrical structure can posses either circumferential slots, axial slots or rectangular cavities. The assignment and a method to solve the various boundary conditions are discussed in a generic manner to enable model application to a wide range of 3D cylindrical structures. The magnetic field solutions are provided, and the model implementation is presented in matrix form. Model validation is presented by means of a comparison of the magnetic fields in a cylindrical structure with a 3D magnetization array and a rectangular cavity calculated using the analytical model and a finite element model.

To calculate the magnetic interactions, i.e., attraction and cogging forces due to permanent magnets, the Maxwell stress tensor is analytically evaluated. The harmonic magnetic field solution is used in this evaluation resulting in compact force equations describing the 3D force components between concentric cylinders.

The 3D harmonic modeling technique is applied to analyze and develop a single body two degrees of freedom (2-DoF) rotary-linear actuator. This actuator replaces cascaded single-DoF actuators, and it is designed for a pick and place machine to populate printed circuit boards. To achieve the specified high force and low torque, a novel magnetization pattern is proposed. Three different realizations of this pattern are presented based on introducing parasitic field effects in a single-DoF linear tubular actuator. Various stator configurations are explored to obtain an actuator with a high force/torque density without introducing a complex manufacturing process. Electromagnetic and thermal analyses are conducted to obtain a final actuator design.

A prototype of the newly developed actuator is manufactured, and the realization and experimental validation are presented. The experimental results demonstrate that the actuator complies with the requirements for the pick and place application, that is, a mover acceleration in the axial direction of $a_z = 150\,\mathrm{ms}^{-2}$ over a stroke of 30 mm for a duty-cycle of 34%, and a static positioning error in this direction of 4 μm, whereas a maximum error of 5 μm is specified. In the rotational direction, a mover acceleration of $\alpha_\theta = 3500\,\mathrm{rads}^{-2}$ for a duty-cycle of 47% is demonstrated, and the static positioning error is less than 0.35 mrad. Furthermore, the combined rotation-translation motion profile results in a continuous dissipation of 13.5 W, causing a temperature rise of the actuator of approximately 30°C. The results of the experimental validation are in good agreement with the results of the developed harmonic model, and demonstrate the applicability of the modeling technique to analyze cylindrical structures containing permanent magnets.

Contents

1

Introduction

Abstract - In this chapter, an introduction is given on the electromagnetic field theory related to magnetostatic fields in electromagnetic devices. Comprehensive equations describing magnetic fields and their interactions are presented, and an overview of methods to solve these equations is given. The limitations of the state-of-the-art field modeling techniques are discussed, which lead to the definition of the research goal of this thesis. The research contributions are presented, and finally the outline of the thesis is given.

1.1 Electromagnetic field theory

Various electrostatic and magnetostatic phenomena have been known from the ancient times. For example, the Greeks experienced the electrification of bodies by friction and other phenomena of electric repulsion and attraction. In due time, numerous experiments were conducted to investigate the magnetic properties of lodestone, a piece of the mineral magnetite which can be naturally magnetized. These properties were discovered because the material attracted other pieces of lodestone and iron parts. Later, lodestone was employed in the first magnetic compasses used for navigation [43].

The experiments on both electrostatics and magnetostatics took place as two independent but closely analogous sciences until about two centuries ago. The phenomena were more systematically investigated by Coulomb, Ampère, Faraday and Oersted in the 18th and 19th century. At that time, the close relation between electric and magnetic phenomena was discovered and people started to formulate a unified electromagnetic field theory. Ultimately, a set of differential equations, called the Maxwell equations, were defined by James Clerk Maxwell describing the macroscopic observable electromagnetic phenomena.

1.1.1 Quasi-static Maxwell equations

The Maxwell equations are a mathematical formulation to describe the interaction of charged matter and the behavior of electromagnetic fields, and provide a fundamental understanding of a wide range of phenomena [84]. In general, electromechanical phenomena can be described by the quasi-static Maxwell equations under the assumption that the effects due to time varying fields are small. This assumption is valid if the time variation of the magnetic field is much smaller than the time required for the field to penetrate the region of interest [34]. For example, consider a cubical region of free space with all sides measuring $1.0\,\mathrm{m}$. As the electromagnetic field travels with a velocity of $c = 3 \times 10^8\,\mathrm{m/s}$, any field variation is felt within $58\,\mathrm{ns}$ throughout the whole region. This system is called quasi-static if the electromagnetic fields change much more slowly than $58\,\mathrm{ns}$. The quasi-static Maxwell equations in differential form are defined as

$$\nabla \times \vec{H} = \vec{J}_f \qquad \text{Ampère's circuit law,} \qquad (1.1)$$

$$\nabla \cdot \vec{B} = 0 \qquad \text{Gauss's law for magnetism,} \qquad (1.2)$$

$$\nabla \times \vec{E} = -\frac{\partial \vec{B}}{\partial t} \qquad \text{Maxwell-Faraday law,} \qquad (1.3)$$

$$\nabla \cdot \vec{D} = \rho \qquad \text{Gauss's law.} \qquad (1.4)$$

In these equations the sources are described by ρ, the free electrical charge density, and $\vec{J}_f$, the current density which can be interpreted as the movement of free charge. The fields are defined as follows; $\vec{H}$ is the magnetic field strength, $\vec{E}$ is the electric field strength, $\vec{B}$ is the magnetic flux density and $\vec{D}$ is the electric flux density. To solve the differential Maxwell equations, an additional set of equations is required to describe the relations between the physical quantities in a specific medium.

Constitutive relations

Two independent equations provide the relations between the field strength and the flux density in equations (1.1) to (1.4) in a given medium. These constitutive relations are in literature generally defined as

$$\vec{B} = \mu_0 \left(\vec{H} + \vec{M} \right), \tag{1.5}$$
$$\vec{D} = \epsilon_0 \vec{E} + \vec{P}, \tag{1.6}$$

where μ_0 and ϵ_0 are the permeability and permittivity of free space, respectively, $\vec{M}$ is the magnetization or magnetic moment, and $\vec{P}$ is the polarization.

Magnetization

In the formulation of the electromagnetic field theory, distinction is made between fields due to sources within a material and those related to currents originated from moving charges. Both sources can be described by currents, the sources within a material can be described by a magnetization current density, J_m, whereas the one describing moving charges is generally called a free current. The equivalence between a magnetized material and a current in terms of its electromagnetic effect was firstly noted by Ampère and Oersted. This concept is useful to treat the microscopic currents on atomic level in a macroscopic theory [119, 135].

In the case that $\vec{B}$ is a single-valued function of $\vec{H}$, i.e. the material exhibits no hysteresis, a common definition of the magnetization, $\vec{M}$, is that it provides a measure for the material response when a magnetic field is applied to it. In this definition the relation between the field strength $\vec{H}$ and the magnetization of the material is given by

$$\vec{M} = \chi_m \vec{H}, \tag{1.7}$$

where χ_m is the magnetic susceptibility that can be a function of $\vec{H}$ in case of non-linear materials. This simplifies the constitutive relation (1.5) to

$$\begin{aligned} \vec{B} &= \mu_0 \left(1 + \chi_m \right) \vec{H} \\ &= \mu \vec{H}, \end{aligned} \tag{1.8}$$

where the permeability μ is defined by the permeability of free space times the relative permeability of the specific material μ_r

$$\mu = \mu_0 \mu_\mathrm{r}. \tag{1.9}$$

Description of a permanent magnet

In hard magnetic material (i.e. a permanent magnet), the orientation of magnetic moments is aligned such that a given volume of this material has a net magnetic moment without an applied external field. This material property can be included by means of χ_m in (1.7). However, a more convenient representation of a permanent magnet is to introduce an additional magnetic moment term, M_0, in the constitutive relation [66, 104, 121]

$$\begin{aligned}
\vec{B} &= \mu_0 \left(\vec{H} + \vec{M} + \vec{M}_0 \right) \\
&= \mu_0 \mu_\mathrm{r} \vec{H} + \mu_0 \vec{M}_0.
\end{aligned} \tag{1.10}$$

In this definition the magnetic moment, $\vec{M}_0$, referred to as the remanent magnetization vector, is defined as

$$\vec{M}_0 = \frac{\vec{B}_\mathrm{rem}}{\mu_0}, \tag{1.11}$$

where $\vec{B}_\mathrm{rem}$ is the remanent flux density of the permanent magnet.

1.1.2   Lorentz force equation

Using the Maxwell equations, the electromagnetic fields originated by currents and permanent magnets are described. In the research on electromechanical systems, the main interest of these electromagnetic fields is the interaction with other electromagnetic fields and materials resulting in a mechanical force. In literature, several methods are described to calculate the exerted force on a body in an electromagnetic field. Historically, the force experienced by a charge q moving with a velocity $\vec{v}$ is described by the experimentally found Lorentz force equation

$$\vec{f} = q \left(\vec{E} + \vec{v} \times \vec{B} \right). \tag{1.12}$$

According to the Lorentz electron theory, the only electromagnetic force of physical significance can be ascribed to electrically charged particles. In literature, the Lorentz force equation is also used as a definition of the magnetic field $\vec{B}$ and the electric field $\vec{E}$ instead of a definition of the force experienced by a charged particle in an electromagnetic field [66, 135]. In this thesis, the equation is solely used as the definition for the force.

The Lorentz force consists of two parts, the first part is the force exerted on a free charge, q, in an electric field, $\vec{E}$. The second force component is the one exerted on moving charges (free current) in a magnetic field, $\vec{B}$. Under the assumption that in the considered electromechanical devices $\vec{E}$ is zero outside the coil-conductor, the first force component does not contribute to the total force and (1.12) can be rewritten as

$$\vec{f} = q\vec{v} \times \vec{B}. \tag{1.13}$$

Using the definition that a current represents movement of charges, the total force on an object is given by the volume integral of $\vec{f}$ [136]

$$\vec{F} = \int_V \vec{J}_f \times \vec{B}\, \mathrm{d}v. \tag{1.14}$$

1.1.3 Maxwell stress tensor

From the Lorentz force equation the force on a current carrying wire in a magnetic field can be directly calculated. However, to obtain the force between two objects, e.g. a permanent magnet and a soft-magnetic object, (1.14) does not provide a direct solution. A more general description of the force on an object due to electromagnetic field interaction is given using the Maxwell stress tensor, $\mathbb{T}$

$$\vec{F} = \int_V \nabla \cdot \mathbb{T}\, \mathrm{d}v, \tag{1.15}$$

where the volume V contains the considered object [37]. Using Gauss's theorem, the Maxwell stress tensor force description can be rewritten to a more convenient equation

$$\vec{F} = \oint_S \mathbb{T} \cdot \vec{n}\, \mathrm{d}s, \tag{1.16}$$

where S is a surface enclosing the considered body. The Maxwell stress tensor, $\mathbb{T}$, is coordinate system independent and defined as

$$\mathbb{T}_{ij} = \frac{B_i B_j}{\mu_0} - \delta_{ij} \frac{|\vec{B}|^2}{2\mu_0}, \tag{1.17}$$

where i and j represent the components in the specific coordinate system and δ_{ij} is the Kronecker delta

$$\delta_{ij} = \begin{cases} 1 & \text{for } i = j, \\ 0 & \text{for } i \neq j. \end{cases} \tag{1.18}$$

As can be seen, the force expressed by means of the Maxwell stress tensor, equation (1.15), consists of the magnetic field only, while the Lorentz force equation is a function of both field and sources. The Maxwell stress tensor force description can

be derived from the Lorentz force equation by including the microscopic currents at atomic level into the current density [66]

$$\vec{F} = \int_V \vec{J} \times \vec{B} \, \mathrm{d}v.$$

(1.19)

Instead of calculating the cross product of the free current density and the magnetic flux density, the total current density in the domain has to be considered, i.e., the sum of all free and microscopic currents at atomic level. In other words, the magnetization, both $\vec{M}$ and $\vec{M}_0$, has to be expressed by means of equivalent currents. Consequently, the magnetic field, as defined by Ampère's circuit law (1.1), is now defined by the total current instead of only the free current, $\vec{J}_f$. As such, the magnetization vanishes from (1.5) and the relation between the total current and the magnetic flux density yields to

$$\nabla \times \vec{B} = \mu_0 \vec{J}.$$

(1.20)

Consequently, (1.19) can be rewritten as

$$\vec{F} = \int_V \left(\nabla \times \frac{\vec{B}}{\mu_0} \right) \times \vec{B} \, \mathrm{d}v.$$

(1.21)

Using vector identities, as given in Appendix A, (1.15) and (1.21) yield to

$$\mu_0 \nabla \cdot \mathbb{T} = \left(\nabla \times \vec{B} \right) \times \vec{B} + \left(\nabla \cdot \vec{B} \right) \vec{B}.$$

(1.22)

Since the divergence of $\vec{B}$ is zero ($\nabla \cdot \vec{B} = 0$), defined in (1.2), the second term vanishes, and one can see that the Lorentz force and the Maxwell stress tensor are equivalent and can be used to calculate the force of electromagnetic origin.

1.1.4   Boundary conditions

As all sets of differential equations describing physical phenomena, the Maxwell equations cannot be solved without applying boundary conditions at the interfaces between different media. The Maxwell equations in differential form, defined in (1.1) to (1.4), describe the magnetic field locally at each time in space. Using the divergence theorem and Stokes' theorem, the Maxwell equations can be cast to the integral form [53]. The resulting Maxwell equations for magnetic fields in integral form become

$$\oint_C \vec{H} \cdot \mathrm{d}\vec{l} = \vec{j}_f,$$

(1.23)

$$\oint_S \vec{B} \cdot \vec{n} \, \mathrm{d}s = 0,$$

(1.24)

where $\vec{j}_f$ is the surface current and $\vec{n}$ is a unit vector normal to the surface S. Consider the closed contour C through medium 1 and medium 2 in Figure 1.1(a) with $l \gg h$. Applying (1.23) to this contour with $h \rightarrow 0$ results in
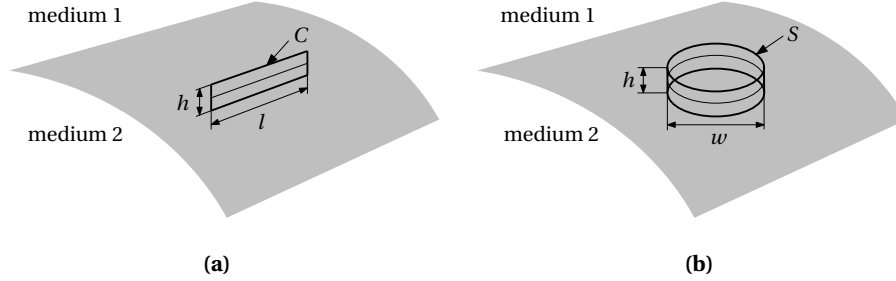
Figure 1.1: Interface between two media for the definition of the boundary conditions.
(a) Closed contour C for the definition of the boundary condition on the magnetic field strength. **(b)** Closed surface S for the definition of the boundary condition on the magnetic flux density.

$$\int_{l_1} \vec{H}_1 \cdot \mathrm{d}\vec{l} - \int_{l_2} \vec{H}_2 \cdot \mathrm{d}\vec{l} = \vec{j}_f, \tag{1.25}$$

where l_1 and l_2 are the parts of C through medium 1 and medium 2, respectively, and $\vec{H}_1$ and $\vec{H}_2$ are the magnetic field strength in medium 1 and medium 2, respectively. Consequently, if the surface current at the interface between the two media is zero, the conclusion drawn from this equation is that the tangential component of the magnetic field strength has to be continuous at the interface.

A general boundary condition for the magnetic flux density is derived similarly using (1.24). In Figure 1.1(b), a Gaussian pill-box is shown with surface S. Consider that $w >> h$ and apply (1.24) to the surface with $h \rightarrow 0$, this yields to

$$\int_{S_1} \vec{B}_1 \cdot \vec{n}\,\mathrm{d}s - \int_{S_2} \vec{B}_2 \cdot \vec{n}\,\mathrm{d}s = 0, \tag{1.26}$$

where S_1 and S_2 are the surfaces at the top and bottom of the Gaussian pill-box, respectively, and $\vec{B}_1$ and $\vec{B}_2$ are the magnetic flux density in medium 1 and medium 2, respectively. Consequently, the normal component of the flux density is continuous at the interface between two media.

1.2   Electromagnetic field analysis

To obtain a numerical or analytical solution for the magnetic fields, the Maxwell equations (1.1) to (1.4) have to be solved considering the constitutive relations as given in (1.5) and (1.6). A direct solution for these differential equations can be obtained, however, the four dependent first order differential equations can be rewritten to two second order differential equations. By solving one of these second order differential equations, the magnetic field solution can be obtained.

1.2.1 Magnetic vector potential

The Maxwell equations can be rewritten by introducing the magnetic vector potential, $\vec{A}$, defined as

$$\nabla \times \vec{A} = \vec{B}, \tag{1.27}$$

By using the vector calculus as given in Appendix A, substitution of (1.27) into (1.1) considering the constitutive relation (1.10) yields to

$$\nabla \left(\nabla \cdot \vec{A} \right) - \nabla^2 \vec{A} = \mu_0 \left(\mu_{\mathrm{r}} \vec{J}_f + \nabla \times \vec{M}_0 \right). \tag{1.28}$$

As the curl of the vector potential is defined in (1.27), the divergence of the vector potential can be chosen arbitrarily. For convenience, $\nabla \cdot \vec{A} = 0$, as such, two second order differential equations define the magnetic vector potential in regions with or without sources, referred to as the Poisson and Laplace equation, respectively

$$\nabla^2 \vec{A} = -\mu_0 \left(\mu_{\mathrm{r}} \vec{J}_f + \nabla \times \vec{M}_0 \right) \qquad \text{Poisson equation,} \tag{1.29}$$

$$\nabla^2 \vec{A} = 0 \qquad \text{Laplace equation.} \tag{1.30}$$

1.2.2 Magnetic scalar potential

The magnetic scalar potential is a second potential to describe the magnetic fields. This potential can be used only in current-free regions, i.e., $J_f = 0$. As such, (1.1) yields to

$$\nabla \times \vec{H} = 0. \tag{1.31}$$

The magnetic scalar potential, φ, is introduced as

$$-\nabla \varphi = \vec{H}. \tag{1.32}$$

Substitution of (1.32) into (1.1) and taking into account the constitutive relation (1.10) yields to another Poisson and Laplace equation for regions with permanent magnets or source free regions,

$$\nabla^2 \varphi = \frac{1}{\mu_{\mathrm{r}}} \nabla \cdot \vec{M}_0 \qquad \text{Poisson equation,} \tag{1.33}$$

$$\nabla^2 \varphi = 0 \qquad \text{Laplace equation.} \tag{1.34}$$

The advantage of the scalar potential is the reduced complexity compared to the vector potential in three dimensional problems where the vector $\vec{A}$ consists of three components. In two dimensional problems the vector potential reduces to a scalar as one of the three components of the flux density has to be zero. Hence, the advantage vanishes in 2D problems.

1.3 Electromagnetic field modeling techniques

A wide variety of modeling techniques is developed over the years to obtain a solution for the partial differential equations (PDEs) describing the potentials and magnetic fields as presented in the preceding sections. The goal of these modeling techniques is to provide an accurate potential or magnetic field description as a function of sources of magnetic fields in an arbitrary geometry. These techniques can be classified as numerical or analytical although the division is not always evident. For example, modeling techniques describing the magnetic fields by means of an infinite Fourier series are sometimes referred to as semi-analytical due to the approximation of the infinite sum [38]. Generally, analytical methods describe the potentials or fields by analytical expressions as a function of physical parameters, e.g., geometric dimensions. Numerical methods do not provide functions but only numerical values of the potentials or magnetic fields at certain points in the geometry.

1.3.1 Numerical methods

The Finite Element Method (FEM) is a commonly used numerical method to find approximate solutions of PDEs [65]. In this method, the geometry of interest is discretized in a finite number of mesh elements small enough to satisfy the assumption that the potential and fields inside these elements can be approximated by a first or second order polynomial. Therefore, an a-priori knowledge of the magnetic field or an iterative adaptive mesh is required to create a suitable mesh distribution. The finite element method obtains the correct solution for a model by minimizing the energy functional [111].

A disadvantage of meshing a structure is the finite number of elements which inherently requires that the geometry should be bounded. In structures with soft-magnetic materials or in structures exhibiting periodicity, the boundaries can be defined by a Neumann or Dirichlet boundary condition. However, in ironless structures without a well defined boundary, a suitable mesh requires a very high number of elements [58]. Meshing large structures with small details where the field varies will result in a very high number of mesh elements as these details require a high mesh density, and a proper mesh has to alter gradually from fine to coarse. The same effect appears in large structures with a small airgap between the moving and stationary part. The energy-conversion takes place in this airgap and therefore, a high mesh density is required. Generally, increasing the mesh density provides more accurate results although numerical instability can occur if the mesh density is too high. Furthermore, the computational time will rise and meshing the structure can become the dominant time factor in the solving process.

Finite element modeling is considered to be the most generic approach to analyze electromagnetic problems as it provides an accurate solution for a wide range of applications, e.g., transient, steady state and multi-physical domains. Furthermore,

complex geometric shapes can be modeled and non-linear non-homogeneous material properties can be considered. The availability of powerful software packages to analyze two and three dimensional structures has made this modeling technique very popular in research and engineering.

One of the oldest numerical methods is the Finite Difference Method (FDM) which uses a similar discretization as FEM to obtain a solution for the potential distribution in the structure. However, in this method the mesh consists of orthogonal, often uniformly spaced, elements which limits the number of geometries that can be accurately discretized. The differential equation in this method is approximated by a finite difference equation that relates the value of the solution of two neighboring nodes. The complete solution is obtained by solving the total set of equations.

A numerical method that meshes only boundaries of permeable objects instead of the complete domain is the boundary element method (BEM). In BEM, the partial differential equations to be solved are formulated as integral equations. The fields are solved only outside the objects using the given boundary conditions to fit boundary values in the integral equation, where FEM and FDM fit values in the differential equations throughout the complete domain. In a post-processing stage, the integral equation is used to calculate the solution at any point in the domain. An advantage over the aforementioned method is the significantly reduced number of required mesh elements, however the accuracy is often lower. Furthermore, as only the boundaries of objects are meshed, only homogeneous linear material properties can be modeled.

1.3.2   Analytical methods

Various analytical methods are developed and being used in analysis, design and optimization of electromagnetic devices. In the following sections a selection of common methods is presented. To obtain an analytical model of electromagnetic fields, one can start from the PDEs describing the magnetic scalar potential and magnetic vector potential as a function of the magnetic and electric sources (Laplace and Poisson equations). Two commonly used approaches to solve the Laplace and Poisson equations are described in this section.

Green functions

The first approach is to find a solution of the Poisson or Laplace equation in a finite volume (or surface in 2D) with either a Dirichlet or a Neumann boundary condition on the bounding surface (or contour in 2D) by means of Green's theorem and so-called Green functions [53]. The simplest Green function providing the solution for

the Poisson equation in an unbounded space is

$$G(\vec{x}, \vec{x}') = \frac{1}{|\vec{x} - \vec{x}'|}, \tag{1.35}$$

where $\vec{x}$ and $\vec{x}'$ are the observation and source point, respectively. This results in the following solution for the vector potential

$$\vec{A}(\vec{x}) = \frac{\mu_0}{4\pi} \int_V \frac{\vec{J}(\vec{x}')}{|\vec{x} - \vec{x}'|} \mathrm{d}v' + \frac{\mu_0}{4\pi} \int_S \frac{\vec{j}(\vec{x}')}{|\vec{x} - \vec{x}'|} \mathrm{d}s', \tag{1.36}$$

where $\vec{J}$ and $\vec{j}$ are the volume and surface current density, respectively [53, 119]. This formulation is known as the Biot-Savart law and can be used to describe the magnetic field due to current filaments [43] and current densities [125].

To find the field distribution due to permanent magnets by means of Biot-Savart, an equivalent (atomic) currents description, mentioned in Section 1.1.3, can be used. The equivalent currents are defined from the remanent magnetization vector $\vec{M}_0$

$$\vec{J}_m = \nabla \times \vec{M}_0 \qquad\qquad \text{Volume current density,} \tag{1.37}$$

$$\vec{j}_m = \vec{M}_0 \times \vec{n} \qquad\qquad \text{Surface current density,} \tag{1.38}$$

where $\vec{n}$ is the unit vector normal to the surface [119]. If the magnetization of the permanent magnet is homogeneous and uniform within the magnet, the volume current density $\vec{J}_m$ is zero. Inserting these magnetization currents in (1.36) provides the magnetic vector potential distribution for a permanent magnet in free space.

The Green function (1.35) can also be applied to solve the Poisson equation for the magnetic scalar potential, as such, (1.33) yields to

$$\varphi(\vec{x}) = \frac{1}{4\pi} \int_V \frac{\nabla' \cdot \vec{M}_0(\vec{x}')}{|\vec{x} - \vec{x}'|} \mathrm{d}v' + \frac{1}{4\pi} \int_S \frac{\vec{M}_0(\vec{x}') \cdot \vec{n}}{|\vec{x} - \vec{x}'|} \mathrm{d}s'. \tag{1.39}$$

The magnetization in this equation is often rewritten by introducing equivalent magnetic charges defined as

$$\rho_m = \nabla \cdot \vec{M}_0 \qquad\qquad \text{Volume charge density,} \tag{1.40}$$

$$\sigma_m = \vec{M}_0 \cdot \vec{n} \qquad\qquad \text{Surface charge density.} \tag{1.41}$$

This method to describe a permanent magnet is therefore referred to as the charge- or Coulombian model [34]. For regular shaped permanent magnets in three dimensional problems, this model is often preferred over the equivalent current model as only two surfaces with charges have to be modeled instead of four surface currents. However, this only holds when the magnetization is uniform within the permanent magnet and perpendicular to four sides.

In literature, modeling of permanent magnets by an equivalent current or equivalent charges is widely described and analytical field equations are presented for different PM shapes [59]. A comparison and extensive literature overview describing these methods can be found in [110]. The main drawback of describing the permanent magnet by an equivalent current or equivalent charges is the assumption of a relative permeability equals one in the permanent magnets.

The Green function providing the Biot-Savart law as given in (1.35) gives a solution for the Poisson equation in an unbounded problem. The form of a Green function providing a solution for the Poisson equation in a bounded region depends on the shape of the boundary. Hence, it is often complex (if not impossible) to determine the appropriate Green function. Therefore, other approaches are developed to solve the Poisson equation with boundary conditions and to obtain the Green functions in an indirect manner. The most common technique is the method of images that replaces a region with boundaries by an enlarged region with images of the sources instead of boundaries [10, 43, 119]. For example, consider a permanent magnet in air with an infinite soft-magnetic plate in the vicinity. Instead of solving the Poisson equation with a Neumann boundary condition on the plate, a second permanent magnet is symmetrically placed with respect to the surface of the soft-magnetic plate. The aforementioned approach with the Green function as given in (1.35) can now be solved in an unbounded domain with two sources. This technique can be expanded to angled interfaces [43, 119], problems with multiple boundaries [60], and materials with finite permeability [43], however it is still limited to simple structures.

Separation of variables

The second approach to find an analytical solution of the Poisson or Laplace equation is separation of variables [16, 34, 53]. Separation of variables is commonly considered an analytical solution method that yields the solution of certain PDEs in terms of an infinite series. The method is based on the assumption that the solution for the potential, $\varphi(u, v, w)$, can be written in the form

$$\varphi(u, v, w) = U(u)V(v)W(w). \tag{1.42}$$

As such, the solution of the partial differential equation can be found in terms of three ordinary differential equations. This technique can be applied in several coordinate systems and is especially suitable to solve boundary value problems. In these problems, the value of the potential (Dirichlet boundary condition) or the value of the normal derivative of the potential (Neumann boundary condition) is defined at the boundary of a finite volume. The form of the functions $U(u), V(v)$ and $W(w)$ in this volume depends on the coordinate system, the boundary conditions and the sources inside the volumes. By dividing the complete domain of the problem into orthogonal contiguous regions (i.e., regions with interfaces orthogonal to one coordinate axis) and applying boundary conditions to the interfaces between the regions, a set of equations with unknown coefficients is obtained from which the

potential or magnetic field can be found in all regions.

This method is widely used to model electromagnetic fields and is generally referred to as harmonic or Fourier modeling or sometimes sub-domain modeling [41, 154]. The solution of the potential in this method is typically an infinite (Fourier) series in one or two directions for 2D or 3D problems, respectively. As such, the method is particularly suitable for periodic or symmetric problems or closed problems with a soft-magnetic boundary where at least one of the magnetic flux density components is zero. For example, rotary machines or long-stroke linear actuators which have a certain periodicity can be modeled by considering one single period of the complete structure. If no geometric periodicity is present, for example due to the finite length of a linear actuator, periodicity can be mimicked by repeating the original geometry [128]. The sources in the geometry, i.e. coils or permanent magnets, are represented by a 1D or 2D Fourier series. As the model can take into account the permeability of soft-magnetic materials in certain situations, global saturation can be modeled by creating an iterative model. To include local saturation, the specific region has to be subdivided into multiple regions each having a homogenous permeability. However, this finer discretization of the domain results in an increased complexity and computation time, and the model will loose its advantages with respect to FEM. In [41] modeling of two dimensional structures in three different coordinate systems (cartesian, polar, axissymmetric) is extensively described. This includes structures with irregular shaped soft-magnetic regions, i.e., slots in the geometry.

Magnetic equivalent circuit

The most basic analytical method that is not directly obtained from the partial differential equations is the magnetic equivalent circuit (MEC) model which is the magnetic equivalent of the electric circuit theory [102, 113]. Instead of finding a direct solution for the Poisson and Laplace equation, an equivalent circuit is constructed based on Ampère's circuit law in integral form. A significant difference between magnetic flux and electric current is that unlike magnetic flux, electric current is generally confined to neat traceable paths. As such, the definition of the magnetic circuit is not as straight-forward as the definition of an electric circuit. To obtain the magnetic circuit, the geometry has to be divided into a network of so-called flux tubes with sources of magneto-motive force (MMF). The flux density is subsequently found by means of Hopkinson's law which is the magnetic equivalent of Ohm's law, i.e., the flux density is the product of the permeance of the flux tube and the MMF.

Similar to FEM, the geometry is discretized in this method, however, in MEC modeling the number of elements (flux-tubes) is generally much smaller. Furthermore, it is assumed that the magnetic flux enters a tube perpendicular to one of its surfaces, is constant in the element, and leaves the opposite surface of the tube perpendicularly. As such, describing a complex geometry requires a high level of discretization. Effects as flux leakage and fringing are difficult to take into account as the flux tubes with

the flux entering and leaving perpendicularly are not well-defined. Therefore, prior-knowledge of the geometry and understanding of the magnetic structure is eminent to define a MEC. Furthermore, the model is very sensitive to geometrical variations as the flux paths tend to change and possibly require a redefinition of the flux tubes.

Local and global saturation can be taken into account by splitting a soft-magnetic object into multiple flux tubes and making the permeance of each tube dependent of the flux through the tube. The resulting network of permeances can be iteratively solved.

In general, MEC modeling can be used to provide an estimation of flux levels in different parts of soft-magnetic structures where the flux tubes are well-defined. The method is inaccurate in ironless structures due to the absence of these well-defined flux tubes. In PM based devices with a large effective airgap, flux leakage and fringing restrain the definition of suitable flux tubes. This method is not favorable to apply in design or optimization routines as geometric variations quickly result in inaccurate results. The same holds if position dependent phenomena in actuators are analyzed.

1.3.3   Hybrid methods

To obtain an analytical model to describe the electromagnetic phenomena in a structure, a set of assumptions is required to confine the complexity, for example, linear and isotropic material properties or geometrical periodicity. The validity of these assumptions depends on the geometry and physical properties of the modeled problem. To overcome model limitations due to certain assumptions, hybrid methods can be created to exploit the advantages of different methods. For example, in [74, 144], a method is presented to couple an analytical magnetic field solution based on a Fourier description in the airgap of an electric machine with standard finite element equations used to model the other parts of the machine. In [51], a Fourier model is coupled to a MEC model to consider saturation. In optimization routines the computationally inexpensive analytical models can be combined with accurate FEM models and space-mapping techniques to create fast and accurate design tools [31].

1.3.4   Limitations of described modeling techniques

By means of FEM, almost all physical electromagnetic phenomena can be analyzed in both two dimensional and three dimensional structures. However, as mentioned before, FEM is less suitable for design and optimization purposes due to the computation time and the absence of providing a direct relation between geometry and outcome. In particular modeling three dimensional structures in FEM is very time-consuming. Even simple structures where creation of the mesh can become the dominant time factor in the solving process. Therefore, analytical methods can be very beneficial especially to analyze three dimensional structures.

The analytical model based on Green functions is applied in the 2D and 3D domain [59]. In a 2D problem, the volume and surface integrals in (1.36) and (1.39) reduce to a surface and a line integral, respectively. In both 2D and 3D, the integrals have analytical solutions for simple coil or PM shapes. To include soft-magnetic regions in the model is complex as derivation of the Green function is more complicated for these structures. In electromagnetic devices soft-magnetic materials are widely used to enhance the force density, hence, this analytical technique is generally less suitable.

In literature, the harmonic modeling technique based on separation of variables is used to model a wide variety of actuators containing soft-magnetic materials. The technique is applied to problems with regular or irregular soft-magnetic shapes where the 3D nature of the geometry is nearly always approximated by a 2D representation. As a result, the existing models provide an accurate electromagnetic field distribution for structures showing periodicity or negligible dependency on one of the three dimensions in space. However, if the electromagnetic field distribution exhibits three dimensional phenomena, the existing models cannot be used. This deficiency of harmonic models that provide a full three dimensional field distribution in cylindrical structures has been identified as one of the areas within electromechanics that still require much additional research.

1.4   Thesis contributions

The research challenge set out in this thesis is: **Derivation of a 3D analytical harmonic model to determine the electromagnetic field distribution in both regular and irregular shaped cylindrical devices.** To evaluate this 3D modeling technique in an application, a second research goal is defined: **Analysis and realization of a 2-DoF rotary-linear actuator for a pick and place application.**

The main contributions of this thesis are summarized as:

Extension of the two dimensional harmonic modeling technique to describe electromagnetic fields in three dimensional cylindrical structures. By means of this extended model, one can describe magnetic fields due to three dimensional permanent magnet arrays in or at cylindrical soft-magnetic tubes [86, 87, 92]. This includes irregular structures with:

- slots in the axial direction of a soft-magnetic tube,
- slots in the circumferential direction of a soft-magnetic tube,
- rectangular cavities in a soft-magnetic tube.

Description of an implementation method for the three dimensional harmonic model. The 3D harmonic modeling technique is based on Fourier series, and the resulting set of equations with unknown coefficients contains summations over these series. The described implementation method can be used to rewrite these equations in a matrix form to be able to obtain the values of the unknown coefficients [87].

Derivation of an analytical description of the passive electromagnetic force in three dimensional cylindrical structures. The force description is based on the Maxwell stress tensor method and employs the electromagnetic field solution in the airgap of an electromagnetic device, calculated by the aforementioned harmonic model [96].

Presentation of a novel permanent magnet array concept for a 2-DoF rotary-linear actuator. A patented magnetization concept is proposed which provides an additional parameter to vary the force-torque ratio within rotary-linear actuators, which is especially useful in applications where the required force and torque densities differ significantly [94, 126].

Introduction of possible realizations of the novel permanent magnet array. The provided realizations can be used in actuators that require a high force density and a reduced torque density [95].

Modeling of a 2-DoF actuator based on an innovative permanent magnet mover and stator. Using the aforementioned 3D modeling technique, a description of the magnetic field distribution in the actuator is obtained. Furthermore,

2D models are created to approximate the actuator enabling elaborated analyses [95].

Design of a 2-DoF actuator for a pick and place application. The aforementioned developed 2D and 3D models are used to obtain an actuator design having a high mover acceleration and low copper loss [91].

Realization of a prototype of the designed actuator. A prototype of the designed actuator with an integrated position sensor is successfully realized.

Experimental validation of the realized prototype in a lab environment. Various experiments are conducted to validate the models used to design the actuator. Furthermore, the performance of the actuator is validated with the requirements.

1.5   Thesis outline

The content of this thesis is split in three parts. The first part elaborates on extension of the harmonic electromagnetic modeling technique, while the second part presents application of this modeling technique to analyze and design a rotary-linear actuator. In the third part the conclusions are drawn and recommendations for future research are presented.

Part I: Modeling

Chapter 2 The harmonic modeling technique is extended to include the three dimensional effects in cylindrical structures. As such, by means of the technique presented in this chapter, one can model a broad class of cylindrical permanent magnet devices. The chapter focuses on model definition, creation of a model of an irregular shaped cylindrical structure and numerical implementation.

Chapter 3 In this chapter, the Maxwell stress tensor is used to calculate passive attraction forces in cylindrical structures. The magnetic field description presented in Chapter 2 is exploited, and analytical expressions are obtained which enable fast and accurate force calculations.

Part II: Application

Chapter 4 This chapter introduces two degree of freedom rotary-linear actuators and specifies the requirements of this type of actuator in a pick and place application. Prior-art rotary-linear actuators are discussed, and supporting and opposing arguments are provided for the presented actuator topologies.

Chapter 5 To obtain an actuator that complies with the requirements as given in Chapter 4, a new actuator topology is presented in Chapter 5. Possible realizations of this type of actuator are discussed, and one configuration is selected for further research. Analytical models for the selected configuration are derived and validated with finite element analyses.

Chapter 6 The analytical models, presented in Chapter 5, are utilized to analyze the selected configuration of the two degrees of freedom actuator. Winding configurations are explored, a thermal analysis is conducted, and the influence of the geometric parameters on the actuator performance is investigated. Subsequently, cogging and electromagnetic damping effects are evaluated. Based on this synthesis, a final actuator design is obtained, which meets the requirements set presented Chapter 4.

Chapter 7 The final design of the 2-DoF actuator, given in the Chapter 6, is realized for experimental verification. The realization of the stator and mover assembly is presented and manufacturing issues are mentioned. The prototype is tested in a lab environment and measurement results are discussed.

Part III: Closing

Chapter 8 In this chapter the main conclusions from the thesis are summarized. Furthermore, recommendations for future research are given.

Part I

Modeling

2

Harmonic modeling of electromagnetic fields in 3D cylindrical structures

Abstract - The harmonic modeling technique discussed in the previous chapter is extended to include the three dimensional electromagnetic effects in cylindrical structures. As such, by means of the technique presented in this chapter, one can model a broad class of cylindrical permanent magnet devices. The chapter starts with a short review on harmonic modeling and the definitions to describe cylindrical structures in 2D and 3D coordinate systems. Subsequently, a model of an example structure is defined, the boundary conditions are evaluated, and the model is validated by means of a finite element analysis.

This chapter is based on:

- K. J. Meessen, J. J. H. Paulides and E. A. Lomonova, "General Formulation of Fringing Fields in 3D Cylindrical Structures Using Fourier Analysis", *Transactions on Magnetics*, 48(8):2307-2323, 2012.

- K. J. Meessen, J. J. H. Paulides and E. A. Lomonova, "Analysis of 3-D Effects in Segmented Cylindrical Quasi-Halbach Magnet Arrays", *Transactions on Magnetics*, 47(4):727-733, 2011.

- K. J. Meessen, B. L. J. Gysen, J. J. H. Paulides and E. A. Lomonova, "Three-Dimensional Magnetic Field Modeling of a Cylindrical Halbach Array", *Transactions on Magnetics*, 46(6):1733-1736, 2010.

- K. J. Meessen, B. L. J. Gysen, J. J. H. Paulides and E. A. Lomonova, "Halbach Permanent Magnet Shape Selection for Slotless Tubular Actuators", *Transactions on Magnetics*, 44(11):4305-4308, 2008.

2.1   Introduction to harmonic modeling

The previous chapter discussed modeling techniques for electromagnetic devices. These analytical techniques provide the basis for fast and accurate analysis and design tools. This chapter elaborates on the harmonic modeling technique to describe 3D magneto-static fields by means of Fourier series. This technique, as introduced in Section 1.3.2, provides a direct solution for the Maxwell equations using separation of variables, and is widely described in literature.

2.1.1   2D magnetic field modeling

The method originates from Hague [43], who described the magnetic field from current carrying wires between two concentric iron cylinders representing a rotor and a stator of an electrical machine in 1929. In this problem, the airgap is the only region considered, and the two cylinders are assumed to have infinite permeability represented by a boundary condition. Mishkin [98] applied the method to model a squirrel-cage induction machine in 1953. However, only the fundamental harmonic of the magnetic field was considered. In 1984, Bolte calculated the magnetic field in both the airgap and the stator slots of an induction machine [13]. By using different spatial harmonics in the stator slots and airgap, he was the first to obtain a complete harmonic model taking into account the effect of the stator slots on the magnetic field in the airgap.

Permanent magnet devices

Since the availability of high-energy rare-earth permanent magnet materials as samarium-cobalt (SmCo) in the 1970s and neodymium-iron-boron (NdFeB) in the 1980s, the analytical calculation of magnetic fields in PM devices has received renewed interest. Numerous publications can be found on modeling of these devices. Boules described in [14] the magnetic fields in a cylindrical rotary machine in the cartesian coordinate system. The permanent magnets in this machine are described by equivalent currents as explained in Section 1.3.2. Furthermore, saturation is taken into account by iteratively varying the airgap length and the stator slotting is considered by means of the Carter coefficient. As the soft-magnetic parts of the machine are modeled having an infinite permeability, the problem consists of only two regions, the airgap and the magnet region. In [15] Boules describes the same structure in the polar coordinate system.

In the same period, Qishan calculated the magnetic field in the airgap of a PM machine by means of the magnetic scalar potential in the cartesian coordinate system [106]. Instead of using an equivalent current description, the permanent magnets are described by a Fourier expansion of the magnetization having a relative permeability equals one. The work was extended in [107] to include the effect of the stator slots on the magnetic field by means of the Carter factor. Subsequently, in 1986 Qishan presented a model to describe fringing due to the finite axial length of a PM electrical

machine [108]. To create a periodic model, he proposed a segmented permanent magnet model where multiple machines are repeated along the machine axis with a certain space between the subsequent machines. The variation along the armature periphery is ignored to reduce the 3D problem to a 2D one. Three regions are distinguished to represent the airgap, permanent magnets, and the space in between the machines. As described before by Bolte [13], different spatial harmonics were considered in the three regions to be able to solve the periodic boundary conditions in the permanent magnet and airgap region. By solving the continuous boundary conditions between the regions by means of mode matching, the fringing due to the finite machine length is modeled.

The aforementioned work describes radial and parallel magnetized PMs in the airgap of rotary machines. In [82] Marinescu complemented this with modeling of permanent magnets magnetized in multiple directions, in particular quasi-Halbach arrays. In 1993, Zhu extended the model by including the relative permeability of the permanent magnets in rotary machines [152]. Subsequently, he described the armature reaction field [149], and included the effect of the stator slots by means of a relative permeance function [150]. All these results were combined to obtain the total magnetic field distribution under load conditions in [151]. Ackermann used the mode matching technique to calculate the magnetic field in a rotary machine in the polar coordinate system [1]. The magnetic field formulation was derived from the magnetic vector potential, and the unknown coefficients were solved iteratively. Liu proposed in 2007 a matrix notation to solve the set of equations obtained by means of mode matching which avoids the iterative solving technique of Ackermann [78]. In [69] Kim introduced the analytical technique for predicting the magnetic field distribution in the airgap region of permanent magnet motors with rotor eccentricity. The governing equations and associated boundary conditions are formulated and solved using a perturbation method. Zhilichev approximated the magnetic fields in a structure with two eccentric cylinders in a cylindrical bipolar coordinate system [146].

Besides rotary electrical machines as presented above, the modeling technique is also applied to linear machines. In 1996 Trumper used the model to describe linear PM xy-stages with a magnetically levitating moving part [123]. The application to tubular linear machines was presented by Wang in [132], where a general framework is described to model various magnetization patterns in the axisymmetric coordinate system. He extended his work to describe tubular linear machines with an axially magnetized mover with soft-magnetic pole pieces in between the permanent magnets and having a non-magnetic core [130]. As such, this was the first paper where a structure was modeled with soft-magnetic blocks surrounded by material with a lower relative permeability. A similar approach as described by Quishan in [108] is applied to investigate the magnetic field at the stator ends of a tubular linear actuator by Wang in [128, 129]. The presented literature comprises the analysis of the magnetic field in electrical machines for slotless structures and structures that can be described by a single slot per airgap period. However, in most situations, the structure contains

multiple slots per airgap period to accommodate the three phase windings. For example, Dubas extended the theory to include an integer slot number per airgap period [30].

In the aforementioned work, the electromagnetic field distribution in two dimensional electromagnetic devices is described. Various papers present particular structures in different coordinate systems. A comprehensive overview of the harmonic modeling technique including model creation and a method to obtain and solve the various boundary conditions is provided by Gysen *et al.* [41]. The work includes the solution for the magnetic vector potential and magnetic flux density to describe fields due to permanent magnets and current sources in the cartesian, polar and axisymmetric coordinate system.

2.1.2   3D magnetic field modeling

The previous section shows that the harmonic modeling technique is widely applied to calculate magnetic fields in two dimensions. As a large number of electromagnetic devices have a negligible dependency in one of the three directions, they can be represented by a 2D model and the results are accurate enough for analysis and design purposes. If the structure does not possess invariancy in one direction, the 2D harmonic model can be extended to a 3D one by describing the sources by a 2D Fourier series instead of a 1D series.

In [133], for example, the magnetic fields in a spherical machine are described by a 3D harmonic model. As the field is described in the spherical coordinate system, sources and fields are expanded into spherical harmonics consisting of the associated Legendre polynomials. In disc-type actuators, neglecting one of the three dimensions to create a 2D model often introduces significant inaccuracies. Quasi-3D models are introduced to approximate the third dimension as shown in [7]. Zhilichev used a Fourier series in circumferential direction and a Hankel transformation over radial direction to create a 3D model. Instead of contiguous regions as used in the literature described before, he uses overlapping regions to model the complete geometry. Subsequently, the Schwartz's method is introduced to solve the boundary conditions of these overlapping regions iteratively [143]. An example of modeling magnetic fields in the 3D cartesian coordinate system is given in [20], where a 2D Fourier expansion is used to model magnetization patterns for planar motors. The last reviewed 3D model represents a cylindrical rotary electrical machine. The finite axial length of the machine as presented in 2D by Qishan [108], is modeled in 3D in [139, 145]. In [145] the permanent magnets are expressed by a 2D magnetization Fourier expansion while [139] uses a charge model to represent the magnets. In both papers, the scalar potential is calculated between two concentric infinitely long cylinders with permanent magnets with a finite axial length in between. As such, the edge effects at the ends of the permanent magnets are considered to investigate the effect of the finite length of rotary machines on their performance.

2.1.3 Model application

In the previous sections, magnetic field modeling by means of Fourier expansion for electromechanical permanent magnet devices is discussed. However, the real quantities of interest are the effects of these magnetic fields. These effects can be calculated from the magnetic field, or directly from the magnetic scalar or vector potential. A short overview of the application of the results of the harmonic model is presented below.

- Emf and force are calculated directly from the harmonic model to predict the actuator performance [127, 128].

- Armature reaction and inductance calculation [4, 6, 40] in tubular surface-inset permanent-magnet actuators, rotary slotless machines, tubular surface-mounted permanent magnet actuators.

- Cogging force calculation, by means of the harmonic model to calculate the airgap flux density and complex permeances to include the slotting effect [142]. Cogging force calculation in tubular actuators by considering the magnetic field in both the airgap and the slot regions [38].

- Unbalanced magnetic pull, forces in the radial direction due to an unbalanced magnetic circuit in rotary electrical machines [147, 153].

- End-effect forces in linear machines due to the finite stator length [129].

- Eddy current calculation in the non-magnetic conductive parts of electro-magnetic devices [5]. Instead of using the diffusion equation, the magnetic field is calculated by the Poisson equation (1.29), and the eddy current loss is approximated from the magnetic field distribution.

- Optimization and design of linear and rotary machines are presented in [39, 83], respectively.

- Control or commutation of planar actuators based on the magnetic field distribution calculated by the analytical model [57].

2.2   Modeling of cylindrical structures

The vast majority of electromagnetic devices have a cylindrical shape, since traditional rotating electrical machines are the most common devices to transform electrical energy in mechanical energy and vice versa. Two dimensional representations of the geometry of these machines are often used to model electromagnetic phenomena to avoid time-consuming 3D analyses. Representing a geometry in a 2D coordinate system implies that this geometry has no, or little, variation in one direction. As such, proper selection of a 2D coordinate system depends on the considered geometry.

2.2.1   2D representation in polar coordinates

The polar coordinate system defines a point in a 2D plane by its distance to the origin, r, and the angle, θ, to a reference as shown in Figure 2.1. To represent a cylindrical machine in the polar coordinate system, the cross-section has a circular shape, and the variation in the axial, z-, direction is neglected. As such, a geometry modeled in the polar coordinate system is assumed to be infinitely long. This coordinate system is widely used to represent rotating electrical machines and provides proper results if the axial length is sufficiently long to neglect the end-effects at the rotor and/or stator ends [152].

The general solution of the Laplace equation in this coordinate system can be found by means of separation of variables. The solution consists of a Fourier series in the
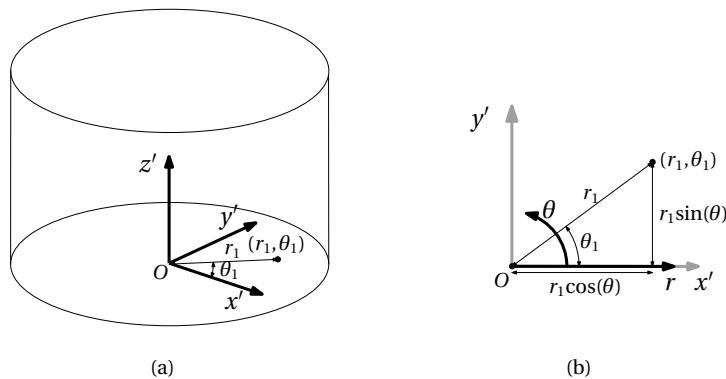
Figure 2.1: (a) A cylinder in the cartesian coordinate system. **(b)** Definition of a point (r_1,θ_1) in the 2D polar coordinate system (r,θ) defined with respect to cartesian coordinate system (x,y).

circumferential direction and a power function in the radial direction

$$
B_r(r,\theta) = \sum_{n=1}^{\infty} \left[\left(a_1 r^{w_n-1} + b_1 r^{-w_n-1} \right) \sin(w_n\theta) + \left(a_2 r^{w_n-1} + b_2 r^{-w_n-1} \right) \cos(w_n\theta) \right],
$$
(2.1)

$$
B_\theta(r,\theta) = \sum_{n=1}^{\infty} \left[\left(a_1 r^{w_n-1} - b_1 r^{-w_n-1} \right) \cos(w_n\theta) - \left(a_2 r^{w_n-1} - b_2 r^{-w_n-1} \right) \sin(w_n\theta) \right],
$$
(2.2)

where w_n is the spatial frequency with harmonic number n and a_1, a_2, b_1 and b_2 are unknown coefficients to be found by applying boundary conditions.

2.2.2   2D representation in the axisymmetric coordinates

The axisymmetric coordinate system defines a point in a 2D plane by its distance to the origin, r, and the distance to the x-y plane, z, illustrated in Figure 2.2. It can be seen that a point in the r-z plane is a circle in the three dimensional cartesian coordinate system. Therefore, to obtain a correct representation of a cylindrical machine in this coordinate system, the structure should have no, or limited, variation in the circumferential direction. An electromagnetic device that can be described in this coordinate system is the tubular linear actuator [11, 90, 132]. As this actuator has no variation in the circumferential direction, i.e. is axisymmetric, no assumption is necessary in the direction normal to the r-z plane to describe this three dimensional structure in a 2D coordinate system. Due to the choice of the Fourier series in the axial, z-, direction to describe the magnetic fields, the model implies symmetry or periodicity in the axial direction. To model the effects of a finite axial length of an axisymmetric structure, one can select the period of the Fourier series in the airgap equal to the total actuator length [128]. The finite length of a permanent magnet translator in a tubular actuator can be approximated by adjusting the period of the magnet array, discussed in Section 6.5.1.

The general solution of the Laplace equation in this coordinate system, obtained from the separation of variables technique, consists of a Fourier series in the axial direction and Bessel functions in the radial direction

$$
B_r(r,z) = \sum_{k=1}^{\infty} \left[\left(a_1 \mathcal{I}_1(m_k r) - b_1 \mathcal{K}_1(m_k r) \right) \sin(m_k z) \right.
$$
$$
\left. + \left(a_2 \mathcal{I}_1(m_k r) - b_2 \mathcal{I}_1(m_k r) \right) \cos(m_k z) \right], \quad (2.3)
$$

$$
B_z(r,z) = \sum_{k=1}^{\infty} \left[\left(a_1 \mathcal{I}_0(m_k r) + b_1 \mathcal{K}_0(m_k r) \right) \cos(m_k z) \right.
$$
$$
\left. - \left(a_2 \mathcal{I}_0(m_k r) + b_2 \mathcal{I}_0(m_k r) \right) \sin(m_k z) \right], \quad (2.4)
$$
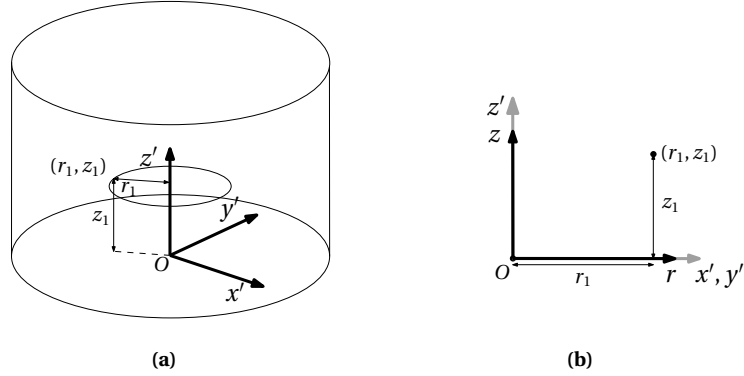
Figure 2.2: (a) A cylinder in the cartesian coordinate system. **(b)** Definition of a point (r_1, z_1) in the 2D axisymmetric coordinate system (r, z) defined with respect to cartesian coordinate system (x, y, z).

where m_k is the spatial frequency with harmonic number k and a_1, a_2, b_1 and b_2 are unknown coefficients to be found by applying boundary conditions. $\mathcal{I}_o(...)$ and $\mathcal{K}_o(...)$ are modified Bessel functions of the first and second kind, respectively, with order o.

2.2.3   Quasi-3D representations

If a cylindrical structure does not exhibit periodicity or symmetry in the axial or circumferential direction, representation of the structure in one of the previous coordinate system does not give accurate results. However, in some structures the magnetic field in the direction normal to the 2D coordinate system is small and can be neglected. In these structures, quasi-3D representations are often used to avoid a full three dimensional model. For example, to model a skewed rotary machine, a multi-sliced model is introduced [134]. The geometry of the machine is split into multiple slices in the axial direction which are rotated with respect to each other to represent skewing. The magnetic field of each slice is obtained using a calculation in the two dimensional polar coordinate system. The total magnetic field of all slices is obtained by superposition of the magnetic fields of the slices. The resulting magnetic field components in the radial and circumferential direction are a good approximation if the magnetic field in the axial direction, between two slices, can be neglected.

Another cylindrical machine that exhibits no periodicity in the axial or circumferential direction is the axial flux machine [36]. This class of machines consists of (at least) two parallel circular discs which rotate with respect to each other. As such, modeling this machine in the polar or axisymmetric coordinate system does not provide accurate results. In [7, 105], a quasi-3D model is presented that starts from a 2D field description in the θ-z plane with a Fourier series in the θ-direction. This plane can be interpreted as a plane in the cartesian, x-y, coordinate system. Consequently, the radial dependency of the flux density has to be included by
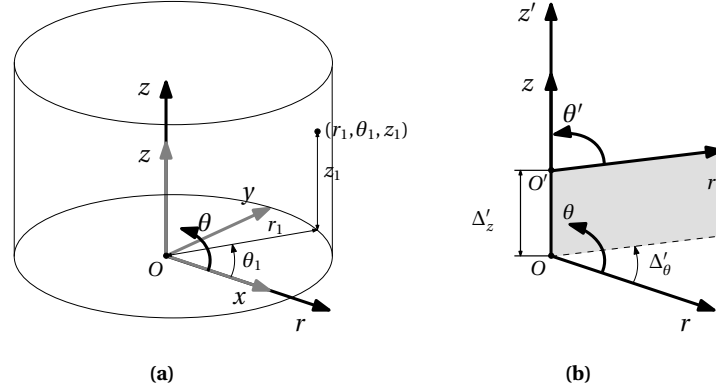
Figure 2.3: **(a)** Definition of a point (r_1, θ_1, z_1) in the 3D cylindrical coordinate system (r, θ, z) defined with respect to cartesian coordinate system (x, y, z). **(b)** Definition of transformation of local coordinate system (r', θ', z') with respect to (r, θ, z), where Δ_θ and Δ_z represent the displacement in the rotational and axial direction, respectively.

means of an approximation function to be able to describe the magnetic field in this cylindrical structure.

2.2.4 3D cylindrical structures

In three dimensional structures where the quasi-3D representation of a cylindrical structure does not provide an accurate description of the geometry, the cylindrical coordinate system can be used. The cylindrical coordinate system (r, θ, z), shown in Figure 2.3, is a combination of the polar and the axisymmetric coordinate system. A point in this coordinate system is defined by its distance to the z-axis, r, the angle around the z-axis in the x-y plane, θ, and the distance to the x-y plane in the cartesian coordinate system, z.

In this chapter, a 3D harmonic model is derived in the cylindrical coordinate system. By means of this model, magnetostatic fields originating from permanent magnets can be calculated in 3D cylindrical structures. These structures should exhibit (quasi-)periodicity or soft-magnetic boundaries in the axial and circumferential direction. However, contrary to the aforementioned 2D representations, the magnetic fields variation in three dimensions due to three dimensional permanent magnet arrays is taken into account . The structure can contain full soft-magnetic cylinders, cylinders containing slots in the axial and circumferential direction, and rectangular cavities. That is, also fringing fields can be predicted accurately. Examples of these 3D cylindrical structures are shown in Figure 2.4. The examples consist of a soft-magnetic core with a PM array, an airgap and a soft-magnetic cylinder enclosing the structure. The first structure, Figure 2.4(a), illustrates a slot in soft-magnetic cylinder in the circumferential direction. Figure 2.4(b) shows a slot in the axial direction, and in Figure 2.4(c) the soft-magnetic cylinder has a rectangular cavity.
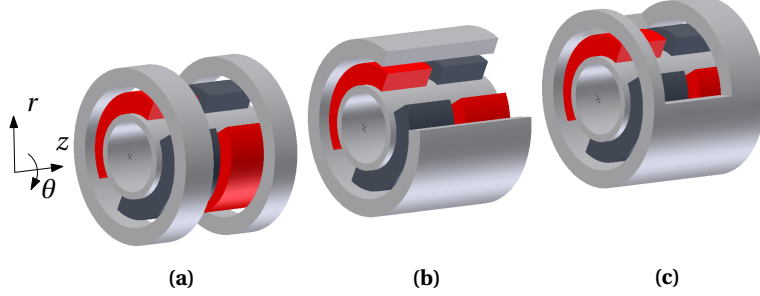
Figure 2.4: Examples of three dimensional structures consisting of a soft-magnetic core with a permanent magnet array, an airgap and a soft-magnetic cylinder enclosing the structure with **(a)** a slot in the circumferential direction, **(b)** a slot in the axial direction, and **(c)** a rectangular cavity.

2.3   Harmonic model definition

The harmonic model definition in the cylindrical coordinate system is similar to the model definition in the 2D coordinate systems which is extensively described in [41]. In the 2D coordinate systems, the magnetic field is described by a 1D Fourier series. In the polar coordinate system (Section 2.2.1), the Fourier series is defined in the θ-direction, and in the axisymmetric coordinate system (Section 2.2.2), the Fourier series is defined in the z-direction. The model in the cylindrical coordinate system as presented in this thesis is based on a 2D Fourier series to describe the magnetic field in the θ- and z-direction.

2.3.1   2D Fourier series

The 2D Fourier series to describe a function in the θ-z plane is defined as follows: Consider a periodic function f as function of θ and z, this function can be described by

$$
\begin{aligned}
f(\theta, z) = &\sum_{k=1}^{\infty} \sum_{n=1}^{\infty} c_1(k, n) \sin\left(\frac{2n\pi}{T_\theta}\theta\right) \sin\left(\frac{2k\pi}{T_z}z\right) + c_2(k, n) \sin\left(\frac{2n\pi}{T_\theta}\theta\right) \cos\left(\frac{2k\pi}{T_z}z\right) \\
&+ \sum_{k=1}^{\infty} \sum_{n=1}^{\infty} c_3(k, n) \cos\left(\frac{2n\pi}{T_\theta}\theta\right) \sin\left(\frac{2k\pi}{T_z}z\right) + c_4(k, n) \cos\left(\frac{2n\pi}{T_\theta}\theta\right) \cos\left(\frac{2k\pi}{T_z}z\right) \\
&+ \sum_{k=1}^{\infty} c_3(k, 0) \sin\left(\frac{2k\pi}{T_z}z\right) + c_4(k, 0) \cos\left(\frac{2k\pi}{T_z}z\right) \\
&+ \sum_{n=1}^{\infty} c_2(0, n) \sin\left(\frac{2n\pi}{T_\theta}\theta\right) + c_4(0, n) \cos\left(\frac{2n\pi}{T_\theta}\theta\right) + c_4(0, 0),
\end{aligned}
\tag{2.5}
$$

where T_θ is the fundamental period of the function f in the circumferential direction, and T_z is the fundamental period in the axial direction. Furthermore, n and k are the harmonic number of the Fourier series in the θ- and z-direction, respectively. The

unknown coefficients $c_1(k,n)$ to $c_4(k,n)$ can be found by solving the following integrals

$$c_1(k,n) = \frac{4}{T_z T_\theta} \int_0^{T_z} \int_0^{T_\theta} f(\theta,z) \sin\left(\frac{2n\pi}{T_\theta}\theta\right) \sin\left(\frac{2k\pi}{T_z}z\right) \mathrm{d}\theta \mathrm{d}z, \tag{2.6}$$

$$c_2(k,n) = \frac{4}{s T_z T_\theta} \int_0^{T_z} \int_0^{T_\theta} f(\theta,z) \sin\left(\frac{2n\pi}{T_\theta}\theta\right) \cos\left(\frac{2k\pi}{T_z}z\right) \mathrm{d}\theta \mathrm{d}z, \tag{2.7}$$

$$c_3(k,n) = \frac{4}{s T_z T_\theta} \int_0^{T_z} \int_0^{T_\theta} f(\theta,z) \cos\left(\frac{2n\pi}{T_\theta}\theta\right) \sin\left(\frac{2k\pi}{T_z}z\right) \mathrm{d}\theta \mathrm{d}z, \tag{2.8}$$

$$c_4(k,n) = \frac{4}{s T_z T_\theta} \int_0^{T_z} \int_0^{T_\theta} f(\theta,z) \cos\left(\frac{2n\pi}{T_\theta}\theta\right) \cos\left(\frac{2k\pi}{T_z}z\right) \mathrm{d}\theta \mathrm{d}z, \tag{2.9}$$

where

$$s = \begin{cases} 1 & \text{for} \quad n > 0, \quad k > 0, \\ 2 & \text{for} \quad n = 0, \quad k > 0, \\ 2 & \text{for} \quad n > 0, \quad k = 0, \\ 4 & \text{for} \quad n = 0, \quad k = 0. \end{cases} \tag{2.10}$$

The variable s is used in the definition of the DC-components in the two directions in the Fourier series.

Tangential and normal direction

Due to the definition of the Fourier series in the θ-z plane, a strong similarity is found in the analysis between the θ- and z-direction. Therefore, the circumferential, θ-, and axial, z-, direction are referred to as the *tangential* direction, and the radial, r-direction is referred to as the *normal* direction.

2.3.2   Model assumptions

To reduce the complexity of the electromagnetic model, the following geometrical and physical assumptions are considered:

1. All material properties are linear, homogeneous and isotropic.

2. The soft-magnetic parts are infinitely permeable.

3. The problem can be described by periodicity in the axial direction or has soft-magnetic interfaces normal to the axial direction.

4. The problem can be described by periodicity in the circumferential direction or has soft-magnetic interfaces normal to the circumferential direction.

5. The problem is current free.

The analytical field solution considers linear, homogeneous and isotropic material properties, hence no saturation, local or global, is taken into account. The permanent magnets are modeled with a linear B-H characteristic, a remanent flux density, B_{rem}, and a relative permeability, μ_{r}.

The soft-magnetic parts within the considered domain are modeled with infinite permeability. This implies that the magnetic field is not calculated in these parts, and that the material is represented by a boundary condition at its surface. Instead of modeling the soft-magnetic parts with an infinite permeability, a finite permeability can be considered under the constraints presented in the next section. Although the permeability of soft-magnetic materials is inherently non-linear, the infinite permeability assumption provides valid results in many devices. Generally, the magnetic circuit contains an airgap and often PMs which have a permeability close to one. As a result, the permeability of these parts is dominant in the flux path and the reduced permeability of the soft-magnetic parts introduces a minor error. Further, the non-linear material properties can be minimized by limiting the magnetic flux density in the material by predicting this flux density by means of a magnetic circuit, and adjusting the geometry accordingly, explained in Section 6.4.4.

The magnetic scalar potential is used to solve the Maxwell equations, as such, the complete domain has to be current free. This implies that the only source terms in the domain are permanent magnets.

2.3.3   Division in regions

To obtain the magnetic field distribution in the structure, the complete structure is divided into concentric orthogonal regions. Within these regions, the field distribution in the tangential direction is described by a Fourier series. The function describing the field distribution in the normal direction follows from the solution of the differential equation in the cylindrical coordinate system and is given in Section 2.4.

Four types of regions can be distinguished each having the following properties:

1. Each region has six interfaces which coincides with a plane having one of its coordinates constant and is either parallel or orthogonal to the other interfaces.

2. A source, if any, is invariant in the radial direction.

3. The permeability within the region is constant.

4. Adjacent regions in the tangential direction have the same permeability.

5. Each interface normal to the tangential direction is either periodic or soft-magnetic with an infinite permeability.
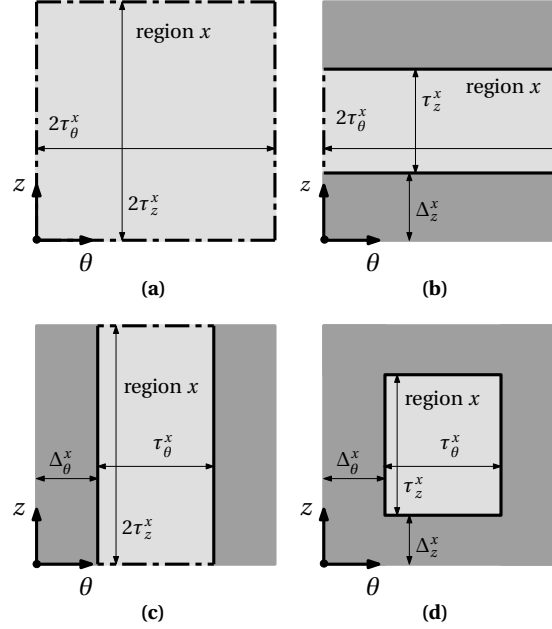
Figure 2.5: Definition of four types of regions considered in this chapter. **(a)** Region with periodicity in both tangential directions. **(b)** Region with periodicity in the θ-direction and soft-magnetic interfaces at $z = \Delta_z$ and $z = \Delta_z^x + \tau_z^x$. **(c)** Region with periodicity in the axial direction and soft-magnetic interfaces at $\theta = \Delta_\theta^x$ and $\theta = \Delta_\theta^x + \tau_\theta^x$. **(d)** Region with soft-magnetic interfaces at $z = \Delta_z^x$, $z = \Delta_z^x + \tau_z^x$, $\theta = \Delta_\theta^x$ and $\theta = \Delta_\theta^x + \tau_\theta^x$.

Each region should have at least two interfaces in the radial direction, and the sources in these regions have to be invariant in the radial direction. This implies that for example trapezoidal permanent magnets or soft-magnetic shapes cannot be considered as a single region. A method to model these shapes is presented in [85] by Meessen *et al.*, where trapezoidal shaped permanent magnets are approximated using a finite number of stacked rectangular shaped permanent magnets.

Since the permeability within a region has to be constant, a region with an array of consecutive PMs with air in between can only be modeled having a constant permeability. However, the permeability of the PMs is generally 5-10% higher than the permeability of vacuum. As the space (air) between the PMs in a PM array is generally small, modeling this space having the same permeability as the permanent magnets introduces only a minor error. If the material adjacent to a region is soft-magnetic, this material can only be modeled as a material having an infinite permeability.

In Figures 2.5 and 2.6, the four region types are shown where x is the region number of interest. These regions are defined by:

1. Figure 2.5(a) : A region with periodicity in both tangential directions and a width
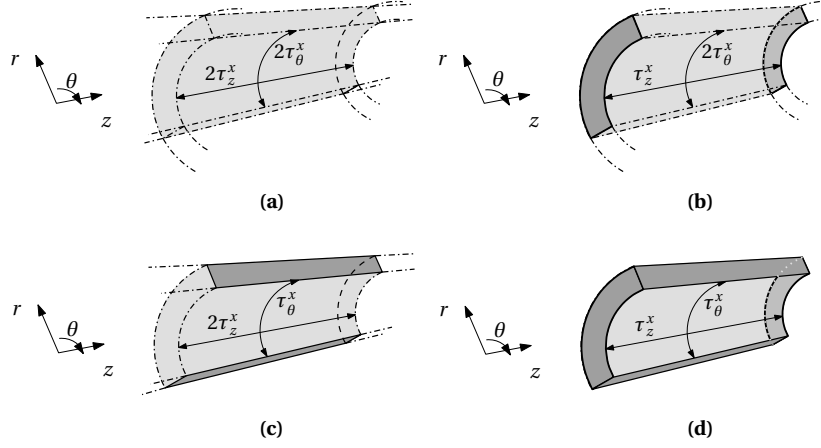
Figure 2.6: Three dimensional view of the four region types defined in Figure 2.5.

of $2\tau_z^x$ in the axial direction and a width of $2\tau_\theta^x$ in the circumferential direction.

2. Figure 2.5(b) : A region representing a slot in soft-magnetic material in the circumferential direction is shown. The region has periodicity in the θ-direction and soft-magnetic interfaces at $z = \Delta_z$ and $z = \Delta_z^x + \tau_z^x$. The width of the slot is τ_z^x and the width in the circumferential direction is $2\tau_\theta^x$.

3. Figure 2.5(c) : A region representing a slot in soft-magnetic material in the axial direction having periodicity in the z-direction and soft-magnetic interfaces at $\theta = \Delta_\theta^x$ and $\theta = \Delta_\theta^x + \tau_\theta^x$ and a slot width of τ_θ^x. The width in the axial direction is $2\tau_\theta^x$.

4. Figure 2.5(d) : A rectangular cavity in soft-magnetic material with soft-magnetic interfaces at the sides. This region has a width of τ_z^x in the axial direction and a width of τ_θ^x in the circumferential direction.

In conclusion, the width of a region with soft-magnetic boundaries is τ^x while the width of a periodic region is $2\tau^x$, the reason for this choice is explained in Section 2.5.

To simplify and generalize the magnetic field description in all regions, each of them has its local coordinate system that is shifted in the axial direction, or rotated in the circumferential direction. This local coordinate system is defined by

$$r^x = r, \tag{2.11}$$
$$\theta^x = \theta - \Delta_\theta^x, \tag{2.12}$$
$$z^x = z - \Delta_z^x, \tag{2.13}$$

where x is the region of interest, and Δ_θ^x and Δ_z^x are the offsets in the circumferential and axial direction, respectively, as shown in Figure 2.3(b). Using these local coordi-
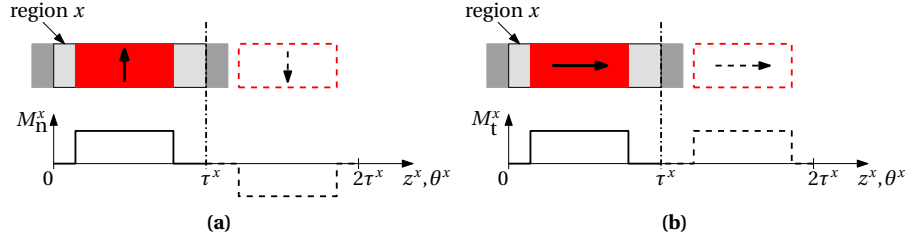
Figure 2.7: Source description in a region with soft-magnetic boundaries. Using the imaging method [43]. **(a)** A permanent magnet with normal magnetization has to be mirrored with respect to the surface $z^x = \tau^x$ and/or $\theta^x = \tau^x$. **(b)** A permanent magnet with a tangential magnetization has to be repeated.

nate systems, regions can be displaced with respect to each other which is useful when a structure consists of a combination of the aforementioned regions.

The fundamental period of a Fourier series in a periodic region is defined by the periodicity of the geometry or the sources in the region. To simplify the analysis in a structure with multiple periodic regions, the fundamental period, $2\tau^x$, of all periodic regions in a structure is equal. If the period of the geometry is different than the period of the sources, one should select the largest period as the fundamental period for all periodic regions.

2.3.4 Magnetic sources

Because the magnetic scalar potential is used in this analysis, only permanent magnets can be considered as sources. In all four types of regions shown in Figure 2.5, sources can be described by the remanent magnetization vector, defined in (1.11). This vector has to be described using a Fourier series, where the coefficients can be obtained using a Fourier expansion, defined in (2.6) to (2.9), where the fundamental period, T_θ or T_z, is equal to the width of the region, $2\tau^x$.

Since the width of a region with soft-magnetic boundaries is τ^x, illustrated in Figure 2.5(b,c,d)), and the fundamental period of the Fourier series is $2\tau^x$, only half of the period of the Fourier series describes the physical magnet. Therefore, the magnetization definition has to be extended to describe a complete period using the imaging method [43]. The resulting remanent magnetization vector is shown in Figure 2.7(a,b). As can be seen, for the normal component of the magnetization, the PM has to be mirrored with respect to the plane $z^x = \tau^x$ and/or $\theta^x = \tau^x$ (Figure 2.7(a)), while for the tangential component of the magnetization, the PM has to be repeated without mirroring (Figure 2.7(a)). Consequently, the Fourier series describing the normal component of the magnetization contains only sine terms, and the Fourier series of the tangential component contains only cosine terms. By applying equations (2.6) to (2.9) to the waveforms shown in Figure 2.7(a,b), the required Fourier coefficients of the magnetization can be found.
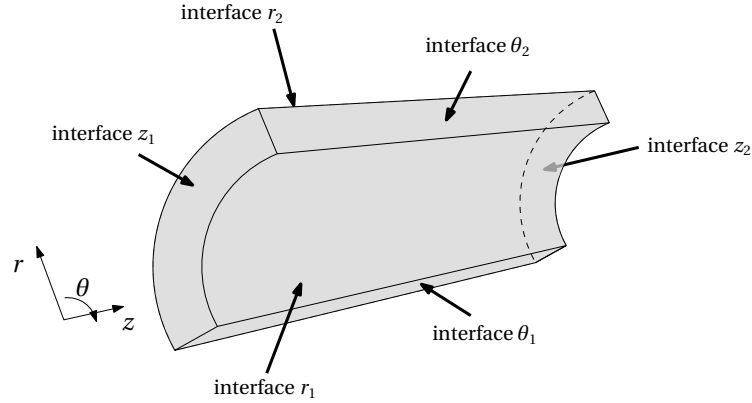
Figure 2.8: Definition of the interfaces of a region.

2.3.5 Boundary conditions

The harmonic modeling technique can be considered as a boundary value problem. In these problems, a solution to a differential equation in a region with constraints on its boundaries is obtained [34]. Boundary value problems can often be solved analytically when each interface of the region coincides with a plane having one of its coordinates constant in a curvilinear orthogonal coordinate system. To obtain the field solution in the complete structure, three general boundary conditions have to be applied as derived in Section 1.1.4:

1. The tangential component of the magnetic field strength, $\vec{H}$, is continuous at the interfaces of a region.

2. The normal component of the magnetic flux density, $\vec{B}$, is continuous at the interfaces of a region.

3. The magnetic scalar potential, φ, is zero at the center of the coordinate system ($r = 0$) and at infinity.

The boundary conditions have to be applied on the six interfaces of a region as shown in Figure 2.8 and can be subdivided into boundary conditions on:

1. interfaces normal to the tangential direction, i.e., on interfaces θ_1, θ_2, z_1 and z_2,

2. interfaces normal to the radial direction, i.e., on interfaces r_1 and r_2.

The evaluation of these boundary conditions is discussed in Section 2.5 and Section 2.6.

2.4   Harmonic field and source description

The magnetic field in the θ-z plane is described by a 2D Fourier series. To complete the 3D magnetic field description, the Fourier components have to be a function of the radial position, r. In this section the complete description of the magnetic field is given derived from the magnetic scalar potential. Using the Laplace equation, defined in (1.34), the homogeneous solution for the magnetic scalar potential can be found. The Poisson equation (1.33) provides the non-homogeneous solution of the magnetic scalar potential defined due to the 2D Fourier description of the magnetization. The complete description of the magnetic scalar potential can be found using the separation of variables technique [16], that is

$$\varphi^x(r,\theta,z) = R(r)\Theta(\theta)Z(z). \tag{2.14}$$

A general solution for $\Theta(\theta)$ and $Z(z)$ that satisfies equations (1.33) and (1.34) is a Fourier series as used in the previous sections

$$\Theta(\theta) = \sum_{n=1}^{\infty} \left(c_1 \sin\left(w_n \theta\right) + c_2 \cos\left(w_n \theta\right) \right), \tag{2.15}$$

$$Z(z) = \sum_{k=1}^{\infty} \left(c_3 \sin\left(m_k z\right) + c_4 \cos\left(m_k z\right) \right). \tag{2.16}$$

The solution for the radial function $R(r)$ is a set of different functions where the one that has to be selected depends on the value of the harmonic numbers k and n [34]

$$R(r) = \begin{cases} c_6 & \text{for} \quad n = 0, k = 0, \\ c_5 r^{w_n} + c_6 r^{-w_n} & \text{for} \quad n > 0, k = 0, \\ c_5 \mathcal{I}_{w_n}\left(m_k r\right) + c_6 \mathcal{K}_{w_n}\left(m_k r\right) & \text{for} \quad n \geq 0, k > 0. \end{cases} \tag{2.17}$$

It can be seen that the solution of $R(r)$ for $n > 0, k = 0$ is the same as in the polar coordinate system presented in Section 2.2.1, while the solution for $R(r)$ for $k > 0, n = 0$ is the solution in the axisymmetric coordinate system, presented in Section 2.2.2. A combination of these functions provides the total solution in the cylindrical coordinate system. From this general form an expression for the magnetic

scalar potential is obtained in the following form

$$
\begin{aligned}
\varphi^x(r,\theta,z) = {} & - \sum_{k=1}^{\infty} \sum_{n=1}^{\infty} \frac{1}{m_k} \Big(\mathcal{R}_7^x(r,k,n) + \mathcal{G}_{\varphi 1}^{\mathrm{x}}(r,k,n) \Big) \sin(w_n\theta)\sin(m_k z) \\
& - \sum_{k=1}^{\infty} \sum_{n=1}^{\infty} \frac{1}{m_k} \Big(\mathcal{R}_8^x(r,k,n) + \mathcal{G}_{\varphi 2}^{\mathrm{x}}(r,k,n) \Big) \sin(w_n\theta)\cos(m_k z) \\
& - \sum_{k=1}^{\infty} \sum_{n=0}^{\infty} \frac{1}{m_k} \Big(\mathcal{R}_9^x(r,k,n) + \mathcal{G}_{\varphi 3}^{\mathrm{x}}(r,k,n) \Big) \cos(w_n\theta)\sin(m_k z) \\
& - \sum_{k=1}^{\infty} \sum_{n=0}^{\infty} \frac{1}{m_k} \Big(\mathcal{R}_{10}^x(r,k,n) + \mathcal{G}_{\varphi 4}^{\mathrm{x}}(r,k,n) \Big) \cos(w_n\theta)\cos(m_k z) \\
& + \sum_{n=1}^{\infty} \frac{1}{w_n} \Big(\mathcal{R}_{11}^x(r,n) + \mathcal{G}_{\varphi 5}^{\mathrm{x}}(r,n) \Big) \sin(w_n\theta) \\
& + \sum_{n=1}^{\infty} \frac{1}{w_n} \Big(\mathcal{R}_{12}^x(r,n) + \mathcal{G}_{\varphi 6}^{\mathrm{x}}(r,n) \Big) \cos(w_n\theta) \\
& + \mathcal{R}_{13}^{\mathrm{x}}(r) + \mathcal{G}_{\varphi 7}^{\mathrm{x}}(r),
\end{aligned}
\tag{2.18}
$$

where $\mathcal{R}$ is the homogeneous solution and $\mathcal{G}$ the non-homogeneous solution for the Poisson equation as given in Appendix B.2. Hence, $\mathcal{G}$ is zero in the source free regions.

Field description

By means of the definition of the magnetic scalar potential, equation (1.32), the magnetic field strength can be obtained

$$
\begin{aligned}
H_r^{\mathrm{x}}(r,\theta,z) = {} & \sum_{k=1}^{\infty} \sum_{n=1}^{\infty} \frac{1}{2} \Big(\mathcal{R}_1^x(r,k,n) + \mathcal{G}_{r1}^{\mathrm{x}}(r,k,n) \Big) \sin(w_n\theta)\sin(m_k z) \\
& + \sum_{k=1}^{\infty} \sum_{n=1}^{\infty} \frac{1}{2} \Big(\mathcal{R}_2^x(r,k,n) + \mathcal{G}_{r2}^{\mathrm{x}}(r,k,n) \Big) \sin(w_n\theta)\cos(m_k z) \\
& + \sum_{k=1}^{\infty} \sum_{n=0}^{\infty} \frac{1}{2} \Big(\mathcal{R}_3^x(r,k,n) + \mathcal{G}_{r3}^{\mathrm{x}}(r,k,n) \Big) \cos(w_n\theta)\sin(m_k z) \\
& + \sum_{k=1}^{\infty} \sum_{n=0}^{\infty} \frac{1}{2} \Big(\mathcal{R}_4^x(r,k,n) + \mathcal{G}_{r4}^{\mathrm{x}}(r,k,n) \Big) \cos(w_n\theta)\cos(m_k z) \\
& - \sum_{n=1}^{\infty} \Big(\mathcal{R}_5^x(r,n) + \mathcal{G}_{r5}^{\mathrm{x}}(r,n) \Big) \sin(w_n\theta) \\
& - \sum_{n=1}^{\infty} \Big(\mathcal{R}_6^x(r,n) + \mathcal{G}_{r6}^{\mathrm{x}}(r,n) \Big) \cos(w_n\theta) \\
& - \mathcal{G}_{r7}^{\mathrm{x}},
\end{aligned}
\tag{2.19}
$$

$$
\begin{aligned}
H_\theta^{\mathrm{x}}(r,\theta,z) = {}& \sum_{k=1}^{\infty}\sum_{n=1}^{\infty}\frac{w_n}{m_k r}\Big(\mathcal{R}_7^x{}_{(r,k,n)}+\mathcal{G}_{\theta 1}^{\mathrm{x}}{}_{(r,k,n)}\Big)\cos(w_n\theta)\sin(m_k z) \\
& + \sum_{k=1}^{\infty}\sum_{n=1}^{\infty}\frac{w_n}{m_k r}\Big(\mathcal{R}_8^x{}_{(r,k,n)}+\mathcal{G}_{\theta 2}^{\mathrm{x}}{}_{(r,k,n)}\Big)\cos(w_n\theta)\cos(m_k z) \\
& - \sum_{k=1}^{\infty}\sum_{n=1}^{\infty}\frac{w_n}{m_k r}\Big(\mathcal{R}_9^x{}_{(r,k,n)}+\mathcal{G}_{\theta 3}^{\mathrm{x}}{}_{(r,k,n)}\Big)\sin(w_n\theta)\sin(m_k z) \\
& - \sum_{k=1}^{\infty}\sum_{n=1}^{\infty}\frac{w_n}{m_k r}\Big(\mathcal{R}_{10}^x{}_{(r,k,n)}+\mathcal{G}_{\theta 4}^{\mathrm{x}}{}_{(r,k,n)}\Big)\sin(w_n\theta)\cos(m_k z) \\
& - \sum_{n=1}^{\infty}\Big(\mathcal{R}_{11}^x{}_{(r,n)}+\mathcal{G}_{\theta 5}^{\mathrm{x}}{}_{(r,n)}\Big)\cos(w_n\theta) \\
& + \sum_{n=1}^{\infty}\Big(\mathcal{R}_{12}^x{}_{(r,n)}+\mathcal{G}_{\theta 6}^{\mathrm{x}}{}_{(r,n)}\Big)\sin(w_n\theta), \qquad\qquad (2.20)
\end{aligned}
$$

$$
\begin{aligned}
H_z^{\mathrm{x}}(r,\theta,z) = {}& \sum_{k=1}^{\infty}\sum_{n=1}^{\infty}\Big(\mathcal{R}_7^x{}_{(r,k,n)}+\mathcal{G}_{z1}^{\mathrm{x}}{}_{(r,k,n)}\Big)\sin(w_n\theta)\cos(m_k z) \\
& - \sum_{k=1}^{\infty}\sum_{n=1}^{\infty}\Big(\mathcal{R}_8^x{}_{(r,k,n)}+\mathcal{G}_{z2}^{\mathrm{x}}{}_{(r,k,n)}\Big)\sin(w_n\theta)\sin(m_k z) \\
& + \sum_{k=1}^{\infty}\sum_{n=0}^{\infty}\Big(\mathcal{R}_9^x{}_{(r,k,n)}+\mathcal{G}_{z3}^{\mathrm{x}}{}_{(r,k,n)}\Big)\cos(w_n\theta)\cos(m_k z) \\
& - \sum_{k=1}^{\infty}\sum_{n=0}^{\infty}\Big(\mathcal{R}_{10}^x{}_{(r,k,n)}+\mathcal{G}_{z4}^{\mathrm{x}}{}_{(r,k,n)}\Big)\cos(w_n\theta)\sin(m_k z), \qquad\qquad (2.21)
\end{aligned}
$$

where $\mathcal{R}$, the homogeneous solution, consists of two parts; the unknown coefficients, $a_{\ldots}^x$ and $b_{\ldots}^x$, that have to be found by applying the boundary conditions and a part that describes the r-dependency of the magnetic field in a region

$$
\begin{aligned}
\mathcal{R}_1^x(r,k,n) = {}& a_1^x{}_{(k,n)}\big(\mathcal{I}_{w_n-1}(m_k r)+\mathcal{I}_{w_n+1}(m_k r)\big) \\
& - b_1^x{}_{(k,n)}\big(\mathcal{K}_{w_n-1}(m_k r)+\mathcal{K}_{w_n+1}(m_k r)\big), \quad (2.22)
\end{aligned}
$$

$$
\begin{aligned}
\mathcal{R}_2^x(r,k,n) = {}& a_2^x{}_{(k,n)}\big(\mathcal{I}_{w_n-1}(m_k r)+\mathcal{I}_{w_n+1}(m_k r)\big) \\
& - b_2^x{}_{(k,n)}\big(\mathcal{K}_{w_n-1}(m_k r)+\mathcal{K}_{w_n+1}(m_k r)\big), \quad (2.23)
\end{aligned}
$$

$$
\begin{aligned}
\mathcal{R}_3^x(r,k,n) = {}& a_3^x{}_{(k,n)}\big(\mathcal{I}_{w_n-1}(m_k r)+\mathcal{I}_{w_n+1}(m_k r)\big) \\
& - b_3^x{}_{(k,n)}\big(\mathcal{K}_{w_n-1}(m_k r)+\mathcal{K}_{w_n+1}(m_k r)\big), \quad (2.24)
\end{aligned}
$$

$$
\begin{aligned}
\mathcal{R}_4^x(r,k,n) = {}& a_4^x{}_{(k,n)}\big(\mathcal{I}_{w_n-1}(m_k r)+\mathcal{I}_{w_n+1}(m_k r)\big) \\
& - b_4^x{}_{(k,n)}\big(\mathcal{K}_{w_n-1}(m_k r)+\mathcal{K}_{w_n+1}(m_k r)\big), \quad (2.25)
\end{aligned}
$$

$$\mathcal{R}_5^x(r,n) = a_5^x(n) r^{w_n-1} + b_5^x(n) r^{-w_n-1}, \tag{2.26}$$

$$\mathcal{R}_6^x(r,n) = a_6^x(n) r^{w_n-1} + b_6^x(n) r^{-w_n-1}, \tag{2.27}$$

$$\mathcal{R}_7^x(r,k,n) = a_1^x(k,n) \mathcal{I}_{w_n}(m_k r) + b_1^x(k,n) \mathcal{K}_{w_n}(m_k r), \tag{2.28}$$

$$\mathcal{R}_8^x(r,k,n) = a_2^x(k,n) \mathcal{I}_{w_n}(m_k r) + b_2^x(k,n) \mathcal{K}_{w_n}(m_k r), \tag{2.29}$$

$$\mathcal{R}_9^x(r,k,n) = a_3^x(k,n) \mathcal{I}_{w_n}(m_k r) + b_3^x(k,n) \mathcal{K}_{w_n}(m_k r), \tag{2.30}$$

$$\mathcal{R}_{10}^x(r,k,n) = a_4^x(k,n) \mathcal{I}_{w_n}(m_k r) + b_4^x(k,n) \mathcal{K}_{w_n}(m_k r), \tag{2.31}$$

$$\mathcal{R}_{11}^x(r,n) = a_5^x(n) r^{w_n-1} - b_5^x(n) r^{-w_n-1}, \tag{2.32}$$

$$\mathcal{R}_{12}^x(r,n) = a_6^x(n) r^{w_n-1} - b_6^x(n) r^{-w_n-1}, \tag{2.33}$$

$$\mathcal{R}_{13}^x(r) = a_7^x. \tag{2.34}$$

Source description

The method to describe permanent magnets by means of the remanent magnetization vector is introduced in Section 2.3.4. To be able to use the magnetization in the analysis, the Fourier terms are defined in the same form as the magnetic field strength in the previous section. As such, the general description of the magnetization, consisting of three components, is described by

$$\vec{M}_0 = \frac{B_{\mathrm{rem}}}{\mu_0} \left(M_r \vec{e}_r + M_\theta \vec{e}_\theta + M_z \vec{e}_z \right) \tag{2.35}$$

$$
\begin{aligned}
M_r(\theta,z) = &\sum_{k=1}^{\infty} \sum_{n=1}^{\infty} M_{rss}(k,n) \sin(w_n\theta) \sin(m_k z) + M_{rsc}(k,n) \sin(w_n\theta) \cos(m_k z) \\
&+ \sum_{k=1}^{\infty} \sum_{n=0}^{\infty} M_{rcs}(k,n) \cos(w_n\theta) \sin(m_k z) + M_{rcc}(k,n) \cos(w_n\theta) \cos(m_k z) \\
&+ \sum_{n=1}^{\infty} M_{rs}(n) \sin(w_n\theta) + M_{rc}(n) \cos(w_n\theta) + M_{r0},
\end{aligned}
\tag{2.36}
$$

$$
\begin{aligned}
M_\theta(\theta,z) = &\sum_{k=1}^{\infty} \sum_{n=1}^{\infty} M_{\theta ss}(k,n) \sin(w_n\theta) \sin(m_k z) + M_{\theta sc}(k,n) \sin(w_n\theta) \cos(m_k z) \\
&+ \sum_{k=1}^{\infty} \sum_{n=0}^{\infty} M_{\theta cs}(k,n) \cos(w_n\theta) \sin(m_k z) + M_{\theta cc}(k,n) \cos(w_n\theta) \cos(m_k z) \\
&+ \sum_{n=1}^{\infty} M_{\theta s} \sin(w_n\theta) + M_{\theta c} \cos(w_n\theta) + M_{\theta 0},
\end{aligned}
\tag{2.37}
$$

$$
\begin{aligned}
M_z(\theta, z) = &\sum_{k=1}^{\infty} \sum_{n=1}^{\infty} M_{zss}(k,n) \sin(w_n\theta) \sin(m_k z) + M_{zsc}(k,n) \sin(w_n\theta) \cos(m_k z) \\
&+ \sum_{k=1}^{\infty} \sum_{n=0}^{\infty} M_{zcs}(k,n) \cos(w_n\theta) \sin(m_k z) + M_{zcc}(k,n) \cos(w_n\theta) \cos(m_k z) \\
&+ \sum_{n=1}^{\infty} M_{zs} \sin(w_n\theta) + M_{zc} \cos(w_n\theta) + M_{z0}.
\end{aligned} \tag{2.38}
$$

Using Fourier expansion defined by (2.6) to (2.9), the magnetization coefficients can be found using the following relations

$$
M_{xss} = \frac{1}{s\tau_z\tau_\theta} \int_0^{2\tau_z} \int_0^{2\tau_\theta} M_x(\theta, z) \sin(w_n\theta) \sin(m_k z) \mathrm{d}\theta \mathrm{d}z \qquad \text{for } k > 0, \tag{2.39}
$$

$$
M_{xsc} = \frac{1}{s\tau_z\tau_\theta} \int_0^{2\tau_z} \int_0^{2\tau_\theta} M_x(\theta, z) \sin(w_n\theta) \cos(m_k z) \mathrm{d}\theta \mathrm{d}z \qquad \text{for } k > 0, \tag{2.40}
$$

$$
M_{xcs} = \frac{1}{s\tau_z\tau_\theta} \int_0^{2\tau_z} \int_0^{2\tau_\theta} M_x(\theta, z) \cos(w_n\theta) \sin(m_k z) \mathrm{d}\theta \mathrm{d}z \qquad \text{for } k > 0, \tag{2.41}
$$

$$
M_{xcc} = \frac{1}{s\tau_z\tau_\theta} \int_0^{2\tau_z} \int_0^{2\tau_\theta} M_x(\theta, z) \cos(w_n\theta) \cos(m_k z) \mathrm{d}\theta \mathrm{d}z \qquad \text{for } k > 0, \tag{2.42}
$$

$$
M_{xs} = \frac{1}{2\tau_z\tau_\theta} \int_0^{2\tau_z} \int_0^{2\tau_\theta} M_x(\theta, z) \sin(w_n\theta) \mathrm{d}\theta \mathrm{d}z \qquad \text{for } n > 0, \tag{2.43}
$$

$$
M_{xc} = \frac{1}{2\tau_z\tau_\theta} \int_0^{2\tau_z} \int_0^{2\tau_\theta} M_x(\theta, z) \cos(w_n\theta) \mathrm{d}\theta \mathrm{d}z \qquad \text{for } n > 0, \tag{2.44}
$$

$$
M_{x0} = \frac{1}{4\tau_z\tau_\theta} \int_0^{2\tau_z} \int_0^{2\tau_\theta} M_x(\theta, z) \mathrm{d}\theta \mathrm{d}z, \tag{2.45}
$$

where x denotes the magnetization component of interest, i.e. r, θ or z and

$$
s = \begin{cases} 1 & \text{for } n > 0, \\ 2 & \text{for } n = 0. \end{cases} \tag{2.46}
$$

2.5 Boundary conditions on interfaces θ_1, θ_2, z_1 and z_2

The magnetic field as a function of the tangential direction is described by a Fourier series, hence, boundary conditions on the interfaces θ_1, θ_2, z_1 and z_2 are inherently solved by selecting the proper fundamental period of the Fourier series. In the 2D Fourier series, used in this analysis, two spatial frequencies are defined,

$$
w_n = \frac{n\pi}{\tau_\theta}, \tag{2.47}
$$

$$
m_k = \frac{k\pi}{\tau_z}. \tag{2.48}
$$

For both Fourier series holds that the fundamental frequency is equal to 2τ. In Figure 2.5, the relation between the width of a region and the fundamental period

Table 2.1: Possible Fourier terms of the magnetic field components to satisfy one set of boundary conditions of the regions as defined in Figure 2.5 where θ^x and z^x are the coordinates in the local coordinate system of the specific region.

	Region a			Region b			Region c			Region d		
	H_r	H_θ	H_z	H_r	H_θ	H_z	H_r	H_θ	H_z	H_r	H_θ	H_z
$\sum\limits_{k=1}^{\infty}\sum\limits_{n=1}^{\infty}\sin(w_n^x\theta^x)\sin(m_k^x z^x)$	•	•	•	•	•		•		•	•		
$\sum\limits_{k=1}^{\infty}\sum\limits_{n=1}^{\infty}\sin(w_n^x\theta^x)\cos(m_k^x z^x)$	•	•	•			•	•		•			•
$\sum\limits_{k=1}^{\infty}\sum\limits_{n=1}^{\infty}\cos(w_n^x\theta^x)\sin(m_k^x z^x)$	•	•	•	•	•			•			•	
$\sum\limits_{k=1}^{\infty}\sum\limits_{n=1}^{\infty}\cos(w_n^x\theta^x)\cos(m_k^x z^x)$	•	•	•			•		•				
$\sum\limits_{k=1}^{\infty}\sin(m_k^x z^x)$	•		•	•								
$\sum\limits_{k=1}^{\infty}\cos(m_k^x z^x)$	•		•			•						
$\sum\limits_{n=1}^{\infty}\sin(w_n^x\theta^x)$	•	•					•					
$\sum\limits_{n=1}^{\infty}\cos(w_n^x\theta^x)$	•	•						•				

of the Fourier series in the z- and θ-direction is shown. As can be seen in this figure, the fundamental period of the magnetic field is equal to $2\tau_p$ when periodic boundary conditions apply. Due to this definition, the periodicity in this direction is inherently obtained.

In Figure 2.5(b,c), the regions are bounded by soft-magnetic material at two sides. At the interfaces at these sides, the components of the magnetic field strength tangential to the interface have to be zero due to the assumption that the permeability of the soft-magnetic material is infinite. By selecting a Fourier series for these magnetic field components having only sine terms in the direction normal to the interface, this boundary condition can be satisfied. To be able to include a DC-term in the magnetic field in this region the width of the region is half the fundamental period of the Fourier series. That is, the fundamental period is $2\tau_p$, and the width of the region is τ_p. In Figure 2.9, the fundamental, second and third harmonic of the Fourier series describing H_θ or H_r in a circumferential slot are shown to illustrate that the boundary condition is satisfied by means of the aforementioned analysis.

The resulting possible Fourier terms for the field components in each region illustrated in Figure 2.5 is shown in Table 2.1. As can be seen, the radial magnetic field component in a periodic region (a) can contain both sine and cosine terms. Conversely, the field components in region (d) consist of solely sine terms due to the soft-magnetic boundaries at four sides of the region.
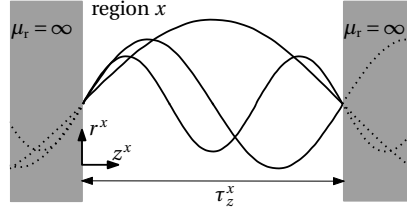
Figure 2.9: Fundamental, second and third harmonic of H_θ or H_r in a circumferential slot, region x, as shown in Figure 2.5(b). As illustrated, the magnetic field strength components tangential to the soft-magnetic interface are set to zero by selecting solely sine terms for the Fourier series to describe the magnetic field.

2.6   Boundary conditions between regions with equal Fourier series

In Figure 2.5, the possible regions in the z-θ plane are shown. Because the complete domain has to be divided into regions, these regions have to be stacked in the radial direction to obtain the complete model. To solve the magnetic fields in all regions, boundary conditions between these (radially) stacked regions have to be solved on the interfaces normal to the radial direction, i.e., r_1 and r_2. In the previous section the boundary conditions on interfaces θ_1, θ_2, z_1 and z_2 are satisfied by selecting a proper period of the Fourier series. In this section the boundary conditions on interfaces r_1 and r_2 of two subsequent regions have to be solved using the coefficients of the Fourier series, a^x and b^x. Three different situations can be recognized for this boundary condition:

1. The interface is a soft-magnetic boundary.

2. The regions at both sides of the interface are periodic in two directions and the two Fourier series have the same fundamental period, τ, and offset, Δ, at both sides. That is, the regions at both sides are of type Figure 2.5(a).

3. One or both fundamental period(s) and or offsets of the Fourier series on both sides of the interface are unequal.

The technique to satisfy the boundary conditions (1) and (2) is explained in the this section where two adjacent regions are considered, region p and region q. Boundary condition (3) is discussed in the next section.

1) Soft-magnetic interface

If the interface r_1 or r_2 of a region is soft-magnetic, the tangential component of the magnetic field strength is set to zero at that radius. As this boundary condition should hold for the complete interface, i.e. for all z^x and θ^x, the Fourier coefficients of these
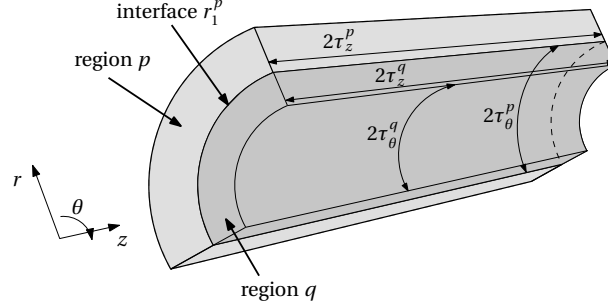
Figure 2.10: Illustration of two periodic regions, region p and region q, and the interface in between, r_1^p.

field components have to be zero at the interface. The normal component of the magnetic field strength is not considered in a boundary condition at this interface.

2) Interface between two periodic regions

In the second case, the interface between two periodic regions, region p and region q shown in Figure 2.10 is considered. As mentioned before, the fundamental period of all periodic regions in a structure are equal. Hence, for the example in Figure 2.10 holds

$$\tau_z^p = \tau_z^q, \tag{2.49}$$
$$\tau_\theta^p = \tau_\theta^q. \tag{2.50}$$

Furthermore, to simplify the analysis one should use the same local coordinate system for two adjacent periodic regions.

Two boundary conditions have to be applied on the interface between two periodic regions; the component of the field strength tangential to the interface and the component of the flux density normal to the interface have to be continuous over the interface. Due to the definition of (2.49) and (2.50), the two boundary conditions can only be satisfied when the values of the Fourier coefficients in region p and region q are equal. If the region is periodic in only one direction, for example the regions in Figure 2.5(b,c), the values of the Fourier coefficients in region p and region q are equal in only that specific direction. To solve the boundary condition for the Fourier series in the other direction, the technique described in the next section has to be applied.

2.7 Boundary conditions between regions with unequal Fourier series

In case that the fundamental period of one of the Fourier series is not equal at both sides of the interface, the previously described approach cannot be used to satisfy the boundary conditions. The same holds when the local coordinate systems of the two regions are displaced, i.e., $\Delta_\theta^p \neq \Delta_\theta^q$ and/or $\Delta_z^p \neq \Delta_z^q$. This section presents an approach to solve the boundary conditions between these two regions.

Consider the geometry shown in Figure 2.11(a) where a cavity in a soft-magnetic shell is enclosed by an air shell. Periodic region p is assigned to the air shell and region q to the cavity having soft-magnetic boundaries in the two tangential directions. To simplify the analysis, only the relative transformation of the two coordinate systems of the regions is used defined by

$$\Delta_z = \Delta_z^q - \Delta_z^p, \tag{2.51}$$

$$\Delta_\theta = \Delta_\theta^q - \Delta_\theta^p. \tag{2.52}$$

The interface where the boundary condition has to be solved is interface r_1^p as

(a)

(b)
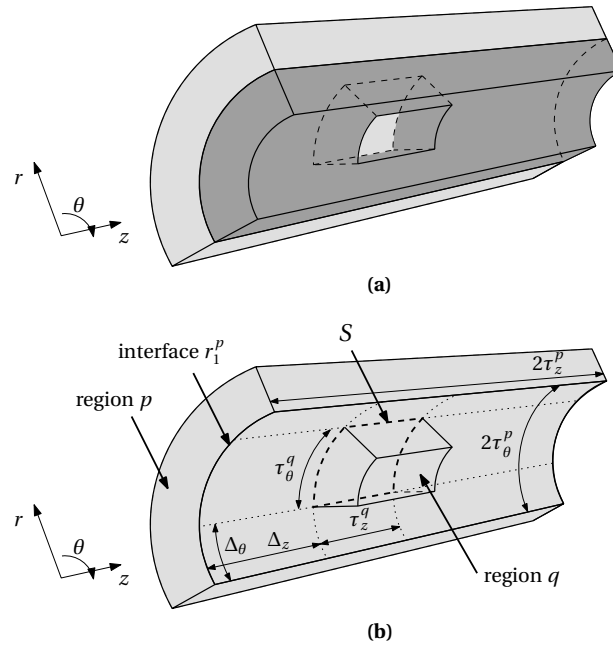
Figure 2.11: (a) Illustration of a cavity in a soft-magnetic shell enclosed by a periodic region. **(b)** Two regions having unequal Fourier series where region p is periodic in two directions, and region q has soft-magnetic boundaries in the axial and circumferential direction. $\mathcal{S}$ is the interface between the two regions.

illustrated in Figure 2.11(b). The surface $\mathcal{S}$ denotes the overlapping part of interface r_1^p and r_2^q. Region q is the only adjacent region of region p, therefore, interface r_1 of region p is soft-magnetic except for the part that coincides with surface $\mathcal{S}$.

Two boundary conditions have to be solved on the interface r_1^p

$$
1. \quad H_{\mathrm{t}}^p = \begin{cases} H_{\mathrm{t}}^q & \text{for } z, \theta \in \mathcal{S}, \\ 0 & \text{elsewhere,} \end{cases}
$$

(2.53)

$$
2. \quad B_{\mathrm{n}}^q = B_{\mathrm{n}}^p \qquad \text{for } z, \theta \in \mathcal{S},
$$

(2.54)

where

$$
H_{\mathrm{t}} = \begin{cases} H_z, \\ H_\theta, \end{cases}
$$

(2.55)

$$
B_{\mathrm{n}} = B_r
$$

(2.56)

$$
= \mu_0 \mu_r H_r + \mu_0 M_r.
$$

(2.57)

Using Table 2.1, the Fourier terms to describe the magnetic field at interface r_1^p in region p are found resulting in

$$
\begin{aligned}
H_r^p(\theta^p, z^p) = & \sum_{k=1}^{\infty} \sum_{n=1}^{\infty} c_1^p{}_{(k,n)} \sin\left(w_n \theta^p\right) \sin\left(m_k z^p\right) + c_2^p{}_{(k,n)} \sin\left(w_n \theta^p\right) \cos\left(m_k z^p\right) \\
& + \sum_{k=1}^{\infty} \sum_{n=0}^{\infty} c_3^p{}_{(k,n)} \cos\left(w_n \theta^p\right) \sin\left(m_k z^p\right) + c_4^p{}_{(k,n)} \cos\left(w_n \theta^p\right) \cos\left(m_k z^p\right) \\
& + \sum_{n=1}^{\infty} c_2^p{}_{(0,n)} \sin\left(w_n \theta^p\right) + c_4^p{}_{(0,n)} \cos\left(w_n \theta^p\right),
\end{aligned}
$$

(2.58)

$$
\begin{aligned}
H_\theta^p(\theta^p, z^p) = & \sum_{k=1}^{\infty} \sum_{n=1}^{\infty} c_5^p{}_{(k,n)} \sin\left(w_n \theta^p\right) \sin\left(m_k z^p\right) + c_6^p{}_{(k,n)} \sin\left(w_n \theta^p\right) \cos\left(m_k z^p\right) \\
& + \sum_{k=1}^{\infty} \sum_{n=1}^{\infty} c_7^p{}_{(k,n)} \cos\left(w_n \theta^p\right) \sin\left(m_k z^p\right) + c_8^p{}_{(k,n)} \cos\left(w_n \theta^p\right) \cos\left(m_k z^p\right) \\
& + \sum_{n=1}^{\infty} c_6^p{}_{(0,n)} \sin\left(w_n \theta^p\right) + c_8^p{}_{(0,n)} \cos\left(w_n \theta^p\right),
\end{aligned}
$$

(2.59)

$$
\begin{aligned}
H_z^p(\theta^p, z^p) = & \sum_{k=1}^{\infty} \sum_{n=1}^{\infty} c_9^p{}_{(k,n)} \sin\left(w_n \theta^p\right) \sin\left(m_k z^p\right) + c_{10}^p{}_{(k,n)} \sin\left(w_n \theta^p\right) \cos\left(m_k z^p\right) \\
& + \sum_{k=1}^{\infty} \sum_{n=0}^{\infty} c_{11}^p{}_{(k,n)} \cos\left(w_n \theta^p\right) \sin\left(m_k z^p\right) + c_{12}^p{}_{(k,n)} \cos\left(w_n \theta^p\right) \cos\left(m_k z^p\right).
\end{aligned}
$$

(2.60)

It can be seen that the magnetic field strength description is simplified by introducing

unknown coefficient $c^p(k,n)$ to replace $\mathcal{R}^p(r,k,n)$ and $\mathcal{G}^p$ used in (2.19) to (2.21). The field components in this definition are independent of r because they are defined at interface r_1^p which has a constant radius.

The Fourier series describing the magnetic field in the cavity at interface r_2^q, which coincides with r_1^p over the surface $\mathcal{S}$, contains fewer components as defined in Table 2.1

$$H_r^q(\theta^q, z^q) = \sum_{l=1}^{\infty} \sum_{j=1}^{\infty} c_1^q(l,j) \sin\left(w_j \theta^q\right) \sin\left(m_l z^q\right), \tag{2.61}$$

$$H_\theta^q(\theta^q, z^q) = \sum_{l=1}^{\infty} \sum_{j=1}^{\infty} c_7^q(l,j) \cos\left(w_j \theta^q\right) \sin\left(m_l z^q\right), \tag{2.62}$$

$$H_z^q(\theta^q, z^q) = \sum_{l=1}^{\infty} \sum_{j=1}^{\infty} c_{10}^q(l,j) \sin\left(w_j \theta^q\right) \cos\left(m_l z^q\right). \tag{2.63}$$

As in both regions different Fourier series are used, two new harmonic numbers are introduced in region q; l and j. Consequently, the two spatial frequencies of the Fourier series, w_j, m_l, in region q are

$$w_j = \frac{j\pi}{\tau_\theta^q}, \tag{2.64}$$

$$m_l = \frac{l\pi}{\tau_z^q}. \tag{2.65}$$

2.7.1 Continuous tangential component of magnetic field

To solve the continuous boundary condition of the tangential component of the magnetic field strength given in (2.53), the Fourier coefficients of H_θ^p are defined by a Fourier expansion of H_θ^q. By means of definition (2.6) to (2.9), this yields to the following set of equations

$$c_5^p(k,n) = \frac{1}{\tau_\theta^p \tau_z^p} \int_0^{2\tau_z^p} \int_0^{2\tau_\theta^p} H_\theta^q(\theta^q, z^q) \sin\left(w_n \theta^p\right) \sin\left(m_k z^p\right) \mathrm{d}\theta^p \mathrm{d}z^p \text{ for } k \geq 1, n \geq 1, \tag{2.66}$$

$$c_6^p(k,n) = \frac{1}{s\tau_\theta^p \tau_z^p} \int_0^{2\tau_z^p} \int_0^{2\tau_\theta^p} H_\theta^q(\theta^q, z^q) \sin\left(w_n \theta^p\right) \cos\left(m_k z^p\right) \mathrm{d}\theta^p \mathrm{d}z^p \text{ for } k \geq 0, n \geq 1, \tag{2.67}$$

$$c_7^p(k,n) = \frac{1}{\tau_\theta^p \tau_z^p} \int_0^{2\tau_z^p} \int_0^{2\tau_\theta^p} H_\theta^q(\theta^q, z^q) \cos\left(w_n \theta^p\right) \sin\left(m_k z^p\right) d\theta^p dz^p \text{ for } k \geq 1, n \geq 1,$$

$$(2.68)$$

$$c_8^p(k,n) = \frac{1}{s\tau_\theta^p \tau_z^p} \int_0^{2\tau_z^p} \int_0^{2\tau_\theta^p} H_\theta^q(\theta^q, z^q) \cos\left(w_n \theta^p\right) \cos\left(m_k z^p\right) d\theta^p dz^p \text{ for } k \geq 0, n \geq 1,$$

$$(2.69)$$

where

$$s = \begin{cases} 1 & \text{for } k > 0, n > 0, \\ 2 & \text{for } k = 0, n > 0. \end{cases} \tag{2.70}$$

For the remainder of the analysis, only equation (2.66) is considered since (2.67) to (2.69) can be solved using the same approach.

Because H_θ^p should be equal to H_θ^q on the surface $\mathcal{S}$ and zero elsewhere, the integration interval is bounded by $\mathcal{S}$. Therefore, (2.66) yields to

$$c_5^p(k,n) = \frac{\lambda}{\tau_\theta^p \tau_z^p} \iint_{\mathcal{S}} H_\theta^q(\theta^q, z^q) \sin\left(w_n \theta^p\right) \sin\left(m_k z^p\right) d\mathcal{S} \qquad \text{for } k \geq 1, n \geq 1, \tag{2.71}$$

where $\lambda = 1$. The equation for H_θ^q is inserted and the surface integral is split into two functions where each function contains an integral over one dimension to create a more general formulation

$$c_5^p(k,n) = \sum_{l=1}^\infty \sum_{j=1}^\infty c_7^q(l,j)\kappa_c(\theta, j, n)\kappa_s(z, l, k) \qquad \text{for } k \geq 1, n \geq 1, \tag{2.72}$$

where

$$\kappa_c(\nu, n^q, n^p) = \frac{\lambda}{s\tau_\nu^p} \int_{\Delta_\nu}^{\Delta_\nu + \tau_\nu^q} \cos\left(\frac{n^q \pi}{\tau_\nu^q} \nu^q\right) \sin\left(\frac{n^p \pi}{\tau_\nu^p} \nu^p\right) d\nu^p, \tag{2.73}$$

$$\kappa_s(\nu, n^q, n^p) = \frac{\lambda}{s\tau_\nu^p} \int_{\Delta_\nu}^{\Delta_\nu + \tau_\nu^q} \sin\left(\frac{n^q \pi}{\tau_\nu^q} \nu^q\right) \sin\left(\frac{n^p \pi}{\tau_\nu^p} \nu^p\right) d\nu^p, \tag{2.74}$$

where ν is either z or θ, $\Delta_\nu = \Delta_\nu^q - \Delta_\nu^p$ and $\lambda = 1$. These function are referred to as correlation functions as they define the correlation between the Fourier series in two subsequent regions. The solution of these correlation functions can be found in Appendix B.1. To be able to evaluate (2.67) to (2.69) in the same manner, two more

functions have to be defined to find the correlation between all Fourier components

$$\varsigma_c(v, n^q, n^p) = \frac{\lambda}{s\tau_v^p} \int_{\Delta_v}^{\Delta_v + \tau_v^q} \cos\left(\frac{n^q \pi}{\tau_v^q} v^q\right) \cos\left(\frac{n^p \pi}{\tau_v^p} v^p\right) \mathrm{d}v^p, \tag{2.75}$$

$$\varsigma_s(v, n^q, n^p) = \frac{\lambda}{s\tau_v^p} \int_{\Delta_v}^{\Delta_v + \tau_v^q} \sin\left(\frac{n^q \pi}{\tau_v^q} v^q\right) \cos\left(\frac{n^p \pi}{\tau_v^p} v^p\right) \mathrm{d}v^p. \tag{2.76}$$

Consequently, equation (2.67) to (2.69) yield to

$$c_6^p(k, n) = \sum_{l=1}^{\infty} \sum_{j=1}^{\infty} c_7^q(l, j) \kappa_c(\theta, j, n) \varsigma_s(z, l, k) \qquad \text{for } k \geq 0, n \geq 1, \tag{2.77}$$

$$c_7^p(k, n) = \sum_{l=1}^{\infty} \sum_{j=1}^{\infty} c_7^q(l, j) \varsigma_c(\theta, j, n) \kappa_s(z, l, k) \qquad \text{for } k \geq 1, n \geq 1, \tag{2.78}$$

$$c_8^p(k, n) = \sum_{l=1}^{\infty} \sum_{j=1}^{\infty} c_7^q(l, j) \varsigma_c(\theta, j, n) \varsigma_s(z, l, k) \qquad \text{for } k \geq 0, n \geq 1. \tag{2.79}$$

In the example, region p is considered to be periodic in the circumferential and the axial direction. In case that region p has soft-magnetic boundaries in the axial direction, the same analysis holds except that $\lambda = 2$ in the aforementioned correlation functions for $v = z$. In case that region p has soft-magnetic boundaries in the circumferential direction, $\lambda = 2$ in the aforementioned correlation functions for $v = \theta$.

The complete boundary condition concerns the tangential component of the magnetic field strength, hence, both the θ-component and the z-component have to be considered to satisfy the boundary condition (2.53). Repeating the aforementioned analysis for H_z results in the same set of equations and two additional equations to describe the relation between $c_{11}^p(k, 0)$, $c_{12}^p(k, 0)$ and $c_{10}^q(l, j)$

$$c_{11}^p(k, 0) = \sum_{l=1}^{\infty} \sum_{j=1}^{\infty} c_{10}^q(l, j) \varsigma_s(\theta, j, 0) \kappa_c(z, l, k) \qquad \text{for } k \geq 1, n = 0, \tag{2.80}$$

$$c_{12}^p(k, 0) = \sum_{l=1}^{\infty} \sum_{j=1}^{\infty} c_{10}^q(l, j) \varsigma_s(\theta, j, 0) \varsigma_c(z, l, k) \qquad \text{for } k \geq 0, n = 0. \tag{2.81}$$

Axial or circumferential slot

In case that region q is a slot in the axial or circumferential direction illustrated in Figure 2.5(b,c), the region will have periodicity in the direction of the slot instead of soft-magnetic boundary conditions. Consequently, the Fourier series used to describe the field in that direction will have the same fundamental period and harmonic number as the Fourier series in region p and the offset between the two regions, Δ_v, can be set to zero without consequences. The integration surface $\mathcal{S}$ used in (2.71) covers a full period in the direction of the slot. By means of the aforementioned

analysis, a similar set of equations with correlation functions can be derived except that the correlation functions in the direction of the slot disappear as the Fourier series in regions p and q are the same in that direction. As such, the correlation functions in the direction of the slot have to be replaced by a Kronecker delta, $\delta_{n^p n^q}$.

Multiple regions with soft-magnetic boundaries

In the aforementioned example illustrated in Figure 2.11, a region p is considered with one adjacent region q having soft-magnetic boundaries. However in most devices or structures, one region has multiple adjacent regions, e.g. a slotted actuator. In these cases, one region p is considered with multiple adjacent regions $q_1, q_2...q_\gamma$. Consequently, equation (2.66) to (2.69) should contain the magnetic field strength in all γ regions. Hence, (2.72),(2.77)-(2.81) have to be rewritten as

$$c_5^p(k,n) = \sum_{i=1}^{\gamma} \left[\sum_{l^i=1}^{\infty} \sum_{j^i=1}^{\infty} c_7^{q^i}(l^i,j^i)\kappa_c(\theta,j^i,n)\kappa_s(z,l^i,k) \right], \tag{2.82}$$

$$c_6^p(k,n) = \sum_{i=1}^{\gamma} \left[\sum_{l^i=1}^{\infty} \sum_{j^i=1}^{\infty} c_7^{q^i}(l^i,j^i)\kappa_c(\theta,j^i,n)\varsigma_s(z,l^i,k) \right], \tag{2.83}$$

$$c_7^p(k,n) = \sum_{i=1}^{\gamma} \left[\sum_{l^i=1}^{\infty} \sum_{j^i=1}^{\infty} c_7^{q^i}(l^i,j^i)\varsigma_c(\theta,j^i,n)\kappa_s(z,l^i,k) \right], \tag{2.84}$$

$$c_8^p(k,n) = \sum_{i=1}^{\gamma} \left[\sum_{l^i=1}^{\infty} \sum_{j^i=1}^{\infty} c_7^{q^i}(l^i,j^i)\varsigma_c(\theta,j^i,n)\varsigma_s(z,l^i,k) \right], \tag{2.85}$$

$$c_{11}^p(k,0) = \sum_{i=1}^{\gamma} \left[\sum_{l^i=1}^{\infty} \sum_{j^i=1}^{\infty} c_{10}^{q^i}(l^i,j^i)\varsigma_s(\theta,j^i,0)\kappa_c(z,l^i,k) \right], \tag{2.86}$$

$$c_{12}^p(k,0) = \sum_{i=1}^{\gamma} \left[\sum_{l^i=1}^{\infty} \sum_{j^i=1}^{\infty} c_{10}^{q^i}(l^i,j^i)\varsigma_s(\theta,j^i,0)\varsigma_c(z,l^i,k) \right]. \tag{2.87}$$

2.7.2   Continuous normal component of magnetic flux density

Besides the continuous tangential magnetic field component on the interface, the normal component of the magnetic flux density has to be continuous over the interface. As in the previous section, two Fourier series having different fundamental periods have to be matched. The same approach is used here, with one difference that instead of writing H^p as function of H^q, the components of B^q are written as a function of B^p.

As defined in (2.57), the radial component of the magnetization has to be taken into account in this boundary condition. Although the example shown in Figure 2.11 does not contain a source, this magnetization component will be taken into account in region p and region q to generalize the analysis. The radial component of the

magnetization in region p and q is defined using Section 2.3.4 and Section 2.4 resulting in

$$M_r^p(\theta, z) = \sum_{k=1}^{\infty} \sum_{n=1}^{\infty} M_{rss}^p(k,n)\sin(w_n^p\theta^p)\sin(m_k^p z^p) + M_{rsc}^p(k,n)\sin(w_n^p\theta^p)\cos(m_k^p z^p)$$

$$+ \sum_{k=1}^{\infty} \sum_{n=0}^{\infty} M_{rcs}^p(k,n)\cos(w_n^p\theta^p)\sin(m_k^p z^p) + M_{rcc}^p(k,n)\cos(w_n^p\theta^p)\cos(m_k^p z^p)$$

$$+ \sum_{n=1}^{\infty} M_{rs}^p(0,n)\sin(w_n^p\theta^p) + M_{rc}^p(0,n)\cos(w_n^p\theta^p), \tag{2.88}$$

$$M_r^q(\theta, z) = \sum_{l=1}^{\infty} \sum_{j=1}^{\infty} M_{rss}^q(l,j)\sin(w_j^q\theta^q)\sin(m_l^q z^q). \tag{2.89}$$

Consequently, combining (2.54) and (2.57) and writing $B_r^q + M_r^q$ as a Fourier expansion of $B_r^p + M_r^p$ yields to

$$\mu_r c_1^q(l,j) + M_{rss}^q = \frac{\lambda}{\tau_\theta^q \tau_z^q} \iint_{\mathcal{S}} \left(\mu_r H_r^p + M_r^p\right)\sin\left(w_j\theta^q\right)\sin\left(m_l z^q\right) \mathrm{d}\mathcal{S} \quad \text{for } l \geq 1, j \geq 1. \tag{2.90}$$

Instead of integrating over one full period of the Fourier series in region q (i.e., $2\tau^q$), the integration is bounded by $\mathcal{S}$ as the boundary condition only applies on this interface. The surface $\mathcal{S}$ has a width of τ_θ^q and a length of τ_z^q, which is half the fundamental period in both directions, hence, the Fourier integral covers only one fourth of one period of the total 2D Fourier series. Because B_r^q is anti-symmetric, i.e. contains only sine components as explained in Section 2.5, $\lambda = 4$ at the right hand side of (2.90). If region q is a slot in the axial or circumferential direction $\lambda = 2$ because $\mathcal{S}$ covers half the period of the 2D Fourier series. Inserting H_r^p and M_r^p into (2.90) and rewriting the equation as in the previous section yields to

$$\mu_r c_1^q(l,j) + M_{rss}^q = \sum_{k=1}^{\infty} \sum_{n=1}^{\infty} \left(\mu_r c_1^p(k,n) + M_{rss}^p\right)\varepsilon_s(\theta,n,j)\varepsilon_s(z,k,l)$$

$$+ \sum_{k=1}^{\infty} \sum_{n=1}^{\infty} \left(\mu_r c_2^p(k,n) + M_{rsc}^p\right)\varepsilon_s(\theta,n,j)\varepsilon_c(z,k,l)$$

$$+ \sum_{k=1}^{\infty} \sum_{n=0}^{\infty} \left(\mu_r c_3^p(k,n) + M_{rcs}^p\right)\varepsilon_c(\theta,n,j)\varepsilon_s(z,k,l)$$

$$+ \sum_{k=0}^{\infty} \sum_{n=0}^{\infty} \left(\mu_r c_4^p(k,n) + M_{rcc}^p\right)\varepsilon_c(\theta,n,j)\varepsilon_c(z,k,l)$$

$$+ \sum_{n=1}^{\infty} \left(\mu_r c_2^p(0,n) + M_{rs}^p\right)\varepsilon_s(\theta,n,j)\varepsilon_c(z,0,l)$$

$$+ \sum_{n=1}^{\infty} \left(\mu_r c_4^p(0,n) + M_{rc}^p\right)\varepsilon_c(\theta,n,j)\varepsilon_c(z,0,l) \quad \text{for } l \geq 1, j \geq 1, \tag{2.91}$$

where the correlation functions, ε_s and ε_c, are defined as

$$\varepsilon_s(v, n^p, n^q) = \frac{2}{\tau_v^q} \int_0^{\tau_v^q} \sin\left(\frac{n^p \pi}{\tau_v^p} v^p\right) \sin\left(\frac{n^q \pi}{\tau_v^q} v^q\right) \mathrm{d}v^q, \tag{2.92}$$

$$\varepsilon_c(v, n^p, n^q) = \frac{2}{\tau_v^q} \int_0^{\tau_v^q} \cos\left(\frac{n^p \pi}{\tau_v^p} v^p\right) \sin\left(\frac{n^q \pi}{\tau_v^q} v^q\right) \mathrm{d}v^q. \tag{2.93}$$

As explained the previous section, the aforementioned correlation functions yield to Kronecker delta functions when the cavity is replaced by a slot in one direction.

2.8   Model validation

The results of the analytical model are compared with results of a linear and a non-linear finite element (FE) model to validate the presented model. The modeled structure consists of three regions and represents a soft-magnetic cylinder with surface mounted permanent magnets in a checkerboard pattern (region I), an airgap (region II) and a soft-magnetic cylinder with a cavity (region III) as shown in Figure 2.12. The permanent magnet array consists of alternating radially magnetized permanent magnets in the circumferential and axial direction. The coordinate system of the permanent magnet and airgap region is defined such that the magnetization
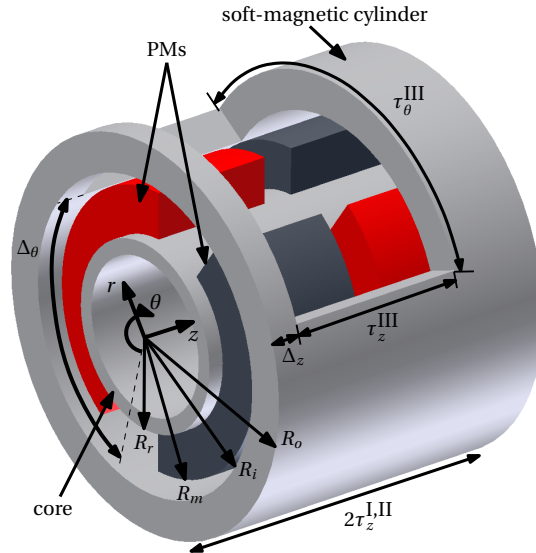
Figure 2.12: 3D illustration of cylindrical structure used for model validation.

Table 2.2: Geometrical dimensions and properties of the structure used for the model validation.

Parameter		Value	Description
R_r	[mm]	6.0	Inner radius PM array
R_m	[mm]	9.0	Outer radius PM array
R_i	[mm]	10.0	Inner radius soft-magnetic cylinder
R_o	[mm]	∞	Outer radius soft-magnetic cylinder
$\tau_z^{\mathrm{I,II}}$	[mm]	10.0	Pole pitch PM array, z-direction
$\tau_\theta^{\mathrm{I,II}}$	[deg]	180	Pole pitch PM array, θ-direction
α_{pz}	[-]	0.8	Pole pitch to magnet pitch ratio, z-direction
$\alpha_{p\theta}$	[-]	0.8	Pole pitch to magnet pitch ratio, θ-direction
τ_z^{III}	[mm]	12.0	Width region III (cavity), z-direction
$\tau_\theta^{\mathrm{III}}$	[deg]	125	Width region III (cavity), θ-direction
Δ_z	[mm]	2.0	Offset region III w.r.t. region I, z-direction
Δ_θ	[deg]	110	Offset region III w.r.t. region I, θ-direction
B_{rem}	[T]	1.2	Remanent flux density PMs
μ_{r}	[-]	1.05	Relative permeability PMs
N	[-]	29	Number of harmonics θ-direction, region I,II
K	[-]	17	Number of harmonics z-direction, region I,II
J	[-]	19	Number of harmonics θ-direction, region III
L	[-]	19	Number of harmonics z-direction, region III

can described by solely sine terms, i.e.,

$$M_{rss}(k,n) = \frac{16 \sin\left(\frac{k\pi}{2}\right) \sin\left(\frac{\alpha_{pz}k\pi}{2}\right) \sin\left(\frac{n\pi}{2}\right) \sin\left(\frac{\alpha_{p\theta}n\pi}{2}\right)}{kn\pi^2}. \tag{2.94}$$

The dimensions and properties of the structure are listed in Table 2.2.

The magnetic field description defined in (2.19) to (2.21) is used where the unknown coefficients are obtained by solving the following boundary conditions:

1. $\varphi^{\mathrm{III}} = 0 \big|_{r=\infty}$ $\hspace{2cm}$ $0 < \theta^{\mathrm{III}} < \tau_\theta^{\mathrm{III}}$,

   $\hspace{6.5cm}$ $0 < z^{\mathrm{III}} < \tau_z^{\mathrm{III}}$,

2. $H_z^{\mathrm{I}} = 0 \big|_{r=R_r}, H_\theta^{\mathrm{I}} = 0 \big|_{r=R_r}$ $\hspace{2cm}$ $\forall \;\; z, \theta$,

3. $H_z^{\mathrm{I}} = H_z^{\mathrm{II}} \big|_{r=R_m}, H_\theta^{\mathrm{I}} = H_\theta^{\mathrm{II}} \big|_{r=R_m}$ $\hspace{1cm}$ $\forall \;\; z, \theta$,

4. $B_r^{\mathrm{I}} = B_r^{\mathrm{II}} \big|_{r=R_m}$ $\hspace{2.7cm}$ $\forall \;\; z, \theta$,

5. $H_z^{\mathrm{II}} = H_z^{\mathrm{III}}\Big|_{r=R_i}, H_\theta^{\mathrm{II}} = H_\theta^{\mathrm{III}}\Big|_{r=R_i}$ $\Delta_\theta < \theta < \Delta_\theta + \tau_\theta^{\mathrm{III}},$

$\Delta_z < z < \Delta_z + \tau_z^{\mathrm{III}},$

$H_z^{\mathrm{II}} = 0\Big|_{r=R_i}, H_\theta^{\mathrm{II}} = 0\Big|_{r=R_i}$ elsewhere,

6. $B_r^{\mathrm{III}} = B_r^{\mathrm{II}}\Big|_{r=R_i}$ $0 < \theta^{\mathrm{III}} < \tau_\theta^{\mathrm{III}},$

$0 < z^{\mathrm{III}} < \tau_z^{\mathrm{III}}.$

The set of equations obtained from the boundary conditions consists of $2(8 \times N \times K + 4 \times K + 4 \times N) + 2 \times L \times J$ equations and unknown coefficients. This set is implemented in MATLAB according to the method described in Appendix B.3. The finite element model used for the validation is constructed in the same manner as the analytical model and implemented in FLUX3D. One period is modeled and periodicity in the axial direction is used to obtain the correct solution. The depth of the cavity in the radial direction is infinite in the analytical model, whereas in the FE model the depth is equal to 25 mm.

2.8.1   Comparison with a linear finite element model

In the first step of the model validation, the results are compared with a linear FE model where the soft-magnetic materials are modeled as boundary conditions, i.e., the tangential component of the magnetic field at the boundary is zero. Hence, the assumptions in the finite element model and the analytical model are the same.

To illustrate the agreement between the two models, the flux density in the airgap is shown in this section. In Figure 2.13 the three components of the flux density are shown in 3D surface plots. These figures show clearly the global agreement between the FE results and the analytical model. To show the accuracy of the analytical model, two dimensional figures are added showing the flux density at a constant z or θ. In Figure 2.14(a,c,e), the radial, circumferential and axial component of the flux density are shown at a constant z. Figure 2.14(b,d,f) show the three components of the flux density versus z at a constant θ crossing the area underneath the cavity. It can be observed that in all figures very good agreement is found between the two models.
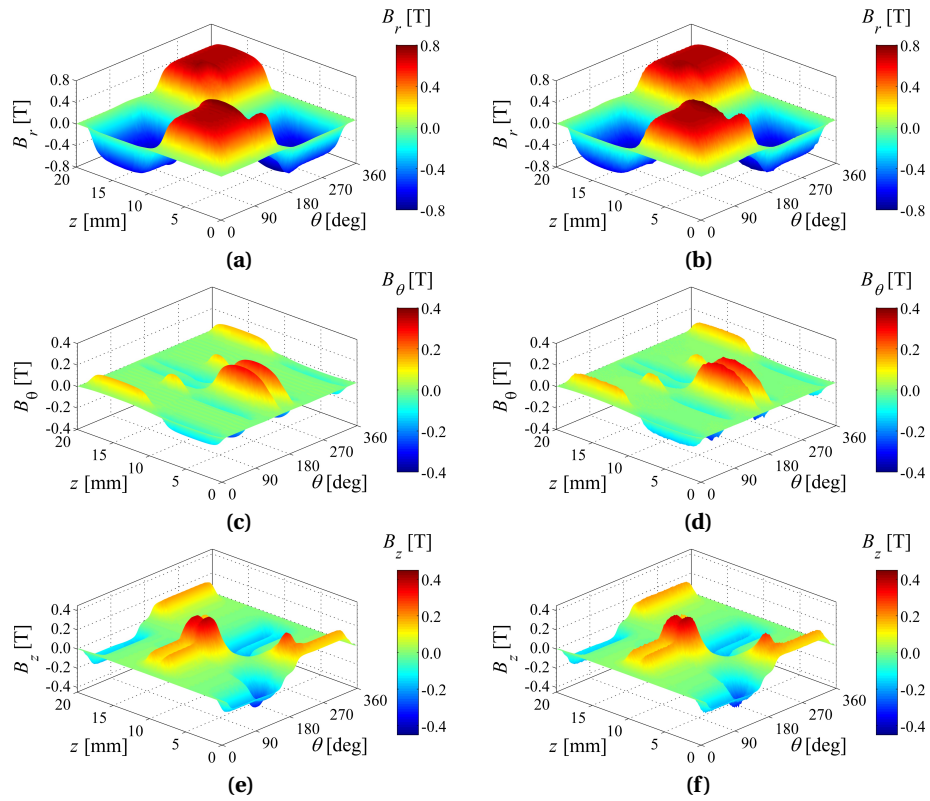
Figure 2.13: Flux density calculated in the middle of the airgap, $r = \frac{R_i + R_m}{2}$ in the structure as illustrated in Figure 2.12 with the dimensions as listed in Table 2.2. **(a)** B_r analytical, **(b)** B_r linear FEM, **(c)** B_θ analytical, **(d)** B_θ linear FEM, **(e)** B_z analytical, **(f)** B_z linear FEM.
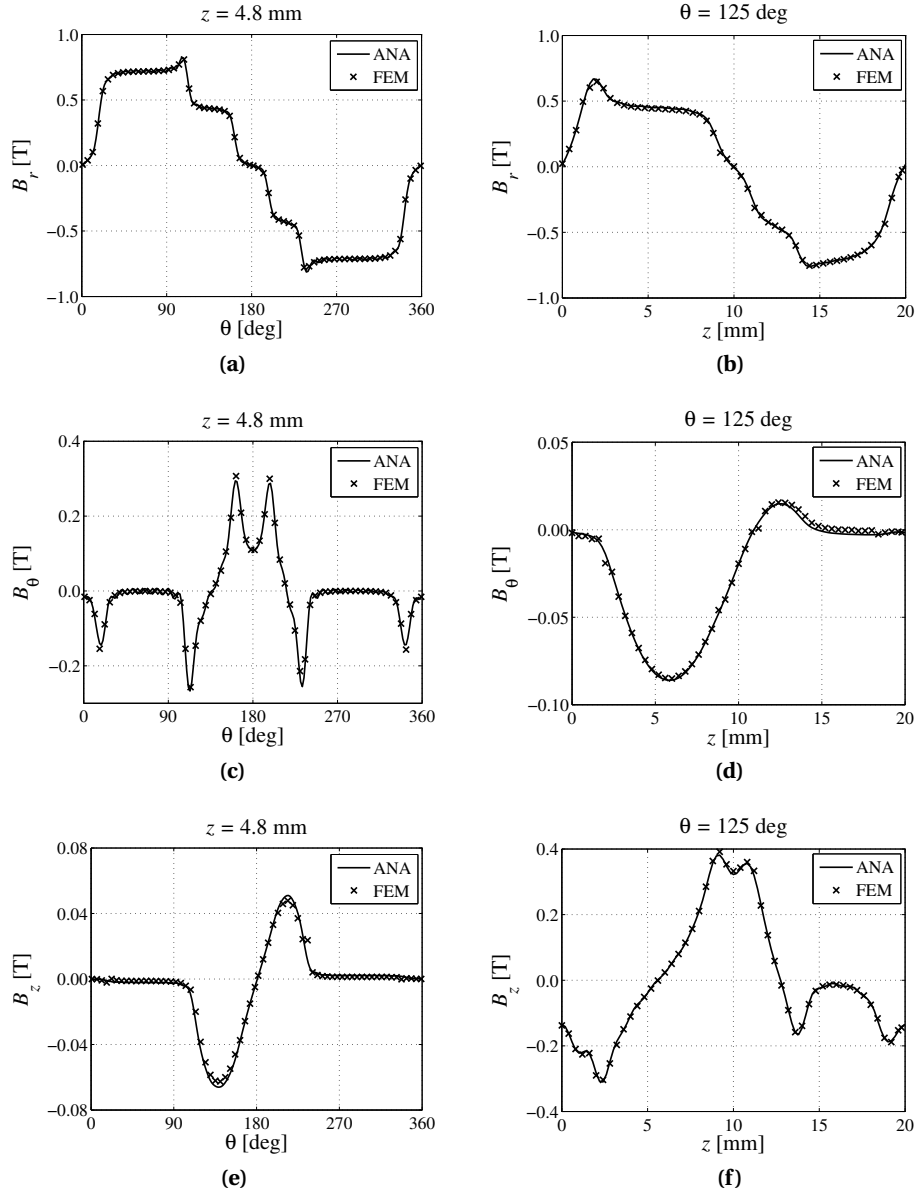
Figure 2.14: Flux density calculated in the middle of the airgap, $r = \frac{R_i + R_m}{2}$ in the structure as illustrated in Figure 2.12 with the dimensions as listed in Table 2.2 by means of the analytical model (ANA) and a linear finite element model (FEM). **(a)** B_r versus θ at $z = 4.8\,$mm, **(b)** B_r versus z at $\theta = 110\,$deg, **(c)** B_θ versus θ at $z = 4.8\,$mm, **(d)** B_θ versus z at $\theta = 110\,$deg, **(e)** B_z versus θ at $z = 4.8\,$mm, **(f)** B_z versus z at $\theta = 110\,$deg.

2.8.2 Comparison with a non-linear finite element model

In Section 2.3.2 is explained that the soft-magnetic materials used in electromagnetic devices have a non-linear permeability. However, this property is not considered in the analytical model, but can be taken into account in the FE model. To evaluate the analytical model in a realistic situation, an additional comparison is conducted with a non-linear FE model. In this model, the core is modeled as a soft-magnetic solid cylinder. The soft-magnetic cylinder and the walls of the cavity are represented by a shell with a thickness of 1.0 mm, illustrated in Figures 2.12 and 2.15. The soft-magnetic material used in this FE model has a non-linear BH-curve with a saturation magnetization of approximately 1.6 T.

The modulus of the magnetic flux density in the soft-magnetic cylinder is shown in Figure 2.15(a). It can be seen that at several positions the flux density exceeds the saturation level. Figure 2.15(b) illustrates the relative permeability distribution in the soft-magnetic cylinder, which is significantly reduced at the positions with a high flux density. To compare the results of the analytical model with the non-linear FE model, the flux density in the airgap is calculated in both models and shown in Figure 2.16. The analytical model still provides a very good approximation of the magnetic flux density in this structure, albeit that it is saturated at various positions.

(a)   **(b)**
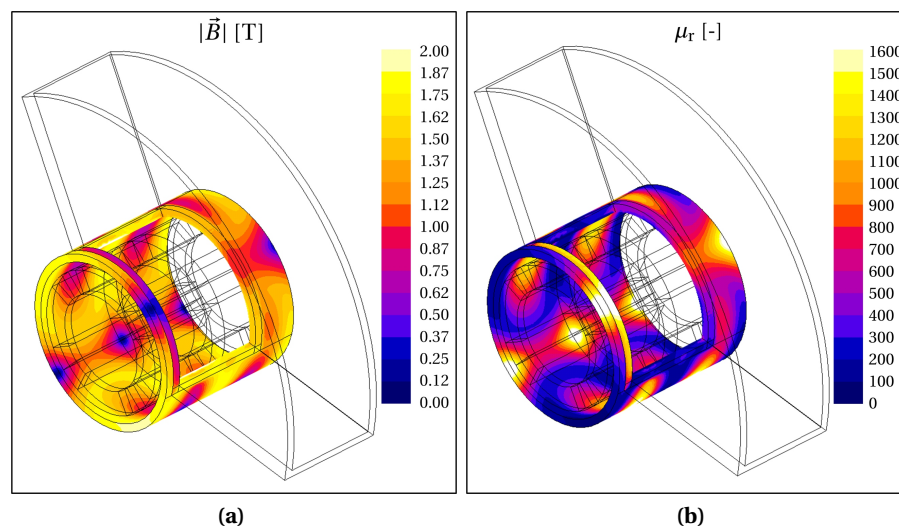
Figure 2.15: Results of the non-linear finite element model of the structure illustrated in Figure 2.12. **(a)** Modulus of the magnetic flux density at the interface of the soft-magnetic cylinder. **(b)** Relative permeability at the interface of the soft-magnetic cylinder.
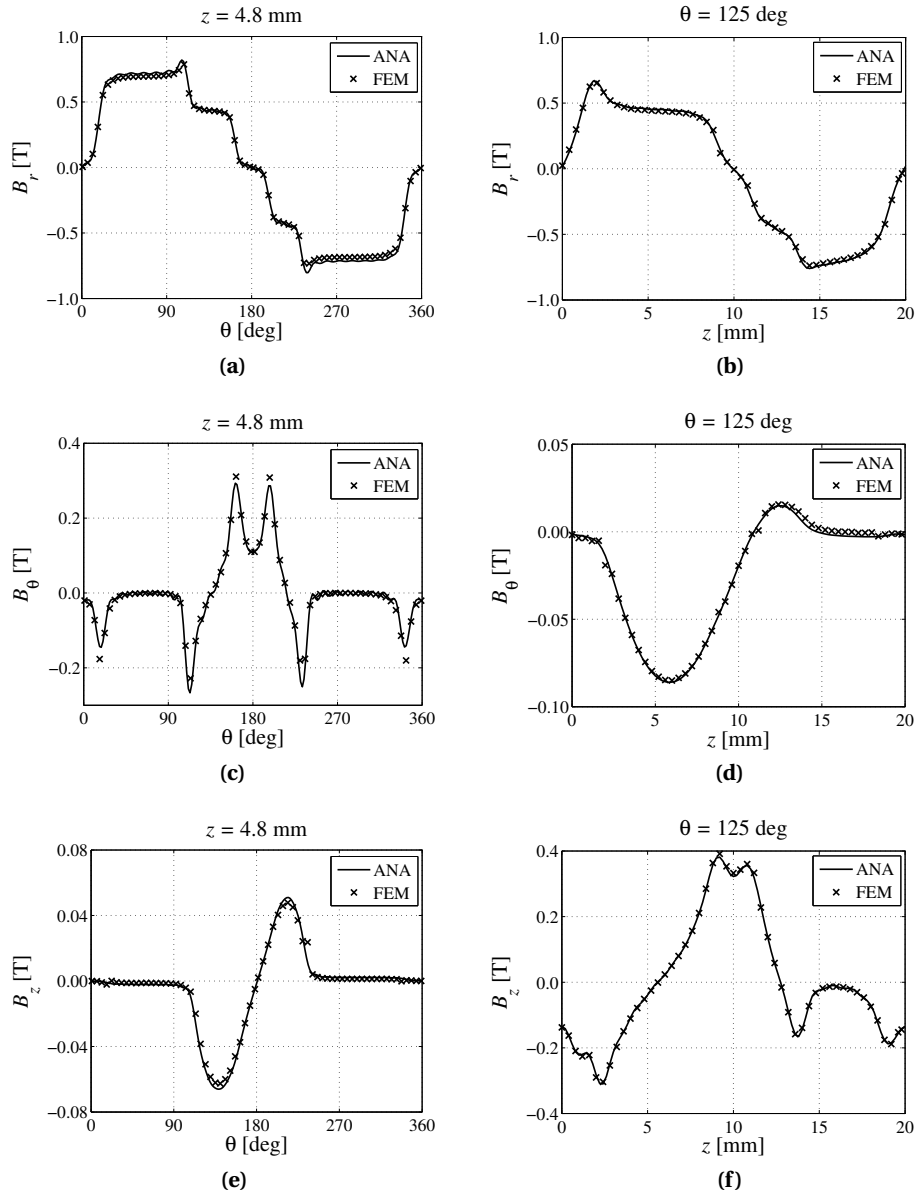
Figure 2.16: Flux density calculated in the middle of the airgap, $r = \frac{R_i + R_m}{2}$ in the structure as illustrated in Figure 2.12 with the dimensions as listed in Table 2.2 by means of the analytical model (ANA) and a non-linear finite element model (FEM). **(a)** B_r versus θ at $z = 4.8$ mm, **(b)** B_r versus z at $\theta = 110$ deg, **(c)** B_θ versus θ at $z = 4.8$ mm, **(d)** B_θ versus z at $\theta = 110$ deg, **(e)** B_z versus θ at $z = 4.8$ mm, **(f)** B_z versus z at $\theta = 110$ deg.

2.9   Discussion

The model presented in this chapter is based on Fourier series to describe sources and magnetic fields. Since these Fourier series do not provide analytical functions but infinite summations to describe magnetic fields and sources, the accuracy of the solution depend on the number of harmonics taken into account for the summations. To implement the equations obtained by applying the boundary conditions, the set of equations is rewritten in matrix form which results in a single linear matrix equation to be solved, given by

$$\mathbf{E}\mathbf{X} = \mathbf{Y}, \tag{2.95}$$

where $\mathbf{E}$ contains all known coefficients, $\mathbf{X}$ contains all unknown coefficients in the equation and $\mathbf{Y}$ contains the functions describing sources (further explained in Appendix B.3). The size of the matrix $\mathbf{E}$ is defined by the number of regions and the number of harmonics taken into account in these regions. The maximum number of harmonics that can be considered depends on the available memory, the desired calculation time and stability of the solution. The matrix $\mathbf{E}$ can become ill-conditioned when the number of harmonics taken into account is increased because $\mathcal{I}_o(m_k r)$ rapidly increases while $\mathcal{K}_o(m_k r)$ rapidly decreases for higher harmonics. Furthermore, in slotted structures, the number of harmonics has to be selected carefully to obtain a correctly converged solution as extensively discussed in [41, 75]. Generally, solving equation (2.95) is the most time-consuming part of the model. As a result, modeling an electromagnetic device with a high number of slots is computationally expensive and the computational effort in terms of solving time can ultimately exceed that of a finite element analysis. However, in contrast to the implementation of the modeling technique presented in this chapter, finite element routines have been optimized over the years. Further, in case of a parametric sweep, the finite element model needs to remesh each step where the computation time of the analytical model does not increase. Hence, the analytical model is very effective for parametric searches.

Limiting the number of harmonics improves the stability and reduces the calculation time, however affects the accuracy of the obtained solution. Especially at interfaces between regions with unequal width, the field solution can become inaccurate. Due to the limited number of harmonics, the Gibbs phenomenon can become dominant at these positions [47]. This makes this model less suitable to investigate local phenomena at, or close to, interfaces. However, the model is perfectly suitable to calculate the magnetic field in, for example, the middle of the airgap region, which is useful for force calculations.

2.10   Summary and Conclusions

The harmonic modeling technique provides a direct solution for the Maxwell equations by means of a Fourier series. The method is widely used to describe magnetic fields in two dimensional coordinate systems. Only a few implementations of this modeling technique for 3D models have been found in literature, which are limited to regular shaped geometries.

In this chapter, the modeling technique has been extended to describe electromagnetic fields due to presence of permanent magnets in regular and irregular shaped 3D cylindrical structures. As such, 3D electromagnetic fields, including fringing, can be investigated without the necessity of more time consuming FEA. The method provides the basis for fast analysis and optimization routines of slotless and slotted 3D cylindrical magnetostatic problems. The model is based on 2D Fourier series to describe the sources and magnetic fields. The modeling technique can be applied to current-free cylindrical problems exhibiting periodicity or a soft-magnetic boundary in the axial direction. The geometry can posses either circumferential slots, axial slots or rectangular cavities. Additionally, these slots or cavities can contain permanent magnets.

The model is created by dividing the geometry in contiguous regions. Each region contains a solution of the magnetic field distribution consisting of unknown Fourier coefficients. The values of these coefficients have to be found by solving boundary conditions on the region interfaces. As a result, the model computational requirements depend on the complexity of the geometry, or more specifically, the number of regions. Therefore, the model accuracy and stability degrades for more complex structures.

The assignment and a method to solve the various boundary conditions have been discussed in a generic manner to enable model application to a wide range of cylindrical structures. The magnetic field solutions have been provided, and the model implementation has been presented in matrix form. The results of the model are compared with a linear and a non-linear finite element model, and very good agreement is found. The analytical model is especially suitable for parametric searches since, contrary to a finite element model, no re-meshing is required after a geometric parameter is updated. Although the accuracy of the predicted field is lower at interfaces between regions due to Gibbs phenomena, the model is perfectly suitable to calculate the magnetic field in the middle of the airgap region, providing the possibility for accurate force predictions as presented in the next chapter.

3

Electromagnetic force calculation in 3D cylindrical structures

Abstract - In this chapter, the Maxwell stress tensor is used to calculate electromagnetic passive attraction forces in cylindrical structures. The magnetic field description, as presented in Chapter 2, is exploited and analytical expressions are obtained which enable fast and accurate force calculations.

3.1   Introduction to electromagnetic force calculations

An accurate force calculation is of great importance during the design of electrome-chanical devices. For example, in high performance actuation systems a smooth force without distortion due to cogging is desired [54]. In high speed machines, cogging torque can lead to unwanted noise and vibrations [9, 50], and in vibration isolation systems, accurate values of the force and the derivative of the force have to be obtained to guarantee proper operation of the device [62].

The electromagnetic interaction between two objects resulting in a force can be calculated using different methods. The most commonly used methods to calculate the force in electromechanical devices are the Maxwell stress tensor, the Lorentz force, and virtual work. These methods can often be applied in both analytical and numerical modeling techniques. However, selecting the most suitable force calculation method depends on the properties of the device and the applied field modeling technique.

To calculate the magnetic force and torque acting on a movable body of an electromagnetic device in a numerical (e.g. finite element) model, the virtual work method is often used [23]. One of the main advantages of this method is that it calculates the force from the volume integral of the energy, whereas the Maxwell stress tensor relies on a surface integral of the magnetic fields. These magnetic fields are obtained by differentiation of the potential introducing inaccuracies. In [17, 22, 81, 99, 100, 112], the advantages and disadvantages of the methods are further discussed. The accuracy of the calculated forces in finite elements models is largely determined by the level of discretization. Furthermore, the path of integration affects the results due to the magnetic field discontinuities at interfaces between two media. The influence of this discretization to calculate cogging forces in finite element models is extensively described in [49]. The virtual work method computes the force on a body by calculating the change of co-energy by a virtual displacement of the body. As a result, this method often requires two calculations. In [67, 68], a force calculation technique is presented based on the virtual work method without the necessity of two calculation steps. The resulting force equations are similar to the force expression of the Maxwell stress tensor, however, this method does not require that the movable body is surrounded by air, which is required when the Maxwell stress tensor is applied.

In analytical models of PM devices, the force is often calculated via the magnetic field distribution by analytical or numerical evaluation of one of the force calculation methods. For example, to calculate the force between PMs, charge models are exploited to calculate the magnetic fields of these PMs [119]. Subsequently, the force is calculated from these analytical magnetic field expressions by means of the virtual work method [2, 138] or the Lorentz force equation [33, 61]. The global force calculated in these papers provides the correct value, however, due to the

mathematical abstraction within these models, the local force distribution has no correct physical meaning. The interpretation of different force calculation methods to calculate the force between two permanent magnets is discussed in [26, 27].

In classical rotating or linear machines, the Maxwell stress tensor, [73, 141, 148], as well as the virtual work method, [25, 29, 35], are often used to calculate the cogging torque. The choice for these field based calculation methods is evident, as the analytical models used in these papers provide an expression for the magnetic field. To elaborate these passive force models to predict the active force, the model can be extended by current sheets representing an arbitrary current distribution. Subsequently, the Lorentz force equation is employed to find the active force [25, 128]. In case of slotless or air-cored coils, the force can be calculated by integrating analytically or numerically over the coil area. Another approach, specifically useful in slotted devices, employs the total field solution including the armature reaction field to calculate the total force using the Maxwell stress tensor [6, 149]. In [64, 77, 153], this Maxwell stress tensor is used to calculate the unbalanced magnetic pull of a PM rotor in a rotating machine. With the generic electromagnetic field analysis described in [40, 42], the total field solution in the airgap can be calculated, including slotting effect and armature reaction. Consequently, the total force in any electromechanical device can be calculated using one of the magnetic field based force calculation methods.

In this chapter, the passive attraction and repulsion force is calculated starting from the three dimensional analytical field description presented in the previous chapter. This can be used to predict cogging forces, unbalanced magnetic pull, and attraction forces due to the finite length of rotary actuators. The total force on the moving part is calculated by means of the Maxwell stress tensor. Analytical expressions for the different force components are derived and the method is validated using a 3D finite element analysis.

3.2   3D force calculation

To calculate the exerted force on a body due to the electromagnetic field distribution, the Maxwell stress tensor as presented in Section 1.1.3 is employed. The Maxwell stress tensor in the cylindrical coordinate system is defined by

$$
\mathbb{T} = \frac{1}{\mu_0} \begin{bmatrix} \frac{B_r^2 - B_\theta^2 - B_z^2}{2} & B_r B_\theta & B_r B_z \\ B_\theta B_r & \frac{B_\theta^2 - B_r^2 - B_z^2}{2} & B_\theta B_z \\ B_z B_r & B_z B_\theta & \frac{B_z^2 - B_r^2 - B_\theta^2}{2} \end{bmatrix}.
\tag{3.1}
$$

The total force on an object can be obtained by integrating the Maxwell stress tensor over a closed surface enclosing the object, as given by (1.16). Generally, in a cylindrical structure or device, two concentric cylinders move with respect to each other. Hence, the force between these two cylinders is the force of interest. Therefore, the integration
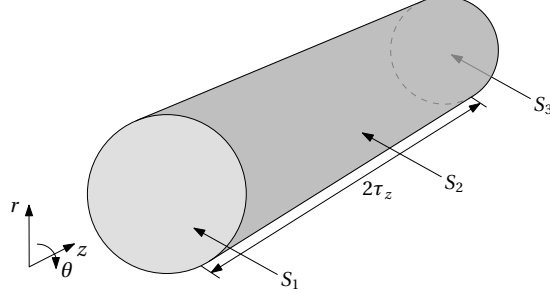
Figure 3.1: Surfaces defining the Maxwell stress tensor integration path.

surface is placed inside the airgap between the two bodies with the normal vector pointing outwards, illustrated in Figure 3.1.

Due to the model definition and the use of Fourier series, the structures are considered to be periodic in the axial direction. Hence, the surface can be chosen such that the integral over S_1 is equal to minus the integral over S_3, i.e., the axial length of S_2 is equal to the period of the airgap region, $2\tau_z$. Consequently, the Maxwell stress tensor has to be evaluated at the surface S_2 only resulting in the force density per period. On this surface, the normal points in the positive radial direction, i.e.,

$$\vec{n} = \vec{e}_r, \tag{3.2}$$

where $\vec{e}_r$ is the unit vector in the radial direction. As such, the three force components exerted on the cylinder are defined as

$$F_z = \frac{1}{\mu_0} \int_{S_2} B_z B_r \, \mathrm{d}s, \tag{3.3}$$

$$F_\theta = \frac{1}{\mu_0} \int_{S_2} B_\theta B_r \, \mathrm{d}s, \tag{3.4}$$

$$F_r = \frac{1}{\mu_0} \int_{S_2} \frac{B_r^2 - B_\theta^2 - B_z^2}{2} \, \mathrm{d}s. \tag{3.5}$$

In the next sections, the three force components are evaluated using the magnetic field description given in the previous section. As the surface enclosing the moving cylinder is placed in the airgap, the Maxwell stress tensor is evaluated in air where the flux density, $\vec{B}$, is defined as

$$\vec{B} = \mu_0 \vec{H}, \tag{3.6}$$

where the components of the magnetic field strength, $\vec{H}$, are defined in (2.19) to (2.21) with the source functions, $\mathcal{G}$, equal to zero.

The integrals describing the force components can be evaluated numerically using

the analytical expression of the magnetic flux density. However, the accuracy of the numerical integral over both θ and z depends on the spatial resolution of these quantities. Furthermore, numerical integration requires the numerical solution of the complete field distribution first resulting in an additional calculation step. Therefore, the integrals are analytically evaluated. Consequently, the force can be calculated in a faster manner, as it is a function of the unknown coefficients of the magnetic field strength which avoids the numerical evaluation of the magnetic fields first.

3.2.1 Force in the axial direction

To calculate the force in the axial, z-, direction, the integral given in (3.3) has to be evaluated. The magnetic fields, defined in (2.19) to (2.21), are inserted in the equation. The integral over an integer multiple of the period of $\sin(\bullet)\cos(\bullet)$, $\cos(\bullet)$ and $\sin(\bullet)$ is zero, hence, (3.3) yields to

$$
\begin{aligned}
F_z = \frac{r\mu_0}{2} \int_0^{2\tau_z}\int_0^{2\pi} \Bigg[&\sum_{k=1}^{\infty}\sum_{n=1}^{\infty} \mathcal{R}_7\mathcal{R}_2 \sin^2(w_n\theta)\cos^2(m_k z) \\
&- \sum_{k=1}^{\infty}\sum_{n=1}^{\infty} \mathcal{R}_8\mathcal{R}_1 \sin^2(w_n\theta)\sin^2(m_k z) \\
&+ \sum_{k=1}^{\infty}\sum_{n=0}^{\infty} \mathcal{R}_9\mathcal{R}_4 \cos^2(w_n\theta)\cos^2(m_k z) \\
&- \sum_{k=1}^{\infty}\sum_{n=0}^{\infty} \mathcal{R}_{10}\mathcal{R}_3 \cos^2(w_n\theta)\sin^2(m_k z) \Bigg] \mathrm{d}\theta \mathrm{d}z,
\end{aligned}
\tag{3.7}
$$

where the functions $\mathcal{R}_{..}$ are defined in (2.22) to (2.34). Evaluating the integrals results in

$$
F_z = \frac{r\mu_0\pi}{2}\tau_z \Bigg[\sum_{k=1}^{\infty}\sum_{n=1}^{\infty} \big[\mathcal{R}_7\mathcal{R}_2 - \mathcal{R}_8\mathcal{R}_1\big] + \sum_{k=1}^{\infty}\sum_{n=0}^{\infty} \lambda_n\big[\mathcal{R}_9\mathcal{R}_4 - \mathcal{R}_{10}\mathcal{R}_3\big] \Bigg],
\tag{3.8}
$$

where λ_n is defined as

$$
\lambda_n = \begin{cases} 2 & \text{for } n = 0, \\ 1 & \text{for } n > 0. \end{cases}
\tag{3.9}
$$

This can be rewritten using (2.22) to (2.34) and the following relation

$$
\mathcal{I}_{w_n}(m_k r)\mathcal{K}_{w_n\pm 1}(m_k r) + \mathcal{K}_{w_n}(m_k r)\mathcal{I}_{w_n\pm 1}(m_k r) = \frac{1}{m_k r},
\tag{3.10}
$$

resulting in

$$F_z = \pi\mu_0\left[\sum_{k=1}^{\infty}\sum_{n=1}^{\infty}\frac{1}{m_k}\Big(c_2(k,n)c_3(k,n) - c_1(k,n)c_4(k,n)\Big)\right.$$
$$\left.+ \sum_{k=1}^{\infty}\sum_{n=0}^{\infty}\frac{\lambda_n}{m_k}\Big(c_6(k,n)c_7(k,n) - c_5(k,n)c_8(k,n)\Big)\right], \quad (3.11)$$

which is the axial force per $2\tau_z$ axial length, given that $\tau_\theta = \pi$. As can be seen, the force in the axial direction, F_z, is only a function of the field coefficients $c_{\cdot}(k,n)$.

3.2.2   Force in the circumferential direction

The same approach as given in the previous section is used to obtain the force F_θ.

$$F_\theta = \frac{1}{\mu_0}\int_{S_2} B_\theta B_r \mathrm{d}s \qquad\qquad\qquad\qquad\qquad (3.12)$$
$$= \frac{1}{\mu_0}\int_0^{2\tau_z}\int_0^{2\pi} B_\theta B_r r d\theta dz. \qquad\qquad\qquad (3.13)$$

Inserting (2.19) to (2.21) and following the analysis of the previous section this yields to

$$F_\theta = \frac{\mu_0\pi}{r}\left[\sum_{k=1}^{\infty}\sum_{n=1}^{\infty}\frac{w_n}{m_k^2}\Big[c_2(k,n)c_5(k,n) - c_1(k,n)c_6(k,n) + c_4(k,n)c_7(k,n) - c_3(k,n)c_8(k,n)\Big]\right.$$
$$\left.+ 2\sum_{n=1}^{\infty} c_9(n)c_{12}(n) - c_{10}(n)c_{11}(n)\right], \quad (3.14)$$

which is the circumferential force per $2\tau_z$ axial length given that $\tau_\theta = \pi$, and can be translated into the torque around the z-axis, T_z, by means of

$$T_z = rF_\theta, \qquad\qquad\qquad\qquad\qquad\qquad\qquad (3.15)$$

where r is the radius where the circumferential force is evaluated.

3.2.3   Force in the radial direction

Due to the definition of the radial direction in the cylindrical coordinate system, the interpretation of the radial force component is ambiguous. As can be seen in Figure 2.3, the radial direction is pointing outwards the cylinder, hence, the obtained value of the radial force does not reflect the distribution over the complete circumference of the cylinder, it provides the magnitude only. A more sensible definition of this force component is to rewrite it into two components F_x, F_y where the x- and y-direction are defined with respect to the cylindrical coordinate system as

illustrated in Figure 2.3. By means of these two force components, the magnetic pull between two concentric cylinders is defined [64, 77, 153].

To obtain F_x and F_y, the force distributions in the radial and circumferential direction are used, $f_r(\theta, z)$ and $f_\theta(\theta, z)$, respectively. Using the definition of the x- and y-direction in Figure 2.3, F_x and F_y are defined as

$$F_x = \int_{S_2} f_r(\theta, z) \cos(\theta) - f_\theta(\theta, z) \sin(\theta) \mathrm{d}s, \tag{3.16}$$

$$F_y = \int_{S_2} f_r(\theta, z) \sin(\theta) + f_\theta(\theta, z) \cos(\theta) \mathrm{d}s, \tag{3.17}$$

where

$$f_r(\theta, z) = \frac{B_r^2(\theta, z) - B_\theta^2(\theta, z) - B_z^2(\theta, z)}{2\mu_0}, \tag{3.18}$$

$$f_\theta(\theta, z) = \frac{B_\theta(\theta, z) B_r(\theta, z)}{\mu_0}. \tag{3.19}$$

In the following sections, the integral equations (3.16) and (3.17) are analytically evaluated.

Force in the x-direction

Combination of (3.16), (3.18) and (3.19) yields to

$$F_x = \frac{1}{\mu_0} \iint_{S_2} \left[\frac{B_r^2 - B_\theta^2 - B_z^2}{2} \cos(\theta) - B_\theta B_r \sin(\theta) \right] r \mathrm{d}\theta \mathrm{d}z. \tag{3.20}$$

To clarify the analysis, the integral is split in four parts.

$$F_{x,1} = \frac{1}{\mu_0} \iint_{S_2} \frac{B_r^2}{2} \cos(\theta) r \mathrm{d}\theta \mathrm{d}z, \tag{3.21}$$

$$F_{x,2} = \frac{1}{\mu_0} \iint_{S_2} \frac{B_t^2}{2} \cos(\theta) r \mathrm{d}\theta \mathrm{d}z, \tag{3.22}$$

$$F_{x,3} = \frac{1}{\mu_0} \iint_{S_2} \frac{B_z^2}{2} \cos(\theta) r \mathrm{d}\theta \mathrm{d}z, \tag{3.23}$$

$$F_{x,4} = \frac{1}{\mu_0} \iint_{S_2} B_\theta B_r \sin(\theta) r \mathrm{d}\theta \mathrm{d}z, \tag{3.24}$$

where

$$F_x = F_{x,1} - F_{x,2} - F_{x,3} - F_{x,4}. \tag{3.25}$$

In the remainder of this analysis the period of the airgap region in the circumferential direction is set to $\tau_\theta = \pi$. Hence, the spatial frequency in this direction is

$$w_n = n. \tag{3.26}$$

This assumption can be used because the Maxwell stress tensor is always evaluated in the airgap where the period of the magnetic field can be set to 2π without constraints. Furthermore, the following relations are used to evaluate the integral

$$\int_0^{2\pi} \left(\sum_{n=1}^{\infty} a_n \sin(w_n\theta) \sum_{n=1}^{\infty} b_n \sin(w_n\theta) \right) \cos(\theta) \mathrm{d}\theta = \frac{\pi}{2} \sum_{n=1}^{\infty} \left(a_n b_{n+1} + a_{n+1} b_n \right), \tag{3.27}$$

$$\int_0^{2\pi} \left(\sum_{n=0}^{\infty} a_n \cos(w_n\theta) \sum_{n=0}^{\infty} b_n \cos(w_n\theta) \right) \cos(\theta) \mathrm{d}\theta$$
$$= \frac{\pi}{2} \sum_{n=1}^{\infty} \left(a_n b_{n+1} + a_{n+1} b_n \right) + \pi \left(a_0 b_1 + a_1 b_0 \right), \tag{3.28}$$

$$\int_0^{2\pi} \left(\sum_{n=1}^{\infty} a_n \sin(w_n\theta) \sum_{n=0}^{\infty} b_n \cos(w_n\theta) \right) \cos(\theta) \mathrm{d}\theta = 0. \tag{3.29}$$

Inserting the magnetic field, (2.19) to (2.21) into (3.20) the first component of F_x yields to

$$F_{x,1} = \frac{r\mu_0\tau_z\pi}{8} \left[\sum_{k=1}^{\infty} \sum_{n=1}^{\infty} \left[\mathcal{R}_1(r,k,n)\mathcal{R}_1(r,k,n+1) + \mathcal{R}_2(r,k,n)\mathcal{R}_2(r,k,n+1) \right] \right.$$
$$+ \sum_{k=1}^{\infty} \sum_{n=0}^{\infty} \lambda_n \left[\mathcal{R}_3^x(r,k,n)\mathcal{R}_3(r,k,n+1) + \mathcal{R}_4(r,k,n)\mathcal{R}_4(r,k,n+1) \right]$$
$$\left. + 8 \sum_{n=1}^{\infty} \mathcal{R}_5(r,n)\mathcal{R}_5(r,n+1) + \mathcal{R}_6(r,n)\mathcal{R}_6(r,n+1) \right], \tag{3.30}$$

where λ_n is defined in (3.9). In the same manner, two other parts of F_x can be found

$$F_{x,2} = \frac{\mu_0\tau_z\pi}{2} \left[\sum_{k=1}^{\infty} \sum_{n=1}^{\infty} \frac{w_n w_{n+1}}{m_k^2 r} \left[\mathcal{R}_9(r,k,n)\mathcal{R}_9(r,k,n+1) + \mathcal{R}_{10}(r,k,n)\mathcal{R}_{10}(r,k,n+1) \right] \right.$$
$$+ \sum_{k=1}^{\infty} \sum_{n=1}^{\infty} \frac{w_n w_{n+1}}{m_k^2 r} \left[\mathcal{R}_7(r,k,n)\mathcal{R}_7(r,k,n+1) + \mathcal{R}_8(r,k,n)\mathcal{R}_8(r,k,n+1) \right]$$
$$\left. + r \sum_{n=1}^{\infty} \mathcal{R}_{12}(r,n)\mathcal{R}_{12}(r,n+1) + \mathcal{R}_{11}(r,n)\mathcal{R}_{11}(r,n+1) \right], \tag{3.31}$$

$$F_{x,3} = \frac{r\mu_0\tau_z\pi}{2}\left[\sum_{k=1}^{\infty}\sum_{n=1}^{\infty}\left[\mathcal{R}_8(r,k,n)\mathcal{R}_8(r,k,n+1) + \mathcal{R}_7(r,k,n)\mathcal{R}_7(r,k,n+1)\right]\right.$$
$$\left. + \sum_{k=1}^{\infty}\sum_{n=0}^{\infty}\lambda_n\left[\mathcal{R}_{10}^x(r,k,n)\mathcal{R}_{10}(r,k,n+1) + \mathcal{R}_9(r,k,n)\mathcal{R}_9(r,k,n+1)\right]\right]. \quad (3.32)$$

The following relations are used to evaluate the fourth integral $F_{x,4}$

$$\int_0^{2\pi}\left(\sum_{n=0}^{\infty}a_n\cos(w_n\theta)\sum_{n=1}^{\infty}b_n\sin(w_n\theta)\right)\sin(\theta)\mathrm{d}\theta = \frac{\pi}{2}\sum_{n=1}^{\infty}\left(a_nb_{n+1} - a_{n+1}b_n\right) + \pi\left(a_0b_1\right),$$
$$(3.33)$$

$$\int_0^{2\pi}\left(\sum_{n=1}^{\infty}a_n\sin(w_n\theta)\sum_{n=1}^{\infty}b_n\sin(w_n\theta)\right)\sin(\theta)\mathrm{d}\theta = 0, \quad (3.34)$$

$$\int_0^{2\pi}\left(\sum_{n=0}^{\infty}a_n\cos(w_n\theta)\sum_{n=0}^{\infty}b_n\cos(w_n\theta)\right)\sin(\theta)\mathrm{d}\theta = 0. \quad (3.35)$$

After applying these relations, $F_{x,4}$ yields to

$$F_{x,4} = \frac{\mu_0\tau_z\pi}{4}\left[\sum_{k=1}^{\infty}\sum_{n=1}^{\infty}\frac{w_n}{m_k}\left[\mathcal{R}_7^x(r,k,n)\mathcal{R}_1^x(r,k,n+1) - \mathcal{R}_7^x(r,k,n+1)\mathcal{R}_1^x(r,k,n)\right]\right.$$
$$+ \sum_{k=1}^{\infty}\sum_{n=1}^{\infty}\frac{w_n}{m_k}\left[\mathcal{R}_8^x(r,k,n)\mathcal{R}_2^x(r,k,n+1) - \mathcal{R}_8^x(r,k,n+1)\mathcal{R}_2^x(r,k,n)\right]$$
$$+ \sum_{k=1}^{\infty}\sum_{n=1}^{\infty}\frac{w_n}{m_k}\left[\mathcal{R}_9^x(r,k,n)\mathcal{R}_3^x(r,k,n+1) - \mathcal{R}_9^x(r,k,n+1)\mathcal{R}_3^x(r,k,n)\right]$$
$$+ \sum_{k=1}^{\infty}\sum_{n=1}^{\infty}\frac{w_n}{m_k}\left[\mathcal{R}_{10}^x(r,k,n)\mathcal{R}_4^x(r,k,n+1) - \mathcal{R}_{10}^x(r,k,n+1)\mathcal{R}_4^x(r,k,n)\right]$$
$$- \sum_{k=1}^{\infty}\frac{2}{m_k}\left[\mathcal{R}_9^x(r,k,1)\mathcal{R}_3^x(r,k,0) + \mathcal{R}_{10}^x(r,k,1)\mathcal{R}_4^x(r,k,0)\right]$$
$$+ 4r\sum_{n=1}^{\infty}\left[\mathcal{R}_{11}^x(r,n)\mathcal{R}_5^x(r,n+1) - \mathcal{R}_5^x(r,n)\mathcal{R}_{11}^x(r,n+1)\right]$$
$$\left. + 4r\sum_{n=1}^{\infty}\left[\mathcal{R}_{12}^x(r,n)\mathcal{R}_6^x(r,n+1) - \mathcal{R}_6^x(r,n)\mathcal{R}_{12}^x(r,n+1)\right]\right]. \quad (3.36)$$

The total force per $2\tau_z$ in the x-direction can be found by subtraction of the four components

$$F_x = F_{x,1} - F_{x,2} - F_{x,3} - F_{x,4}. \quad (3.37)$$

Force in the y-direction

The force in the y-direction is derived using the same approach, starting from (3.17)

$$F_{y,1} = \frac{1}{\mu_0} \iint_{S_2} \frac{B_r^2}{2} \sin(\theta)\, r\mathrm{d}\theta\mathrm{d}z, \tag{3.38}$$

$$F_{y,2} = \frac{1}{\mu_0} \iint_{S_2} \frac{B_t^2}{2} \sin(\theta)\, r\mathrm{d}\theta\mathrm{d}z, \tag{3.39}$$

$$F_{y,3} = \frac{1}{\mu_0} \iint_{S_2} \frac{B_z^2}{2} \sin(\theta)\, r\mathrm{d}\theta\mathrm{d}z, \tag{3.40}$$

$$F_{y,4} = \frac{1}{\mu_0} \iint_{S_2} B_\theta B_r \cos(\theta)\, r\mathrm{d}\theta\mathrm{d}z. \tag{3.41}$$

Evaluation of these integrals by inserting the magnetic field, (2.19) to (2.21), and applying the relations (3.27) to (3.29) and (3.33) to (3.35) yields to the solution of the aforementioned equations.

$$
\begin{aligned}
F_{y,1} = \frac{-r\mu_0\tau_z\pi}{8}\bigg[&\sum_{k=1}^{\infty}\sum_{n=1}^{\infty}\left[\mathcal{R}_1^x(r,k,n)\mathcal{R}_3^x(r,k,n+1)+\mathcal{R}_2^x(r,k,n)\mathcal{R}_4^x(r,k,n+1)\right] \\
&-\sum_{k=1}^{\infty}\sum_{n=0}^{\infty}\lambda_n\left[\mathcal{R}_3^x(r,k,n)\mathcal{R}_1^x(r,k,n+1)+\mathcal{R}_4^x(r,k,n)\mathcal{R}_2^x(r,k,n+1)\right] \\
&+8\sum_{n=1}^{\infty}\left[\mathcal{R}_5^x(r,n)\mathcal{R}_6^x(r,n+1)-\mathcal{R}_6^x(r,n)\mathcal{R}_5^x(r,n+1)\right]\bigg],
\end{aligned}
\tag{3.42}
$$

$$
\begin{aligned}
F_{y,2} = \frac{-\mu_0\tau_z\pi}{2}\bigg[&\sum_{k=1}^{\infty}\sum_{n=1}^{\infty}\frac{w_n w_{n+1}}{m_k^2 r}\left[\mathcal{R}_7^x(r,k,n)\mathcal{R}_9^x(r,k,n+1)-\mathcal{R}_9^x(r,k,n)\mathcal{R}_7^x(r,k,n+1)\right] \\
&+\sum_{k=1}^{\infty}\sum_{n=1}^{\infty}\frac{w_n w_{n+1}}{m_k^2 r}\left[\mathcal{R}_8^x(r,k,n)\mathcal{R}_{10}^x(r,k,n+1)+\mathcal{R}_{10}^x(r,k,n)\mathcal{R}_8^x(r,k,n+1)\right] \\
&-2r\sum_{n=1}^{\infty}\left[\mathcal{R}_{12}^x(r,n)\mathcal{R}_{11}^x(r,n+1)-\mathcal{R}_{11}^x(r,n)\mathcal{R}_{12}^x(r,n+1)\right]\bigg],
\end{aligned}
\tag{3.43}
$$

$$
\begin{aligned}
F_{y,3} = \frac{r\mu_0\tau_z\pi}{2}\bigg[&\sum_{k=1}^{\infty}\sum_{n=1}^{\infty}\left[\mathcal{R}_9^x(r,k,n)\mathcal{R}_7^x(r,k,n+1)+\mathcal{R}_{10}^x(r,k,n)\mathcal{R}_8^x(r,k,n+1)\right] \\
&-\sum_{k=1}^{\infty}\sum_{n=0}^{\infty}\lambda_n\left[\mathcal{R}_7^x(r,k,n)\mathcal{R}_9^x(r,k,n+1)+\mathcal{R}_8^x(r,k,n)\mathcal{R}_{10}^x(r,k,n+1)\right]\bigg],
\end{aligned}
\tag{3.44}
$$

$$F_{y,4} = \frac{\mu_0 \tau_z \pi}{4} \Bigg[\sum_{k=1}^{\infty} \sum_{n=1}^{\infty} \frac{w_n}{m_k} \big[\mathcal{R}_7^x(r,k,n) \mathcal{R}_3^x(r,k,n+1) + \mathcal{R}_7^x(r,k,n+1) \mathcal{R}_3^x(r,k,n) \big]$$

$$+ \sum_{k=1}^{\infty} \sum_{n=1}^{\infty} \frac{w_n}{m_k} \big[\mathcal{R}_8^x(r,k,n) \mathcal{R}_4^x(r,k,n+1) + \mathcal{R}_8^x(r,k,n+1) \mathcal{R}_4^x(r,k,n) \big]$$

$$- \sum_{k=1}^{\infty} \sum_{n=1}^{\infty} \frac{w_n}{m_k} \big[\mathcal{R}_9^x(r,k,n) \mathcal{R}_1^x(r,k,n+1) + \mathcal{R}_9^x(r,k,n+1) \mathcal{R}_1^x(r,k,n) \big]$$

$$- \sum_{k=1}^{\infty} \sum_{n=1}^{\infty} \frac{w_n}{m_k} \big[\mathcal{R}_{10}^x(r,k,n) \mathcal{R}_2^x(r,k,n+1) + \mathcal{R}_{10}^x(r,k,n+1) \mathcal{R}_2^x(r,k,n) \big]$$

$$+ \sum_{k=1}^{\infty} \frac{2}{m_k} \big[\mathcal{R}_7^x(r,k,1) \mathcal{R}_3^x(r,k,0) + \mathcal{R}_8^x(r,k,1) \mathcal{R}_4^x(r,k,0) \big]$$

$$+ 4r \sum_{n=1}^{\infty} \big[\mathcal{R}_{11}^x(r,n) \mathcal{R}_6^x(r,n+1) + \mathcal{R}_6^x(r,n) \mathcal{R}_{11}^x(r,n+1) \big]$$

$$- 4r \sum_{n=1}^{\infty} \big[\mathcal{R}_{12}^x(r,n) \mathcal{R}_5^x(r,n+1) + \mathcal{R}_5^x(r,n) \mathcal{R}_{12}^x(r,n+1) \big] \Bigg]. \tag{3.45}$$

Consequently, the total force per $2\tau_z$ in the y-direction can be found by

$$F_y = F_{y,1} - F_{y,2} - F_{y,3} + F_{y,4}. \tag{3.46}$$

3.3 Model validation

To validate the aforementioned force formulations, the equations (3.8), (3.14), (3.37) and (3.46) are implemented in MATLAB and their results are compared with two finite element analyses for the cylindrical structure illustrated in Figure 2.12. The magnetic fields in this structure, based upon which the four force components are calculated, are obtained by the analytical model which is presented in the previous chapter. The structure consists of a cylindrical core with a checkerboard magnetization and a soft-magnetic tube with a rectangular cavity. The dimensions of the structure are given in Table 2.2 in Section 2.8. The Maxwell stress tensor is evaluated in the center of the airgap, region II, between the PM pattern and the cylindrical outer tube with the rectangular cavity.

Two coordinate systems are defined to provide a solvable model definition as presented in the previous chapter. A stationary coordinate system is assigned to the complete structure excluding the cavity, and a secondary coordinate system is assigned to the geometry and magnetic fields within the cavity in the soft-magnetic cylinder. The secondary coordinate system can be translated and/or rotated with respect to the stationary coordinate system by means of Δ_z and Δ_θ as illustrated in Figure 2.3(b). That is, the cavity is displaced with respect to the rest of the structure. The Maxwell stress tensor is evaluated in the airgap, hence the force components are defined with respect to the stationary coordinate system and provide the total force on the PMs and the soft-magnetic core, i.e., the mover. To validate the force

Figure 3.2: Torque, T_z, around the z-axis versus circumferential displacement. Calculated by means of a linear FE model (FEM) and the analytical model (ANA).

components, the cavity is rotated with respect to the mover over 360 degrees and the force is calculated for a model with a length of $2\tau_z^{\mathrm{I,II}}$, which is the period of the model and the Fourier series in the axial direction.

3.3.1 Comparison with a linear finite element model

In this section, the results of the analytical model are compared with a linear FE model where the soft-magnetic materials are modeled as boundary conditions. Hence, the assumptions in the finite element model and the analytical model are the same. In Figure 3.2, the cogging torque around the z-axis is shown as a function of the rotation, Δ_θ, being a waveform with a period of 180 degrees, clearly caused by the presence of two poles (PMs) along the circumference interacting with one cavity. Figure 3.3 shows
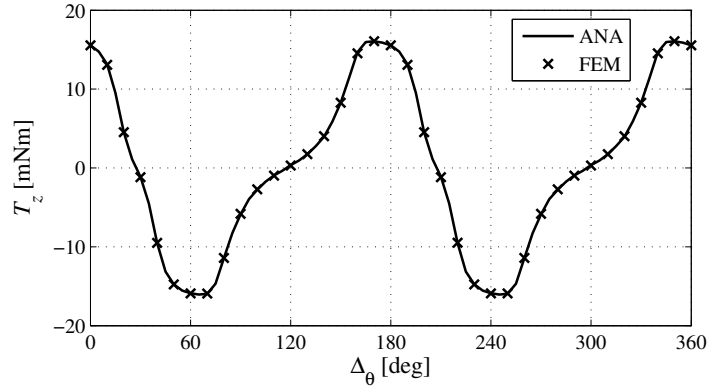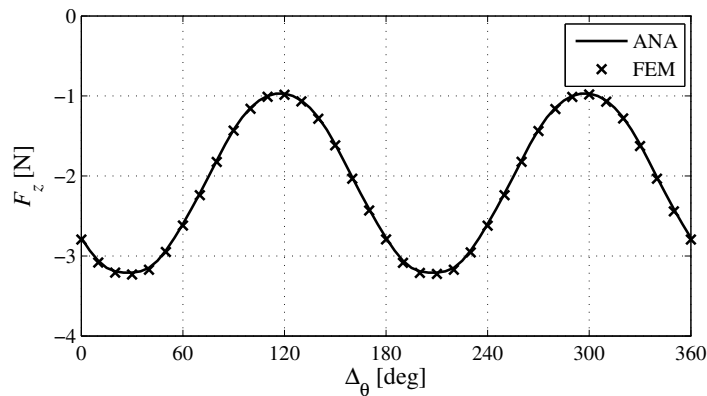

Figure 3.3: Force, F_z, in axial direction versus circumferential displacement, calculated by means of a linear FE model (FEM) and the analytical model (ANA).
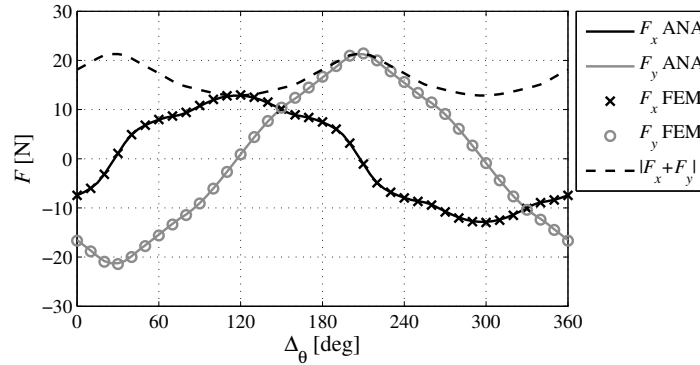
Figure 3.4: Magnetic pull or force in the x-and y-direction versus circumferential displacement. The total magnetic pull is presented as the modulus of F_x and F_y. Calculated by means of a linear FE model (FEM) and the analytical model (ANA).

the force in the axial direction, F_z, as a function of the rotation. Due to the position of the cavity with respect to the PMs in the z-direction, illustrated in Figure 2.12, the center of the cavity tends to align with the transition of the PMs. This results in a negative force on the mover. Although the axial position of the cavity is fixed, F_z has a sinusoidal profile due to the finite width of the cavity in the circumferential direction, $\tau_\theta^{\mathrm{III}}$. As can be seen in Figure 3.2 and Figure 3.3, excellent agreement is found between the FE model and the analytical model for the cogging torque and the axial force component. The two other force components that are validated represent the magnetic pull of the mover to the outer soft-magnetic cylinder. As introduced in Section 3.2.3, the magnetic pull is split into a force component in the x- and y- direction. These two components are shown in Figure 3.4, note that the force is calculated in the stationary coordinate system. That is, the cavity revolves with respect to the x- and y-axis resulting in a symmetric waveform around zero force. The total magnetic pull of the mover to the outer cylinder is also shown being the modulus of F_x and F_y. Also for these force components, the analytical and the FE model show excellent agreement.

3.3.2 Comparison with a non-linear finite element model

To validate the force calculations in realistic situations, the analytical model is compared to a finite element model where the soft-magnetic material has non-linear properties. In this FE model, the soft-magnetic cylinder is a shell with a thickness of 1.0 mm, presented in Section 2.8.2 and Figure 2.15. It can be seen in this figure that the permeability of the soft-magnetic cylinder is significantly reduced.

The four force components, presented in this chapter, are compared with the results of this non-linear FE model. The torque, T_z, around the z-axis is still in very good agreement, the difference is less than 1 %. The amplitude of the force in the axial
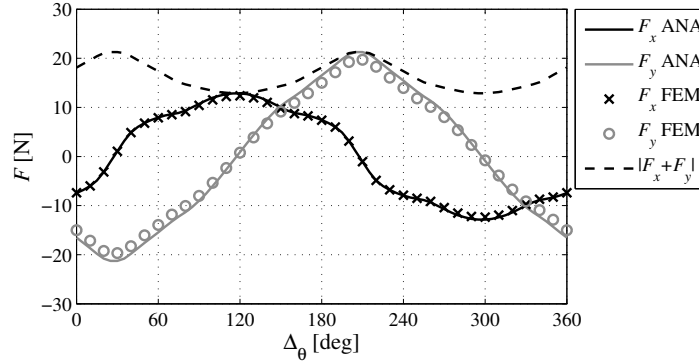
Figure 3.5: Magnetic pull or force in the x-and y-direction versus circumferential displacement. The total magnetic pull is presented as the modulus of F_x and F_y. Calculated by means of a non-linear FE model (FEM) and the analytical model (ANA).

direction, F_z, is reduced by approximately 4 %, while the waveform is not affected. The force in the y-direction is shows the most significant difference as illustrated in Figure 3.5. The difference between the analytical model and F_y is approximately 7 %, caused by the reduced permeability of the soft-magnetic cylinder which results in a lower attraction force of the PMs towards this cylinder. In conclusion, although the BH-curve of the soft-magnetic cylinder is non-linear, and parts of the structure are magnetically saturated, the analytical model still provides a good estimation of the four force components.

3.4   Discussion

Model application

The 3D magnetic field model used as basis for the presented analysis can be used to model electromagnetic fields due to PMs only. Consequently, the force that can be calculated by means of the expressions derived in this chapter is limited to passive attraction and cogging forces. Although the 3D model assumes linear material properties, validation with a non-linear FE model shows good agreement. However, if the modeled device has multiple teeth with a high level of saturation, both the amplitude and the waveform of the cogging force can be affected, and validation with a non-linear FE model is recommended. The model is based on dividing the structure in contiguous regions. Complex structures require a high number of regions to obtain a proper model, resulting in a high number of boundary conditions that have to be solved. As a result, increasing the structure complexity decreases the numerical stability and accuracy as discussed in the previous chapter.

Division in regions

Definition of boundary conditions

Solving set of equations

Magnetic field description   Force description

Force description
(Numerical integration)
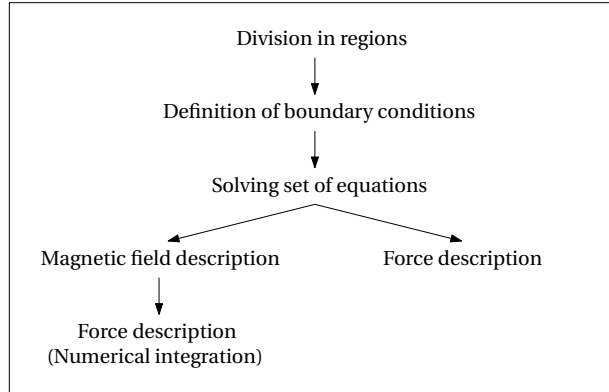
Figure 3.6: Diagram illustrating the analytical and numerical method to calculate the force from the harmonic model presented in the previous chapter.

Numerical versus analytical evaluation

To calculate the four force components, one can integrate (3.3), (3.4), (3.16) and (3.17) numerically or implement the analytical expression as presented in the previous sections and illustrated in Figure 3.6. Two advantages of the analytical implementation are the reduced calculation time of the force, and the independency of the spatial discretization of the magnetic field in the θ- and z-direction. By means of a MATLAB implementation of the structure in the previous section, the calculation time of the two methods are compared. In the numerical integration, 50 points are used to describe the field over one period in the axial and circumferential direction, i.e., integration over 2500 points. The difference between the calculated force components is less than 0.5%. However, the mean calculation time of the analytical implementation is approximately 160 times faster than the numerical calculation. Although this difference is significant, one should note that the computation time of the numerical calculation of the force components is less than 0.5% of the calculation time to find the unknown field coefficients.

Another advantage of the analytical force description is the simple form of F_z and F_θ. In a cylindrical device, the most common direction of movement will be the axial and the circumferential direction. Therefore, the force components of interest are generally F_z and F_θ. The analytical descriptions of these components, (3.8) and (3.14), consists solely of the field coefficients and have a simpler form than the magnetic field description. Therefore, the implementation of this analytical formulation is easier than implementation of the numerical one.

One of the main arguments to use analytical methods to calculate the force in electromagnetic devices is the reduced computation time compared to a finite element model. However, determination of the computation time is difficult as it depends on the required accuracy. The number of harmonics in the semi-analytical model has

to be gradually reduced and the results have to be compared to find the minimum required spatial discretization. The same holds for the number of mesh elements in the finite element model unless an automatic meshing algorithm is used. Solving the resulting semi-analytical model in this chapter is approximately six times faster than solving the (linear and periodic) finite element model, which contains 176000 tetrahedral volume elements. However, the computational effort of the semi-analytical model might be reduced by means of a more efficient implementation, whereas the commercial finite element software takes advantage of years of optimization.

3.5   Summary and conclusions

Force calculation methods using the magnetic field solution of analytical models have been investigated. The Maxwell stress tensor has been selected and is evaluated to calculate the cogging and attraction forces. Due to ambiguity of a global radial force, F_r, on a cylindrical object, the radial force has been split into two components (F_x, F_y) in the Cartesian coordinate system representing the magnetic pull. The resulting four force equations (F_z, F_θ, F_x, F_y) are obtained as a function of the unknown coefficients of the magnetic field equations. This provides that no numerical integration of the magnetic fields is needed to obtain the force components. The main advantages of these analytical force equations are their simple form and the independency of the spatial discretization of the magnetic field in the θ- and z-direction. Good agreement is found between the results of the analytical model and the results of a linear as well as a non-linear finite element model. The presented semi-analytical model is approximately six times faster than the (linear and periodic) finite element model.

Part II

Application

4

Background

Abstract - In this second part, the developed modeling technique of Part I is applied to analyze and design a rotary-linear actuator. This chapter introduces the pick and place application for this 2-DoF actuator and presents its requirements. Prior-art actuators are presented and supporting and opposing arguments of various actuator topologies are discussed.

4.1 Introduction to multi-degrees of freedom systems

Robotic systems are nowadays commonly used in fully automated industrial production lines. An example of such a robotic system is shown in Figure 4.1, where ABB robots are used in an automotive production line. Another example is shown in Figure 4.2(a) which illustrates an Assembléon pick and place (P&P) machine to populate printed circuit boards (PCBs). These systems are generally based on cascading single degree of freedom (DoF) actuators to enable multi-DoF movement. For example, in the robot illustrated in Figure 4.1, rotary machines are stacked such that the end-effector can provide six degrees of freedom.
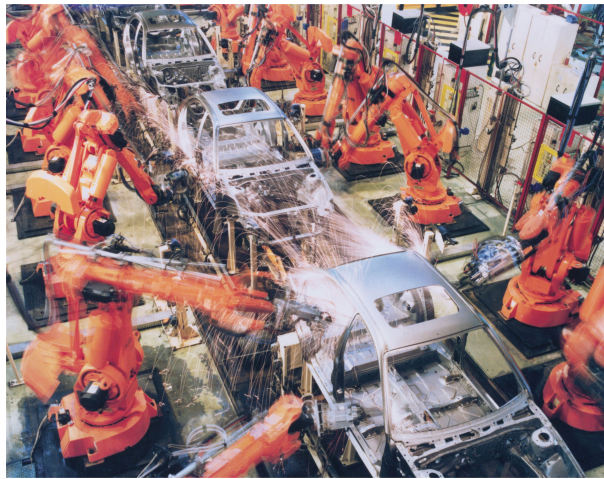
Figure 4.1: *ABB* robots in an automotive production line.

In the second example in Figure 4.2(a), the system can provide four degrees of freedom. Movement in the xy-plane is provided by means of three linear actuators in a H-configuration, referred to as an H-drive. The placement head, Figure 4.2(b), is displaced in the xy-plane by the H-drive and enables movement in the vertical z-direction as well as rotation around this axis. In this placement head, a voice-coil actuator is used as a linear actuator to move the complete rotary actuator with auxiliaries in the vertical direction. As such, the moving mass is relatively high, and the reliability and accuracy of the placement head are impeded by moving cables.

To improve the dynamic performance, reliability and efficiency of stacked systems with mechanical couplings, multi-DoF direct-drive electromagnetic actuators emerge as an alternative. For example, planar actuators are investigated to replace xy-stages in lithographic machines [24, 56, 70]. These actuators provide six degrees of freedom including magnetic levitation enabling vacuum operation. Furthermore, spherical actuators with three degrees of freedom can be used to mimic a shoulder joint without mechanical couplings [133, 137].

(a)   **(b)**
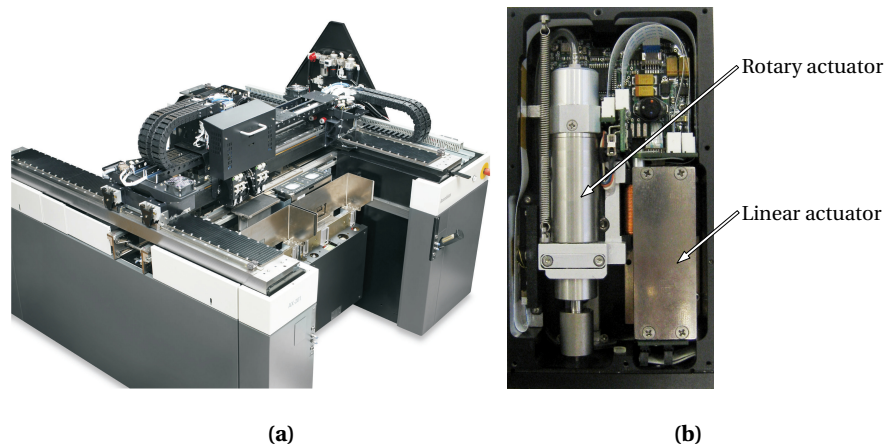
Figure 4.2: (a) Assembléon pick and place machine for placement of surface mounted devices. **(b)** *SMAC* placement head for a pick and place machine.

Part II of this thesis focuses on the combination of rotation and translation in a single actuator, specifically for application in a P&P machine. The goal is to replace stacked manipulators, as for example illustrated in Figure 4.2(b), by a 2-DoF direct-drive electromagnetic actuator to enhance reliability and throughput. In this chapter, a complete set of requirements of the actuator is presented in Section 4.2. In Section 4.3, prior art rotary-linear actuators are discussed and the feasibility of these actuators for the P&P application is discussed. Chapter 5 starts from the prior-art actuators and presents a new patented actuator configuration. Furthermore, the modeling technique presented in part I is applied to create a model of this actuator to provide an accurate description of the magnetic field distribution. Chapter 6 employs this model to analyze the effect of various design parameters on the actuator performance. A final design of a 2-DoF actuator is presented to meet the requirements for the P&P application. In Chapter 7, the realization of the designed actuator is described and experimental verification is presented.

4.2   2-DoF actuator requirements for a pick-and-place robot

The requirements of the 2-DoF rotary-linear actuator are based on the specifications of the P&P machine shown in Figure 4.2. The actuator is intended to be used to place a wide range of components, from very small passive components, for example resistors and capacitors of type SMD 01005 with dimensions of 0.2x0.4 mm, to larger integrated circuits (ICs) with a high number of pins. Furthermore, the actuator will be used to push connectors firmly on the PCBs. To place the small components in a fast way, a high acceleration in the vertical direction is essential. Accurate placement of the ICs demands an accurate rotational positioning system. The components are picked from

a feeder by means of a vacuum, therefore, the mover should be hollow for the transport of air. During the last stage of placing a component on a PCB, sensorless force control is used. The nozzle of the mover contains a mechanical spring and the collision of the component with the PCB is detected by analyzing the actuator currents. As the actuator has to replace the current placement head, shown in Figure 4.2(b), the maximum actuator width is constrained to 34.8 mm. Furthermore, the maximum actuator housing temperature relative to the ambient is $\Delta T = 40$ °C. The specific requirements per axis are given in the next sections.

4.2.1 Translational requirements

The aforementioned requirements for the translational movement of the actuator are quantified in Table 4.1. The required placement force has a resolution of 0.1 N. To obtain this force level accurately from the actuator current, the force-current relation has to be predictable and non-linear effects as friction have to be minimized. The maximum payload of 100 g consists of the tool-bit or nozzle and the component, excluding the moving actuator mass.

As the values given in Table 4.1 are maximum values, a worst case pick and place motion profile, shown in Figure 4.3, is defined to specify the maximum continuous actuator load. The profile describes a complete P&P cycle of 275 ms which consists of:

- movement towards pick position in x, y and z ($t < 34$ ms),
- pick a component from the feeder (at $t = 34$ ms),
- move towards place position in xy-plane and $z = 0$ to identify component orientation ($t > 34$ ms),
- move component to PCB (at $t > 137$ ms),
- place component on PCB (at $t = 171$ ms),
- return to top position ($t > 171$ ms).

Table 4.1: Translational requirements of rotary-linear actuator.

Description		Value	Parameter
Maximum stroke	[mm]	45	-
Maximum velocity	[ms^{-1}]	2.0	v_z
Maximum acceleration	[ms^{-2}]	150	a_z
Maximum jerk	[ms^{-3}]	8.0×10^4	j_z
Maximum position error (static)	[μm]	5	e_z
Minimum encoder resolution	[μm]	1	-
Maximum placement force	[N]	40	F_z
Placement force resolution	[N]	0.1	-
Maximum payload	[kg]	0.1	m_{load}
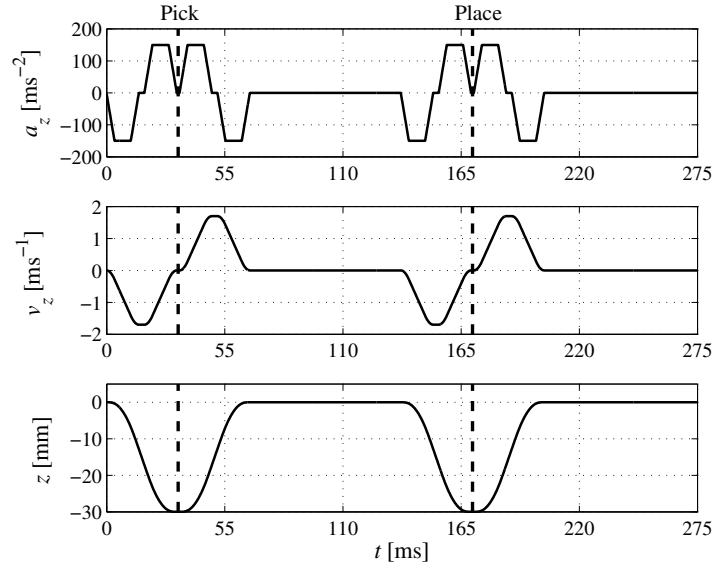
Figure 4.3: Worst case motion profile for the z-axis of the actuator showing the acceleration, velocity and position. The motion profile shows a complete P&P cycle of 275 ms where a component is picked at $t = 34$ ms and placed at $t = 171$ ms.

The actuator has to be designed to follow this motion profile continuously. This worst case motion profile considers the placement of small SMD components, i.e., $m_{\text{load}} \ll 1.0$ g. As such, during the motion profile shown in Figure 4.3, the payload is assumed to be negligible compared to the moving actuator mass.

4.2.2 Rotational requirements

The requirements for the rotational movement of the actuator are specified in Table 4.2. A worst case motion profile is defined to specify the maximum continuous load on the rotational part of the 2-DoF actuator. This profile is illustrated in Figure 4.4 and has the same pick and place times as the motion profile for the translational movement shown in Figure 4.3. Consequently, the complete P&P cycle of 275 ms can be subdivided in the following stages for rotation:

- movement towards pick position in x, y and z, no rotation ($t < 34$ ms),

- pick a component from the feeder, no rotation (at $t = 34$ ms),

- move towards place position in xy-plane as well as z, meanwhile rotating the component to identify and adjust the orientation of the component ($t < 171$ ms),

- place component on PCB, no rotation (at $t = 171$ ms),

- return to pick position and rotate the mover back to the pick orientation ($t > 171$ ms).

Table 4.2: Rotational requirements of rotary-linear actuator.

Description		Value	Parameter
Maximum angular stroke	[rad]	∞	-
Maximum angular velocity	[rad s^{-1}]	126	ω_θ
Maximum angular acceleration	[rad s^{-2}]	3500	α_θ
Maximum angular jerk	[rad s^{-3}]	3.0×10^5	γ_θ
Maximum position error (static)	[mrad]	0.350	e_θ
Minimum encoder resolution	[mrad]	0.158	-
Maximum payload	[kgm^2]	3.0×10^{-5}	I_{load}

Besides the maximum requirements listed in Table 4.2, the rotational part of the actuator has to be designed to follow the motion profile, shown in Figure 4.4, continuously. As mentioned before, this worst case motion profile is employed to place small SMD components. The moment of inertia of these components is typically $I_{\text{load}} \approx 3 \times 10^{-11}$ kgm^2 (estimated for a common component of type SMD 1206), which is assumed to be negligible compared to the moment of inertia of the moving part of the actuator.
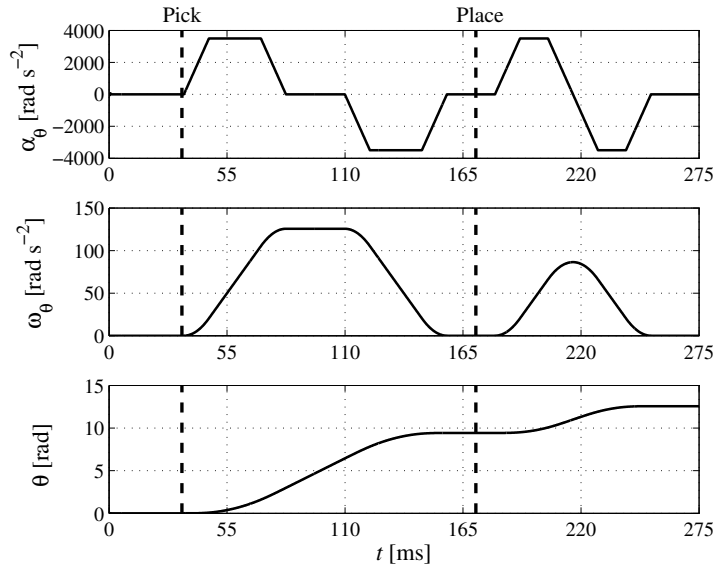
Figure 4.4: Worst case motion profile for the θ-axis of the actuator showing the angular acceleration, speed and position. The motion profile shows a complete P&P cycle of 275 ms where a component is picked at $t = 34$ ms and placed at $t = 171$ ms. To align the component, it is rotated to identify the orientation and subsequently rotated until the correct position is reached. After placing the component, the actuator nozzle is rotated to the original orientation.

4.3   Overview of 2-DoF manipulators

The combination of rotational and linear motion is widely used in modern tooling machines and robotics. As a result, it has been a research topic for years and various actuator topologies are described in literature and patents. Generally, rotary-linear manipulators can be divided in three topologies as illustrated in Figure 4.5.

(a) Parallel coupled actuators

The first topology comprises parallel coupled conventional rotary and linear actuators as shown in Figure 4.5(a) and Figure 4.2(b). Because of the two separate actuators, the stator field is completely used to produce either force or torque. The major disadvantages of this solution are the relatively high moving mass, since the linear actuator has to move the complete rotary actuator. Furthermore, the moving cables for the rotary actuator impede the reliability and introduce disturbance forces.

(b) Series coupled actuators

Series coupled rotary and linear actuators, illustrated in Figure 4.5(b), have a single mover and two separate stationary parts. As such, two active surfaces can be distinguished, one for rotation and another one for translation. Contrary to topology (a), the force is produced in line with the end-effector of the moving part. Generally, the distance in the axial direction between the stationary parts for rotation and translation has to be at least as long as the actuator stroke. Hence, increasing the stroke elongates both the stator and the mover of this actuator type. The control of these actuators is

Figure 4.5: Three possible topologies of a 2-DoF manipulator; **(a)** parallel coupled, **(b)** series coupled, **(c)** integrated topology.

in general simple since the two actuators are physically decoupled, i.e., the force and torque are separately produced.

(c) Integrated actuators

An integrated actuator consists of a single mover and a single stationary part, shown in Figure 4.5(c). The geometry of the mover is the same for rotation and translation, i.e., the length of the stationary part is independent of the stroke contrary to the previous topology. Whereas in topology (b) rotation and translation are fully decoupled, they are magnetically coupled in this topology, and only one active surface is present for both rotation and translation.

Topology (b) and (c) can be considered as single actuators and are widely described in literature and patents as presented by means of an overview in [71]. In the next sections, a selection of prior-art 2-DoF actuators is described and classified by the type of electromagnetic conversion being exploited in the actuator.

4.3.1   Switched reluctance actuators

In [21, 48, 115, 116], switched reluctance machines (SRM) are proposed as a possible candidate to provide the two degrees of freedom. The topology of these actuators is typically the series coupled actuator. The simplicity of the geometry makes the switched reluctance machine a viable actuator for various general purpose adjustable speed applications. The system used in [21, 115], consists of one mover and two cascaded stators which can be independently excited as shown in Figure 4.6. Simultaneous, but unequal, excitation of the same phase windings in each stator section produces the torque and the force. The torque is the sum of the same directional reluctance torque on the mover in both stator 1 and stator 2. The force in the axial direction is produced by the difference in excitation of both stators. In [115] is shown that the two degrees of freedom can be controlled independently. As the stators are

Figure 4.6: Rotary-linear actuator based on the stators of two switched reluctance machines and a single rotor [115].

Figure 4.7: Rotary-linear actuator using two induction motors on a single mover [28].

stacked in the axial direction the axial length of each individual stator will be small. This results inherently in large end-windings compared to the active length of the stator which will decrease the efficiency of the actuator since these end-windings do not contribute to the force or torque. The primary disadvantage of SRMs is the high force/torque ripple compared with conventional machines and the non-linear current-force/torque relation. Due to this non-linearity, sensorless force control is difficult to realize.

4.3.2 Induction actuators

A second class of actuators used for rotary-linear systems is the induction actuator. Several publications are found where induction machines are combined to provide the two degrees of freedom. In [63, 101], an example of stacking multiple rotary induction machines in the axial direction is presented that can provide the thrust force and torque. By controlling the phase of the supply voltage for each stator winding, the mover can produce a rotary, linear and a combined motion. An induction actuator with conventional windings of a rotary machine and a tubular linear machine is discu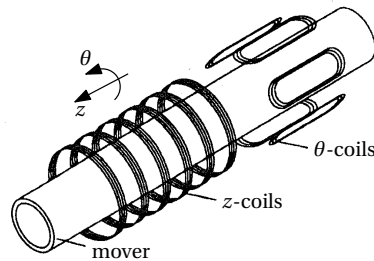ssed in [97]. In [3, 109] a linear-helical motion induction motor is presented that can be used in a stacked arrangement to provide pure rotary, pure linear, or helical motion. The actuator produces a helical motion due to skewed windings and different conductor layers in the rotor. In [28] a 2-DoF actuator consisting of one mover and two stators is proposed for a pick and place module, see Figure 4.7. It consists of an aluminum mover and two sets of coils to provide rotation and translation. In [32] an actuator with the same geometry is analyzed and experimentally verified.

The force/torque density and efficiency of the induction actuator are generally lower than in a SRM or an actuator using permanent magnet materials. Furthermore, due to the principle of operation of induction actuators, position control of the mover is more complicated. On the other hand, the induction actuator has an easy and low cost geometry, e.g. the mover in the induction machine in Figure 4.7 is only an aluminum tube. Furthermore, due to the absence of hard-magnetic material in the mover, no (soft-) magnetic dust is attracted to the mover, and no disturbing reluctance forces are apparent.

4.3.3   Permanent magnet actuators

Rotary-linear actuators using permanent magnets are the most researched actuators. Due to the availability of high energy rare earth permanent magnet materials compact actuators with a high efficiency can be realized. Furthermore, permanent magnet actuators show often good servo-characteristics which makes this class of actuators attractive for robotic applications. In the next three sections, an overview of permanent magnet based 2-DoF actuators is provided.

Series coupled actuators

In [12], a similar topology as shown in Figure 4.6 is used where two stators are stacked in combination with a single mover. The actuator is based on two or more permanent magnet actuators with a single moving magnet translator. In [76], an overview of rotary-linear actuators is given and a new design, optimized for high speed applications, is proposed. The system is based on two actuators having one mover and two stators with air-bearings in between.

In [91, 122, 124] actuators based on one mover with two different magnetization patterns are proposed for the two degrees of freedom. These two patterns interact
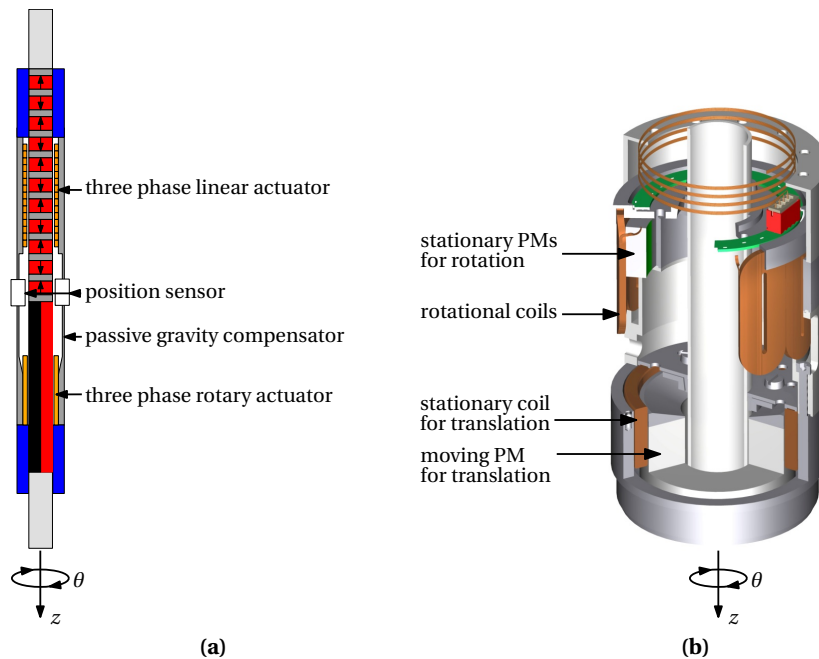

Figure 4.8: (a) Rotary-linear system based on a three phase rotary actuator and a three phase linear actuator by Meessen *et al.* [91]. **(b)** Rotary-linear system based on a three phase PM rotary actuator and a voice coil actuator [103].
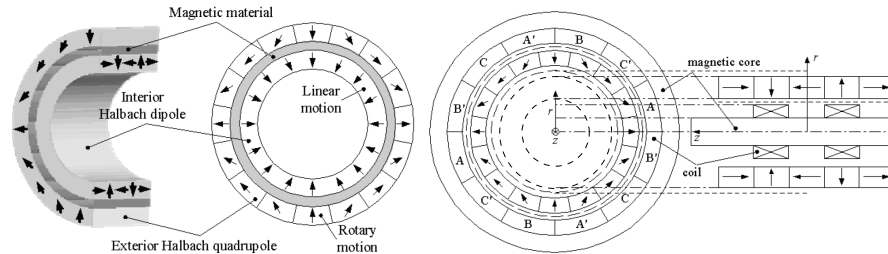
Figure 4.9: Rotary-linear actuator using two concentric quasi-Halbach permanent magnet arrays on one mover [55].

with two different coil sets. One coil set is wound in the longitudinal direction to create torque, and the second coil set is wound in the circumferential direction to create force in the axial direction. Figure 4.8(a) shows a cross-section of the actuator presented in Meessen *et al.* [91]. The distance between the stationary part of the coils for rotation and translation, is used for a position sensor and gravity over-compensation. This provides a relatively compact solution of a series coupled actuator. The actuator is designed for the pick and place module illustrated in Figure 4.2. In this application the passive gravity over compensation is used to prevent machine damage at a power failure, by retracting the mover upwards if the coils are not powered.

Another type of a series coupled actuator is presented in [103], where a voice coil actuator and a synchronous machine are combined. An illustration of this actuator is shown in Figure 4.8(b). The length of the rotational coil is larger than the length of the rotational PMs due to the moving coil configuration. This decreases the efficiency as only a small part of the coil is effective. Although moving coil configurations generally have a low moving mass, the stroke in the circumferential direction is impeded.

In Figure 4.9, a series coupled actuator is shown where two actuators are concentrically stacked [55]. The cylindrical mover of this actuator consists of a soft-magnetic tube with two quasi-Halbach permanent magnet arrays. At the outer surface of the tube, a PM array is realized to create a magnetic field that varies in the circumferential direction to enable rotation. At the inner surface of the tube, the PMs are oriented such that the field varies in the axial direction to enable translation. Due to the self-shielding properties of the quasi-Halbach magnet arrays, the magnetic field in the soft-magnetic tube is low and the two magnet arrays do not interact. Compared to the aforementioned series coupled actuators, the stationary part of this topology has a shorter axial length which is independent of the linear stroke.

Integrated actuators

In [18, 19, 72, 120], actuators are presented with a single magnetization pattern on the mover and a set of coils to provide the two directions of motion. The magnetization in

these actuators has a checkerboard orientation, i.e., magnets with opposing polarity are alternatingly placed in the axial- and circumferential direction. The variation of the magnetic field of the PMs in the circumferential direction is used to produce torque while the magnetic field variation in the axial direction is used to produce force in the axial direction.

Both actuators in [19] and [120] have a mover with a checkerboard magnetization pattern shown in Figure 4.10. Two different sets of coils enclose the mover. One set of windings is oriented in the axial direction to provide rotary motion, the second set is oriented in the circumferential direction to provide linear motion. The advantage of these integrated actuators is the reduced axial length. For example, Figure 4.10(a) shows that the two sets of coils are placed at two sides of the actuator.

It can be seen in Figure 4.10(b) that the magnetization pattern covers only 50% of the mover surface with magnets. At a fixed z, the magnet polarization is equal at all circumferential positions and similarly, at a fixed θ, the magnet polarization is equal at all axial positions. The advantage of this magnet configuration is that two coil sets, which are oriented orthogonally to the direction of motion, can be used as shown in Figure 4.10(b). For example, a coil covering multiple magnets in the axial direction will see a varying flux if the mover is rotated. Conversely, if the same coil configuration applied to the magnet array shown in Figure 4.11, no net flux is seen by the coil if an even number of magnets is covered. Hence, a more complex coil structure has to be used in this actuator, for example multiple coils each covering a single PM as shown in Figure 4.11. In this actuator the (moving) permanent magnets are glued in
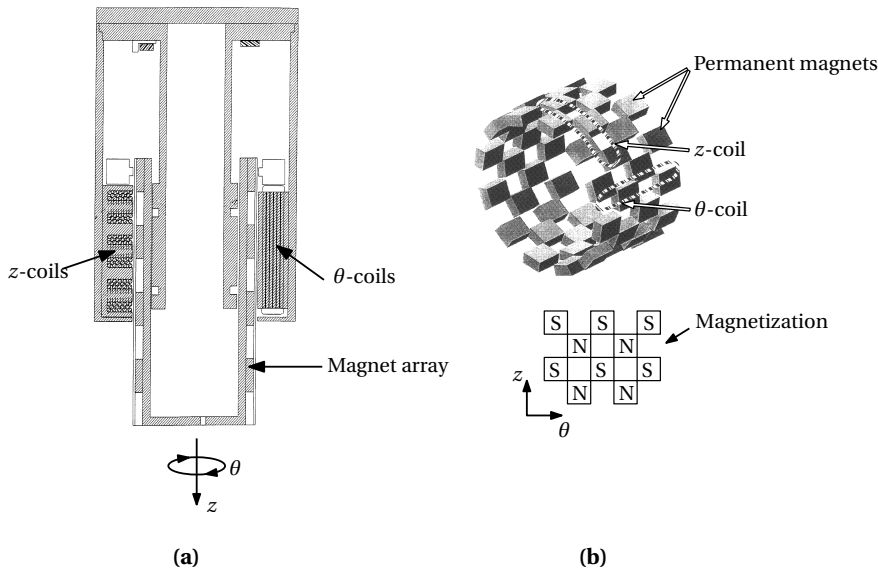
Figure 4.10: Integrated rotary-linear actuator using one mover with a checkerboard magnetization pattern [19]; **(a)** the complete actuator, **(b)** the magnetization pattern.
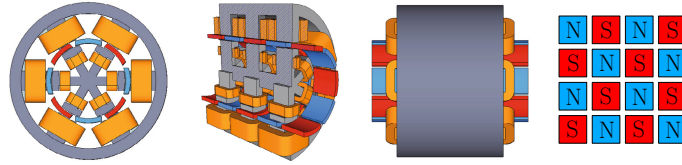
Figure 4.11: Rotary-linear actuator using a checkerboard permanent magnet array on the mover [72] with coils inside and outside the mover.

a cylindrical shape resulting in a mover with a low mass, and at the inner and outer side of this cylinder, coils are wound around soft-magnetic teeth.An alternative coil configuration can be used in a slotless variant of the actuator with the magnet array shown in Figure 4.11. Elongated coils in a herringbone structure, as used in the planar actuator presented in [56], will provide torque and force. However, fabrication of these bended coils is difficult and the force and torque are not physically decoupled which complicates the control of these actuators.

4.3.4 Comparison of actuator classes

To summarize the aforementioned prior-art 2-DoF actuators, the advantages and disadvantages of the three actuator classes are listed below.

Switched reluctance actuators

+ high force/torque density

+ no passive attraction between mover and stator

+ simple mover structure

- large force/torque ripple

- non-linear current and position to force/torque relation

Induction actuators

+ simple mover structure

- low force/torque density

- difficult to use for position control

Permanent magnet actuators

+ high force/torque density

+ linear current - force/torque relation

+ good servo characteristics

- passive attraction between mover and stator

- more expensive due to permanent magnet material

The class of permanent magnet actuators shows the most promising characteristics to be able to meet the requirements of the 2-DoF actuator to be applied in a P&P machine. Therefore, this class of actuators is further researched. The examples of series coupled and integrated actuators presented in this section exhibit required properties, however, do not meet all requirements given in Section 4.2. As such, a new actuator concept is presented in the next chapter that combines the requirements with good manufacturability.

4.4   Summary and conclusions

To enhance the reliability and performance of robotic systems with multiple degrees of freedom, single body direct-drive actuators emerge to replace the cascaded single-DoF actuators. One specific example of a robotic system with four degrees of freedom is a P&P machine to populate printed circuit boards. Two degrees of freedom enable displacement in the xy-plane and two additional degrees of freedom are necessary to pick and place the components, i.e. translation and rotation.

The requirements for this single body 2-DoF rotary-linear actuator have been provided by means of a set of maximum values, and a worst case motion profile has been specified to define its maximum continuous load. That is, for linear movement a static force of 40 N and a mover acceleration of $150\,\mathrm{ms^{-2}}$ with a duty cycle of 34%. For rotational movement the mover acceleration should be $3500\,\mathrm{rads^{-2}}$ with a duty cycle of 47%. Furthermore, the position sensor resolution should be $1\,\mu\mathrm{m}$ and $0.158\,\mathrm{mrad}$ for translation and rotation, respectively.

A brief literature overview has been given describing various rotary-linear actuators. A classification of the different topologies has been defined and examples of each topology are provided. Actuators based on three different types of electromagnetic conversion are presented, i.e., reluctance-, induction- and permanent magnet. Taking into considerations the demanding requirements, an actuator employing PMs has been deemed essential for this P&P application.

5

Actuator configuration and modeling

Abstract - To obtain an actuator that complies with the requirements given in Chapter 4, a new actuator topology is presented. Possible realizations of this type of actuators are discussed and one configuration is selected for further research. Analytical models for the selected configuration are derived and validated with finite element analyses.

5.1   Mover configuration

In Section 4.3.3, integrated and series coupled permanent magnet actuators are presented, and the supporting and opposing arguments for these actuator classes have been discussed. To obtain an actuator that provides rotation and translation according to the specifications given in Section 4.2, the class of integrated actuators with a checkerboard magnetization is further investigated in this chapter.

The existing coil and magnet configurations for integrated 2-DoF actuators can be generalized by means of the illustration in Figure 5.1, where two different magnetization patterns are distinguished:

1. A checkerboard magnetization consisting of PMs with opposing magnetization direction along both θ- and z-direction (Figure 5.1(a,b)).

2. A checkerboard magnetization consisting of PMs with equal magnetization direction in the θ- and z-direction (Figure 5.1(c)).

It can be seen that selection of a specific magnetization pattern constrains the possible coil configurations. Due to the alternating polarity of the permanent magnets in the first magnetization configuration, a single coil covering the complete circumference, shown in Figure 5.1(c), cannot be used as the net flux linkage will be zero. Instead, multiple smaller coils or diagonal coils, shown in Figure 5.1(a,b), have to be used. These coils are more difficult to manufacture and assemble, particularly in actuators with a small diameter. Conversely, the magnetization pattern illustrated in Figure 5.1(c) can be used in combination with two ordinary orthogonal windings due to the spacing between the adjacent PMs. However, the magnetic loading is lower due to a reduced amount of hard magnetic material.

In all three magnetization patterns shown in Figure 5.1, the magnetic field variation in the θ- and z-direction is inherently coupled due to the symmetry of the pattern. Furthermore, the force components in the axial- and circumferential direction are
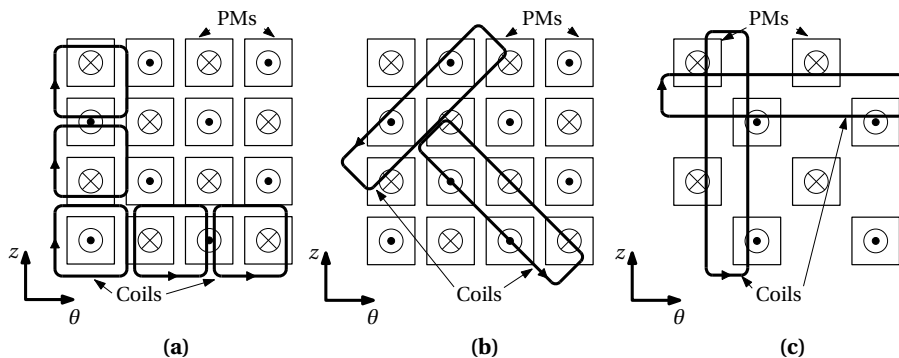
Figure 5.1: Magnetization pattern with **(a)** concentrated square coils, **(b)** coils covering a set of PMs in the diagonal direction, and **(c)** coils covering a set of PMs in the axial or circumferential direction.
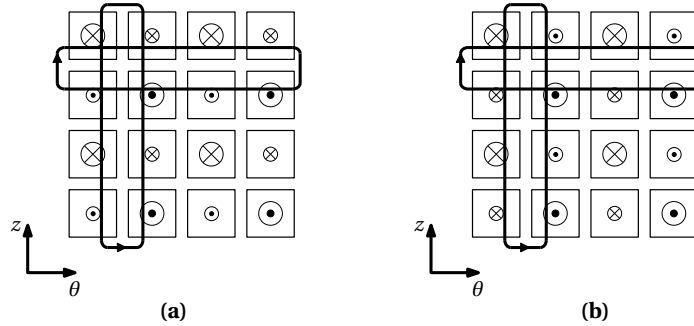
Figure 5.2: New magnetization concept based on inserting weaker magnets in between the poles to **(a)** increase the axial force, **(b)** increase the torque.

produced by the radial component of the flux density. Consequently, increasing the torque by enhancing the radial component of the flux density results in most situations also in a higher force capability. This can restrain the applicability of these topologies as in many applications the force and torque requirements differ significantly. A new magnetization pattern is introduced to avoid this limitation of checkerboard magnetization patterns presented by Meessen *et al.* in [93, 126].

Patented magnetization configuration

To avoid the aforementioned drawbacks of the magnetization patterns illustrated in Figure 5.1, a new magnetization concept is proposed, illustrated in Figure 5.2. It starts from the pattern shown in Figure 5.1(c) and is based on inserting weaker PMs in between the existing magnetic poles. In the pattern shown in Figure 5.2(a), the magnetization direction of the inserted magnets is such that all PMs along the θ-direction have the same magnetization orientation. As a result, the coil wound in the circumferential direction experiences an increased flux density compared to the original configuration. The net flux seen by the coil wound in the axial direction, however, is reduced but still non-zero because the inserted magnets are weaker than the original poles. The resulting actuator has an improved force density and a reduced torque density, where the ratio between the two can be altered by adjusting the strength of the inserted PMs. Figure 5.2(b) shows the configuration with the opposite results. That is, the orientation of the inserted PMs is such that they have the same direction of magnetization in the z-direction.

The weaker PMs, inserted between the poles as illustrated in Figure 5.2, can be realized by different approaches. For example, the remanent flux density can be lowered, or PMs with smaller dimensions can be used. Another approach is to start from an existing one dimensional magnetization for a single DoF actuator, and alter the geometry such that the concept of Figure 5.2 is obtained. Because of the requirements for the pick and place application presented in the previous chapter, this thesis focuses on an actuator with a high axial force and a relatively low torque. Therefore, the topology illustrated in Figure 5.2(a) is further investigated.

Magnetization realization

To find a magnetization pattern in accordance with the concept illustrated in Figure 5.2(a), the research starts from a linear tubular permanent magnet actuator (TPMA) [90]. This class of linear actuators consists of a cylindrical PM array and cylindrical coils wound in the circumferential direction. The coils and PMs enclose the full circumference and do not have end-windings. Consequently, the magnetic field of the PM is completely used without leakage resulting in a high force density. Due to the cylindrical shape, rotational movement of the coils or the PMs does not affect the force, which makes the TPMA an obvious linear actuator for a rotary-linear actuator [88, 90]. The PMs can be mounted interiorly or exteriorly as described in [39]. The topology with interior magnets has the advantage that the dissipated power in the coils does not flow through the PMs. The TPMA is most commonly used as a three phase actuator in long stroke applications where either the coils or the PMs are the moving part, referred to as translator. The moving coil configuration can be beneficial if the moving mass has to be low [89], however, the moving cables introduce wear and disturbance forces. Furthermore, the moving part of the TPMA should allow for infinite rotation in this application. Therefore, the interior moving magnet topology is selected and further investigated. Three magnetization patterns are described in literature for three phase TPMAs which are presented in the next sections.

Radially magnetized TPMA

The first magnetization topology of the TPMA originates from a classical rotary machine. It consists of a soft-magnetic core enclosed by radially magnetized PMs with alternating polarity, shown in Figure 5.3(a). The soft-magnetic core is necessary to create a high permeable flux path in the axial direction between two consecutive poles. As a result, the translator mass of this magnetization topology is relative high because the amount of soft-magnetic material has to be sufficient to prevent saturation. Magnetizing the radially magnetized rings, shown in Figure 5.3(a), is a difficult and expensive process. Therefore, these rings are often approximated by several diametrically magnetized segments as described in [92].

Figure 5.3(b) shows ring magnets approximated by only two diametrically magnetized segments. As a result, along the circumference of one ring magnet, two magnetic poles with a normal strength, and two poles with a weaker strength can be distinguished, denoted by (N) and (N) or (S) and (S). If these ring magnets are stacked and rotated by 90 degrees with respect to each other, the magnetization concept illustrated in Figure 5.2(a) is realized. A disadvantage of this configuration is the inability to vary the ratio between the regular and weaker poles (N and N) as they are inherently coupled.
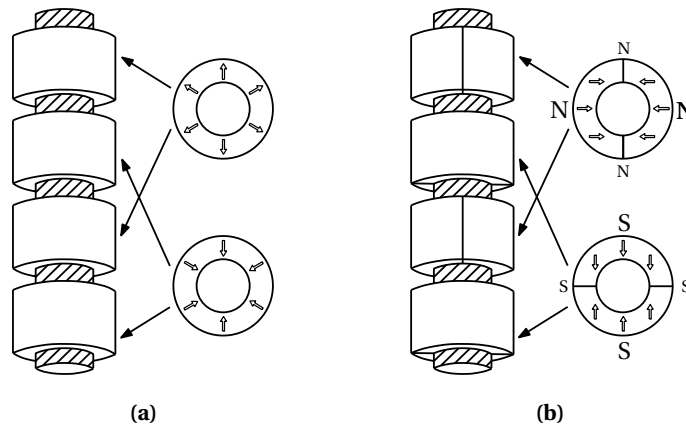
Figure 5.3: PM array of a radially magnetized tubular permanent magnet actuator consisting of a soft-magnetic core enclosed by **(a)** radially magnetized rings, **(b)** rings consisting of two diametrically magnetized segments to create weaker poles, (N,S), in between regular poles, (N,S).

Axially magnetized TPMA

The second possible realization of the concept illustrated in Figure 5.2(a) is derived from a tubular linear actuator with an axially magnetized translator [88, 90]. The translator of this actuator consists of axially magnetized PMs of alternating polarity with soft-magnetic rings in between, see Figure 5.4(a). The flux is focused in the airgap through the soft-magnetic ring uniformly along the circumference. To realize a magnetization shown in Figure 5.2(a), the circumferential symmetry has to be eliminated. A possible approach is illustrated in Figure 5.4(b), where the soft-magnetic rings are replaced by rings with two flattened sides. The rings are rotated by 90 degrees with respect to each other and a weak south pole appears between two north poles and vice versa in the axial direction. A similar configuration is shown in Figure 5.4(c) where both the PMs and the soft-magnetic rings are altered to remove the circumferential symmetry. Instead of removing material from the soft-magnetic ring, material is added to force the flux to leave or enter the translator at that position.

Contrary to the topology with the radially magnetized PMs, shown in Figure 5.3(b), the ratio between the regular and the weaker poles can be varied by altering the shape of the pole-pieces. The disadvantage of the topology with the flattened pole pieces, Figure 5.4(b), is the reduced mechanical strength due to the removed material from the pole pieces. The topology shown in Figure 5.4(c) does not exhibit this issue, however, due to the complex shape of the PMs and the pole-pieces, this topology is more difficult to manufacture.

(a)   **(b)**   **(c)**
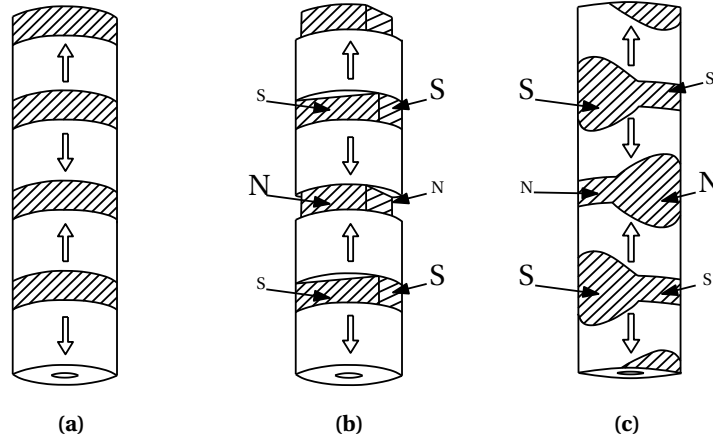
Figure 5.4: PM array of an axially magnetized tubular permanent magnet actuator
consisting of axially magnetized PMs with **(a)** regular soft-magnetic pole pieces (dashed
part) **(b)** soft-magnetic pole pieces with two flattened sides to create weaker poles, (N,S),
in between regular poles, (N,S). **(c)** soft-magnetic pole pieces widened at two sides to
create weaker poles, (N,S), in between regular poles, (N,S).

Quasi-Halbach magnetized TPMA

The third magnetization topology used in TPMAs consists of a quasi-Halbach perma-
nent magnet array, shown in Figure 5.5(a). In this topology, the soft-magnetic pole
pieces used in Figure 5.4(a) are replaced by radially magnetized rings. Due to this
magnet configuration, the magnetic field is focused on one side of the PM array and no
soft-magnetic core is required as a flux return path [44, 80]. As mentioned before, the
radial ring magnets are difficult to produce and diametrically magnetized segments
are used to approximate an ideal radial ring magnet. The effect of this segmentation
is extensively modeled and described in [86, 92] by Meessen *et al.*. The segmentation
of the PMs results in a variation of the radial component of the flux density along the
circumference which is reduced if the number of segments is increased. This variation
is exploited to realize the magnetization concept shown in Figure 5.2(a). Two segments
are used to approximate the radially magnetized ring magnet and the resulting rings
are stacked and rotated 90 degrees with respect to each other, see Figure 5.5(b). The
axially magnetized magnets are placed in between these PMs with alternating polarity
[95].

The ratio between the regular and the weaker poles (N and N) of the magnetization
pattern shown in Figure 5.5(b) is inherently coupled. However, the ratio between the
flux seen by a coil in the circumferential direction and a coil in the axial direction can
be altered by adjusting the ratio between the height of the axially magnetized PMs
and the height of the segmented ring magnet. The disadvantages of the previous
configurations are absent here since no soft-magnetic core is required, the mechanical
strength of the structure is not affected due to odd shaped magnets or pole pieces,
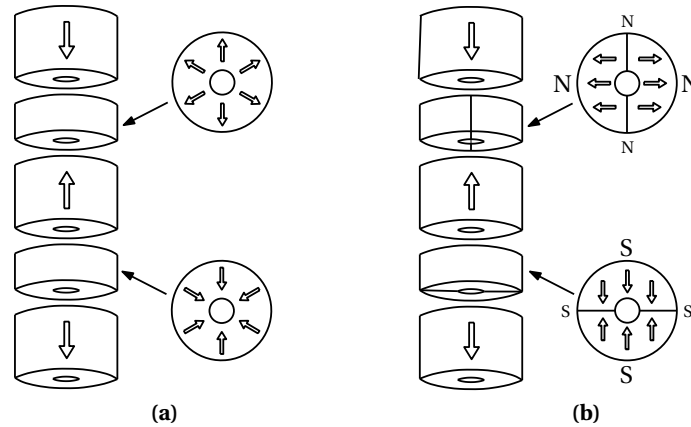
Figure 5.5: (a) Quasi-Halbach permanent magnet array for a TPMA consisting of axially magnetized rings with radially magnetized rings in between. **(b)** Altered quasi-Halbach permanent magnet array where the radially magnetized rings are replaced by rings consisting of two diametrically magnetized segments. The rings are stacked with an offset of 90 degrees with respect to each other to create the magnetization concept shown in Figure 5.2(a), where (N,S) are the weaker poles in between the regular poles, (N,S).

and all components are relatively easy to manufacture. A cost-disadvantage of this topology is the larger amount of permanent magnet material used in the assembly.

Magnetization topology comparison

The topologies described in the previous sections are summarized in Table 5.1. From the table can be concluded that the quasi-Halbach topology exhibits the most promising characteristics. Therefore, this topology is selected and further investigated.

Table 5.1: Comparison of tubular permanent magnet magnetization patterns to realize a 2-DoF magnetic field distribution.

	Radial	Axial a/b	Quasi-Halbach
Mass/magnetic loading ratio	-	+	++
Adjustable force/torque ratio	-	+	+
Manufacturability	++	-	+

5.2   Stator configuration

The stationary part of the actuator, referred to as stator, accommodates two coil sets, one for rotation and one for translation. The coils for rotation are oriented in the axial direction and the coils for translation are oriented in the circumferential direction as illustrated in Figure 5.2(a). Consequently, coil configurations used in TPMAs and ordinary rotary actuators can be used. In general, the stator of an actuator can be slotless or slotted, illustrated in Figure 5.6.

Slotted stator

In an actuator with a slotted stator, the winding is placed inside slots in the soft-magnetic stator back-iron illustrated in Figure 5.6(a). That is, the winding is wound around soft-magnetic teeth. These teeth provide a high permeable path and in combination with the small airgap, a high flux linkage of the winding is obtained. Due to the slot openings, the stator permeance is not constant along the circumference of the airgap. As a result, cogging torque/force is present in actuators with a slotted stator, however, this disturbance torque/force can be minimized be selecting an appropriate pole-slot combination or by optimization of the tooth shape.

Slotless stator

In a slotless stator, the winding is accommodated between the moving part and the stator back-iron shown in Figure 5.6(b). Due to the absence of the high permeable teeth through the winding, the magnetic loading is generally lower than in slotted actuators resulting in a lower torque/force density. An advantage of the slotless actuator is that due to the absence of the teeth, the stator permeance is constant along the circumference and no cogging torque/force is apparent. Furthermore, the geometry of the stator is simpler and easier to manufacture and assemble.
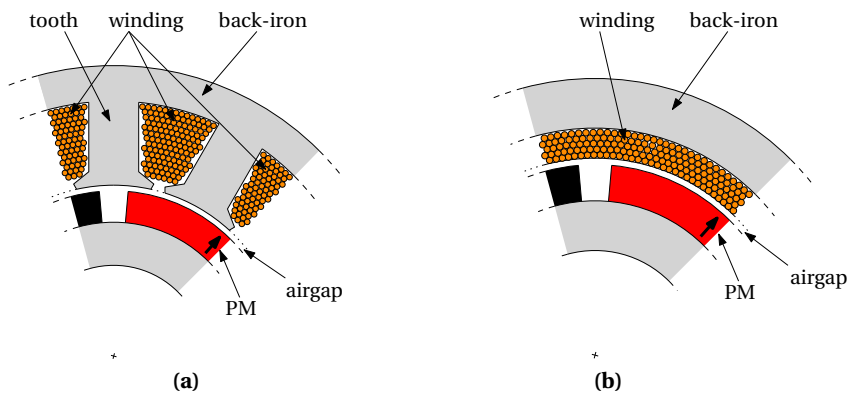
Figure 5.6: Illustration of two exterior stators of a PM rotary machine. **(a)** Slotted stator with winding accommodated inside slots in back-iron. **(b)** Slotless stator with winding accommodated inside the airgap.
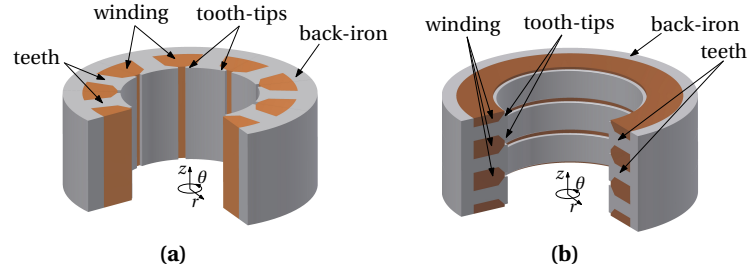
Figure 5.7: **(a)** Illustration of a slotted stator with winding for rotary machine. **(b)** Illustration of a slotted stator with winding for a linear tubular PM actuator.

5.2.1   2-DoF actuator stator configuration

To create a compact stator, the two orthogonal coil sets, illustrated in Figure 5.2(a), are concentrically placed in the stator. Both the windings for rotation and translation can be placed inside the airgap or inside slots, hence, six stator configurations are possible. Hence, the stator can be both slotted and slotless. Therefore, in the remainder of the analysis, a winding placed inside slots is referred to as a slotted winding. A winding placed inside the airgap is referred to as a slotless winding.

An example of a slotted stator for the rotational part of the actuator is shown in Figure 5.7(a) where the winding and teeth are oriented in the axial direction. Figure 5.7(b) shows a slotted stator for the translational part of the actuator which is an example of a typical slotted stator of a TPMA.

Double slotted stator

Integration of the two presented slotted stators concentrically results in a double slotted stator, illustrated in Figure 5.8. In Figure 5.8(a), the tooth-tips of an ordinary slotted stator of a rotary actuator, shown in Figure 5.7(a), are enlarged to accommodate a slotted winding of a TPMA. Torque is generated by flux crossing the airgap in the radial direction and flowing in the $r\theta$-plane between consequent poles in the circumferential direction of the mover. The flux from the mover crosses the airgap, entering the teeth for translation, flowing through a tooth for rotation and passing through the back-iron in the circumferential direction to one of the next teeth for rotation and back to the mover. As a result, the flux is linked by the winding for rotation. The force in the axial direction is generated by flux crossing the airgap in the radial direction and flowing in the rz-plane between consequent poles in the axial direction of the mover. The flux enters a tooth for translation and flows through one or more teeth for rotation in the axial direction to one of the next teeth for translation and back through the airgap. Since the flux flows in the rz-plane, the winding for translation links this flux. The same holds for the topology shown in Figure 5.8(b), except that the winding for rotation is located inside the elongated tooth-tips of the teeth for translation.
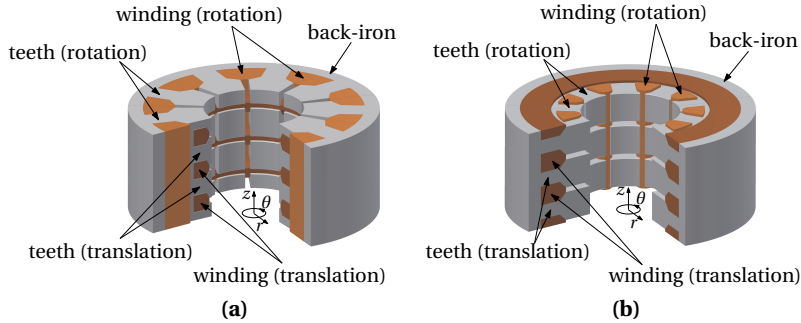
Figure 5.8: Double concentric slotted stator for 2-DoF actuator **(a)** Double slotted stator with winding for rotation and winding for translation embedded in tooth-tips of teeth for rotation. **(b)** Double slotted stator with winding for translation and winding for rotation embedded in tooth-tips of teeth for translation.

The advantage of the topologies illustrated in Figure 5.8 is the high magnetic and electrical loading due to the double slotted stator. Furthermore, because of the soft-magnetic structure, the dissipated heat can easily be transferred to the outside of the stator. The main drawback is the complexity of the structure. To be able to place the coils in this double slotted stator, it has to be divided into multiple small soft-magnetic sections.

Single slotted stator

The topologies illustrated in Figure 5.9 have one slotless and one slotted winding. As a result, the stator structure is less complex and hence, easier to realize. The stator illustrated in Figure 5.9(a) is based on the slotted stator shown in Figure 5.7(a) with an enlarged airgap to accommodate a slotless winding for translation. The flux flowing between two consequent poles in the axial direction is linked by the circumferential
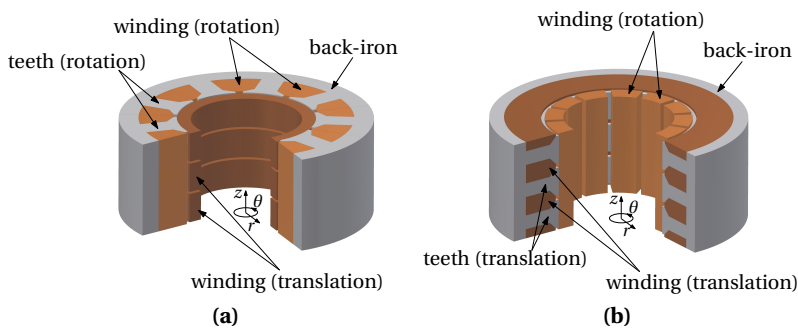
Figure 5.9: **(a)** Slotted stator for rotation with slotless winding for translation accommodated in the airgap. **(b)** Slotted stator for translation with slotless winding for rotation accommodated in the airgap.

coils and is used to generate force in the axial direction. The teeth and tooth-tips for rotation provide a high-permeable flux path in the axial direction and can be regarded as the back-iron of the slotless winding. Figure 5.7(b) shows a similar configuration where the slotted winding provides translation and the slotless winding rotation. The stator of these topologies is slotted in one direction and cogging force/torque is only present in one direction of motion. The distance between the PMs and the stator is significantly larger in the single slotted topology resulting in a lower permeance variation and hence, lower cogging force/torque.

Slotless stator

Two more stator configurations are possible where both the winding for translation and rotation are slotless and concentrically placed in the airgap. The resulting stator structure is simple as it is just a cylindrical tube and hence, no cogging torque or force is present. Since the airgap has to accommodate two winding sets, the magnetic loading and the torque/force density of this configuration will be lower than for the four previously presented topologies. Furthermore, the dissipated heat in the inner winding has to cross the outer winding and the back-iron before it can leave the actuator. The thermal conductivity of a winding is much lower than that of iron, typically $1.5\mathrm{Wm}^{-1}\mathrm{K}^{-1}$ versus $50\mathrm{Wm}^{-1}\mathrm{K}^{-1}$, hence, the dissipation in the inner winding has to be lower compared to the single or double slotted stator where the winding is placed in direct contact with the teeth and/or back-iron.

In all presented stator configurations, the force and torque are fully decoupled if the material properties of the soft-magnetic part are considered to be linear in the working range. The validity of this assumption depends on the flux density level in the inherently non-linear soft-magnetic material. This depends on the final design of the stator part and can be considered as one of the optimization criteria in a design optimization.

5.2.2 Stator configuration selection

A comparison of the aforementioned stator configurations is presented in Table 5.2. Although the specific properties of each topology depend on the final design, for example, the cogging force/torque can be significantly diminished by selecting a proper pole/slot combination, the table provides a basis for the stator topology selection. The single slotted actuator is considered to be the best compromise between force/torque density and complexity of the structure to be applied in the 2-DoF actuator. The configuration with the slotted winding for rotation and the slotless winding for translation, illustrated in Figure 5.9(b), is selected based on the following arguments:

- A slotless TPMA can provide the required acceleration in this application, based on the results presented in [88, 90] by Meessen *et al.*

Table 5.2: Comparison of stator configurations for a 2-DoF actuator.

	Double slotted	Single slotted	Slotless
Force/torque density	++	+	-
Cogging force/torque	−	-	++
Thermal properties	++	+	-
Manufacturability	−	+	++

- The stator structure is simpler than the topology shown in Figure 5.9(a), where the stator should consist of multiple segments to be able to place the coils for translation inside the slots.

- The leads of the coil for translation can be placed inside the slot-openings of the slots for the winding for rotation, while the topology shown in Figure 5.9(b) requires an additional slit or hole for the lead wires.

Another argument to place the winding for translation concentrically inside the winding for rotation is inherently derived from the relation between the force and the mean radius of the winding. In the following analysis, the effect of the position of the winding (inside or outside the winding for the other direction of movement) is estimated. An actuator with a fixed outer radius of the stator is considered and the copper loss is regarded to be the same for the inner and the outer winding. The force on a single coil of the winding is considered to be

$$F \propto B_r i l, \tag{5.1}$$

where B_r is the radial component of the magnetic flux density, i is the current through that coil and l is the length of the coil.

Translation The total copper loss in the winding for translation is $P_z \propto i_z^2 R_z$ where R_z is the resistance of a single coil

$$R_z = \rho \frac{l}{A}, \tag{5.2}$$

where ρ is the resistivity of copper, l is the coil length, and A is the area of the coil cross-section. The resistance is proportional to the coil radius as the length of the coil is proportional to the radius and the cross-section is considered constant

$$R_z \propto r. \tag{5.3}$$

Considering a constant copper loss, P_z, this yields to

$$i_z \propto \frac{1}{\sqrt{r}}. \tag{5.4}$$

Rotation The total copper loss in the coil for rotation is $P_\theta = i_\theta^2 R_\theta$ where R_θ is the resistance of the coil

$$R_\theta = \rho \frac{l}{A}. \tag{5.5}$$

The resistance is proportional to one over the radius as the cross-section of the coil is proportional to the radius and the coil length is independent of the radius.

$$R_\theta \propto \frac{1}{r}. \tag{5.6}$$

Considering a constant copper loss, P_θ, this yields to

$$i_\theta \propto \sqrt{r}. \tag{5.7}$$

Combining (5.1) with (5.4) and (5.7) yields to

$$F_z \propto B_r \sqrt{r}, \tag{5.8}$$
$$F_\theta \propto B_r \sqrt{r}. \tag{5.9}$$

However, the torque on the coil is

$$T_z = r F_\theta \tag{5.10}$$
$$\propto B_r r \sqrt{r}, \tag{5.11}$$

Both force components depend on the radial component of the flux density, hence, the effect of the relation between the flux density and the radius is the same for the torque and the force in the axial direction. In conclusion, the effect of a larger winding radius is more significant on the torque than on the force.

5.3 3D actuator model

In the previous sections, various 2-DoF actuator topologies are presented. The altered quasi-Halbach topology with the single slotted stator with slotless coils for translation, shown in Figure 5.5(b) and Figure 5.9(a), respectively, is selected to be the most promising combination. In this section, a 3D analytical electromagnetic model of this actuator topology is derived based on the theory presented in Chapter 2. The model provides the magnetic field distribution due to the presence of the PM-array.

5.3.1 Division in regions

To derive a model for the actuator, the geometry has to be divided into multiple regions as presented in Section 2.3.3. The selected stator topology, illustrated in Figure 5.9(a), can be divided into the following regions:
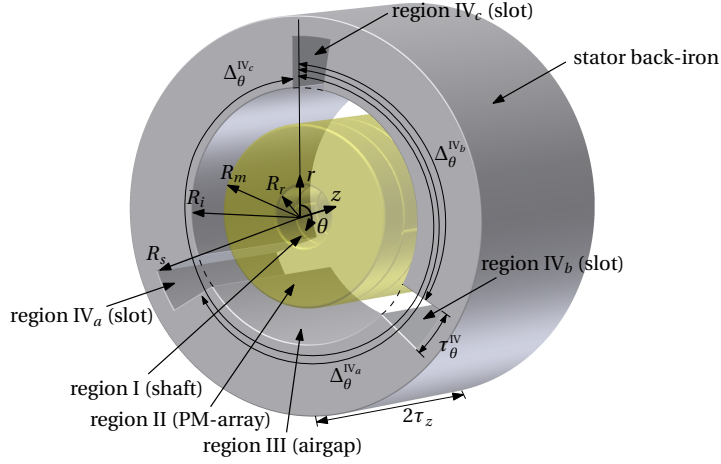
Figure 5.10: Model definition of the 2-DoF actuator topology consisting of a PM-array and a soft-magnetic cylinder with three slots in the axial direction.

  I the non-magnetic shaft of the mover,

 II the PM-array of the mover,

III the (magnetic) airgap region, this includes the coil area for translation as the magnetic field of solely the PMs is calculated in the 3D model,

IV the stator slots in the axial direction. The subscripts $a, b, \dots$ are used to denote each individual slot.

The harmonic modeling technique, described in Chapter 2, can consider slots in either the circumferential or the axial direction. Therefore, the finite axial length of the actuator is not taken into account in this model since slots in the axial direction are considered. To calculate the effects of this finite length, a second model has to be constructed without slots in the axial direction which is explained in Section 6.5.1.

  A three phase winding for rotation is selected resulting in a minimum of three slots. The number of slots can be extended by expanding the number of sub-regions $IV_{a,b,c}$. One full period of the model is illustrated in Figure 5.10 with the geometrical parameters listed in Table 5.3. The origin of the coordinate systems of regions I, II and III coincide, i.e., $\Delta_\theta^{I} = \Delta_\theta^{II} = \Delta_\theta^{III} = 0$ and $\Delta_z^{I} = \Delta_z^{II} = \Delta_z^{III} = 0$. To enable rotation of the slots with respect to the PM-array, $\Delta_\theta^{IV_a}, \Delta_\theta^{IV_b}$ and $\Delta_\theta^{IV_c}$ are introduced defining the displacement of the slots in the circumferential direction. As the stator reveals no variation in the axial direction, displacement in this direction is not considered, i.e., $\Delta_z^{IV_a} = \Delta_z^{IV_b} = \Delta_z^{IV_c} = 0$. The pole pitch in the axial direction, τ_z, originates from the periodicity of the PM-array shown in Figure 5.11. This dimension fixes the fundamental period of the Fourier series to describe the magnetic field in all regions in the axial direction to be $2\tau_z$. In the circumferential direction, the

Table 5.3: List of geometrical parameters of the 3D structure illustrated in Figure 5.10 representing one periodic section of the 2-DoF actuator.

Parameter		Description
R_r	[mm]	Inner radius PM array
R_m	[mm]	Outer radius PM array
R_i	[mm]	Inner radius stator back-iron
R_s	[mm]	Outer radius slot
τ_θ^{IV}	[deg]	Slot width
τ_z	[mm]	Pole pitch in the axial direction
$\Delta_\theta^{\text{IV}_a,\text{IV}_b,\text{IV}_c}$	[deg]	Offset of slot w.r.t. region I in the θ-direction

fundamental period of the Fourier series is $\tau_\theta = 2\pi$ in regions I, II and III. In the slot regions, IV$_a$, IV$_b$ and IV$_c$, the fundamental period is defined by means of the slot width, τ_θ^{IV}, according to the theory described in Section 2.5.

5.3.2 Magnetization description

To calculate the magnetic field due to the presence of permanent magnets, the PM-array has to be described by a remanent magnetization vector based on a Fourier expansion defined in (2.35) in Section 2.4. The remanent magnetization vector of a standard quasi-Halbach array for a TPMA, shown in Figure 5.5(a), contains a radial and an axial component. As the radially magnetized rings are replaced by diametrically magnetized segments, the circumferential, θ-, component of the magnetization appears in the magnetization vector describing the PM-array of Figure 5.5(b). One period of the PM-array is shown in Figure 5.11, where τ_z is the pole pitch and half a period, and α_{pz} is the ratio between the axial length of an axially magnetized ring and the pole pitch, τ_z. The radial magnetization component of one diametrically magnetized segment is sinusoidal whereas the circumferential component is a cosine function. The three components of the magnetization vector, M_r, M_θ and M_z are
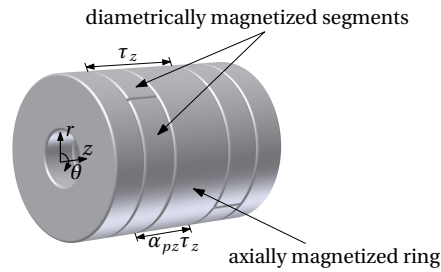
Figure 5.11: Altered quasi-Halbach magnetization array consisting of axially magnetized rings and diametrically magnetized segments.

(a)

(b)

(c)
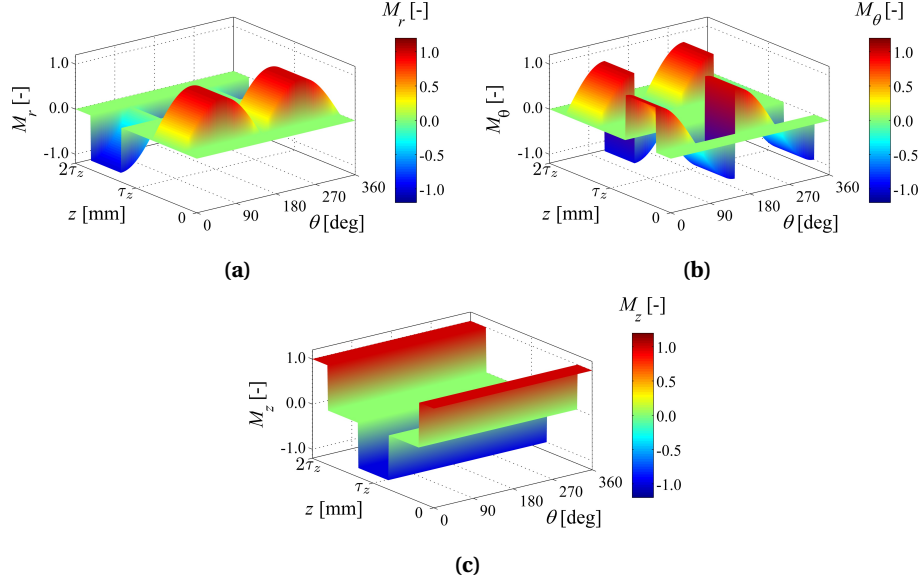
Figure 5.12: Three components of the remanent magnetization of the altered quasi-Halbach permanent magnet array illustrated in Figure 5.5(b). **(a)** Radial component of the magnetization, M_r, **(b)** circumferential component of the magnetization, M_θ, and **(c)** axial component of the magnetization, M_z.

illustrated in Figure 5.12 as a function of the axial and circumferential position in the PM array. The components in the radial and circumferential direction, shown in Figure 5.12(a,b), describe the diametrically magnetized segments, while the axial component in Figure 5.12(c) describes the axially magnetized ring.

Remanent magnetization vector

Using Fourier expansion, defined by (2.6) to (2.9), the coefficients of the magnetization shown in Figure 5.12 are found

$$M_{rss} = 0, \tag{5.12}$$

$$M_{rsc} = 0, \tag{5.13}$$

$$M_{rcs} = \begin{cases} -\dfrac{16\left((-1)^k + \sin^2\left(\frac{n\pi}{4}\right)\right)(-1)^n \cos\left(\frac{n\pi}{2}\right)\sin\left(\frac{k\pi}{2}\right)\sin\left(\frac{k\pi(\alpha_{pz}-1)}{2}\right)}{k(n^2-1)\pi^2}, & n > 1, \\[2ex] -\dfrac{4\left((-1)^k - 1\right)\cos\left(\frac{\alpha_{pz}k\pi}{2}\right)}{k\pi^2}, & n = 0, \\[2ex] 0, & n = 1, \end{cases} \tag{5.14}$$

$$M_{rcc} = \begin{cases} \dfrac{-4\cos\left(\frac{3k\pi}{2}\right)\left(\cos\left(\frac{n\pi}{2}\right)+\cos\left(\frac{3n\pi}{2}\right)\right)\sin\left(\frac{k\pi(\alpha_{pz}-1)}{2}\right)+\left(1+(-1)^k\right)\left(1+(-1)^n\right)^2\sin\left(\frac{k\pi\alpha_{pz}}{2}\right)}{k(n^2-1)\pi^2}, & n > 1, \\[2ex] = 0, & n = 0, 1, \end{cases}$$
$$\tag{5.15}$$

$$M_{rs} = 0 \tag{5.16}$$

$$M_{rc} = 0 \begin{cases} \frac{(\alpha_{pz}-1)\left(1+(-1)^n-\cos\left(\frac{n\pi}{2}\right)-\cos\left(\frac{3n\pi}{2}\right)\right)}{(n^2-1)\pi}, & n > 1, \\ 0, & n = 1, \end{cases}$$

$$M_{r0} = 0, \tag{5.17}$$

$$M_{\theta ss} = \begin{cases} \frac{16\left((-1)^k+\sin^2\left(\frac{n\pi}{4}\right)\right)n(-1)^n\cos\left(\frac{n\pi}{2}\right)\sin\left(\frac{k\pi}{2}\right)\sin\left(\frac{k\pi(\alpha_{pz}-1)}{2}\right)}{k(n^2-1)\pi^2}, & n > 1, \\ 0, & n = 1, \end{cases} \tag{5.18}$$

$$M_{\theta sc} = \begin{cases} \frac{4n\cos\left(\frac{3k\pi}{2}\right)\left(\cos\left(\frac{n\pi}{2}\right)+\cos\left(\frac{3n\pi}{2}\right)\right)\sin\left(\frac{k\pi(\alpha_{pz}-1)}{2}\right)-n\left(1+(-1)^k\right)\left(1+(-1)^n\right)^2\sin\left(\frac{k\pi\alpha_{pz}}{2}\right)}{k(n^2-1)\pi^2}, & n > 1, \\ 0, & n = 1, \end{cases}$$

$$\tag{5.19}$$

$$M_{\theta cs} = 0, \tag{5.20}$$

$$M_{\theta cc} = 0, \tag{5.21}$$

$$M_{\theta s} = \begin{cases} \frac{n(\alpha_{pz}-1)\left(-1-(-1)^n+\cos\left(\frac{n\pi}{2}\right)+\cos\left(\frac{3n\pi}{2}\right)\right)}{(n^2-1)\pi}, & n > 1, \\ 0, & n = 1, \end{cases} \tag{5.22}$$

$$M_{\theta c} = 0, \tag{5.23}$$

$$M_{\theta 0} = 0, \tag{5.24}$$

$$M_{zss} = 0, \tag{5.25}$$

$$M_{zsc} = 0, \tag{5.26}$$

$$M_{zcs} = 0, \tag{5.27}$$

$$M_{zcc} = \begin{cases} -\frac{2\left((-1)^k-1\right)\sin\left(\frac{\alpha_{pz}k\pi}{2}\right)}{k\pi}, & n = 0, \\ 0, & n > 0, \end{cases} \tag{5.28}$$

$$M_{zs} = 0, \tag{5.29}$$

$$M_{zc} = 0, \tag{5.30}$$

$$M_{z0} = 0. \tag{5.31}$$

The origin of the coordinate system of the model is defined such that M_z can be described by solely cosine terms.

5.3.3 Boundary conditions

To obtain the values of the unknown coefficients in the magnetic field description, the boundary conditions at the interfaces of the regions have to be solved. The boundary conditions that are not inherently solved by selecting proper Fourier terms

and periods (explained in Section 2.5) are listed below.

1. $H_r^{\mathrm{I}} = 0\Big|_{r=0}, H_\theta^{\mathrm{I}} = 0\Big|_{r=0}$ $\qquad\qquad \forall \quad z, \theta,$ $\hfill (5.32)$

2. $H_z^{\mathrm{I}} = H_z^{\mathrm{II}}\Big|_{r=R_r}, H_\theta^{\mathrm{I}} = H_\theta^{\mathrm{II}}\Big|_{r=R_r}$ $\qquad \forall \quad z, \theta,$ $\hfill (5.33)$

3. $B_r^{\mathrm{I}} = B_r^{\mathrm{II}}\Big|_{r=R_r}$ $\qquad\qquad\qquad \forall \quad z, \theta,$ $\hfill (5.34)$

4. $H_z^{\mathrm{II}} = H_z^{\mathrm{III}}\Big|_{r=R_m}, H_\theta^{\mathrm{II}} = H_\theta^{\mathrm{III}}\Big|_{r=R_m}$ $\qquad \forall \quad z, \theta,$ $\hfill (5.35)$

5. $B_r^{\mathrm{II}} = B_r^{\mathrm{III}}\Big|_{r=R_m}$ $\qquad\qquad\qquad \forall \quad z, \theta,$ $\hfill (5.36)$

6. $H_z^{\mathrm{III}} = H_z^{\mathrm{IV}a}\Big|_{r=R_i}, H_\theta^{\mathrm{III}} = H_\theta^{\mathrm{IV}a}\Big|_{r=R_i}$ $\qquad$ for $\quad \Delta_\theta^{\mathrm{IV}a} < \theta < \Delta_\theta^{\mathrm{IV}a} + \tau_\theta^{\mathrm{IV}a}, \forall z,$ $\hfill (5.37)$

    $H_z^{\mathrm{III}} = H_z^{\mathrm{IV}b}\Big|_{r=R_i}, H_\theta^{\mathrm{III}} = H_\theta^{\mathrm{IV}b}\Big|_{r=R_i}$ $\qquad$ for $\quad \Delta_\theta^{\mathrm{IV}b} < \theta < \Delta_\theta^{\mathrm{IV}b} + \tau_\theta^{\mathrm{IV}b}, \forall z,$ $\hfill (5.38)$

    $H_z^{\mathrm{III}} = H_z^{\mathrm{IV}c}\Big|_{r=R_i}, H_\theta^{\mathrm{III}} = H_\theta^{\mathrm{IV}c}\Big|_{r=R_i}$ $\qquad$ for $\quad \Delta_\theta^{\mathrm{IV}c} < \theta < \Delta_\theta^{\mathrm{IV}c} + \tau_\theta^{\mathrm{IV}c}, \forall z,$ $\hfill (5.39)$

    $H_z^{\mathrm{III}} = 0\Big|_{r=R_i}, H_\theta^{\mathrm{III}} = 0\Big|_{r=R_i}$ $\qquad$ elsewhere, $\hfill (5.40)$

7a. $B_r^{\mathrm{IV}a} = B_r^{\mathrm{III}}\Big|_{r=R_i}$ $\qquad$ for $\quad 0 < \theta^{\mathrm{IV}a} < \tau_\theta^{\mathrm{IV}a}, \forall z,$ $\hfill (5.41)$

7b. $B_r^{\mathrm{IV}b} = B_r^{\mathrm{III}}\Big|_{r=R_i}$ $\qquad$ for $\quad 0 < \theta^{\mathrm{IV}b} < \tau_\theta^{\mathrm{IV}b}, \forall z,$ $\hfill (5.42)$

7c. $B_r^{\mathrm{IV}c} = B_r^{\mathrm{III}}\Big|_{r=R_i}$ $\qquad$ for $\quad 0 < \theta^{\mathrm{IV}c} < \tau_\theta^{\mathrm{IV}c}, \forall z,$ $\hfill (5.43)$

8a. $H_z^{\mathrm{IV}a} = 0\Big|_{r=R_s}, H_\theta^{\mathrm{IV}a} = 0\Big|_{r=R_s}$ $\qquad$ for $\quad 0 < \theta^{\mathrm{IV}a} < \tau_\theta^{\mathrm{IV}a}, \forall z,$ $\hfill (5.44)$

8b. $H_z^{\mathrm{IV}b} = 0\Big|_{r=R_s}, H_\theta^{\mathrm{IV}b} = 0\Big|_{r=R_s}$ $\qquad$ for $\quad 0 < \theta^{\mathrm{IV}b} < \tau_\theta^{\mathrm{IV}b}, \forall z,$ $\hfill (5.45)$

8c. $H_z^{\mathrm{IV}c} = 0\Big|_{r=R_s}, H_\theta^{\mathrm{IV}c} = 0\Big|_{r=R_s}$ $\qquad$ for $\quad 0 < \theta^{\mathrm{IV}c} < \tau_\theta^{\mathrm{IV}c}, \forall z.$ $\hfill (5.46)$

A method to solve this set of boundary conditions, is presented in Chapter 2. Boundary conditions 2 to 5 are continuous boundary conditions between regions with equal Fourier series described in Section 2.6. Boundary condition 6 imposes the tangential component of magnetic field to be continuous at $r = R_i$ and can be solved by means of the analysis of Section 2.7.1. Boundary conditions 7a,b,c, impose the normal component of the magnetic flux density to be continuous at the interface $r = R_i$, described in Section 2.7.2. The last boundary conditions 8a,b,c are continuous boundary conditions at the soft-magnetic interface at $r = R_s$, described in Section 2.6.

Table 5.4: Geometrical dimensions and properties of the 2-DoF actuator used for the model validation

Parameter		Value	Description
R_r	[mm]	4.0	Inner radius PM array
R_m	[mm]	9.0	Outer radius PM array
R_i	[mm]	12.0	Inner radius stator
R_s	[mm]	16.0	Outer radius slot
τ_z	[mm]	15.0	Pole pitch in the axial direction
$\tau_\theta^{\mathrm{IV}}$	[deg]	20.0	Slot width
α_{pz}	[-]	0.5	Pole pitch to magnet pitch ratio
$\Delta_\theta^{\mathrm{IV}a}$	[deg]	80.0	Offset region IVa w.r.t. region I, θ-direction
$\Delta_\theta^{\mathrm{IV}b}$	[deg]	200.0	Offset region IVb w.r.t. region I, θ-direction
$\Delta_\theta^{\mathrm{IV}c}$	[deg]	320.0	Offset region IVc w.r.t. region I, θ-direction
B_{rem}	[T]	1.2	Remanent flux density PMs
μ_{r}	[-]	1.05	Relative permeability PMs
N	[-]	21	Number of harmonics in θ-direction, regions I,II,III
K	[-]	11	Number of harmonics in z-direction, regions I,II,III,IV
J	[-]	5	Number of harmonics in θ-direction, regions IVa,b,c

5.3.4 Model validation

To validate the model, the set of equations is implemented in MATLAB and the results are compared with a 3D finite element model. The dimensions of the model are listed in Table 5.4 where the values are selected such that the actuator does not exceed the maximum envelope given in Section 4.2. To compare the results of both methods, the flux density is calculated in the middle of the airgap (region III) at $r = \frac{R_m+R_i}{2}$. The resulting waveforms calculated by the analytical model are shown in Figure 5.13. The position of the first slot is clearly visible in Figure 5.13(a), which shows the radial component of the magnetic flux density. Figure 5.13(b) shows the circumferential direction and reveals the position of the two other slots.

To illustrate the differences between the results of the FE and the analytical model, the magnetic flux density is calculated at various positions ($r = \frac{R_m+R_i}{2}, \theta, z$) and represented two dimensionally in Figure 5.14. The left column shows the B_r, B_θ and B_z versus axial position z at a constant angular position $\theta = 90\,\mathrm{deg}$. The right column shows the three components of $\vec{B}$ versus angular position θ at constant $z = 7.3\,\mathrm{mm}$. Very good agreement between the two models is found, except for small deviations in Figure 5.14(c) and Figure 5.14(f) where the values calculated by means of FE contain more noise than the analytical model resulting in discrepancies. Therefore, the deviation between the two models can be attributed to the finite element model and is caused by the relatively low values of the magnetic flux density.
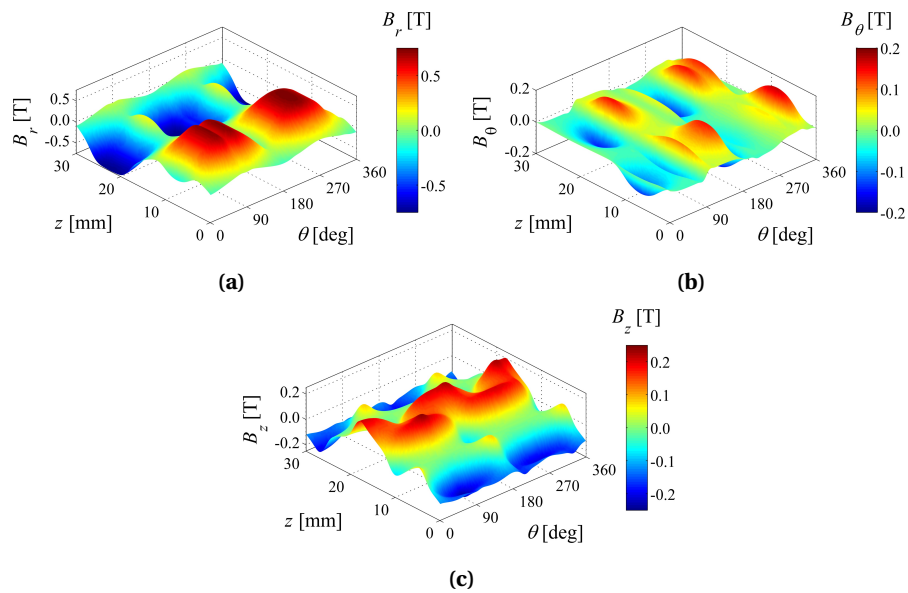
Figure 5.13: 3D representation of the magnetic flux density in the middle of region III of the structure illustrated in Figure 5.10, calculated by the analytical model. **(a)** Radial component, B_r, **(b)** circumferential component, B_θ, **(c)** axial component of the magnetic flux density, B_z.
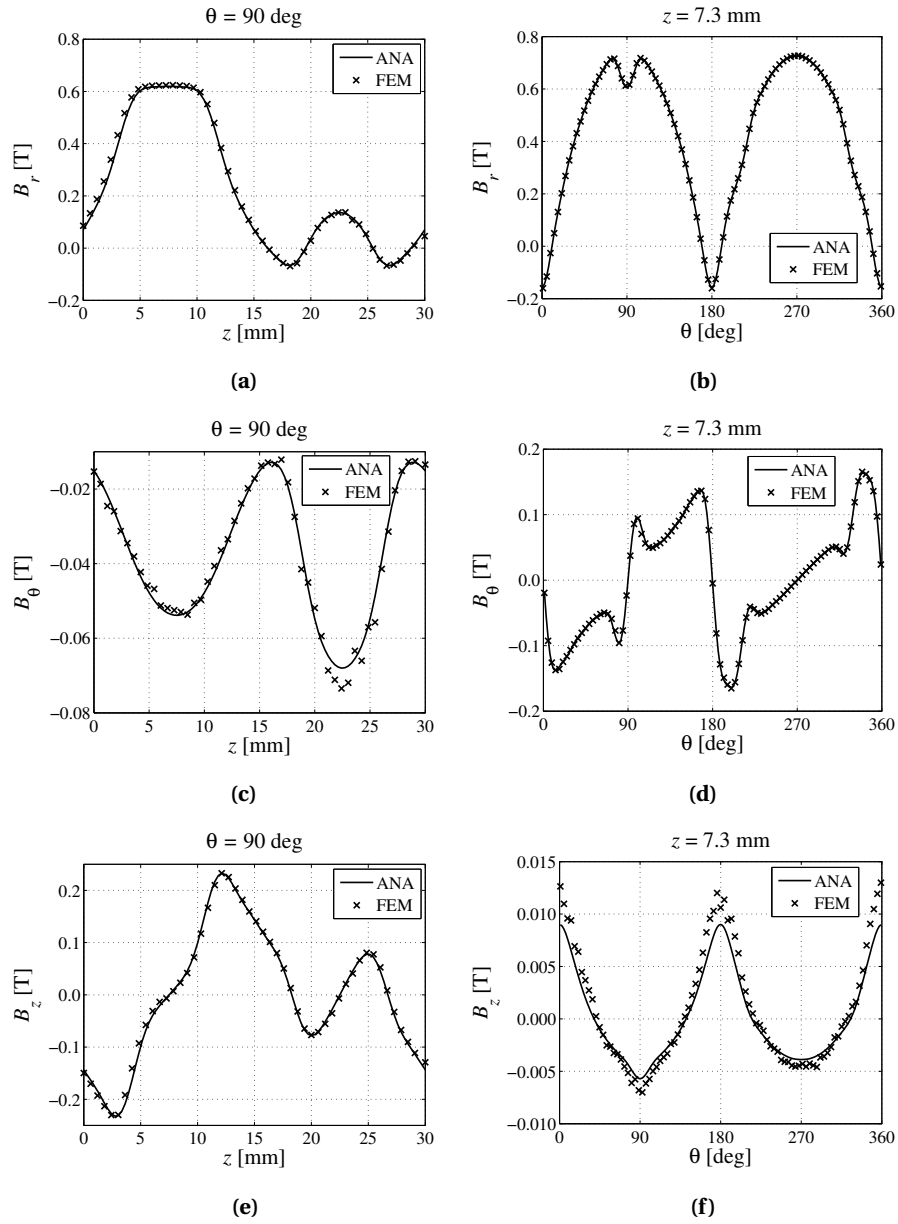
Figure 5.14: 3D finite element validation of magnetic flux density represented in 2D plots. **(a)** Radial component, B_r, at fixed $\theta = 90$ deg, **(b)** radial component, B_r, at fixed $z = 7.3$ mm, **(c)** circumferential component, B_θ, at fixed $\theta = 90$ deg. **(d)** circumferential component, B_θ, at fixed $z = 7.3$ mm, **(e)** axial component, B_z, at fixed $\theta = 90$ deg, **(f)** axial component, B_z, at fixed $z = 7.3$ mm.

5.3.5   Discussion

The goal of the new checkerboard concept is to create weaker poles in between the regular poles, as presented in Section 5.1. In Figure 5.15(a) this checkerboard concept is shown and Figure 5.15(b) illustrates the radial component of the magnetic flux density in the airgap of the altered quasi-Halbach topology presented in Figure 5.5(b). The positions of the regular poles and weaker poles, defined in Figure 5.15(a), are illustrated by the dashed lines in Figure 5.15(b). Although the altered quasi-Halbach magnetization does not contain physical weak and strong PMs, the pattern inherently results in the required checkerboard pattern if the magnetic field of each pole is averaged over its surface illustrated by the dashed lines.

The coils for rotation and translation are orthogonally oriented in the circumferential and axial direction as illustrated in Figure 5.2(a). The coils for translation enclose the full circumference, see Figure 5.9. Accordingly, the magnetic field variation along the circumference is averaged by each coil. The same holds for the coils for rotation if its axial length is equal to an integer multiple of $2\tau_z$, i.e., a multiple of the period of the magnetic field in the axial direction.

Average field seen by circumferentially oriented coil

The average magnetic field seen by the coils for translation, $B_{r,z}^{\mathrm{III}}(r,z), B_{\theta,z}^{\mathrm{III}}(r,z)$ and $B_{z,z}^{\mathrm{III}}(r,z)$, can be calculated by means of

$$B_{r,z}^{\mathrm{III}}(r,z) = \frac{1}{2\pi}\int_0^{2\pi} B_r^{\mathrm{III}}(r,\theta,z)\mathrm{d}\theta, \tag{5.47}$$

$$B_{\theta,z}^{\mathrm{III}}(r,z) = \frac{1}{2\pi}\int_0^{2\pi} B_\theta^{\mathrm{III}}(r,\theta,z)\mathrm{d}\theta, \tag{5.48}$$

$$B_{z,z}^{\mathrm{III}}(r,z) = \frac{1}{2\pi}\int_0^{2\pi} B_z^{\mathrm{III}}(r,\theta,z)\mathrm{d}\theta, \tag{5.49}$$

where $B_r^{\mathrm{III}}, B_\theta^{\mathrm{III}}$ and B_z^{III} are the magnetic flux density components in the region III (the airgap) defined in (2.19) to (2.21). Evaluating these integrals yield to

$$B_{r,z}^{\mathrm{III}}(r,z) = \mu_0 \sum_{k=1}^{\infty} \frac{1}{2}\mathcal{R}_3^{\mathrm{III}}(r,k,0)\sin(m_k z) + \mathcal{R}_4^{\mathrm{III}}(r,k,0)\cos(m_k z), \tag{5.50}$$

$$B_{\theta,z}^{\mathrm{III}}(r,z) = 0, \tag{5.51}$$

$$B_{z,z}^{\mathrm{III}}(r,z) = \mu_0 \sum_{k=1}^{\infty} \mathcal{R}_9^{\mathrm{III}}(r,k,0)\cos(m_k z) - \mathcal{R}_{10}^{x}(r,k,0)\sin(m_k z), \tag{5.52}$$

where $\mathcal{R}_3^{\mathrm{III}}(r,k,0), \mathcal{R}_4^{\mathrm{III}}(r,k,0), \mathcal{R}_9^{\mathrm{III}}(r,k,0)$ and $\mathcal{R}_{10}^{\mathrm{III}}(r,k,0)$ are defined in (2.22) to (2.34). Due to the integration interval of 2π the circumferential component of the magnetic flux density vanishes. The expression of the radial and axial components of the magnetic flux density are the same as in the axisymmetric coordinate system presented in
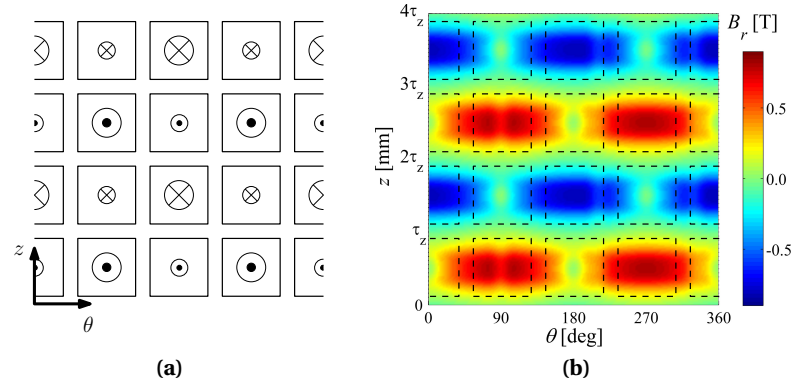
Figure 5.15: (a) Checkerboard topology with weaker poles inserted between regular poles. **(b)** Radial component of flux density of altered quasi-Halbach PM array, and illustration of the poles defined in (a) by means of the dashed squares.

Section 2.2.2. The resulting waveforms of the radial and axial component of the magnetic flux density are shown in Figure 5.16(a). The waveforms are calculated by the analytical model with the dimensions listed in Table 5.4. It can be seen from the figure that no distortion occurs due to the presence of the slots as they are oriented in the axial direction.
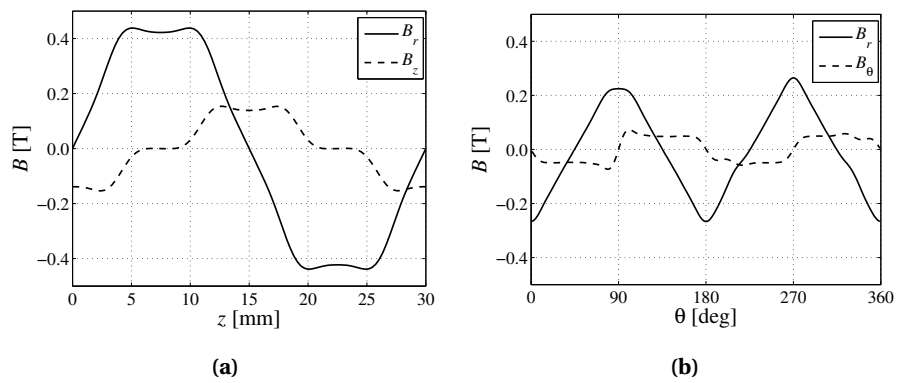
Figure 5.16: Magnetic field calculated in the airgap (region III) of the structure shown in Figure 5.10. **(a)** Radial and axial component of the flux density seen by the circumferential coils, i.e., average magnetic field along the circumference. **(b)** Radial and circumferential component of the flux density seen by the axially oriented coils, i.e., average magnetic field along the one period in the axial direction.

Average field seen by axially oriented coil

In the same manner the average magnetic field seen by the coils for rotation, $B_{r,\theta}^{\mathrm{III}}(r,\theta)$, $B_{\theta,\theta}^{\mathrm{III}}(r,\theta)$ and $B_{z,\theta}^{\mathrm{III}}(r,\theta)$, can be calculated

$$B_{r,\theta}^{\mathrm{III}}(r,\theta) = \frac{1}{2\tau_z} \int_0^{2\tau_z} B_r^{\mathrm{III}}(r,\theta,z)\mathrm{d}z, \tag{5.53}$$

$$B_{\theta,\theta}^{\mathrm{III}}(r,\theta) = \frac{1}{2\tau_z} \int_0^{2\tau_z} B_\theta^{\mathrm{III}}(r,\theta,z)\mathrm{d}z, \tag{5.54}$$

$$B_{z,\theta}^{\mathrm{III}}(r,\theta) = \frac{1}{2\tau_z} \int_0^{2\tau_z} B_z^{\mathrm{III}}(r,\theta,z)\mathrm{d}z. \tag{5.55}$$

Evaluating these integrals by inserting the magnetic field definitions, (2.19) to (2.21), yield to

$$B_{r,\theta}^{\mathrm{III}}(r,\theta) = -\mu_0 \sum_{n=1}^{\infty} \left[\mathcal{R}_5^{\mathrm{III}}(r,n)\sin(w_n\theta) + \mathcal{R}_6^{\mathrm{III}}(r,n)\cos(w_n\theta) \right], \tag{5.56}$$

$$B_{\theta,\theta}^{\mathrm{III}}(r,\theta) = -\mu_0 \sum_{n=1}^{\infty} \left[\mathcal{R}_{11}^{\mathrm{III}}(r,n)\cos(w_n\theta) - \mathcal{R}_{12}^{\mathrm{III}}(r,n)\sin(w_n\theta) \right], \tag{5.57}$$

$$B_{z,\theta}^{\mathrm{III}}(r,\theta) = 0, \tag{5.58}$$

where $\mathcal{R}_5^{\mathrm{III}}(r,n)$, $\mathcal{R}_6^{\mathrm{III}}(r,n)$, $\mathcal{R}_{11}^{\mathrm{III}}(r,n)$ and $\mathcal{R}_{12}^{\mathrm{III}}(r,n)$ are defined in (2.22) to (2.34). These expressions of the magnetic field components have the same form as presented in Section 2.2.1. By means of these equations, the magnetic field averaged over $2\tau_z$ as a function of the circumferential position is calculated and shown in Figure 5.16(b). Both components show distortion at the slot positions, i.e., 80-100 degrees, 200-220 degrees and 320-340 degrees.

The two 2D representations of the magnetic field for translation and rotation, presented by (5.50), (5.51), (5.56) and (5.57), respectively, can be used to calculate the force and torque of the actuator. The analytical model assumes linear material properties, hence superposition is valid and translation and rotation are fully decoupled, as such, the force and torque can be calculated individually.

One of the drawbacks of the three dimensional analytical model is the inability to include current carrying regions. Therefore, the magnetic flux density has to be inserted in the Lorentz force equation to calculate the force. Another approach is presented in the next section where two 2D models are introduced to approximate the 3D structure.

5.4 2D approximation

Due to the orthogonality of the windings for rotation and translation, the magnetic fields seen by the two windings can be described in the axisymmetric and polar coordinate system given by (5.50), (5.51), (5.56) and (5.57). The coefficients in these equations are calculated by the 3D model. However, the formulations of the magnetic fields have the same form as the formulation in the axisymmetric and polar coordinate system. Hence, 2D models in these coordinate systems can be used to approximate the force and torque separately. Therefore, two models are derived in this section and the results are compared with the results of the 3D model shown in the previous section.

5.4.1 2D model in axisymmetric coordinate system

A 2D model in the axisymmetric r-z-coordinate system is derived to approximate the translational performance of the actuator. The model, illustrated in Figure 5.17, is a simplification of the structure shown in Figure 5.10. Due to the selected coordinate system, the model is invariant in the circumferential direction. As such, the slots in the axial direction cannot be taken into account, and the stator back-iron is modeled as a non-salient soft-magnetic cylinder with infinite permeability. Four cylindrical concentric regions are defined as shown in Figure 5.17:

   I the non-magnetic shaft of the mover,

  II the PM-array of the mover,

 III the (mechanical) airgap,

 IV the slotless winding for translation.

To calculate the magnetic fields due to the PM-array and the coils, the magnetic vector potential is exploited as defined in Section 1.2.1. The vector potential reduces to a scalar in a 2D model and the theory described in Chapter 2 can be applied to solve the boundary conditions. The advantage of exploiting the magnetic vector potential is that the current carrying winding can be taken into account in the analysis, and
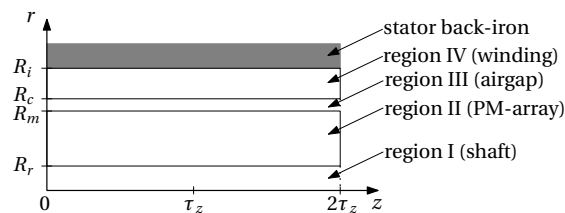
Figure 5.17: 2D model definition in the axisymmetric coordinate system to calculate the translational performance.

that the force can be calculated by means of applying the Maxwell stress tensor in the airgap, described in Chapter 3. Note that the formulated model is typically used to calculate magnetic fields in TPMAs [41, 85, 90].

To create a 2D approximation of the PM-array in the axisymmetric coordinate system, the mean value of the components of the remanent magnetization vector, $\vec{M}_0'$, along the circumference is calculated

$$M_r'(z) = \frac{1}{2\pi} \int_0^{2\pi} M_r(\theta, z) \mathrm{d}\theta, \tag{5.59}$$

$$M_\theta'(z) = \frac{1}{2\pi} \int_0^{2\pi} M_\theta(\theta, z) \mathrm{d}\theta, \tag{5.60}$$

$$M_z'(z) = \frac{1}{2\pi} \int_0^{2\pi} M_z(\theta, z) \mathrm{d}\theta, \tag{5.61}$$

where M_r, M_θ and M_z are defined in (2.36) to (2.38). Inserting these definitions and evaluation of the integrals yield to

$$M_r'(z) = \sum_{k=1}^{\infty} M_{rcs}(k,0) \sin(m_k z) + M_{rcc}(k,0) \cos(m_k z) + M_{r0}, \tag{5.62}$$

$$M_\theta'(z) = \sum_{k=1}^{\infty} M_{\theta cs}(k,0) \sin(m_k z) + M_{\theta cc}(k,0) \cos(m_k z) + M_{\theta 0}, \tag{5.63}$$

$$M_z'(z) = \sum_{k=1}^{\infty} M_{zcs}(k,0) \sin(m_k z) + M_{zcc}(k,0) \cos(m_k z) + M_{z0}, \tag{5.64}$$

where the magnetization coefficients of the altered quasi-Halbach magnetization are defined by (5.12) to (5.31). Inserting these coefficients simplifies the expressions to

$$M_r'(z) = \sum_{k=1}^{\infty} \frac{-4\left((-1)^k - 1\right) \cos\left(\frac{\alpha_{pz} k\pi}{2}\right)}{k\pi^2} \sin(m_k z), \tag{5.65}$$

$$M_\theta'(z) = 0, \tag{5.66}$$

$$M_z'(z) = \sum_{k=1}^{\infty} \frac{-2\left((-1)^k - 1\right) \sin\left(\frac{\alpha_{pz} k\pi}{2}\right)}{k\pi} \cos(m_k z). \tag{5.67}$$

The resulting equations describe a regular quasi-Halbach magnetization of a TPMA where the remanent flux density of the radially magnetized magnets is reduced by a factor $\frac{2}{\pi}$. The resulting waveform is shown in Figure 5.18(a).

To compare the magnetic field approximation of this 2D model with the results of the 3D model, the magnetic flux density due to the PM-array at $r = \frac{R_m + R_i}{2}$ is calculated. The model dimensions listed in Table 5.4 are considered and the resulting magnetic flux density waveform is shown in Figure 5.19. Due to the slots in the axial direction, which are modeled in the 3D model and neglected in the 2D model, the radial component of the flux density is approximately 1% higher in the 2D model.
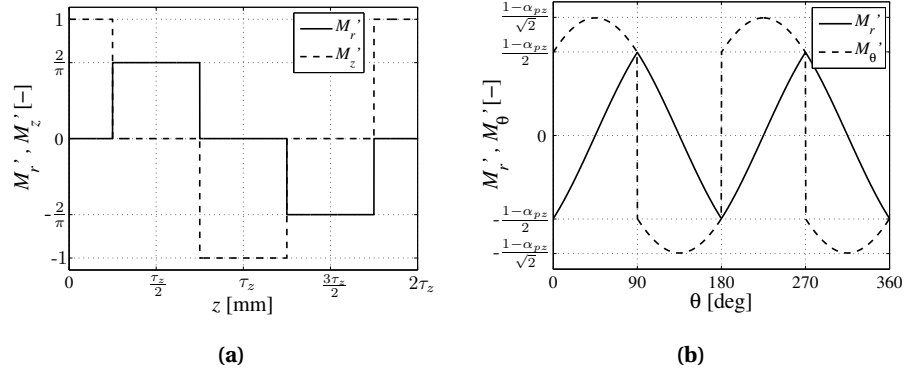
Figure 5.18: Two dimensional representation of the altered quasi-Halbach magnetization presented in Section 5.3.2. **(a)** Representation of radial and axial magnetization component in axisymmetric coordinate system. **(b)** Representation of radial and circumferential magnetization component in polar coordinate system.

Conversely, the axial component of the magnetic flux density is approximately 4% lower in the 2D model. This component can be considered as flux leakage and is somewhat more significant in the 3D structure due to presence of the slots. If the width of the slots is increased, the difference between the resulting magnetic field in the two models will increase and vice versa. In conclusion, the 2D and 3D model show good agreement for the selected parameters, and only the values are scaled due to the presence of the slots in the axial direction. As such, the 2D model can be used to approximate the performance in the translational direction while the 3D model can be used to calculate the performance reduction due to the presence of the slots.

Figure 5.19: Magnetic flux density calculated at $r = \frac{R_m + R_i}{2}$ by means of the 3D analytical model and the 2D approximation model in the axisymmetric coordinate system with the dimensions listed in Table 5.4.
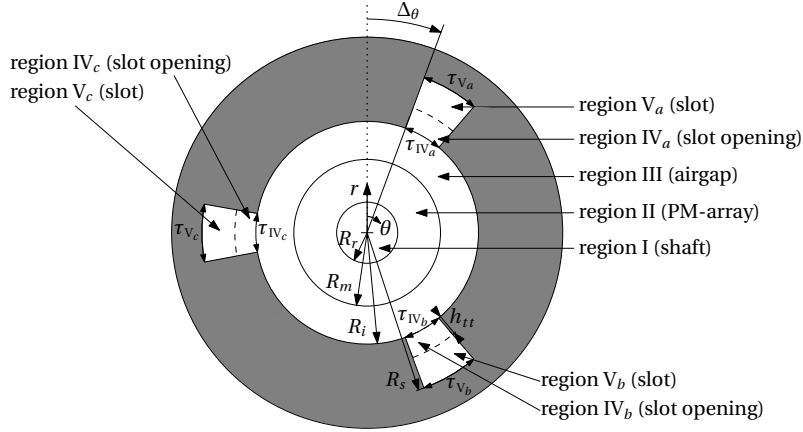
Figure 5.20: 2D model definition in the polar coordinate system to calculate the magnetic fields for rotation.

5.4.2   2D model in polar coordinate system

To calculate the performance of the rotational part of the actuator, a two dimensional model in the polar coordinate system is derived. The model, illustrated in Figure 5.20, represents the 3D structure, shown in Figure 5.10, in the polar coordinate system. The following regions are defined in the model:

   I the non-magnetic shaft of the mover,

  II the PM-array of the mover,

 III the (magnetic) airgap,

 IV (a,b,c) the slot openings,

  V (a,b,c) the slots to accommodate the winding for rotation.

Due to the stator back-iron being invariant in the axial direction, the stator structure is not simplified in this 2D representation. The slot regions, defined in the 3D model illustrated in Figure 5.10, are split in two parts where the outer part, regions $V_{a,b,c}$, accommodates the winding. The width of these slots is generally larger than the width of the slot-openings, regions $IV_{a,b,c}$, in a real machine. For comparison with the 3D model, the width of the slot and the slot opening are equal.

To calculate the 2D approximation of the PM-array in the polar coordinate system, the mean value of the components of the magnetization vector, $\vec{M}'_0$, in the axial

direction over $2\tau_z$ is calculated

$$M'_r(\theta) = \frac{1}{2\tau_z}\int_0^{2\tau_z} M_r(\theta, z)\mathrm{d}z, \tag{5.68}$$

$$M'_\theta(\theta) = \frac{1}{2\tau_z}\int_0^{2\tau_z} M_\theta(\theta, z)\mathrm{d}z, \tag{5.69}$$

$$M'_z(\theta) = \frac{1}{2\tau_z}\int_0^{2\tau_z} M_z(\theta, z)\mathrm{d}z, \tag{5.70}$$

where M_r, M_θ and M_z are defined in (2.36) to (2.38). Inserting the coefficients provided by (5.12) to (5.31) and evaluating the integrals yield to

$$M'_r(\theta) = \sum_{n=1}^{\infty} M_{rc}(n)\cos(w_n\theta), \tag{5.71}$$

$$M'_\theta(\theta) = \sum_{n=1}^{\infty} M_{\theta s}(n)\sin(w_n\theta), \tag{5.72}$$

$$M'_z(\theta) = 0, \tag{5.73}$$

where M_{rc} and $M_{\theta s}$ are defined in (5.17) and (5.22), respectively. The resulting waveforms are shown in Figure 5.18(b). It can be seen that the radial component of the magnetization, M'_r, is a triangular waveform with an amplitude of $\frac{1-\alpha_{pz}}{2}$, and the circumferential component, M'_θ, has a more rectangular shape with an amplitude of $\frac{1-\alpha_{pz}}{\sqrt{2}}$. As such, the amplitude of the magnetization components for rotation increases if the ratio between the axially magnetized ring and the diametrically magnetized segments, α_{pz} reduces.

To validate the results of this 2D model, the results, by means of the magnetic flux density in the airgap due to the PM-array, are compared with the results of the 3D model. The magnetic flux density is calculated at $r = \frac{R_m + R_i}{2}$ for a model with dimensions listed in Table 5.4. The results of both models are shown in Figure 5.21. Excellent agreement between the results is found, as expected, because the stator structure is invariant in the axial direction.
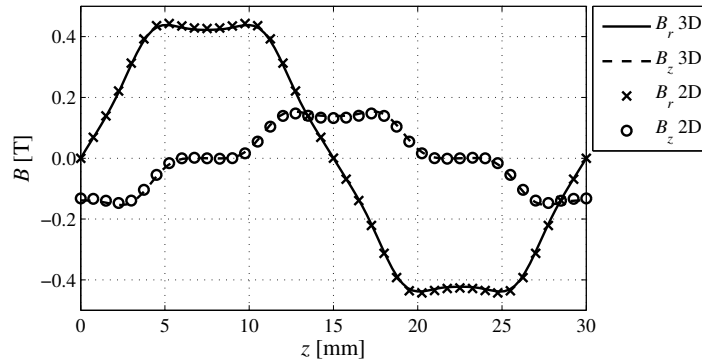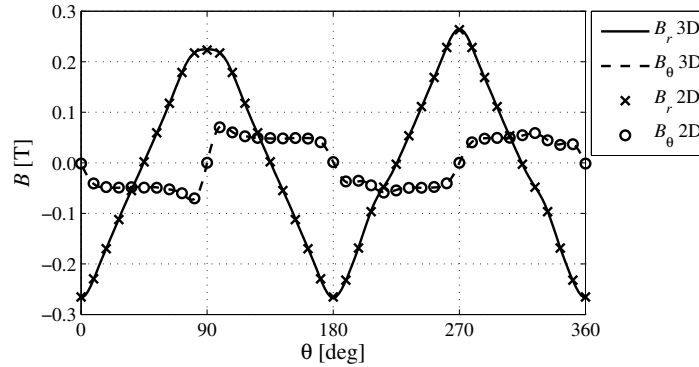
Figure 5.21: Magnetic flux density calculated at $r = \frac{R_m + R_i}{2}$ by means of the 3D analytical model and the 2D approximation model in the polar coordinate system with the dimensions listed in Table 5.4.

### 5.4.3   Discussion

In the two latter sections, two 2D models are presented to approximate the actuator performance in the translational and rotational direction. The motivation for the introduction of these models is the ability to apply the magnetic vector potential which enables direct calculation of force and torque due to a current through the coils. However, due to the three dimensional nature of the actuator, the 2D models provide only an approximation of the real behavior. Therefore, the validity of these models is discussed.

The introduction of two separate models for translation and rotation implies that superposition is valid. However, due to the non-linear material properties of the soft-magnetic back-iron, the validity of superposition cannot be guaranteed. Consequently, the dimensions of the stator back-iron geometry have to be validated by a 3D model that does include non-linear material properties. Another approach is to use the linear 3D model presented in Section 5.3 to estimate the flux density level in the soft-magnetic material and alter the structure such that the flux density levels do not exceed a predefined level. This is further discussed in Section 6.4.4.

2D model for translational performance

The model to calculate the force in the axial direction is derived in the axisymmetric coordinate system and hence, is inherently invariant in the circumferential direction. That is, the slots in the axial direction are not taken into account and the validity of the 2D model depends on the slot width. The coils for rotation enclose the full circumference, illustrated in Figure 5.9(a), and can be fully described in the axisymmetric coordinate system. Consequently, the 2D model can be used in an optimization routine to approximate the force, while the 3D model can be used to calculate the influence of the slots on the magnetic field distribution.
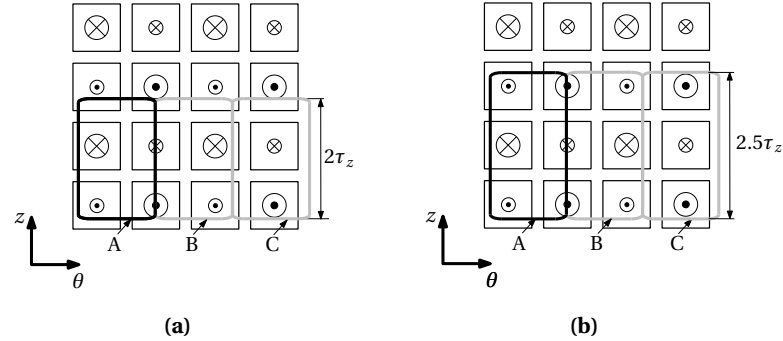
Figure 5.22: Example of three phase coil set (A,B,C) for rotation, **(a)** coils spanning $2\tau_z$ in the axial direction, **(b)** coils spanning $2.5\tau_z$ in the axial direction.

2D model for rotational performance

To calculate the torque produced by the actuator, a model is derived in the polar coordinate system which inherently does not consider dependency in the axial direction. Because the stator geometry, modeled by the 3D model in Section 5.3, exhibits no variation in the axial direction, the stator back-iron is completely modeled in 2D. However, the coils for rotation have a finite length that cannot be considered by the 2D model. The model presented in Section 5.4.2 is based on integration of the 3D model over one period in the axial direction, i.e., $2\tau_z$. As a result, the 2D model provides an accurate torque prediction if the coil length is an integer multiple of $2\tau_z$, shown in Figure 5.21(a). However, when the axial length of the coil for rotation is not equal to an integer multiple of $2\tau_z$, Figure 5.22(b), the agreement between the 3D and 2D model is lost, and the flux seen by the coil becomes dependent on the axial position.

In Figure 5.22, two possible coil sets for rotation are illustrated where the coils of Figure 5.22(a) span $2\tau_z$ in the axial direction resulting in:

- During rotation and translation, the ratio between the weak and strong poles covered by a coil is constant.

- The flux linkage and the induced voltage of the three coils, A,B,C, are balanced during rotation.

- The flux linkage is constant during translation and hence, the induced voltage is zero.

- The two 2D models provide an accurate approximation of the produced force and the torque.

Figure 5.22(b) shows a coil set that spans $2.5\tau_z$ in the axial direction. For a single coil holds that:

- During rotation the flux linkage waveform has an offset due to the varying ratio between the covered weak and strong poles.

- During rotation the induced voltage is balanced without offset.

- During translation the flux linkage varies as the number of weak and strong poles covered by the coil is not constant.

- During translation a voltage is induced in the coils for rotation.

- During helical motion the induced voltage by the coils for rotation is unbalanced.

- Due to this cross-coupling, the 2D models can give erroneous results.

In conclusion, the 2D model for rotation provides a good approximation only when the axial length of the coils for rotation is equal to an integer multiple of $2\tau_z$.

Force and torque scalability

In the previous sections it is shown that the proposed magnetization pattern introduces an additional parameter to vary the ratio between the force and torque, i.e., α_{pz}. To illustrate the effect of this parameter, the force and torque capability is estimated by means of the amplitude of the fundamental frequency of the flux density, i.e., $2\tau_z$ and $2\tau_\theta$, in the airgap. In Figure 5.23, the normalized force and torque are shown as a function of the ratio, α_{pz}, calculated by means of the two presented analytical models. The force is normalized to the maximum force that can be obtained if the radially magnetized ring is not approximated by diametrically magnetized segments, but consists of an ideal ring magnet. If α_{pz} is zero, the maximum torque can be produced, conversely, for $\alpha_{pz} = 1$, the magnet array contains solely axially magnetized PMs and the magnetic field variation in the circumferential direction is absent resulting in no torque capability.
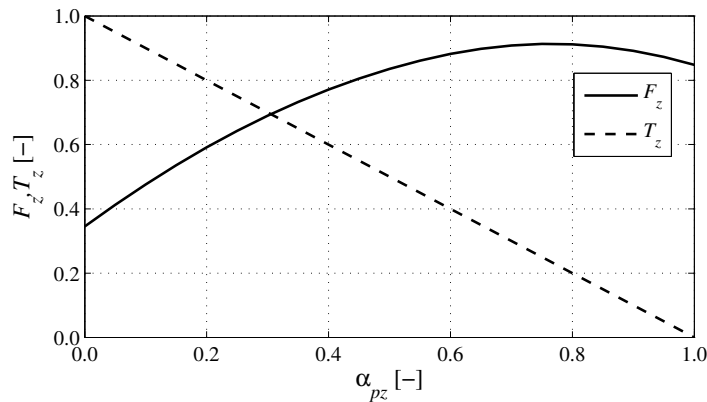
Figure 5.23: Normalized force and torque versus α_{pz} estimated by means of the amplitude of the fundamental frequency of the flux density in the airgap.

The torque scales linearly with α_{pz}, which can be explained by the linear relation between the magnetization and α_{pz} shown in Figure 5.18(b). The force, however, shows a non-linear relation with respect to α_{pz} because the Halbach magnetization ratio, shown in Figure 5.18(a), is altered. This affects both the waveform and the amplitude of the flux density. As a result, variation of α_{pz} affects besides the maximum force the force ripple as well.

5.5   Summary and conclusions

The integrated PM actuator topology presented in the previous chapter has been further investigated in this chapter. Generally, this type of actuator employs a checkerboard magnetization on the mover. Its inherent force and torque coupling is a major disadvantage of this actuator topology, therefore a new magnetization concept has been proposed and patented. Furthermore, this allows for two simple orthogonal windings to create torque and force. To achieve the specific high force and low torque, various possible realizations of the magnetization pattern have been proposed starting from the tubular PM actuator. Specifically, three permanent magnet configurations have been presented, where the altered quasi-Halbach magnetization topology has been selected based on the high magnetic loading, the adjustable force/torque ratio, and the manufacturability. The normally parasitic field effect of this tubular actuator is exploited to produce torque. Different stator configurations have been explored to obtain an actuator with a high force/torque density without introducing a complex manufacturing process. The single slotted actuator is selected, which has a slotless winding for translation enclosed by a slotted winding for rotation.

The analytical modeling technique presented in part I is used to create a fast and accurate three dimensional field description due to the presence of the altered quasi-Halbach magnetization. Further, two 2D models, i.e. rotational and translational, have been created to approximate the torque and force, since the 3D model cannot include current carrying conductors. The resulting 2D field solutions due to the presence of the PM array have been validated using the analytical 3D model. The 2D model for the rotational movement provides a very accurate approximation if the axial length of the actuator is an integer multiple of the period of the PM array. The accuracy of the translational model depends on the slot configuration of the rotational part, where in the modeled structure this introduces an error of approximately 1%.

6

Actuator synthesis

Abstract - The analytical models, presented in Chapter 5, are utilized to analyze the selected configuration of the two degrees of freedom actuator. Winding configurations are explored, a thermal analysis is conducted, and the influence of the geometric parameters on the actuator performance is investigated. Subsequently, cogging and electromagnetic damping effects are evaluated. Based on these analyses, a final actuator design is obtained, which meets the requirements set out in Chapter 4.

This chapter is based on:

- K. J. Meessen, J. J. H. Paulides, E. A. Lomonova, "Analysis and design considerations of a 2-DoF rotary-linear actuator", *Proceedings IEEE International Electric Machines & Drives Conference (IEMDC11)*, 15-18 May 2011, Niagara Falls, Canada. pp. 343-348.

- K. J. Meessen, J. J. H. Paulides, E. A. Lomonova, "Analysis and design of a slotless tubular permanent magnet actuator for high acceleration applications" *Journal of Applied Physics*, 2009, 105, 07F110-1-3.

6.1   Actuator configuration

In the previous chapter, stator and mover geometries for the 2-DoF actuator are presented. The combination of an altered quasi-Halbach magnetization and a stator with a slotted and a slotless winding is selected as the most promising solution. The aim of this chapter is to synthesize various phenomena of the selected actuator to obtain a design that meets the requirements. In Section 6.2, various winding configurations are presented and windings for rotation and translation are selected. Section 6.3 discusses the thermal aspects in the actuator, which are used in Section 6.4 to obtain the relation between the geometric parameters, dissipation, and actuator performance. Based on the results, an actuator design is obtained. In Section 6.5, parasitic effects are described and a final actuator design is defined. This actuator will be built and experimentally verified, which is presented in the next chapter. In the first section of this chapter, the actuator configuration is further detailed.

   To create a compact actuator, the actuator configuration shown in Figure 6.1 is proposed. The moving part is a cylindrical shaft with a uniform diameter containing the PM-array. The stationary part consists of two air-bearings, two stator back-iron sections and a position sensor in between. The bearings provide two degrees of freedom and should exhibit no unpredictable friction, specified in the requirements in Section 4.2. Therefore, porous air bearings are selected. No hardened sleeve is required to enclose the mover to limit wear because the bearing is contactless. A disadvantage of this bearing type is its size to provide the necessary stiffness, and the air consumption. The 2-DoF position sensor is based on two single DoF optical linear incremental encoders. A 2D sensor grid is put on the mover and two encoder heads are orthogonally placed on the stationary part to measure both rotation and translation. To avoid contamination and damage of this sensor grid, the position sensor is placed between two stator back-iron sections. Consequently, the assumption is made that the length of the sensor grid, which is at least equal to the stroke of the actuator, is smaller than the axial length of one stator section and one air bearing. Placement of the sensor grid on the mover implies that the PM-array of the mover is enclosed by a sleeve that contains the sensor grid. A more detailed description of the position sensor is provided in the next chapter.
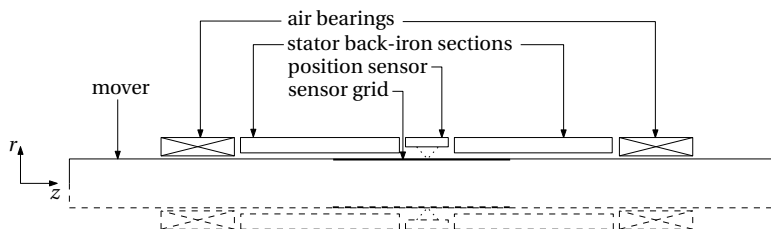
Figure 6.1: Basic actuator configuration consisting of two air bearings, two stator back-iron sections and, in between, a position sensor.

6.2 Electromagnetic analysis

6.2.1 Permanent magnet array

The magnetic loading of an actuator is determined by the PM-array configuration. In classical actuators, various PM configurations can be selected to obtain a specific waveform or level of the flux density in the airgap. In this actuator, however, the PM-array is defined by the selected actuator topology, i.e., the altered quasi-Halbach magnetization presented in the previous chapter. From the 2D magnetization waveforms, shown in Figure 5.18, the main properties of the PM-array for rotation and translation are obtained, that is:

- **Rotation :** A four pole configuration with a triangular shaped magnetization waveform.

- **Translation :** A quasi-Halbach magnetization with a reduced radial magnetization component.

Based on these magnetization properties, suitable winding configurations are investigated in the next sections.

6.2.2 Winding for rotation

The two stator sections contain a slotless winding for translation and a slotted winding for rotation. In literature, numerous winding configurations are presented and their advantages and disadvantages have been discussed [45, 46]. The selection of a suitable winding configuration depends on the application, e.g., low mmf harmonics to limit iron losses, a low induced voltage in high speed machines, and a high effectiveness in high performance actuators. A measure for the effectiveness of the winding in classical machines is the winding factor which defines the amount of flux that is linked by all coils of one phase normalized to the theoretical maximum that can physically be linked. The winding factor is generally applied to slotted windings and consists of three components

$$k_w = k_p k_d k_s, \tag{6.1}$$

where k_p is the pitch factor, defined by the span of the two conductors of one coil of the winding, k_d is the distribution factor which defines the alignment of multiple coils of one phase, and k_s is the skewing factor representing the skewing angle of the stator or rotor.

Generally, winding configurations can be subdivided in two classes; distributed and concentrated ones. In distributed windings, the two conductors of a coil span multiple teeth resulting in large end-windings. Conversely, in a concentrated winding the coils
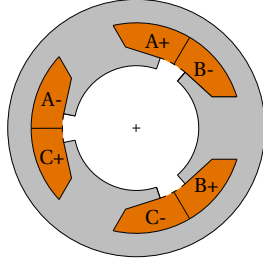
Figure 6.2: Selected winding configuration for rotation; concentrated winding with three slots.

are wound around a single tooth, hence, the end-windings are shorter and coils of different phases do not overlap one another. In for example [79], winding factors of permanent magnet machines with concentrated windings are discussed. The number of feasible winding configurations for rotation are limited as the number of poles is inherently defined. Three feasible pole slot combinations for a four pole machine are provided. The highest winding factor for a concentrated winding configuration is $k_w = 0.866$ for a stator with three or six slots, while a distributed winding with twelve slots has a winding factor of one. Due to the small dimensions of the actuator and the complexity of the stator with two orthogonal windings, the concentrated winding with three slots, illustrated in Figure 6.2, is selected being the most favorable candidate.

6.2.3 Winding for translation

In most three phase linear actuators, the winding consists of multiple coils with two anti-parallel conductors having multiple turns. That is, each coil has two conductors with current flowing in opposite directions. Conversely, the coils in tubular actuators can be described by a single conductor in the circumferential direction. This results in coils without end-windings, and hence lower copper losses. Generally, tubular actuators will have anti-parallel coils within a single phase with current flowing in the opposite direction. However, since these coils are physically separated components, one phase of a winding does not necessarily have clockwise and counter-clockwise wound conductors. To create a general analysis of windings in slotless actuators, single conductors are considered instead of coils with two anti-parallel conductors. Consequently, the results can be applied to both tubular and rotating actuators.

Four examples of slotless windings are illustrated in Figure 6.3. The first winding, shown in Figure 6.3(a), is full pitch distributed with one coil conductor per pole, $N_{cpp} = 1$. Figure 6.3(b,c) show a short pitch and a full pitch concentrated winding with $N_{cpp} = 1$ and $N_{cpp} = \frac{1}{2}$, respectively. Figure 6.3(d) illustrates a winding that can only be used in a tubular actuator as it consists of positive conductors only. Although the two anti-parallel coil conductors are physically separated in tubular actuators, and the advantage of small end-windings in a concentrated winding is not present, this
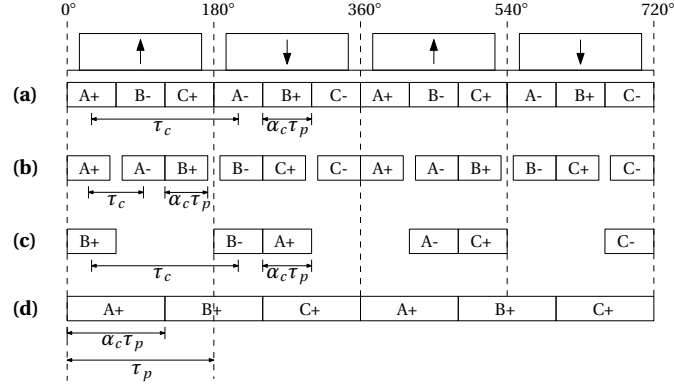
Figure 6.3: Four slotless winding configurations, **(a)** full pitch distributed winding, $\tau_c = \tau_p$, $N_{\text{cpp}} = 1$, **(b)** short pitch concentrated winding, $N_{\text{cpp}} = 1$, **(c)** full pitch concentrated winding, $N_{\text{cpp}} = \frac{1}{2}$, **(d)** distributed winding having only positive coil conductors per phase, $N_{\text{cpp}} = \frac{1}{2}$ (only feasible in TPMA).

winding configuration is described to make the analysis of the slotless winding more generic. The winding factor, presented in (6.1), is employed to provide a measure for the effectiveness of the windings presented in Figure 6.3. The components of the winding factor are discussed in the next sections.

Pitch factor

The pitch factor is the ratio between the coil pitch, τ_c, and the pole pitch, τ_p. If the coil pitch is equal to the coil pitch, the two anti-parallel coil conductors are displaced by 180 electrical degrees resulting in an optimal flux linkage. The winding configurations in Figure 6.3(a,c) have a coil pitch equal to the pole pitch resulting in a pitch factor of one, i.e. full pitch windings. The concentrated winding, shown in Figure 6.3(b), has a coil pitch which is smaller than the pole pitch. This reduces the pitch factor and, hence, the winding factor. The pitch factor for winding configuration Figure 6.3(d) is not defined since the coils in this configuration do not consist of two anti-parallel conductors.

In general, distributed slotless windings are full pitch resulting in a pitch factor equals one. In concentrated windings the pitch factor can be calculated using the following equation

$$k_p = \sin\left(\frac{q\pi}{2}\right),\tag{6.2}$$

where q is the ratio between the coil pitch and the pole pitch

$$q = \frac{\tau_c}{\tau_p}.\tag{6.3}$$
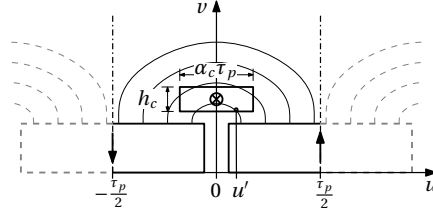
Figure 6.4: Illustration of flux leakage through a single coil conductor of one phase in the u-v coordinate system.

In the definition of the pitch factor presented before, flux leakage through the coil conductor, is not taken into account. This assumption is valid in slotted machines where almost all flux flows through the teeth resulting in an almost constant flux linkage for all turns. However, in slotless machines, the flux leakage through the coil is significantly higher because no high permeable predefined or concentrated flux path through the airgap exists. Consequently, the flux linkage of all turns within one conductor varies. Therefore, an additional component in the winding factor is defined in this thesis, k_l, which yields to the following winding factor for slotless actuators

$$k_w = k_p k_d k_s k_l. \tag{6.4}$$

Flux link factor

The flux link factor is a measure for the mean flux linkage of all turns within one conductor. In slotless actuators, there is no preferred flux path through the coils resulting in flux leakage through the conductor as illustrated in Figure 6.4. Due to this effect, the flux linkage is not equal for all turns resulting in a flux link factor lower than unity. Both the height of the conductor, h_c, and the width of the conductor $\alpha_c \tau_p$, affect the flux linkage of the conductor. The dependency of the conductor height is not considered since it is the same for all four winding configurations shown in Figure 6.3, hence, the coil height, h_c is considered to be constant in the analysis.

To obtain the flux link factor of a winding configuration, the analysis starts from the flux linkage of a single turn, λ_t, at position $u = u'$

$$\lambda_t(u') = \int_{u'}^{\frac{\tau_p}{2}} B_v(u) \mathrm{d}u, \tag{6.5}$$

where the normal component of the flux density, B_v, is described by a sum of sine functions with a fundamental period of $2\tau_p$ defined as

$$B_v(u) = \sum_{n=1}^{\infty} \hat{B}_{v,n} \sin\left(\frac{n\pi}{\tau_p} u\right). \tag{6.6}$$

It can be seen in Figure 6.4 that the conductor and the flux lines are symmetrical

around $u = 0$. Therefore, only half of the coil conductor is considered to calculate the link factor. The average flux linkage, λ_{avg}, of the conductor shown in Figure 6.4 is

$$\lambda_{\mathrm{avg}} = \frac{2}{\alpha_c \tau_p} \int_0^{\frac{\alpha_c \tau_p}{2}} \lambda_t(u')\mathrm{d}u'. \tag{6.7}$$

Using the definition of the flux density, given by (6.6), this yields to the following equation for the flux linkage as a function of the harmonic number n

$$\lambda_{\mathrm{avg}}(n) = \frac{\hat{B}_{v,n}\tau_p}{n\pi} \frac{\sin\left(\frac{n\pi}{2}\alpha_c\right)}{\frac{n\pi}{2}\alpha_c}. \tag{6.8}$$

To simplify the analysis, in the remainder of the analysis only the fundamental harmonic is taken into account because this harmonic is generally dominant in the force production. It can be seen from Figure 6.4 that the maximum flux linkage is obtained when $\lim \alpha_c \to 0$, consequently, the maximum flux linkage, $\hat{\lambda}_{\mathrm{avg}}$, is

$$\hat{\lambda}_{\mathrm{avg}}(1) = \frac{\tau_p}{\pi} \hat{B}_{v,1}. \tag{6.9}$$

The link factor is a measure for the flux linked by the conductor divided by the maximum flux that can be linked, hence, the link factor for the first harmonic is defined by

$$k_{l,1} = \frac{\sin\left(\frac{\pi}{2}\alpha_c\right)}{\frac{\pi}{2}\alpha_c}. \tag{6.10}$$

Distribution factor

The distribution factor accounts for the distribution of the coils over the stator. This factor is mainly used in slotted actuator, where slots can be filled by more than one phase. The slotless winding configurations considered in this research have a distribution factor equals one

$$k_d = 1. \tag{6.11}$$

Winding factor versus copper loss

In the previous sections is observed that the link factor approaches unity if α_c approaches zero. Consequently, to obtain a high winding factor, the conductor area should be as small as possible. However, this reduced coil area results in an increased copper loss which is not taken into account in the definition of the winding factor. The copper loss in a conductor, P_{Cu}, excluding the end-windings and leads, is

$$P_{\mathrm{Cu}} = i_c^2 R_c, \tag{6.12}$$

where i_c is the current through a conductor with a resistance R_c. For the conductor described in Figure 6.4, the resistance, and hence copper loss, is proportional to the geometry according to the following relation

$$R_c \propto \frac{l_c}{\alpha_c \tau_p h_c k_{\text{ff}}}, \tag{6.13}$$

where k_{ff} is the coil filling factor. Since the number of conductors of a winding depends on the winding configuration, as illustrated in Figure 6.3, the total length of the winding is proportional to the number of conductors per pole

$$l_c \propto N_{\text{cpp}}. \tag{6.14}$$

Consequently, if a constant copper loss is considered for all winding configurations, the current through the conductor, i_c, depends on the geometry of the winding

$$i_c \propto \sqrt{\frac{\alpha_c \tau_p}{N_{\text{cpp}}}}, \tag{6.15}$$

where h_c and k_{ff} are considered to be equal for each configuration and, hence, are neglected. In permanent magnet actuators, the force or torque on one conductor is linearly related to the flux linkage and the current. Consequently, the total force or torque on the total winding is proportional to

$$F \propto i_c k_w N_{\text{cpp}}. \tag{6.16}$$

In conclusion, to compare different slotless winding configurations by means of copper losses and achievable force, the following definition can be used

$$F \propto \sqrt{\alpha_c \tau_p N_{\text{cpp}}} \frac{\sin\left(\frac{\pi}{2}\alpha_c\right)}{\frac{\pi}{2}\alpha_c} \sin\left(\frac{q\pi}{2}\right). \tag{6.17}$$

This equation is applied to the four winding configurations illustrated in Figure 6.3 and the results are shown in Figure 6.5. The force is normalized to the value that would be achieved if the winding has a winding factor of one, and the complete coil area is filled with copper. It can be seen that the configurations (a) and (b) are only physically possible when $0 < \alpha_c < \frac{1}{3}$, while (c) and (d) are only valid for $0 < \alpha_c < \frac{2}{3}$. For the distributed windings, (a) and (d), the optimum is found when the complete coil area is covered by conductors, i.e., $\alpha_c = \frac{1}{3}$ and $\alpha_c = \frac{2}{3}$, respectively. The concentrated windings, (b) and (c), show an optimum when a small coil opening is present between the two adjacent coil conductors of one phase, i.e., $\alpha_c = 0.23$ and $\alpha_c = 0.53$, respectively. The results are summarized in Table 6.1.

The results in Table 6.1 do not take into account the additional copper loss in the end-windings. However, as mentioned before, the cylindrical coils for translation
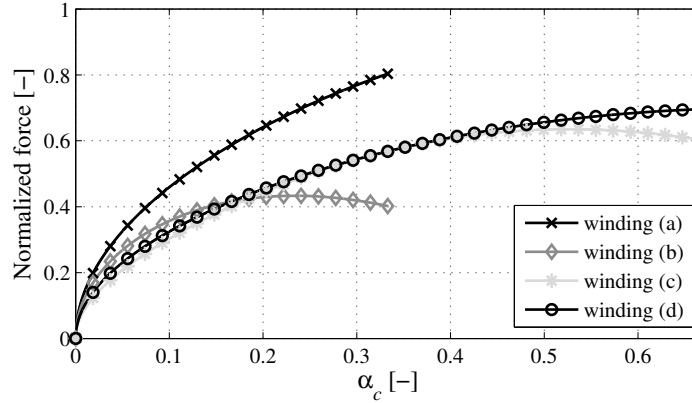
Figure 6.5: Normalized force that can be obtained by using the winding configurations illustrated in Figure 6.3 versus α_c. The copper loss is equal in all winding configurations.

have no end-windings. Therefore, the full pitch distributed winding, illustrated in Figure 6.3(a), is the most efficient configuration and is therefore selected for the translational part of the actuator.

Table 6.1: Normalized force optima from Figure 6.5 for slotless winding configurations illustrated in Figure 6.3.

Configuration	Range of α_c	Optimal α_c	Maximum normalized force
(a)	$0 < \alpha_c \leq \frac{1}{3}$	$\frac{1}{3}$	0.80
(b)	$0 < \alpha_c \leq \frac{1}{3}$	0.23	0.43
(c)	$0 < \alpha_c \leq \frac{2}{3}$	0.53	0.63
(d)	$0 < \alpha_c \leq \frac{2}{3}$	$\frac{2}{3}$	0.70

6.3 Thermal analysis

The performance of an electromagnetic actuator is often limited by its temperature. The actuator temperature rises due to losses, i.e., copper loss, iron losses and mechanical losses. To prevent permanent damage, the temperature should be limited to avoid degradation of the wire insulation or glue. Furthermore, the temperature affects the performance of the actuator directly by two means:

1. The conductivity of copper depends on temperature.

2. The remanent flux density and coercivity of the PMs depend on temperature.

Both effects can be linearized for temperatures around room temperature and can be described by the following equations

$$\sigma_{Cu}(T) = \sigma_{Cu,20}\,(1 - \alpha_{Cu}\Delta T),\tag{6.18}$$

$$B_{rem}(T) = B_{rem,20}\,(1 - \alpha_{rem}\Delta T),\tag{6.19}$$

$$H_{cb}(T) = H_{cb,20}\,(1 - \alpha_{coer}\Delta T),\tag{6.20}$$

where $B_{rem,20}$, $H_{cb,20}$ and $\sigma_{Cu,20}$ are the remanent flux density and the coercivity of a PM, and the conductivity of copper, respectively, at $T = 20\,°C$. The temperature coefficient of the conductivity of copper is $\alpha_{Cu} = 3.9\,‰K^{-1}$, while the two temperature coefficients of N45H type permanent magnets are $\alpha_{rem} = 1.7\,‰K^{-1}$ and $\alpha_{coer} = 2.7\,‰K^{-1}$, illustrated in Appendix C.1.

The maximum actuator housing temperature relative to the ambient one is specified at $\Delta T = 40\,°C$. In the design analysis, the ambient temperature is set to $T = 20\,°C$ resulting in a maximum actuator temperature of $T = 60\,°C$. To comply with this constraint during the design procedure, a steady state thermal equivalent circuit of the actuator is created to estimate the temperature.

Thermal equivalent circuit

The temperature distribution in a structure can be estimated by means of a thermal equivalent circuit representing the geometry. Three types of heat transfer mechanisms can be distinguished resulting from a temperature gradient in the geometry

$$q_{cond} = (T_1 - T_2)\frac{kA}{dl}\qquad \text{Conduction through a solid or a stationary fluid,}\tag{6.21}$$

$$q_{conv} = (T_1 - T_2)h_{conv}A\quad \text{Convection from a surface to a moving fluid,}\tag{6.22}$$

$$q_{rad} = (T_1^4 - T_2^4)\varepsilon\sigma A\qquad \text{Radiation between two surfaces,}\tag{6.23}$$

where q_{cond}, q_{conv} and q_{rad} are the rate of heat transfer due to conduction, convection and radiation, respectively, as a result of a temperature gradient $\Delta T = T_1 - T_2$ [52]. In the aforementioned equations, A represents the area of the interface normal to the direction of heat flow, and l is the length of the material in the direction of heat flow. The coefficients k, h_{conv} and ε represent the thermal conductivity, the convection coefficient, and the emissivity, respectively, while σ is the Stefan-Boltzmann constant, $\sigma = 5.67 \times 10^{-8}\,Wm^{-1}K^{-4}$. Thermal conduction results in heat transfer from the coils inside the actuator to the outer surface whereas convection and radiation cause heat transfer from the actuator to the ambient.

The thermal radiation is proportional to the temperature difference to the power four. This radiation can be rewritten to a more canonical expression similar to the

expression for convection

$$q_{\text{rad}} = \Delta T h_{\text{rad}} A, \tag{6.24}$$

where h_{rad} is the equivalent radiation heat transfer coefficient

$$h_{\text{rad}} = (T_1 + T_2)(T_1^2 + T_2^2)\varepsilon\sigma. \tag{6.25}$$

The resulting value of h_{rad} in the temperature range considered in this thesis yields to

$$h_{\text{rad}} = 5.7\varepsilon \qquad\qquad\qquad \text{at } 20\,^{\circ}\text{C}, \tag{6.26}$$
$$h_{\text{rad}} = 7.0\varepsilon \qquad\qquad\qquad \text{at } 60\,^{\circ}\text{C}. \tag{6.27}$$

The emissivity, ε, varies between 0.1 for light oxidized aluminum and polished steel up to 0.8 for anodized aluminum and oxidized steel [52].

To create a thermal equivalent circuit, conduction, convection and radiation are represented by thermal resistances. The values of these thermal resistances can be calculated by means of the material properties and the dimensions according to

$$\Re_{\text{cond}} = \frac{l}{kA}, \tag{6.28}$$
$$\Re_{\text{conv}} = \frac{1}{h_{\text{conv}}A}, \tag{6.29}$$
$$\Re_{\text{rad}} = \frac{1}{h_{\text{rad}}A}, \tag{6.30}$$

where $\Re_{\text{cond}}, \Re_{\text{conv}}$ and $\Re_{\text{rad}}$ represent conduction, convection and radiation thermal resistances, respectively. By means of a network consisting of thermal resistances, a steady state model can be created. Thermal capacitors can be added to estimate the transient thermal behavior [114].

In Figure 6.6(a), the actuator structure and the location of the heat sources are illustrated in two dimensions. To create a complete thermal equivalent circuit, the coils, the stator back-iron, and the interfaces between coils and the stator back-iron have to be represented by thermal resistances. Two additional thermal resistances have to be included to represent the convection and radiation from the stator back-iron to the ambient. The thermal barriers in the actuator, e.g., electrical isolation between coils and stator back-iron, are small due to the small actuator dimensions. Therefore, the temperature gradient in the actuator is small and the dominant thermal resistances are the ones representing the convection and radiation. Furthermore, the main heat flow is in the radial direction, and the heat flow in the axial direction is neglected to create a worst case model. Therefore, the thermal equivalent circuit is simplified to a 1D model, illustrated in Figure 6.6(b). By means of this simple model, the actuator and coil temperature are estimated based on the values of $\Re_1$ and $\Re_2$ and the total losses in the actuator, P_{tot}, where $\Re_2 = \frac{1}{(h_{\text{conv}} + h_{\text{rad}})A}$. From simulations
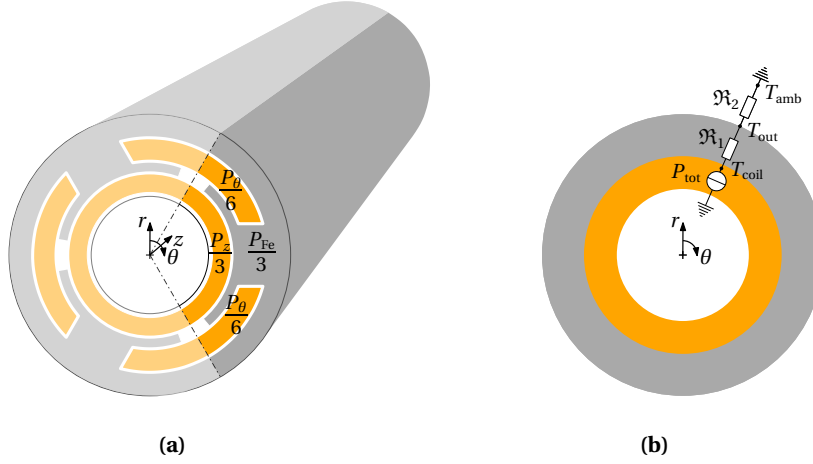
Figure 6.6: (a) Illustration of heat sources in actuator, **(b)** thermal equivalent circuit of actuator used in design analysis.

and measurements it is found that in this type of structures with these dimensions and a combined convection and radiation coefficient of $h_{\mathrm{conv}} + h_{\mathrm{rad}} \approx 20\,\mathrm{Wm^{-2}K^{-1}}$, the ratio between $\mathfrak{R}_1$ and $\mathfrak{R}_2$ can be considered as [90]

$$\mathfrak{R}_1 \leq \frac{\mathfrak{R}_2}{10}. \tag{6.31}$$

Consequently, the relative coil temperature is $\leq 10\,\%$ higher than the relative actuator periphery temperature.

6.4   Geometric parameter analysis

To obtain the relation between geometric parameters and the actuator performance, a parametric analysis is conducted. The actuator has the following properties as described in the previous sections:

- The translator consists of an altered quasi-Halbach array, described in Section 5.1 and illustrated in Figure 5.5.

- The translator shaft is hollow to enable the feed-through of air.

- The stator consists of a slotless winding for translation and a slotted winding for rotation, discussed in Section 5.2.1 and shown in Figure 5.9.

- The slotted stator part for rotation consists of three slots and a concentrated winding, presented in Section 6.2.2 and shown in Figure 6.2.
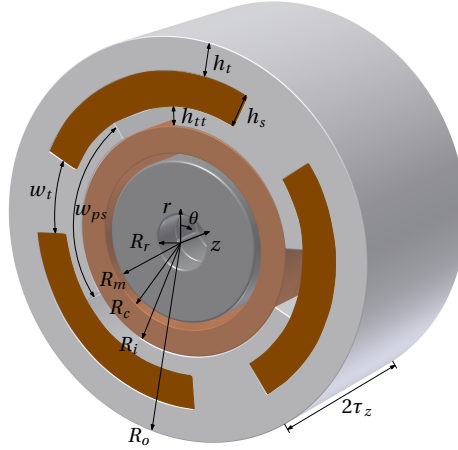
Figure 6.7: Definition of the geometric parameters of one periodic section of the actuator.

- The stationary part for translation is a full pitch concentrated slotless winding defined in Section 6.2.2 and illustrated in Figure 6.3(a).

One periodic section of the actuator and the geometric parameters that are varied during the analysis are illustrated in Figure 6.7. The final goal of the parametric analysis is to find optimal values for geometric parameters to create an actuator that meets the specifications given in Section 4.2. The following constraints are considered

$$R_o \leq 14.4\,\text{mm}, \tag{6.32}$$

$$R_r \geq 2.0\,\text{mm}, \tag{6.33}$$

$$l_g = 0.5\,\text{mm}, \tag{6.34}$$

where l_g is the airgap length defined by $R_c - R_m$ which includes the sleeve of the mover that contains the sensor grid. Although a maximum outer radius of 17.4 mm is specified, the maximum outer radius of the stator back-iron is set to $R_o = 14.4\,\text{mm}$ to allow for an actuator housing with a thickness of maximum 3.0 mm.

The actuator performance is thermally limited by convection and radiation from the actuator to the ambient. This implies that the allowable dissipation inside the actuator is limited by the outer actuator periphery. The actuator outer radius is constrained to $R = 17.4\,\text{mm}$. Consequently, the parametric analysis is focused on minimization of the total dissipation instead of minimization of the dissipation per volume. If the final design of the actuator has a smaller radius than $R = 17.4\,\text{mm}$, the convection area can easily be enlarged within the specified maximum outer radius. As a result, the total dissipation is a more important constraint than the dissipation per actuator volume.

6.4.1 Relation between mover radius and mover acceleration

To obtain the relation between the mover radius and the actuator performance, the rudimentary force relations presented in Section 5.2.2 are used. In that section it is shown that for a fixed copper loss

$$F_z \propto B_r \sqrt{r}, \tag{6.35}$$

$$T_z \propto B_r r \sqrt{r}. \tag{6.36}$$

To obtain the angular and linear mover acceleration from these equations, the moment of inertia, I_{mover}, and the mover mass, m_{mover}, are calculated

$$I_{\mathrm{mover}} \propto m_{\mathrm{mover}}(R_m^2 + R_r^2), \tag{6.37}$$

$$m_{\mathrm{mover}} \propto R_m^2 - R_r^2. \tag{6.38}$$

In the analysis it is assumed that the outer radius of the actuator is linearly related to the mover radius. Consequently, the relation between the accelerations a_z and α_θ and the force F_z and torque T_z versus the mover radius can be estimated. To simplify the analysis, the magnetic loading, or B_r, is assumed to be constant for all radii which is valid because other geometric parameters can be varied to satisfy this criteria. Furthermore a linear relation between the inner and outer radius of the translator is considered. The results, shown in Figure 6.8, reveal that if the mover diameter is increased, the force capability rises, however, the acceleration degrades rapidly. Figure 6.8(b) shows that increasing the mover diameter has an even stronger effect on the angular acceleration, α_θ. The requirements, given in Section 4.2, imply that for fast component placement, a high acceleration in the axial, z-, direction is required. Hence, a small diameter is desired. Conversely, a high peak force is required to mount connectors. Furthermore, the position sensor utilizes the mover surface,
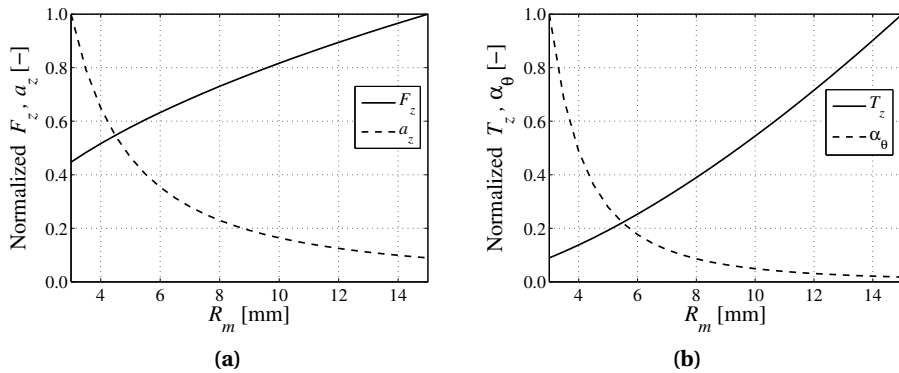
Figure 6.8: **(a)** Normalized force, F_z, and acceleration a_z in the axial direction versus the mover radius, R_m, estimated by means of rudimentary equations. **(b)** Normalized torque, T_z, and angular acceleration α_θ around the z-axis versus the mover radius, R_m,

and a small diameter affects the attainable rotational resolution. Lastly, reduction of the mover diameter affects the stiffness of the mover heavily which causes inaccuracy in the position measurement due to deflection of the mover. Therefore, a mover diameter of $R_m = 6.0$ mm is selected based on preliminary calculations.

To obtain the relation between the other geometric parameters and the 2-DoF performance, the two 2D models, presented in the previous chapter, are firstly used to investigate translation and rotation separately. Secondly, the combined performance is examined by means of the two 2D models and the 3D model.

6.4.2 Translational performance

In this section the effect of the PM and coil dimensions on the axial force and acceleration is examined. In the previous section it is shown that a small mover radius is favorable to achieve a high mover acceleration if the magnetic field is considered to be constant. Subsequently, a mover radius of $R_m = 6.0$ mm is selected. The results in this section are presented by means of ratios of geometric parameters with respect to the mover radius. Because the dependency of these results on the mover radius is limited, they provide insight for a bounded range of R_m, i.e., 5.0 mm $\leq R_m \leq 8.0$ mm.

In the first analysis, the relation between acceleration and force, and the magnet- and coil length is investigated. The inner translator radius, R_r, and the outer coil radius, R_i, are varied while for each calculation the optimal value for the pole pitch, τ_z, is searched. The normalized results, calculated per meter axial length, are shown in Figure 6.9. If R_r is increased, the magnetic field lowers due to the decreased amount of PM material and hence, the force degrades significantly. Although the mover mass
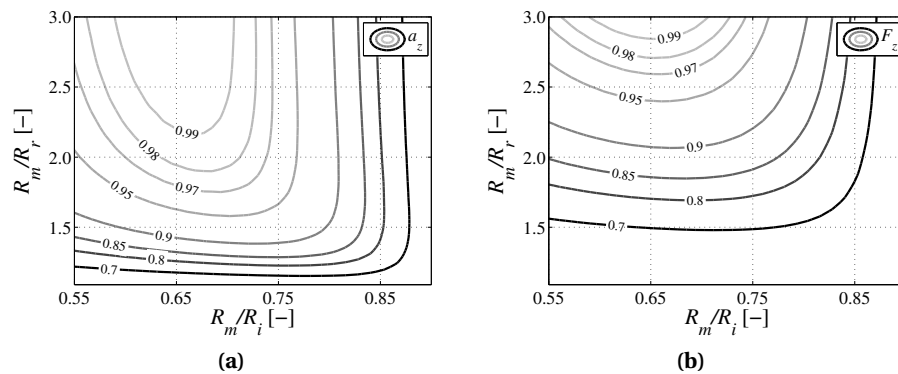
Figure 6.9: Normalized force and acceleration versus the mover outer radius to mover inner radius ratio and the mover outer radius to back-iron inner radius ratio. The pole pitch, τ_z, is optimized in each calculation, and the acceleration and force are normalized. **(a)** Normalized acceleration, a_z, **(b)** normalized force, F_z.
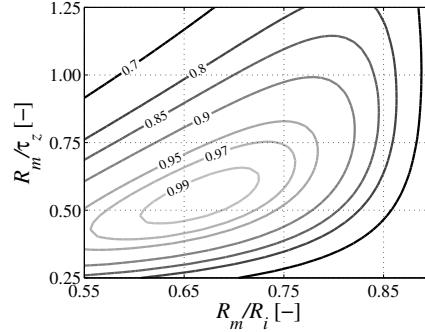
Figure 6.10: Normalized acceleration, a_z, versus the mover radius to back-iron inner radius ratio and the mover radius to pole pitch ratio.

reduces if the inner radius of the mover is increased, the force degrades faster resulting in a lower acceleration. Note that the mover mass includes an inner aluminium tube for the vacuum feed-through. It can be seen that a ratio of $\frac{R_m}{R_i} \approx 0.65$ provides the highest force and acceleration for small values of R_r.

In the second analysis, the relation between the acceleration, and the pole pitch and coil outer radius is investigated. The inner radius of the mover is set to $R_r = 2.0\,\text{mm}$. Consequently, the mover mass is constant for each calculation and the acceleration and force show the same trend. In Figure 6.10 the results of the analysis are shown. A clear optimum can be found for $\frac{R_m}{\tau_z} \approx 0.55$ and $\frac{R_m}{R_i} \approx 0.66$. More generally, one can observe that if τ_z is reduced, R_i should be to reduced too.

6.4.3   Rotational performance

To analyze the rotational performance, the relation between the angular acceleration, and the magnet length and stator back-iron inner radius is investigated. Initially, the coil dimensions are chosen arbitrarily within the specified space to exclude this parameter variation in the analysis. In Figure 6.11, the normalized angular acceleration is shown. As expected, the maximum angular acceleration is achieved if the value of R_i approaches that of R_m because this reduces the airgap and hence, increases the magnetic field seen by the coil for rotation. Furthermore, increasing the inner radius of the mover reduces the maximum achievable angular acceleration. Although the mover moment of inertia reduces by increasing the inner diameter, the magnetic field reduces more rapidly similar to the effect on the translational performance.

To obtain the highest rotational performance, the tooth and coil dimensions have to be optimized. From Figure 6.7 it can be seen that minimizing h_{tt}, w_t and increasing h_s result in a larger coil and hence, in a higher torque for constant copper loss in the
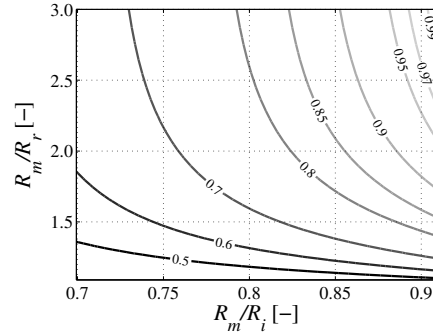
Figure 6.11: Normalized angular acceleration, α_θ, versus the mover outer radius to mover inner radius ratio and the mover outer radius to back-iron inner radius ratio.

coil. However, optimization of these parameters requires more insight in the magnetic field distribution to prevent saturation. This is further discussed in the next section.

6.4.4 Stator back-iron sizing

The soft-magnetic stator back-iron in electromagnetic actuators provides a high permeable flux path for the electromagnetic field. Due to the non-linear nature of soft-magnetic materials, the magnetic flux density in the back-iron has to be limited to maintain its high permeance. The analytical modeling technique used in the analysis does not provide a solution for the magnetic field inside the soft-magnetic material. Therefore, magnetic circuits are used to estimate the magnetic field distribution in the stator back-iron based on the results of the 3D analytical model of the previous chapter. This estimation is used to set the sizes for the stator back-iron to prevent saturation.

The magnetic field exhibits a three dimensional distribution, hence, the magnetic circuit to describe the magnetic field accurately within the structure is very complex. Therefore, three simple circuits are developed based on the magnetic field distribution in the back-iron calculated by a finite element model. Three main flux paths are identified represented by the tubes which cross-sections are denoted by the surfaces shown in Figure 6.12. The maximum flux through these tubes is estimated by means of the three magnetic circuits and the results of the 3D analytical model. The cross-section of each tube is adjusted to comply with a given maximum flux density.

Magnetic circuit 1 The first magnetic circuit is used to estimate the maximum flux flowing through the tooth tip in the axial direction. It is based on the assumption that all flux that enters or leaves surface S_1 or S_2 should flow through surface S_3, as illustrated in Figure 6.12(b). Consequently, the assumption is made that no flux flows through the tooth in the axial direction. The flux that enters S_1, is not necessarily equal
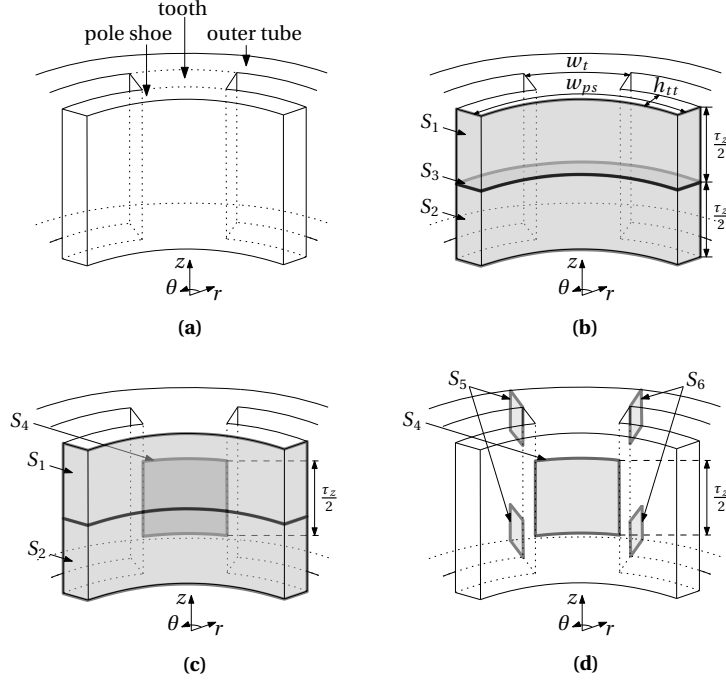
Figure 6.12: Surface definitions used in the magnetic circuit of the stator back-iron.
(a) Definition of the tooth, pole shoe and the outer tube. **(b)** Surfaces to estimate
flux density in tooth-tips, **(c)** surfaces to estimate flux density in tooth, **(d)** surfaces to
estimate flux density in outer tube.

to the flux that leaves S_2, illustrated in Figure 6.13. Therefore, a worst case model is
considered which yields to

$$\int_{S_3} \vec{B} \cdot d\vec{s} = \max\left(\left|\int_{S_1} \vec{B} \cdot d\vec{s}\right|, \left|\int_{S_2} \vec{B} \cdot d\vec{s}\right|\right). \tag{6.39}$$

Magnetic circuit 2 To estimate the flux through the teeth of the stator back-iron, a
second magnetic circuit is created, illustrated in Figure 6.12(c). It is based on the
assumption that the flux that enters surface S_1 should leave either surface S_2 or S_4

$$\int_{S_4} \vec{B} \cdot d\vec{s} = \int_{S_1} \vec{B} \cdot d\vec{s} - \int_{S_2} \vec{B} \cdot d\vec{s}. \tag{6.40}$$

The height of surface S_4 is equal to $\frac{\tau_z}{2}$ which provides a good representation of the flux
flow calculated by means of the finite element model.

Magnetic circuit 3 By means of the third magnetic circuit, the magnetic flux density
is estimated in the outer back-iron tube. By means of the surfaces illustrated in
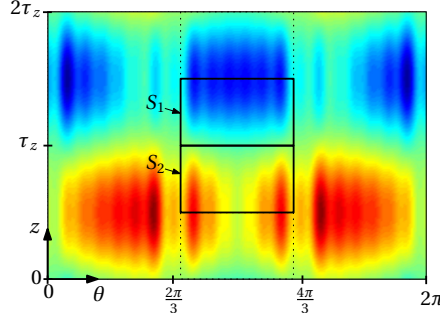
Figure 6.13: Magnetic field at the inner radius of the stator, $r = R_i$, calculated by means of the 3D analytical model. The surfaces S_1 and S_2 correspond to the surfaces in Figure 6.12, and are used to estimate the flux through the tooth-tips.

Figure 6.12(d), the following magnetic circuit is created

$$\int_{S_5} \vec{B} \cdot d\vec{s} + \int_{S_6} \vec{B} \cdot d\vec{s} = \int_{S_4} \vec{B} \cdot d\vec{s}. \tag{6.41}$$

The finite element model shows that the maximum flux through S_5 or S_6 is approximately 60% of the maximum flux through S_4.

To solve the three magnetic circuits, one has to start by calculating the maximum flux through S_1 or S_2 by means of the 3D analytical model to find the maximum flux through S_3. Subsequently, the maximum flux through S_4 can be calculated and the maximum flux in S_5 or S_6 can be obtained from that value. To calculate the total flux entering surfaces S_1 and S_2, the results of the 3D model and the 2D models can be superimposed. That is, the magnetic field distribution due to the PMs is calculated by means of the 3D model while the 2D models are used to calculate the armature reaction field. This requires an iterative calculation because the armature reaction field of the rotational part depends on the back-iron dimensions. A simpler model can be created by considering the armature reaction field significantly smaller than the magnetic field due to the PMs which requires solely the magnetic field of the 3D analytical model to determine appropriate dimensions of the stator back-iron.

Combined rotational and translational performance

The geometric parameter that affects the performance in the translational and rotational direction most contradictorily is the inner stator back-iron radius, R_i. Figures 6.10 and 6.11 show the effect of this parameter on translation and rotation, respectively, and different optimum values are found. A model is created that combines the aforementioned aspects to obtain the influence of this parameter on the total dissipation in the actuator.

First, the acceleration requirements, presented in Section 4.2, are translated to
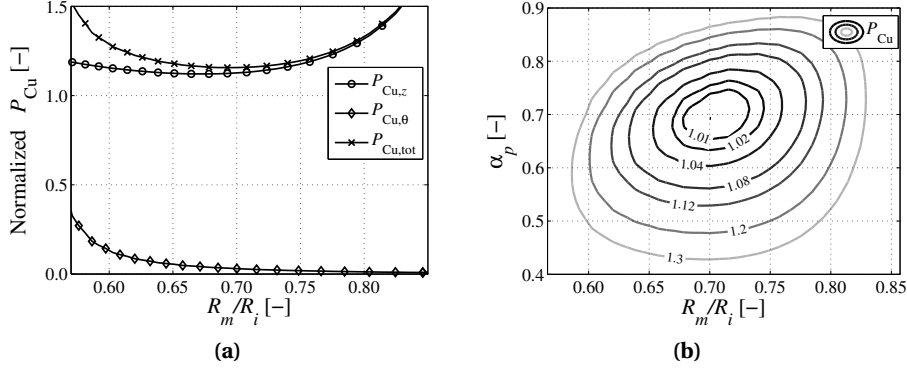
Figure 6.14: (a) Normalized copper losses in rotational and translational part of the actuator versus $\frac{R_m}{R_i}$ for $\alpha_p = 0.5$. **(b)** Normalized total copper loss in the actuator versus $\frac{R_m}{R_i}$ and α_p where $P_{\text{Cu}} = 1$ is the minimum copper loss.

a constant actuator load. That is for translation an acceleration of $a_z = 150\,\text{ms}^{-2}$ with a duty-cycle of 34%, and for rotation an acceleration of $\alpha_\theta = 3500\,\text{rads}^{-2}$ with a duty-cycle of 47%. Subsequently, a model is created that calculates the dissipated copper losses in the two parts of the actuator to meet these requirements. The calculation is performed for an actuator with arbitrary length, whereas the copper losses are normalized to the minimum total copper loss. The model includes the magnetic models, presented in the previous section, to set the required stator back-iron dimensions. To guarantee that the actuator can be manufactured, the following minimum sizes for the stator back-iron are set

$$h_{tt} > 1.0\,\text{mm}, \tag{6.42}$$

$$w_t > 12\,\text{deg}, \tag{6.43}$$

$$h_t > 2.0\,\text{mm}. \tag{6.44}$$

The inner mover radius is fixed to $R_r = 2.0\,\text{mm}$ in the analysis, while the optimal value of the pole pitch is obtained during each calculation step. The geometric ratio $\frac{R_m}{R_i}$ and the magnet ratio α_{pz} are varied. Figure 6.14(a) illustrates the effect of $\frac{R_m}{R_i}$ on the copper losses for a fixed value of $\alpha_p = 0.5$. It can be seen that the dissipation in the winding for translation is significantly higher than the dissipation in the winding for rotation. Consequently, the optimal $\frac{R_m}{R_i}$ is mainly defined by minimization of dissipation in the winding for translation. Figure 6.14 shows the total copper loss normalized to the minimum dissipation in the actuator as a function of α_{pz} and $\frac{R_m}{R_i}$. A clear optimum is found where the inner circle comprises the area where the total copper loss is within 1% of the minimum copper loss. Note that due to the specified maximum acceleration levels and duty cycles the optimum is found at this position. If, for example, a higher angular acceleration is required, the optimum shifts to a smaller α_p and a larger $\frac{R_m}{R_i}$.

Table 6.2: Geometrical dimensions of the preliminary design of the 2-DoF actuator.

Parameter		Value	Description
R_r	[mm]	2.0	Inner radius PM array
R_m	[mm]	6.0	Outer radius PM array
R_c	[mm]	6.5	Inner radius translational winding
R_i	[mm]	8.3	Inner radius stator
R_o	[mm]	14.2	Outer radius stator back-iron
τ_z	[mm]	8.0	Pole pitch in the axial direction
α_{pz}	[-]	0.65	Magnet pitch to pole pitch ratio
h_{tt}	[mm]	1.3	Tooth tip height
h_s	[mm]	2.0	Slot height
h_t	[mm]	2.5	Back-iron tube thickness
w_t	[deg]	24.0	Tooth width
$k_{\text{ff},z}$	[-]	0.65	Coil filling factor translation
$k_{\text{ff},\theta}$	[-]	0.5	Coil filling factor rotation
$l_{\text{stat,act}}$	[mm]	96.0	Active stator length
$l_{\text{mov,act}}$	[mm]	176.0	Active mover length
$l_{\text{mov,tot}}$	[mm]	236.0	Total mover length

6.4.5 Actuator design based on parametric analysis

In the preceding sections, the effects of geometric parameters on the actuator performance are presented by means of the force, torque and accelerations as a function of the copper loss. Based on the results of these analyses, a preliminary actuator design is obtained. The values of the geometric parameters are given in Table 6.2. For manufacturing reasons, the values of some geometric parameters deviate slightly from the optimal values. As a result, the design provides approximately 2.5% less force than the theoretical optimal of the preceding sections.

An active stator length of 96.0 mm is selected to provide sufficient force and torque to accelerate the mover with $a_z = 150\,\text{ms}^{-2}$ and $\alpha_\theta = 3500\,\text{rads}^{-2}$, respectively, and to be able to provide a static force of 40 N. The coil filling factors, $k_{\text{ff}z}, k_{\text{ff}\theta}$, are based on preliminary design studies [88]. The stator consists of two active sections with the position sensor in between, illustrated in Figure 6.1. The length of a single section is 48 mm and the distance between the sections is considered to be equal to the encoder head width of 14 mm. The active mover length, $l_{\text{mov,act}}$, that is the part containing the PM array, is equal to 160 mm to enable a stroke of 45 mm. The total mover is enlarged to $l_{\text{mov,tot}} = 220\,\text{mm}$ because of the two bearings with a length of 30 mm at the stator ends, illustrated in Figure 6.1.

To follow the specified trajectory for translation and rotation depicted in Figures 4.3 and 4.4, the continuous dissipation in the winding for translation is 5.8 W and 0.5 W in the winding for rotation. According to the thermal model of Section 6.3, a combined convection and radiation coefficient of $h = 15\,\mathrm{Wm^{-2}K^{-1}}$ is required to maintain the actuator housing temperature relative to the ambient of $\Delta T = 40\,°\mathrm{C}$, if the area of the stator housing is considered as convection surface. To obtain a final actuator design, parasitic effects in the actuator are considered and presented in the next section.

6.5 Parasitic effects

In the previous section, a preliminary design is presented based on the analyses of the preceding sections where the effects of geometric parameters on the force and torque capabilities are analyzed. Besides the treated active actuator force and torque, parasitic aspects are present which have to be taken into account. In this section two parasitic effects are discussed, viz, disturbance force and torque due to cogging and electromagnetic damping. Based on these analyses, the final design of the actuator is obtained.

6.5.1 Cogging force and torque

Cogging torque and force are caused by permeance variations due to relative movement of two parts of a magnetic circuit with respect to each other. A cogging torque is present in the actuator due to the slotted stator structure as mentioned in Section 6.2.2. The opening between adjacent slots causes the permeance variation resulting in a disturbance torque referred to as cogging torque. Although the stator does not exhibit slotting in the axial direction, an axial cogging force is present in the actuator due to the finite stator length.

Cogging torque minimization

The cogging torque is caused due to interaction between the magnetic poles and the stator slots, consequently, its profile exhibits periodicity. The fundamental spatial frequency is equal to the least common multiple of the number of poles and slots. The fundamental spatial frequency of the cogging torque in this actuator is equal to twelve per rotation due to the selected pole slot combination of four poles and three slots. One of the key geometric parameters to minimize the cogging torque is the width of the pole-shoe, w_{ps}. The relation between the pole-shoe width and the peak value of the cogging torque is shown in Figure 6.15(a) for a tooth width of $w_t = \frac{w_{ps}}{2}$ calculated by the 3D model presented in the previous chapter. Three minima are obtained at $w_{ps} = 47\,\mathrm{deg}$, $w_{ps} = 80\,\mathrm{deg}$ and $w_{ps} = 120\,\mathrm{deg}$, where the latter one is clearly caused due to the absence of an opening between adjacent slots.
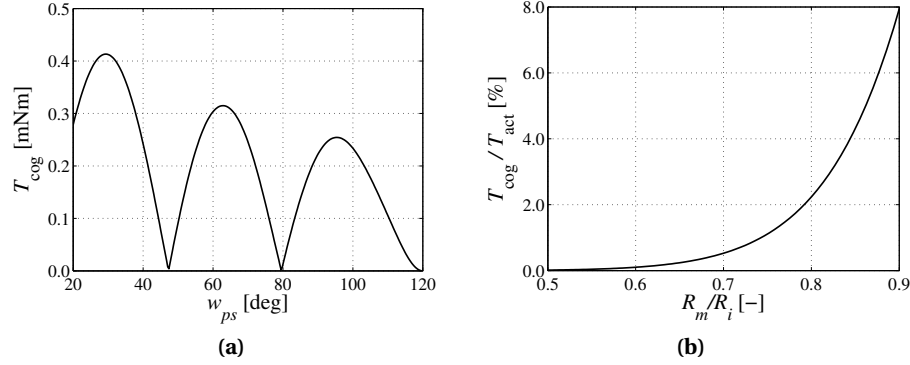
Figure 6.15: (a) Peak value of the cogging torque, T_{cog}, versus the pole shoe width, w_{ps}. **(b)** Cogging torque as percentage of the active torque versus R_m/R_i.

A second evident geometric parameter that affects the cogging torque is the airgap length, i.e., the distance between the mover and the stator back-iron. Increasing the airgap length reduces the magnetic field at the inner stator back-iron surface resulting in lower cogging torque. Secondly, due to the larger airgap, the permeance variation due to the slot-opening is lower. However, the larger airgap affects the active torque that can be produced as well. Figure 6.15(b) illustrates the cogging torque as a percentage of the active torque versus the ratio between R_m and R_i for $w_{ps} = 90\,\text{deg}$.

The pole shoe of the tooth is the back-iron of the translational part of the actuator. Reducing its width affects the force that can be produced as explained in Section 5.4.1. Therefore, a pole shoe width of $w_{ps} = 110\,\text{deg}$ is selected instead of a value where the cogging torque is at its minimum.

Cogging force due to end effects

In rotary actuators the PMs are generally enclosed by the stator back-iron. Conversely, in long stroke linear actuators, the PMs are often not fully covered by the stator back-iron. As a result, the permanent magnet array experiences a local permeance variation during movement of the PM-array with respect to the stator back-iron which causes the end-effect cogging force. To reduce this disturbance force, the axial length of the stator can be adjusted such that the effects at the two stator ends cancel each other. To reduce the force even further, skewing can be applied to the stator-end [131]. However, in a 2-DoF actuator, this skewing results in an additional cogging torque component. Therefore, only the axial length variation is analyzed.

The analytical modeling technique presented in this thesis describes periodic structures. Therefore, a periodic model is created that approximates the effect of the finite stator length. It is based on repetition of the complete actuator in the axial direction where one period of the model describes the complete actuator, see
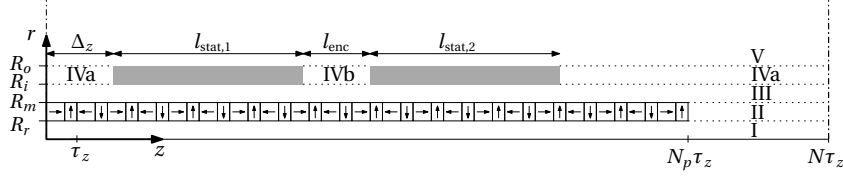
Figure 6.16: Model definition to calculate the end-effect cogging force due to the finite stator and translator length.

Figure 6.16. A high number of harmonics has to be considered in the airgap because the period of the PM-array is $\frac{N}{2}$ times smaller than the period of the complete model. As a result, the implementation method described in this thesis of the 3D representation of this model is not suitable because it results in numerical instability. Therefore, the structure is approximated by a 2D axisymmetric model where the PM array is represented by the rms value of the magnetization along the circumference. One period of this model is illustrated in Figure 6.16. The model contains five regions where regions I, II, III and V are periodic and regions IVa and IVb have iron boundaries at the sides. The period of the model is $N\tau_z$ while the PM array contains N_p poles. The finite translator length can be considered by selecting $N_p < N$. The parameters $l_{\text{stat,1}}$ and $l_{\text{stat,2}}$ represent the length of the two stator parts, and l_{enc} is the spacing between the two stator parts for the position sensor. By means of variation of Δ_z, the cogging force as a function of the axial displacement can be calculated.

To determine the back-iron dimensions having minimum end-effect cogging force, the geometric parameters $l_{\text{stat,1}}$, $l_{\text{stat,2}}$ and l_{enc} are varied, and the rms value of the force is calculated over the complete stroke of 45 mm. In Figure 6.17(a), the results are shown for $l_{\text{stat,1}} = l_{\text{stat,2}}$. The minimum value of F_{ee} can be found if $l_{\text{stat}} \approx 52$ mm. Furthermore, increasing l_{enc} reduces the rms value of the cogging force even further.
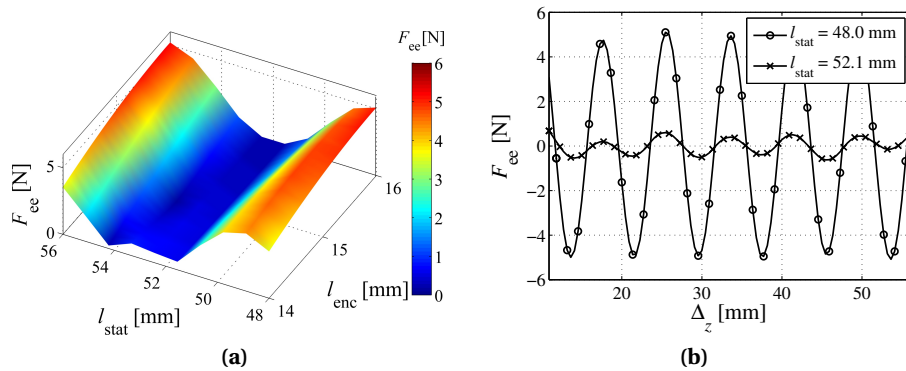
Figure 6.17: (a) The rms value of the end-effect cogging force, F_{ee}, versus the stator section length $l_{\text{stat,1}} = l_{\text{stat,2}} = l_{\text{stat}}$ and the spacing between the stator section l_{enc}. **(a)** End-effect force versus displacement Δ_z for the preliminary design, $l_{\text{stat}} = 48.0$ mm, and the final design, $l_{\text{stat}} = 52.1$ mm.

However, the mover length has to be increased as well, therefore, $l_{\mathrm{enc}} = 14\,\mathrm{mm}$ is selected for the final design. In Figure 6.17(b), the end effect cogging force profile is shown for the preliminary design and for the final design. It can be seen that the amplitude of the end-effect force is reduced by a factor ten.

Flux linkage variation due to end effects

The two dimensional approximation for the rotational part of the actuator is only valid if each stator section comprises an integer multiple of two times the pole pitch $2\tau_z$, as explained in Section 5.4.3. If the stator length is not equal to an integer multiple of $2\tau_z$, the flux linkage of each coil for rotation becomes a function of both the linear and rotational position. Consequently, two undesired effects arise.

1) Due to the flux linkage variation as a function of translational displacement, current through a coil for rotation results in a force component in the axial direction. In Figure 5.22 in Section 5.4.3 it is shown that a single coil of the three phase winding for rotation experiences a varying magnetic field due to movement in the axial direction. Consequently, a current through a coil results in a force in the axial direction. However, the winding for rotation is a three phase one, and the sum of the currents through the three coils is zero if it is star-connected. Consequently, the force in the axial direction on the three coils cancels, and the correlation between force and torque is negligible.

2) The torque constant, i.e., Newton meter per Ampère, becomes a function of the axial mover position. For this effect, the same conclusion can be drawn as for effect 1. That is, the torque constant variation of a single coil is almost completely canceled by the other two coils of the three phase windings. Simulations show that the torque ripple due to the end-effects is approximately 3% for the dimensions obtained in the previous section.

6.5.2 Electromagnetic damping

The analytical modeling technique presented in part I of this thesis provides the static magnetic field distribution in 3D cylindrical structures. The dynamic effects are not taken into account in the analysis of the preceding sections, hence, the validity of the results depends partly on the assumption that the dynamic effects are negligible. Due to variation of the magnetic fields in the soft-magnetic parts of the actuator, iron losses appear resulting in electromagnetic damping. These iron losses, P_{Fe}, are generally subdivided in three components

$$P_{\mathrm{Fe}} = P_{\mathrm{hyst}} + P_{\mathrm{excess}} + P_{\mathrm{eddy}}, \tag{6.45}$$

where P_{hyst} is the loss component due to hysteresis, P_{excess} is the excess loss component, and P_{eddy} is the eddy current loss component [8]. The value of each loss
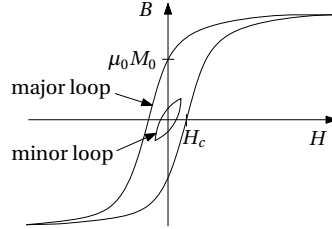
Figure 6.18: Illustration of a magnetic hysteresis curve, showing a major and a minor loop.

component depends on the material properties and the shape of the soft-magnetic parts.

Hysteresis exists in all magnetic materials due to the presence of magnetic domains having a magnetization in a specific direction. If an external field, H, is applied to the material, these domains tend to align with the applied field. After removing the external field, not all domains return to their original state. As a result, a remanent magnetization component, M_0, will be present which is illustrated in Figure 6.18. Applying a reversed external field reduces this component to zero. In case of the moving magnet actuator discussed in this thesis, the external field applied to the soft-magnetic stator back-iron varies during displacement of the mover. The state of the domains in the stator back-iron will depend on history and follows the major and minor loops illustrated in Figure 6.18. Changing the orientation of the domains requires an amount of energy which is equal to the area of the loop. Hence, displacement of the mover results in a power loss proportional to the frequency, f, of the magnetic field variation

$$P_{\mathrm{hyst}} \propto f. \tag{6.46}$$

The excess loss component, P_{excess}, occurs due to the alignment of the aforementioned magnetic domains. If a domain aligns with the external applied field, the probability that a neighboring domains aligns as well is affected. The hysteresis loss component does not consider this effect. This additional loss component is empirically determined to be proportional to

$$P_{\mathrm{excess}} \propto f^{3/2}. \tag{6.47}$$

The third iron loss component is the eddy current loss which appears in electrically conducting materials due to time varying magnetic fields. These fields induce an electric field inside the material resulting in an electric current. Consequently, the eddy current loss is proportional to

$$P_{\mathrm{eddy}} \propto f^2. \tag{6.48}$$

According to Lenz's law, the current flows in a direction such that the magnetic field produced by this current, opposes the magnetic field that has caused the current [53]. In electromagnetic actuators, the eddy currents are generally reduced by laminating the back-iron. The lamination direction is selected such that the effect on the magnetic flux path is negligible while the electric current path is interrupted due to the isolated lamination sheets. However, the flux paths for rotation and translation are orthogonal and lamination for rotation affects the flux path for translation and vice versa. Therefore, lamination cannot be used.

The frequency in (6.46), (6.47) and (6.48) is proportional to the speed of the mover in the rotational or translational direction. Consequently, the electromagnetic damping force, F_d, and torque, T_d, are defined as

$$F_d = d_{\text{hyst},z} + d_{\text{excess},z}\sqrt{v_z} + d_{\text{eddy},z}\,v_z, \tag{6.49}$$

$$T_d = d_{\text{hyst},\theta} + d_{\text{excess},\theta}\sqrt{\omega_\theta} + d_{\text{eddy},\theta}\,\omega_\theta, \tag{6.50}$$

where d represents the damping coefficient caused by a specific loss component. The eddy current component in the damping force and torque is considered to be the dominant term, since lamination of the stator back-iron is not possible. Therefore, 3D finite element models are created to estimate the damping if solid steel is used for the stator back-iron.

Eddy currents due to translation

The eddy current damping is obtained from a no-load simulation by calculating the damping at a constant speed. As a result, the reduction of armature reaction field is not taken into account in the analysis. The selected back-iron material is *steel S235* with an electrical resistivity of $\rho = 1.4 \times 10^{-7}\,\Omega\text{m}$.

The magnetic flux path in a tubular permanent magnet actuator is oriented in the radial and axial direction. Consequently, the eddy currents flow mainly in the circumferential direction through the stator back-iron. In the 2-DoF actuator, the main flux paths for translation are the pole shoes and the eddy current path in the circumferential direction is split into three due to the slot openings. Therefore, eddy currents for translation are inherently reduced due to the slotted stator.

To estimate the eddy currents, a transient finite element model is created where the mover has an imposed speed of $v_z = 1.5\,\text{ms}^{-1}$. The obtained damping constant is linearly approximated by $d_{\text{eddy},z} = 0.88\,\text{Nsm}^{-1}$. By means of a dynamic simulation with the motion profile specified in Figure 4.3 the effect on the performance is calculated. The additional copper loss due to the damping is only 0.5% because the period of constant speed is small, and the damping reduces the amount of active force required during deceleration. Furthermore, the eddy currents result in an additional heat source of 0.5 W, which is approximately 6% of the copper loss.

Eddy currents due to rotation

The magnetic flux path in a classical rotational actuator is oriented in the radial and circumferential direction. Consequently, the eddy currents flow in the axial direction and the circumferential direction to close the electric path. However, the magnetic field in the actuator presented in this thesis does not have a uniform distribution along the axial direction. As a result, the eddy current loops are smaller resulting in lower losses. To estimate the eddy currents, the same transient 3D finite element model is used with an imposed rotational speed of $\omega_\theta = 125\,\mathrm{rads^{-1}}$. The damping constant for rotation is linearly approximated by $d_{\mathrm{eddy},\theta} = 3.4 \times 10^{-5}\,\mathrm{Nmsrad^{-1}}$ which has a significantly higher impact on the performance than the damping for the translational direction. The performance reduction results in 10% increased copper losses and an additional heat source of 0.16 W, which is approximately 20% of the copper loss.

An alternative to reduce the eddy currents is to use a soft magnetic composite as stator back-iron material. The electric resistivity of this material can be up to four orders of magnitude higher than regular steel. However, machining of soft magnetic composites is difficult and expensive which makes it less suitable for application in this actuator.

6.6   Final actuator design

This section concludes the various analyses presented in this chapter. Based on the results, a final design of a 2-DoF actuator is obtained. The differences between the final design and the preliminary design are the length of the stator back-iron and mover, and the pole shoe width, which are selected based on the analysis of the cogging force and torque. The adapted values of the geometric parameters listed in Table 6.2 are given in Table 6.3.

Table 6.3: Geometrical dimensions of the final design of the 2-DoF actuator in addition to the parameters given in Table 6.2.

Parameter		Value	Description
w_{ps}	[deg]	110.0	Pole shoe width
$l_{\mathrm{stat,act},z}$	[mm]	96.0	Active stator length translation
$l_{\mathrm{stat,act},\theta}$	[mm]	84.2	Active stator length rotation
l_{stat}	[mm]	52.1	Stator section length
l_{enc}	[mm]	14.0	Spacing between stator sections for encoder
$l_{\mathrm{mov,act}}$	[mm]	189.2	Active mover length
$l_{\mathrm{mov,tot}}$	[mm]	253.2	Total mover length
m_{mov}	[kg]	0.176	Mover mass
I_{mov}	[kgm^2]	3.9×10^{-6}	Mover moment of inertia
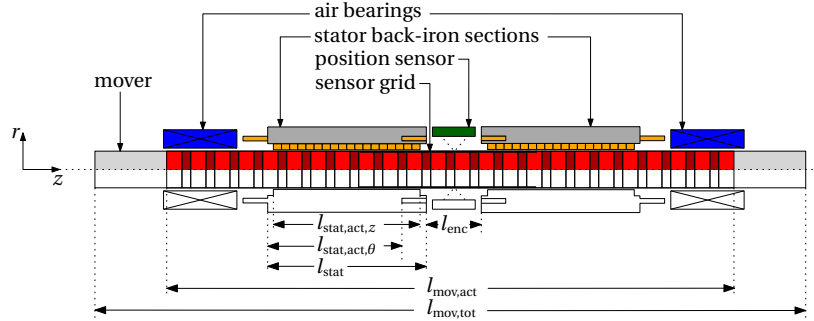
Figure 6.19: Final actuator configuration consisting of two air bearings, two stator back-iron sections and a position sensor in between.

In Section 6.5.1, the length of the stator sections and the spacing between the two sections are determined. However, the end-windings for rotation are not considered in that analysis, consequently, the actuator length has to be adjusted. The spacing between the stator sections is set to $l_{enc} = 14.0\,mm$, which is equal to the width of the encoder, consequently, the end-windings have to be embedded in the stator back-iron as illustrated in Figure 6.19. The resulting active stator length for rotation is reduced to two times 42.1 mm instead of two times 52.1 mm since the length of the end-winding is considered to be 10 mm. The active mover length is $l_{mov,act} = 189.2\,mm$ which is equal to $23\tau_z + \alpha_{pz}\tau_z$ as can be seen in Figure 6.19. The total mover length is $l_{mov,tot} = 253.2\,mm$ to enable the stroke of 45 mm.

The analytical models used in the analysis assume linear material properties. However, the soft-magnetic materials used in electromagnetic devices have a non-linear BH-curve which cause model discrepancies as presented in Section 2.8.2 and Section 3.3.2. To evaluate the effect of the non-linear material properties on the actuator performance, a periodic non-linear 3D finite element model is created. First, the actuator performance degradation is calculated if non-linear iron is used with a saturation magnetization of 1.6 T, and the peak current is supplied to the winding for rotation and translation. Compared to the analytical model, the torque is reduced by 3 %, while the effect on the axial force in negligible. The stronger effect on the rotational performance is caused by the slotted winding for rotation. As a result, a larger part of the magnetic path is soft-magnetic compared to the magnetic path of the flux for translation. If the soft-magnetic part of the actuator is replaced by a material with a constant permeability of $\mu_r = 500$, the rotational and translational performance are decreased by 8.5 % and 0.5 %, respectively. The selected material for the stator back-iron has a saturation magnetization of 1.6 T, hence, the analytical models provide a good approximation of the force and torque.

The total dissipation to follow the specified trajectory including the eddy current loss is equal to $P_z = 8.3\,W$ and $P_\theta = 0.8\,W$ for a coil and magnet temperature of 65 °C. To maintain an actuator housing temperature relative to the ambient of $\Delta T = 40\,°C$, a convection and radiation coefficient of $h = 21\,Wm^{-2}K^{-1}$ is required.

6.7   Summary and conclusions

Synthesis of various phenomena of the selected actuator topology has been conducted to obtain a design that meets the requirements. To fulfil this objective, firstly the actuator configuration is presented including auxiliaries, i.e., position sensor and bearings. Successively, an electromagnetic analysis has been performed to select suitable winding configurations for rotation and translation. To compare various slotless windings for translation, the winding factor is extended with the link factor to take into account the flux leakage through the winding. The effectiveness is subsequently quantified by means of the force versus copper loss. To estimate the maximum electrical loading, a thermal analysis has been performed and a simple thermal equivalent circuit is presented to approximate the winding and housing temperature.

The selected winding configuration and the thermal model are combined with the electromagnetic model presented in the previous chapter. An analysis has been performed to obtain the relation between the geometrical parameters and the mover acceleration while minimizing the copper losses. The stator dimensions have been determined using the 3D analytical model presented in the previous chapter. Based on the results, a preliminary design is presented which can meet the specifications described in Section 4.2. The copper losses during the required trajectory are 8.3 W and 0.8 W for translation and rotation, respectively. Parasitic effects have been analyzed to complete the synthesis, i.e., cogging force/torque and electromagnetic damping. By means of a 2D and a 3D analytical model the end-effect and rotational slot cogging force are analyzed and stator back-iron dimensions are selected to minimize this disturbance force resulting in 0.5 N end-effect force, and 0.1 mNm cogging torque. The effect of the tooth shape of the stator back-iron on the cogging torque is presented and final dimensions are selected. Lastly, the performance degradation due to electromagnetic damping is analyzed by means of transient 3D finite element analyses. The resulting iron losses are 0.5 W and 0.16 W for translation and rotation, respectively. Although damping effects are present if solid steel is used for the stator back-iron, this type of material is selected to enhance the manufacturability and maintain the better magnetic properties.

7

Realization and experimental verification

Abstract - The final design of the 2-DoF actuator, given in Chapter 6, is realized for experimental verification. The realization of the stator and mover assembly are presented and manufacturing issues are mentioned. The prototype is tested in a lab environment and measurement results are discussed.

7.1 2-DoF actuator realization

Part I of this thesis presented a modeling framework to model electromagnetic fields in three dimensional cylindrical structures. In part II, the modeling technique is applied to analyze electromagnetic fields in 2-DoF rotary-linear actuators. Chapter 4 discusses prior art rotary-linear actuators and presents the requirements of a 2-DoF actuator applied in a pick and place machine. In Chapter 5, a novel magnetization array is presented and 3D and 2D electromagnetic models of this new actuator topology are proposed. Subsequently, these models are used in Chapter 6 to obtain a design of the proposed actuator. To validate the models and to show the feasibility of the actuator design, a prototype has been realized and measurements are conducted as presented in this chapter.

In the first section of this chapter, the complete actuator construction is presented and the mover and stator assembly are discussed. Realization issues are considered and pictures of the realized prototype are shown. Section 7.2.1 presents the no-load validation of the realized actuator by means of measurement results of the emf. A system identification is presented in Section 7.2.2. Validation of the electromagnetic damping and cogging force and torque are presented in Section 7.2.3 and Section 7.2.4, respectively. Furthermore, the actuator performance is validated by means of the specified 2-DoF trajectory in Section 7.3.1. The last section presents the results of thermal measurements.
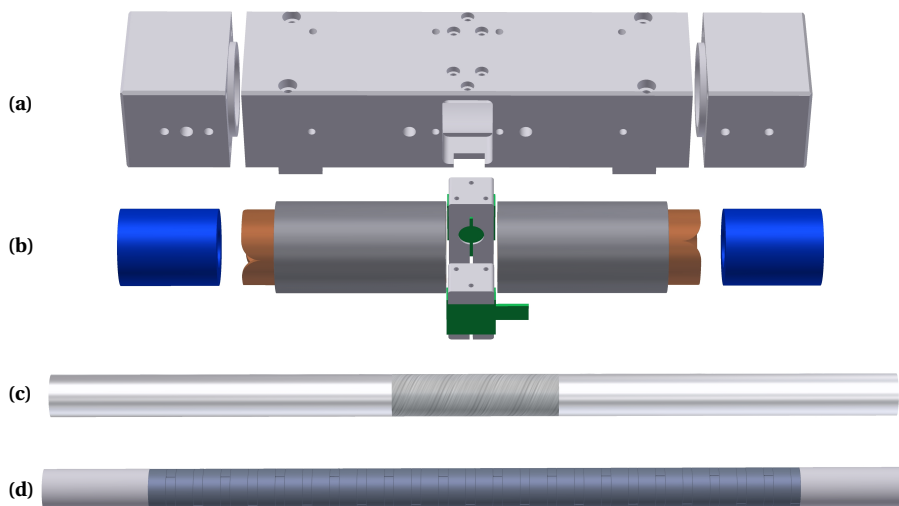
Figure 7.1: Exploded view of prototype of the 2-DoF actuator. **(a)** Aluminum housing consisting of central part to accommodate stator sections and encoder head, and two bearing housings at the sides.**(b)** Two stator sections with encoder heads in the middle and two air-bearings at each end. **(c)** Aluminum mover sleeve with sensor grid. **(d)** PM mover consisting of 12 pole pairs and two aluminum plugs at the ends.
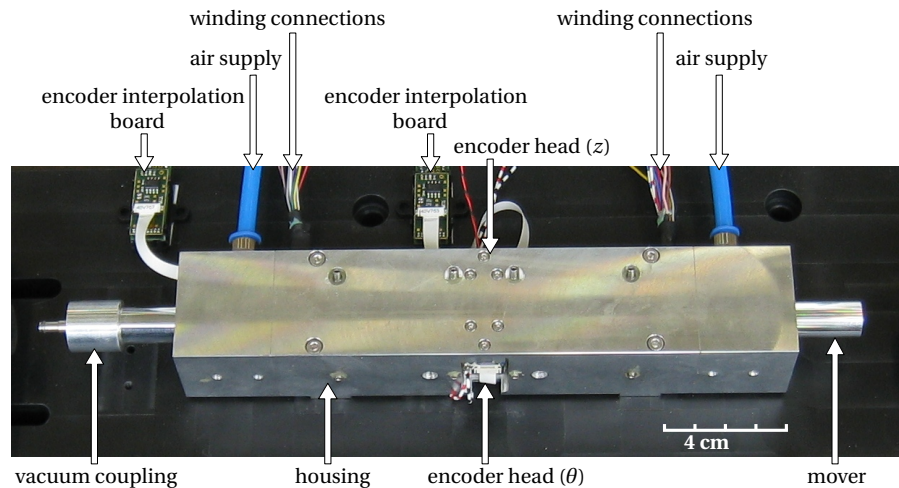
Figure 7.2: Picture of the realized actuator.

7.1.1 Actuator construction

Figure 7.1 shows an exploded view of the different parts of the complete actuator prototype. Figure 7.1(a) shows the aluminum actuator housing consisting of three parts. The central part accommodates the stator sections and two encoder heads, where the stator sections are aligned by means of setscrews. Two aluminum parts at the ends of the housing are used to mount the air-bearings. Figure 7.1(b) illustrates the two air-bearings, the two stator sections and the encoder heads. One end-winding of the winding for rotation is embedded at one side of each stator section which will be further discussed in Section 7.1.3. Figure 7.1(c) and Figure 7.1(d) show the aluminum sleeve with the sensor grid in the middle and the PM-array. The mover is discussed in more detail in Section 7.1.2. In Figure 7.2, a picture of the complete realized actuator is shown.

7.1.2 Mover assembly

The PM mover of the 2-DoF actuator consists of the altered quasi-Halbach magnetization pattern discussed in Section 5.1. The array consists of three different PMs as shown in Figure 7.3. Two half rings with opposing magnetization are glued together to create a ring magnet which is illustrated in Figure 7.3(a). The shape of the half rings is such that the realized ring has a square opening in the center with sides of 3.0 mm. The opening is used to fix the orientation of the rings during assembly of the complete mover, see Figure 7.3(b). Together with the axially magnetized rings, the complete PM array is constructed as illustrated in Figure 7.3(c). A picture of one third of the realized PM array is shown in Figure 7.4(a).

(a)   **(b)**   **(c)**
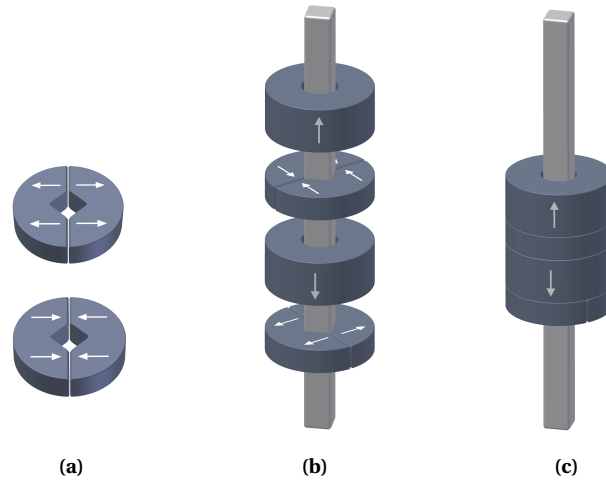
Figure 7.3: Illustration of the permanent magnet array assembly. **(a)** Ring magnet consisting of two half rings with opposing magnetization direction with square opening in the center for assembling. **(b)** Stack of four ring magnets along a bar to ensure correct orientation of the rings. **(c)** Assembled and glued pole pair.

After assembly of the PM array, the complete stack is glued in an aluminum tube with two aluminum plugs at the ends illustrated in Figure 7.1(d). Subsequently, the aluminum tube is machined to a diameter of 12.7 mm, resulting in a sleeve thickness of 0.35 mm. The sensor grid is put on the middle of the tube by means of a lathe over the complete circumference, as shown in Figure 7.4(b).

From measurements on the realized mover was found that the bending stiffness is approximately 2.5 times lower than the required stiffness. As a results, the deflection of the mover will be larger than expected due to unbalanced magnetic pull caused

(a)   **(b)**
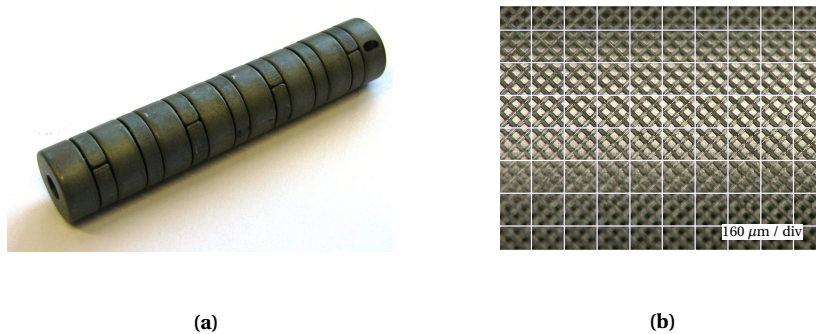
Figure 7.4: (a) Picture of one third of realized permanent magnet array. **(b)** Microscopic picture of the sensor grid on the mover.
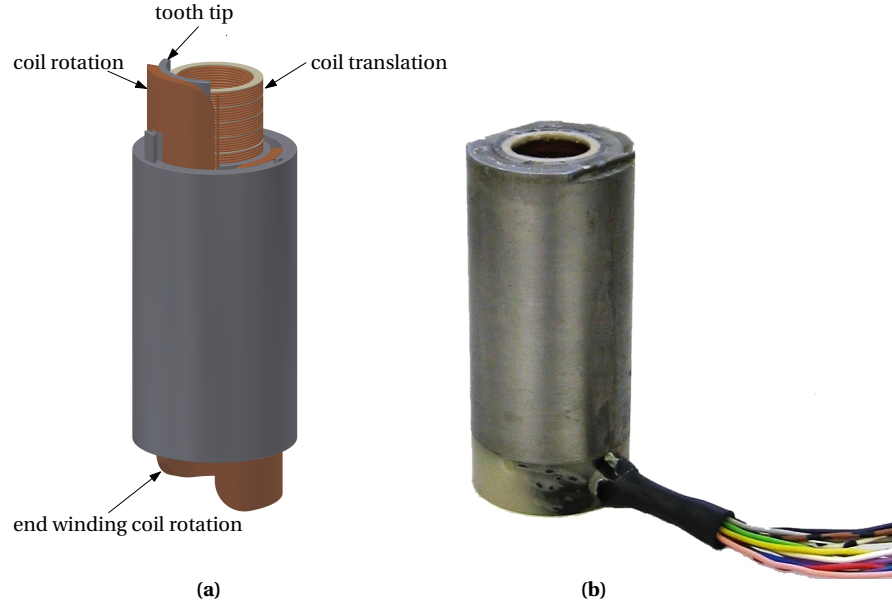
Figure 7.5: Stator section consisting of stator-back-iron and windings for rotation and translation. **(a)** Illustration to clarify the assembly of the stator section. **(b)** Picture of realized stator section.

by eccentricity. To avoid contact between the mover and the stationary part, the inner radius of the coil for translation, R_c is increased to $R_c = 6.60\,\text{mm}$ to enlarge the mechanical airgap from $l_g = 0.15\,\text{mm}$ to $l_g = 0.25\,\text{mm}$. Consequently, the filling factor of the coil for translation is reduced to $k_{\text{ff},z} = 0.55$ and the dissipation in the winding for translation is increased by 40%.

7.1.3 Stator assembly

The stator back-iron consists of two sections to be able to place the two encoder heads in between. The encoder head is a *Renishaw RGH34* which provides an analogue sine-cosine quadrature signal based on reflection of light from the sensor grid on the mover. The two encoder heads are mounted orthogonally at two mover sides to measure rotation and translation separately. Each stator section contains two windings, a slotless winding for translation enclosed by a slotted winding for translation (discussed in Section 5.2.1). To reduce the axial length of the stator back iron, one of the two end-windings of the coils for rotation is embedded in the back-iron as illustrated in Figure 7.5(a). The tooth tip has the same length as the stator back-iron because it is the back-iron for the winding for translation.

The cylindrical coils of one phase of the winding for translation are wound as a

single strand. Hence, the coils are already wound in series and no interconnections have to be made afterwards. The slot-openings in the back-iron are used to place the coil interconnections and the winding leads as illustrated in Figure 7.5(a). The stator back-iron consists of three separate teeth and a tube to simplify the assembly of a stator section. The coils for rotation can be placed around each tooth which can be slid into the tube subsequently. To join the parts into one solid structure, the stator section is potted in a mold with epoxy resin. A picture of a potted stator section is shown in Figure 7.5(b).

7.2 2-DoF actuator identification

7.2.1 Electromotive force

To validate the realized actuator, first, the electromotive force (emf) is measured by moving the mover by means of an external force. The actuator consists of two stator sections each containing a three phase winding for rotation and a three phase winding for translation. The two stator sections are aligned to be able to connect the two stator sections in series. The voltage is measured at the phase terminals of the two stator sections separately to verify the alignment.

Translational electromotive force

The emf of the winding for translation is measured while moving the mover with approximately $v_z = 0.25\,\mathrm{ms}^{-1}$ in the axial direction. The measured terminal voltage is successively divided by the instantaneous velocity to obtain the emf constant. In Figure 7.6, the emf of one phase of the two stator sections is shown versus
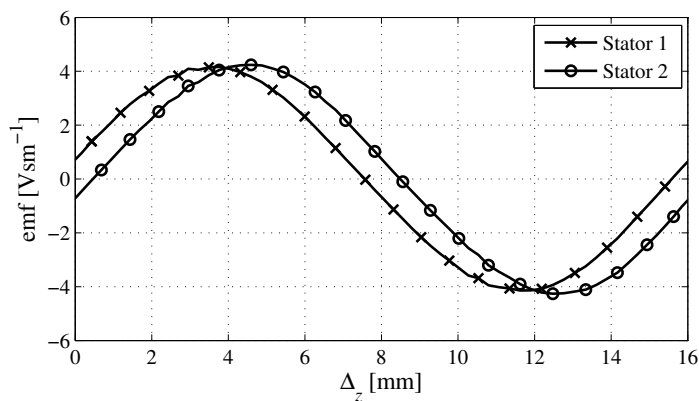
Figure 7.6: Electromotive force induced in one phase of the two sections of the winding for translation.
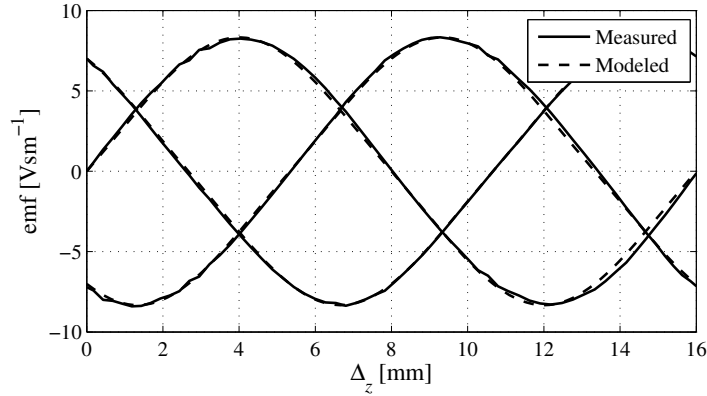
Figure 7.7: Measured and modeled three phase electromotive force of the winding for translation versus displacement, Δ_z. The winding in the two stator sections are connected in series.

displacement, Δ_z. The amplitude of the two waveforms is in agreement, however, the two waveforms have a phase difference of approximately 0.9 mm, or 20 deg electrically. As a result, the first harmonic of the total emf is reduced by 1.6% and the third harmonic is reduced by 14% to 2.9% of the first harmonic.

Figure 7.7 shows the emf of the three phases if the two windings in the stator sections are connected in series. The measurements are in good agreement with the results from the analytical model, although the emf is slightly reduced due to the misalignment of the stator sections. Note that the model does not reflect the final design, but the realized design with $R_i = 6.60$ mm.

Rotational electromotive force

The emf of the winding for rotation is measured by means of the same approach. The mover is rotated with an angular velocity of approximately $\omega_\theta = 30$ rads[-1]. The emf, normalized to $\omega_\theta = 1$ rads[-1], of one phase measured in the two stator sections is shown in Figure 7.8. The rotational misalignment of the two stator sections is less than 2 deg mechanically, as can be seen from the waveform. Furthermore, the amplitude of the waveform deviates slightly along one rotation. This is caused by eccentricity of the PM-array inside the mover or due to misalignment of the PMs with respect to each other.

Figure 7.9 shows the three phase emf for the rotational winding after connecting the two stator sections in series. The measured phase emf is approximately 6% higher than the emf obtained from the analytical model due to the non-modeled overhang of the stator underneath the end windings illustrated in Figure 7.5(a). This results in an increased area to focus the flux through the coil. In the analytical model, the length of
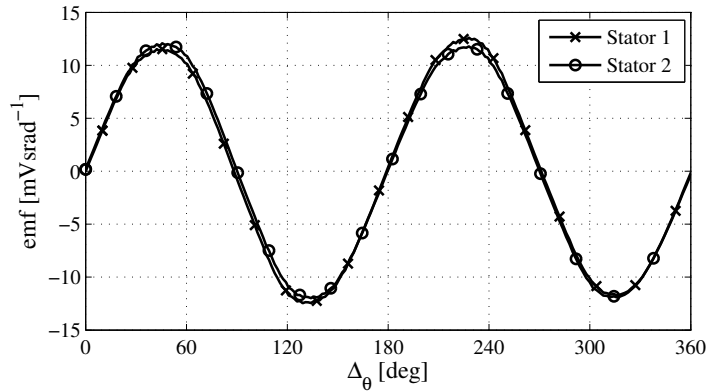
Figure 7.8: Electromotive force induced in one phase of the two sections of the winding for rotation.

the coil opening is considered to be the effective length of the coil, resulting in a lower flux linkage and emf.
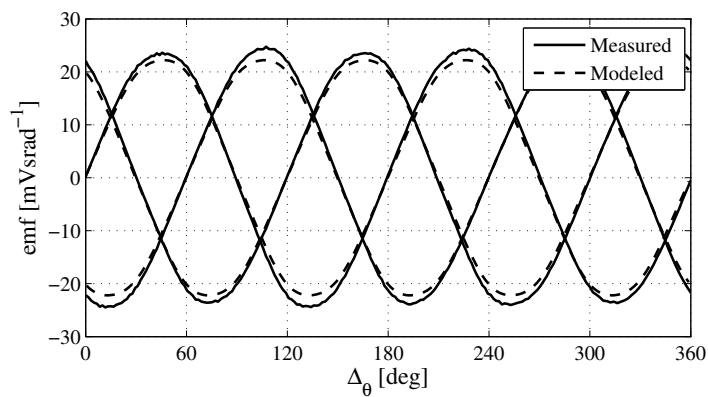
Figure 7.9: Measured and modeled three phase electromotive force of the winding for rotation versus displacement, Δ_θ. The windings in the two stator sections are connected in series.
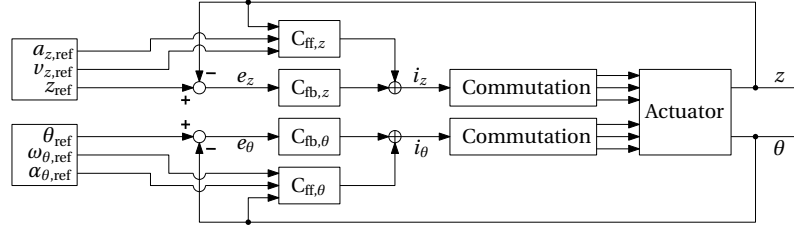
Figure 7.10: Controller structure.

7.2.2 System identification and controller design

In Chapter 5 and Chapter 6 the decoupling of the two degrees of freedom of the actuator is discussed. By selecting the magnetization pattern and the two orthogonal winding sets, the actuator is considered to be physically decoupled. To verify this assumption, the actuator is analyzed by means of a full multi-input multi-output (MIMO) identification. The identification is performed under closed loop using the controller structure illustrated in Figure 7.10. Based on the models, two single-input single output (SISO) 15 Hz PD controllers are created and used for translation and rotation, $C_{\mathrm{fb},z}$ and $C_{\mathrm{fb},\theta}$, while the feed-forward controllers, $C_{\mathrm{ff},z}$ and $C_{\mathrm{ff},\theta}$, are set to zero. A sinusoidal position reference with a frequency of 0.2 Hz is used to measure an average transfer function over the complete stroke of rotation and translation. Two separate experiments have been carried out. In the first experiment noise is injected in the top loop, just before the input i_z, and in the second experiment noise is injected in the lower loop, just before the input i_θ. During the experiment, the error signals, e_z and e_θ, the input signals, i_z and i_θ, and the injected noise are measured. As such, the input sensitivity

$$\mathbf{S}_i = (\mathbf{I} + \mathbf{C}\mathbf{G})^{-1}, \tag{7.1}$$

can be measured column-wise, where $\mathbf{I}$ is the identity matrix, $\mathbf{G}$ is the MIMO plant, and $\mathbf{C}$ is the MIMO controller which in this case consists of the two SISO controllers $C_{\mathrm{fb},z}$ and $C_{\mathrm{fb},\theta}$. The process sensitivity

$$\mathbf{PS} = (\mathbf{I} + \mathbf{G}\mathbf{C})^{-1}\mathbf{G} \tag{7.2}$$
$$= \mathbf{G}(\mathbf{I} + \mathbf{C}\mathbf{G})^{-1} \tag{7.3}$$
$$= \mathbf{G}\mathbf{S}_i, \tag{7.4}$$

can be measured column-wise as well. Successively, the full MIMO frequency response can be constructed by combining the measurements of the two experiments, where the MIMO plant, $\mathbf{G}$, can be extracted using

$$\mathbf{G} = \mathbf{PS}\,\mathbf{S}_i^{-1}. \tag{7.5}$$
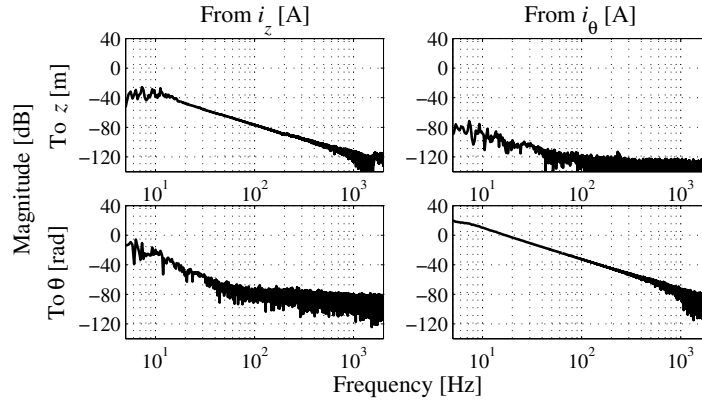
Figure 7.11: Bode magnitude plot obtained by MIMO identification.

The resulting measured plant is given in Figure 7.11. It can be seen that the diagonal terms show a line with a slope of -40 dB/decade without resonances up to 1500 Hz, which is as expected since the actuator consist of a single moving mass/moment of inertia. The noise below -120 dB and -76 dB for z and θ, respectively, is caused by quantization noise due to the finite position sensor resolution. The off-diagonal terms are significantly smaller, which indicates that the plant is well-decoupled. To analyze the decoupling in more detail, a relative gain array (RGA) is constructed which provides a measure of interaction for MIMO systems independent of input and output scaling [118].

From the RGA, shown in Figure 7.12, it can be seen that the diagonal terms are close to unity for frequencies up to 1 kHz, while the off-diagonal terms are close to zero. This
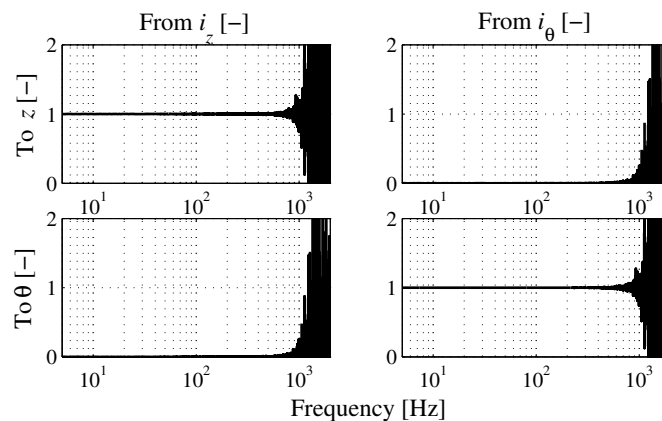
Figure 7.12: Relative gain array obtained by MIMO identification.
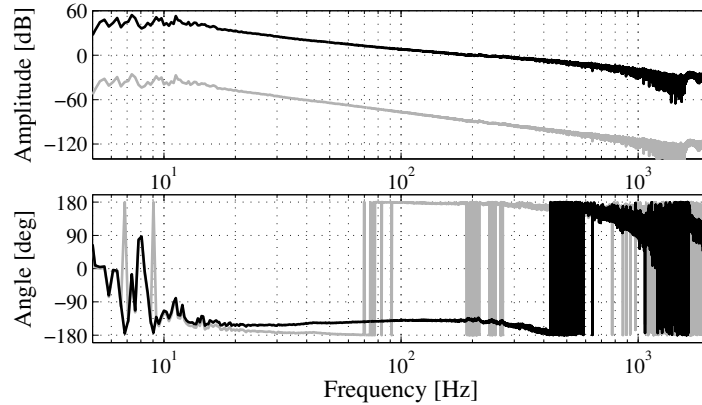
Figure 7.13: Bode plot of G_{zz} (gray) and open-loop response with 200 Hz lead-lag controller (black).

indicates that the plant can be considered fully decoupled, hence two SISO controllers can be used to control the two degrees of freedom.

Two SISO lead-lag controllers with a low pass filter and a bandwidth of $f_{\text{BW},z} = 200$ Hz and $f_{\text{BW},\theta} = 180$ Hz for translation and rotation, respectively, are designed by means of loop shaping. That is, a zero at $\frac{f_{\text{BW}}}{3}$, a pole at $3f_{\text{BW}}$, and a first order low-pass filter at $5f_{\text{BW}}$. The bandwidth is selected based on the results of the next section to be able to follow the trajectory within the specified positioning errors. The open-loop response is shown by the black line in Figure 7.13 and Figure 7.14.
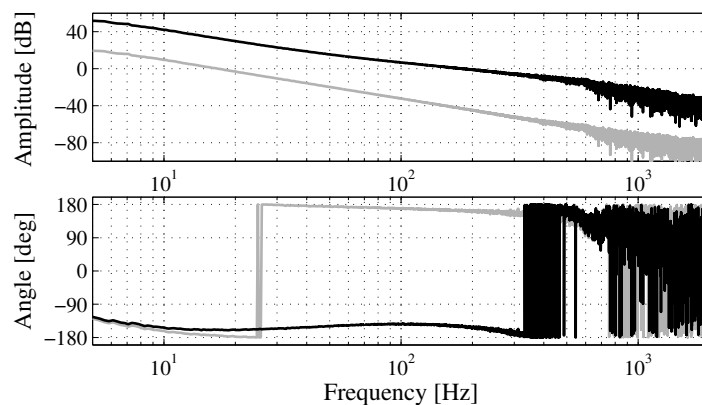
Figure 7.14: Bode plot of $G_{\theta\theta}$ (gray) and open-loop response with 180 Hz lead-lag controller (black).

The two feedback controllers are implemented by means of the control structure shown in Figure 7.10 and used to quantify the parasitic non-linear effects, i.e., cogging torque and force, and electromagnetic damping. The obtained information, complemented with gravity and the acceleration, is subsequently used to create the feed-forward controllers $C_{\text{ff},z}$ and $C_{\text{ff},\theta}$. The complete control structure is implemented to validate the actuator performance by means of the trajectory specified in Section 4.2. The results of this validation are presented in Section 7.3.1.

7.2.3 Electromagnetic damping

To estimate the actuator damping in the θ- and z-direction, the mover is displaced with a constant velocity and the output of the feedback controllers is considered to be the current required to maintain constant speed. To eliminate position dependent distortion, the end-effect force is compensated by the feed forward controller, and the controller output is averaged over one revolution and two times the pole pitch for rotation and translation, respectively. The results of these measurements at different speeds are shown in Figure 7.15.

The mechanical friction component in this measurement is considered to be negligible due to the selection of porous air bearings. A function is fitted through the measured values, based on the iron loss components described by (6.49) and (6.50) in Section 6.5.2. The fitted function is shown in Figure 7.15 and the obtained values are listed in Table 7.1.

From the table it can be seen that the measured eddy current damping in the translational direction, $d_{\text{eddy},z}$, is approximately 30% higher than the modeled one. Conversely, the measured eddy current damping for rotation is 35% lower than the
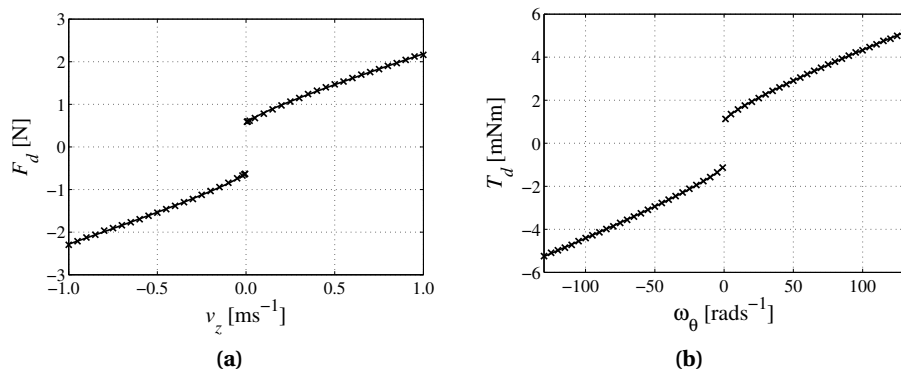
Figure 7.15: **(a)** Measured damping force versus velocity, v_z. **(b)** Measured damping torque versus angular velocity, ω_θ. The solid line shows a fit through the measured data.

Table 7.1: Comparison of modeled and measured electromagnetic damping.

Damping coefficient		Modeled	Measured
$d_{\mathrm{hyst},z}$	[N]	-	0.52
$d_{\mathrm{excess},z}$	[N$\sqrt{\mathrm{sm}^{-1}}$]	-	0.53
$d_{\mathrm{eddy},z}$	[Nsm^{-1}]	0.88	1.15
$d_{\mathrm{hyst},\theta}$	[Nm]	-	9.7×10^{-4}
$d_{\mathrm{excess},\theta}$	[Nm$\sqrt{\mathrm{srad}^{-1}}$]	-	1.2×10^{-4}
$d_{\mathrm{eddy},\theta}$	[Nmsrad^{-1}]	3.4×10^{-5}	2.2×10^{-5}

modeled one. This significant deviation can be caused by the anisotropic conductivity of the back-iron material which is not considered in the finite element analysis. The additional damping in the translational direction does not affect the actuator performance significantly as discussed in Section 6.5.2.

In Section 6.5.2, the three iron loss components are discussed and the eddy current damping is assumed to be the dominant term. The hysteresis and excess loss component are not quantified and considered negligible. However, the measurements show that the hysteresis component is clearly present in the electromagnetic damping. Measurements on a sample of the back-iron material are conducted to confirm the presence of a significant hysteresis component in the electromagnetic damping. The results are given in Figure C.2 in Appendix C.2. The measured value of H_c of the major loop is approximately $600\,\mathrm{Am}^{-1}$. This value is two to ten times higher than often used magnetic materials as low carbon mild steels and silicon steels (IEC 60404-1). The electromagnetic damping is measured over a stroke of two times the pole pitch and a full rotation, hence, the state of the material moves along the same hysteresis loop each time (see Figure 6.18). Consequently, the damping force for this movement can be accurately predicted and compensated by means of a feed-forward controller. However, for small displacements, the value of $d_{\mathrm{hyst},z}$ and $d_{\mathrm{hyst},\theta}$ given in Table 7.1 are not valid. Further research is required to investigate the effect of hysteresis while using force control, mentioned as one of the requirements in Section 4.2.

7.2.4 Cogging torque and force

The cogging torque and force are measured by moving the mover slowly over the complete stroke in the θ- and z-direction, respectively. The output of the feedback controller is used as a measure for the cogging torque/force. A low speed is selected to minimize distortion due to dynamic effects. First the cogging torque is investigated. However, due to the low level of cogging, only 0.1 mNm according to the models, it could not be identified from the measurements.
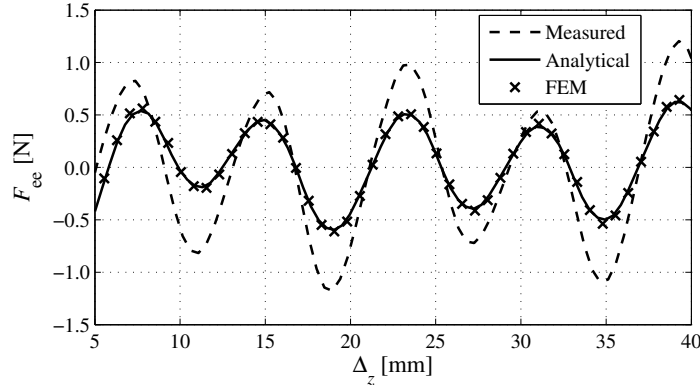
Figure 7.16: Measured and modeled end-effect force versus axial displacement.

The end-effect cogging force is measured while making a reciprocating movement along the axial direction with a velocity of $v_z = 5\,\text{mms}^{-1}$. The force obtained from the filtered control signal is shown in Figure 7.16 by the dashed line. The solid line and the markers show the results from the 2D analytical and the 2D finite element model, respectively. The 2D finite element model is an axisymmetric representation of the actuator including the space between the pole-shoe overhang and the stator back-iron. It can be seen that the finite element model and the analytical model are in good agreement. However, the measured end-effect force is at various positions two times higher than the modeled force. This model mismatch is highly likely caused by manufacturing and assembly tolerances and hysteresis as discussed in the previous section. From in Figure 6.17 can be seen that variation of the axial stator length heavily affects the end-effect force. Due to hysteresis, the stator exhibits locally a remanent magnetization whereas in the model used to predict the end-effects, the soft-magnetic material is modeled with an infinite permeability without any remanence. This remanence can cause additional attraction and repulsion forces at the stator ends. Both the hysteresis and the effects of manufacturing tolerances are very difficult to model either analytically or numerically in 3D. Therefore, extensive additional research is required to quantify these effects.

7.3   2-DoF actuator performance validation

7.3.1   Trajectory validation

During the design procedure of the actuator, the pick and place trajectories presented in Section 4.2 are considered as the main requirement for the actuator. That is, the actuator should be able to follow the trajectory within certain thermal limits. To validate this, two series of measurements are conducted. In this section, the feasibility
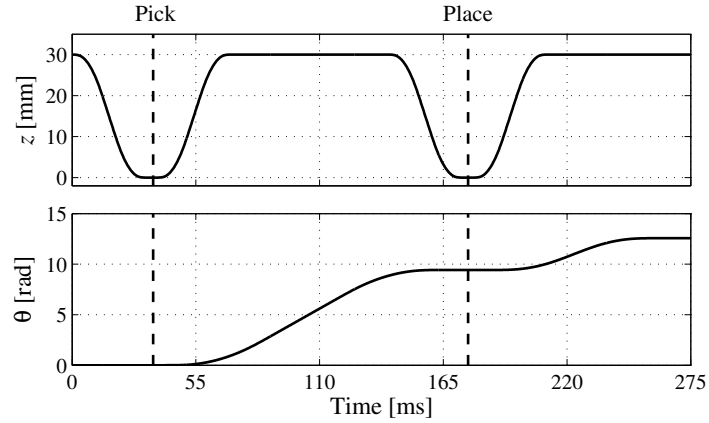
Figure 7.17: Rotational and translational position reference for pick and place trajectory.

to follow the trajectory is considered and the dissipated power is calculated. The next section focuses on the thermal aspects.

The third order trajectories for translation and rotation, illustrated in Figures 4.3, 4.4 and 7.17, are used as setpoints for the mover. Figure 7.18 shows the position error during one cycle of the trajectory. The position errors at the pick and place time are $e_z = 4\,\mu$m and $e_\theta = 0.32$ mrad for translation and rotation, respectively. Hence, the requirement for the static position error are met.
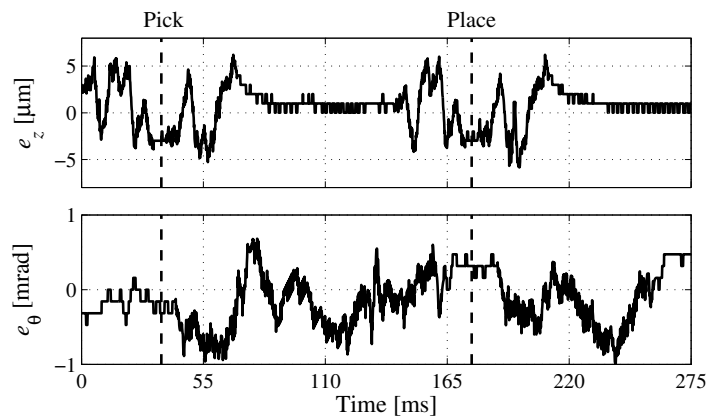
Figure 7.18: Position error in translational and rotational direction, e_z and e_θ, respectively, during trajectory specified in Figure 7.17.
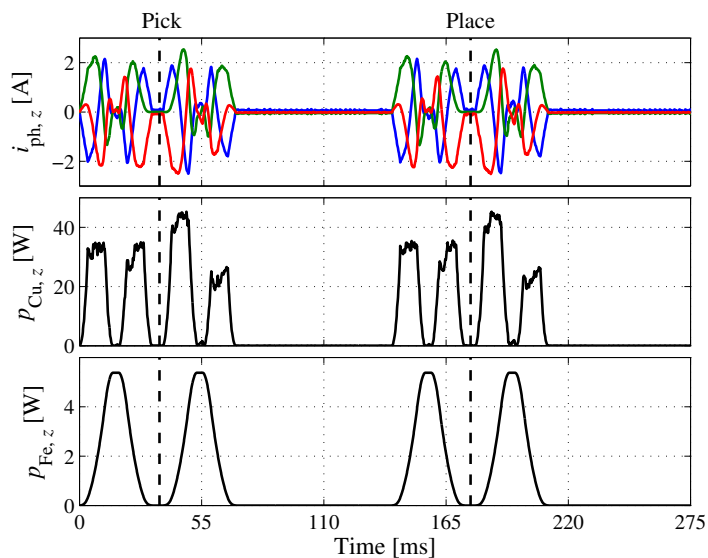
Figure 7.19: Instantaneous phase currents, $i_{\mathrm{ph},z}$, copper loss, $p_{\mathrm{Cu},z}$ and iron loss, $p_{\mathrm{Fe},z}$ for translational displacement during the trajectory specified in Figure 7.17.
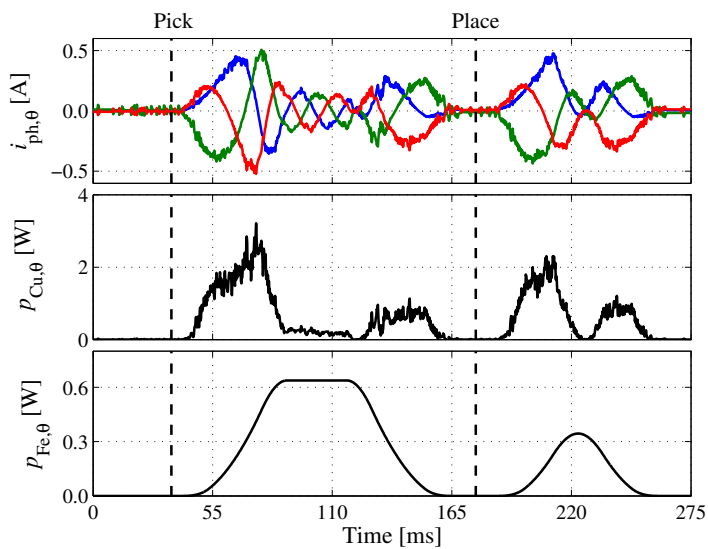
Figure 7.20: Instantaneous phase currents, $i_{\mathrm{ph},\theta}$, copper loss, $p_{\mathrm{Cu},\theta}$ and iron loss, $p_{\mathrm{Fe},\theta}$ for rotational displacement during the trajectory specified in Figure 7.17.

To obtain the total copper loss in the two windings, the aforementioned trajectory is repeated several times and the dissipation is calculated from the phase current setpoints. The instantaneous phase current and copper loss during one pick and place cycle are illustrated in Figures 7.19 and 7.20 for translation and rotation, respectively. The acceleration and deceleration phase of the trajectory are clearly visible in the copper loss. Furthermore, by means of the measured electromagnetic damping constants, listed in Table 7.1, the iron loss in the actuator is estimated. The average copper loss during one pick and place cycle in the two windings is $P_{\mathrm{Cu},\theta} = 0.52\,\mathrm{W}$ and $P_{\mathrm{Cu},z} = 9.45\,\mathrm{W}$ at 23 °C. The additional average heat generated in the actuator due to the iron losses is $P_{\mathrm{Fe},\theta} = 0.19\,\mathrm{W}$ and $P_{\mathrm{Fe},z} = 1.15\,\mathrm{W}$ at 23 °C for rotation and translation, respectively.

7.3.2 Thermal validation

The main constraint considered in the design of the actuator is the maximum temperature inside and at the surface of the actuator. Therefore, the thermal model as presented in the previous chapter is validated in this section. The goal of the validation is to:

1. Verify that the difference between the coil temperature and the housing temperature is less than 10% of the housing temperature relative to the ambient.

2. Verify that the thermal limits are not violated if the actuator dissipates 9.1 W, which reflects the dissipation in the final design of the actuator during the trajectory specified in Section 4.2.

The thermal measurement is conducted in a lab environment with an ambient temperature of approximately 23 °C. The actuator is mounted on a PVC base with negligible thermal conductivity compared to the convection of the actuator to the ambient. Consequently, the base does not act as a heat sink. A constant power is applied to the winding for translation and rotation to maintain a constant dissipation. The temperature is measured by means of one PT100 temperature sensor inside the stator assembly, two PT100 temperature sensors at the housing of the actuator, and by measuring the resistance of the two windings. From the winding resistance the temperature of the coils is reconstructed. The data from the PT100 and the coil resistances is averaged to represent the coil temperature. The mean value of the two temperature sensors at the housing is considered to be the housing temperature.

Two measurements are performed, one with a constant dissipation of 4.5 W, and a second one with a constant dissipation of 9.1 W. Figure 7.21 shows the resulting relative temperature of the actuator versus time. If 4.5 W is dissipated inside the actuator, the coil temperature relative to the ambient rises to approximately $\Delta T = 10.8\,°\mathrm{C}$ and the housing temperature to $\Delta T = 10.0\,°\mathrm{C}$. For a dissipation of 9.1 W, the temperature
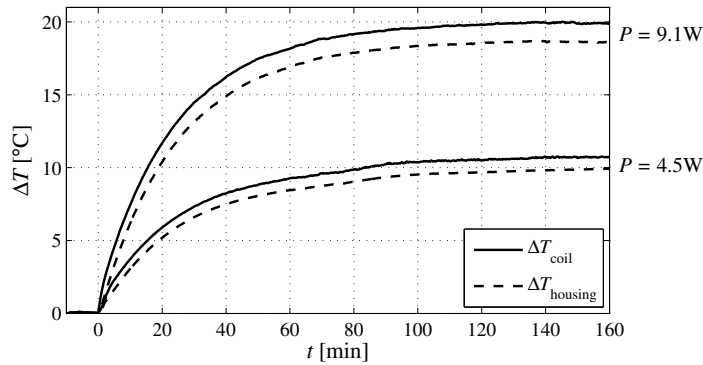
Figure 7.21: Measured coil and housing temperature relative to the ambient versus time for a constant dissipation in the coils of $P = 4.5\,\text{W}$ and $P = 9.1\,\text{W}$.

of the coil and the housing rises to $\Delta T = 20\,°\text{C}$ and $\Delta T = 18.7\,°\text{C}$, respectively. Consequently, the difference between the coil and the housing temperature is approximately 8%.

In conclusion, the designed actuator (with a constant dissipation of 9.1 W) does not violate the thermal limit of $\Delta T = 40\,°\text{C}$. This is mainly caused by the larger convection area of the housing and an additional heat-flow due to the air-bearings. Furthermore, the temperature difference between the coils and the housing does not exceed 10% of the relative housing temperature, which is assumed in the design analysis.

The total dissipation in the built prototype is 10.0 W due to copper loss and 1.3 W because of iron losses at 23 °C, see Figures 7.19 and 7.20. Consequently, the relative coil temperature will increase to approximately $\Delta T = 30\,°\text{C}$ with a dissipation of approximately 13.5 W.

The thermal behavior of the actuator is only verified statically up to $\Delta T = 20\,°\text{C}$. A full dynamic thermal verification is not conducted to prevent the mover from irreversible damage. The stiffness reduction might be caused during the gluing process and can be further affected by higher temperatures during operation.

7.4   Summary and conclusions

In this chapter, the realization and measurements of the 2-DoF actuator prototype have been presented. The stator and mover construction and the assembly of the various parts have been discussed. A summary of the comparison of the final design and the realized prototype is given in Table 7.2. To validate the no-load properties of the actuator, the emf is measured for rotation and translation. The modeled and measured emf for translation differ approximately 1% in amplitude. For rotation, the measured value is approximately 7% higher than the modeled value due to the non-modeled overhang of the stator teeth underneath the end windings. A MIMO identification is performed to obtain the frequency response of the total system. That includes the data-acquisition and control system, the power amplifiers, the actuator and the position sensors. The results of the system identification show that rotation and translation are physically decoupled. Two lead-lag controllers have been designed with a bandwidth of 200 Hz and 180 Hz for translation and rotation, respectively. The damping at $1\,\mathrm{ms}^{-1}$ and 1000 rpm are 2.2 N and 4.5 mNm in the translational and rotational direction, respectively. In the translational direction the eddy current damping is approximately 30% higher while in the rotational direction this component is 35% lower than modeled, i.e., $1.15\,\mathrm{Nms}^{-1}$ and $2.2 \times 10^{-2}\,\mathrm{mNmsrad}^{-1}$, respectively. Furthermore, hysteresis and excess loss components have been identified. These damping components can be predicted accurately, however, for small displacements the compensation of this damping is

Table 7.2: Comparison of the actuator design and the realized prototype.

Parameter		Design	Proto	Description
$k_{\mathrm{ff},z}$	[-]	0.65	0.55	Coil filling factor z
$k_{\mathrm{ff},\theta}$	[-]	0.5	0.67	Coil filling factor θ
N_z	[-]	38	30	Number of turns per coil z
N_θ	[-]	126	125	Number of turns per coil θ
L_z	[μH]	260	160	Inductance total winding z
L_θ	[mH]	8.6	9.1	Inductance total winding θ
R_z	[Ω]	4.6*	4.5*	Resistance total winding z
R_θ	[Ω]	7.7*	6.8*	Resistance total winding θ
$k_{f,z}$	[NA^{-1}]	15.4*	12.2*	Force constant
$k_{f,\theta}$	[mNmA^{-1}]	31.8*	34.1*	Torque constant
$d_{\mathrm{eddy},z}$	[Nsm^{-1}]	0.88	1.15	Damping constant z
$d_{\mathrm{eddy},\theta}$	[Nmsrad^{-1}]	3.4×10^{-5}	2.2×10^{-5}	Damping constant θ
$P_{\mathrm{Cu},z}$	[W]	6.5*	9.45*	Copper loss during trajectory z
$P_{\mathrm{Cu},\theta}$	[W]	0.6*	0.52*	Copper loss during trajectory θ

*Modeled/measured at 23 °C

not correct and further research is required to obtain a more accurate model. The end-effect cogging force is found to be up to two times higher than modeled, i.e. 0.5 N and 1.0 N respectively. This model mismatch is highly likely the result of manufacturing and assembly tolerances and hysteresis, which are very difficult to model either analytically or numerically in 3D. The cogging torque due to slotting has not been identified due to its low level, i.e., 0.1mNm in the analytical model. The electromagnetic damping in two directions has been measured at different velocities.

To validate the actuator performance, the trajectory given by the requirements is implemented. The non-linear effects are compensated by means of a feed-forward controller and the two feedback controllers are used to comply with the required maximum static position error. The dissipated power during the trajectory has been calculated and is 1.3 W and 12.2 W due to iron losses and copper losses, respectively. Static thermal measurements have been conducted to validate the thermal model used in the design procedure. Two aspects are verified; the relative housing temperature does not exceed the 45 °C, and the difference between the coil and the housing temperature is within 10% of the relative housing temperature. Furthermore, due to the increased convection area of the aluminum housing and additional cooling caused by the airflow of the air-bearings, the actuator temperature is 30% lower than modeled.

The actuator complies with the requirements, that is, a mover acceleration in the axial direction of $a_z = 150\,\mathrm{ms}^{-2}$ over a stroke of 30 mm for a duty-cycle of 34% has been shown and the static positioning error in this direction is 4 μm, where a maximum error of 5 μm is specified. A mover acceleration in the rotational direction of $\alpha_\theta = 3500\,\mathrm{rads}^{-2}$ for a duty-cycle of 47% has been shown and the static positioning error is less than 0.35 mrad. Furthermore, the combined rotation-translation motion profile results in a continuous dissipation of 13.5 W, resulting in a temperature rise of the actuator of approximately $\Delta T = 30\,°\mathrm{C}$.

Part III

Closing

8

Conclusions and Recommendations

Abstract - In this chapter the main conclusions from the thesis are summarized. Furthermore, recommendations for future research are given.

8.1   Conclusions

8.1.1   Part I: Modeling

Accurate and fast electromagnetic field prediction is required to analyze new electromagnetic devices. Various modeling methods have been discussed, e.g., the harmonic modeling technique, which is an accurate and fast method to describe these fields in devices containing linearized soft-magnetic materials. This technique is widely implemented to describe magnetic fields in two dimensional coordinate systems. However, very few implementations of this modeling technique for 3D models have been found in literature, which are all limited to regular shaped geometries. This thesis has presented the derivation of a general applicable 3D analytical harmonic model to determine the 3D electromagnetic field distribution in cylindrical devices. Furthermore, this technique has been extended to include both regular and irregular cylindrical shapes.

The employed harmonic modeling technique is based on 2D Fourier series to describe sources and magnetic fields. It is limited to current-free cylindrical problems exhibiting periodicity or a soft-magnetic boundary in the axial direction, and it assumes linear material properties. However, either circumferential slots, axial slots or rectangular cavities have been accounted for. The computational requirements of this model depend on the complexity of the geometry, or more specifically, the number of regions. As a result, the model-accuracy and -stability degrades for more complex devices. The model is especially suitable for parametric searches since, contrary to a finite element model, no re-meshing is required after a geometric parameter is updated, which reduces the computation time significantly.

The assignment and method to solve the various boundary conditions have been discussed in a generic manner to enable model application to a large class of cylindrical devices. The magnetic field solutions have been provided, and the model implementation has been presented in matrix form. An example has illustrated the accuracy of the magnetic field distribution compared with finite element models employing either linear or non-linear soft-magnetic material properties. Compared to the model with the non-linear material properties, the harmonic model still provides a good approximation of the magnetic flux density, even when the structure is saturated at various positions.

To predict the electromagnetic force components in cylindrical structures based on the harmonic field model, the Maxwell stress tensor is evaluated to calculate the cogging and attraction forces. Four force components $(F_z, F_\theta, F_x, F_y)$ have been obtained without numerical integration of the magnetic fields. The main advantages of these analytical force equations are their simple form and the independency of the spatial discretization of the magnetic field in the θ- and z-direction. The presented semi-analytical model is approximately six times faster than a (linear and periodic) finite element model containing 176000 tetrahedral volume elements, and

an excellent agreement is found for all force components. Further, although the analytical model assumes linear material properties of the soft-magnetic parts of the structure, it provides a good estimation of the force components compared to the results of a finite element model with non-linear material properties.

8.1.2 Part II: Application

To evaluate this generic 3D modeling technique, part II of this thesis has focused on the analysis and realization of a novel two degrees of freedom rotary-linear actuator for an industrial robotic application. This single body direct-drive actuator should replace the cascaded single-DoF actuators for a demanding pick-and-place (P&P) application. In the linear direction a static force of 40 N, and a mover acceleration of 150 ms^{-2} with a duty cycle of 34% are required. For rotational movement the mover acceleration should be 3500 rads^{-2} with a duty cycle of 47%. Furthermore, the required position sensor resolution is 1 μm and 0.158 mrad for translation and rotation, respectively.

A classification of the different topologies has been defined and examples of each topology are provided. Electromagnetic actuators based on three different types of electromagnetic energy conversion are presented, i.e., reluctance-, induction- and permanent magnet actuators. Taking into consideration the demanding requirements, an integrated permanent magnet actuator has been deemed essential for this demanding P&P application.

A new patented magnetization concept has been presented that allows for two simple orthogonal windings to create torque and force. To achieve the specific high force and low torque, various possible realizations of the magnetization pattern have been proposed starting from the linear tubular PM actuator. The altered quasi-Halbach magnetization topology is selected based on the force/torque density, the ratio between the force and torque that can be adjusted by means of a geometric parameter, and the manufacturability. In this configuration, a normally parasitic field effect is exploited to produce torque without introducing a complex manufacturing process.

The single slotted actuator is selected, which has a slotless winding for translation enclosed by a slotted winding for rotation. The developed 3D analytical modeling technique has been used to describe the three dimensional field of this altered quasi-Halbach magnetization. Further, two 2D models, i.e. rotational and translational, have been created to approximate the torque and force. The 2D model for the rotational movement provides a very accurate approximation if the axial length of the actuator is an integer multiple of the period of the PM array. The accuracy of the translational model depends on the slot configuration of the rotational part, where in the modeled structure this introduces an error of approximately 1%.

An electromagnetic analysis has been performed to select the most suitable winding configuration for both rotation and translation. The definition of the winding factor has been extended with the link factor to account for the flux leakage in slotless stator configurations. The winding effectiveness is subsequently quantified by means of the force versus copper loss. A magnetostatic and thermal analysis have been performed to obtain the relation between geometrical parameters and mover acceleration while minimizing the copper loss. An actuator design has been obtained from the results of these analyses. The copper losses of the actuator during the required trajectory are 8.3 W and 0.8 W for translation and rotation, respectively. Successively, parasitic effects have been analyzed, i.e., cogging force/torque and electromagnetic damping. By means of two analytical models, the end-effect force and rotational slot cogging torque have been analyzed to select appropriate stator back-iron dimensions. Further, by means of transient 3D finite element analyses the performance degradation due to electromagnetic damping is estimated, i.e., 0.5 W and 0.16 W additional dissipation during the specified motion profile for translation and rotation, respectively.

The realization and measurements of the novel integrated 2-DoF actuator prototype and the assembly of the various parts have been discussed. The modeled and measured emf for translation differ approximately 1% in amplitude. For rotation, the measured value is approximately 7% higher than the modeled value due to the non-modeled overhang of the stator teeth underneath the end windings. A MIMO identification is performed to obtain the frequency response of the total positioning system. That includes the data-acquisition system, the power amplifiers, the actuator and the position sensors. The results of the system identification show that rotation and translation are physically decoupled. Two (SISO) lead-lag controllers have been designed with a bandwidth of 200 Hz and 180 Hz for translation and rotation, respectively.

The electromagnetic damping in two directions has been measured at different velocities, the linearized results are: 2.2 N at $1\,\text{ms}^{-1}$ and 4.5 mNm at 1000 rpm, respectively. In the translational direction the eddy current damping is approximately 30% higher while in the rotational direction this component is 35% lower than modeled. Furthermore, hysteresis and excess loss components have been identified, being significantly larger than expected. These damping components can be predicted accurately, however, for small displacements the compensation of this damping is not correct, and further research is required to obtain a more accurate model. The translational end-effect cogging force is found to be up to two times higher than modeled, i.e., 1.0 N instead of 0.5 N. This deviation is caused by manufacturing tolerances and the magnetic hysteresis in the stator back-iron. The rotational cogging torque due to slotting has not been identified due to its low level, i.e., approximately 0.1mNm.

To validate the actuator performance, the specified P&P trajectory has been implemented. The dissipated power during the trajectory has been measured and is

1.3 W and 12.2 W due to iron losses and copper loss, respectively. Static thermal measurements have been conducted to validate the thermal model used in the design procedure. Two aspects are verified; the relative housing temperature should not exceed the 45 °C, and the difference between the coil and the housing temperature is within 10% of the relative housing temperature. Furthermore, due to the increased convection area of the aluminum housing and additional cooling caused by the airflow of the air-bearings, the actuator temperature is 30% lower than modeled.

From the measurements is found that the actuator complies with the positioning requirements, that is:

- a mover acceleration in the axial direction of $a_z = 150\,\text{ms}^{-2}$ over a stroke of 30 mm for a duty-cycle of 34%,

- a 4 μm static translational positioning error,

- a mover acceleration in the rotational direction of $\alpha_\theta = 3500\,\text{rads}^{-2}$ for a duty-cycle of 47%,

- a 0.35 mrad static rotational positioning error.

Furthermore, the combined rotation-translation motion profile results in a continuous dissipation of 13.5 W, causing a temperature rise of the actuator of approximately $\Delta T = 30\,^\circ\text{C}$.

Overall, it can be concluded that the generic 3D modeling technique provides a viable model to analyze and dimension the patented integrated 2-DoF actuator. Further, the presented fast and position-accurate integrated actuator will enable future P&P machines to achieve a significant increase in throughput and component handling capabilities.

8.2   Recommendations

8.2.1   Harmonic modeling

- The 3D harmonic modeling technique utilizes the magnetic scalar potential to solve the Maxwell equations. Employment of this scalar potential limits the application of the method to current free problems. Using the vector potential or the reduced scalar potential, the range of electromagnetic devices that can be modeled is significantly extended.

- Chapter 2 discusses the modeling of three types of irregular soft-magnetic structures, i.e., rectangular cavities, slots in the axial direction or slots in the circumferential direction. Most structures however, posses a combination of the slots in two directions. For example, the 2-DoF actuator presented in this thesis has slots in the axial direction to accommodate the winding, whereas the finite length of the stator can be considered as a slot in the circumferential direction. An evident extension of the method would be to model the combination of these slots. A similar problem in the Cartesian coordinate system is presented in [117].

- The modeling method described in this thesis can model soft-magnetic parts of a structure by considering an infinite permeability, or by assuming a linear finite permeability. However, adjacent regions in the tangential direction need to have the same permeability. As a result, the teeth in a slotted structure are modeled with infinite permeability due to the adjacent air regions. The ability to include the finite permeability of this region would be a significant improvement, since the field distribution in the teeth can be used to estimate and model saturation.

- The magnetostatic harmonic model assumes that all regions are current free and non-conducting. Modeling the electrical conduction of the material would improve the model to be able to estimate dynamic effects due to eddy currents.

8.2.2   Two degrees of freedom actuator

- The 2-DoF actuator topology is specifically selected for the P&P application and the synthesis of Chapter 6 has led to an actuator design that meets the corresponding specifications. To apply the actuator in more applications, an investigation of the scalability of the actuator is a useful addition of the research.

- The built actuator complies with the requirements, however, a comparison with current placement head in the P&P machine is required to evaluate the profit by means of machine output and costs.

- In the P&P application, passive gravity overcompensation is a desirable feature to prevent damage during a power failure. The actuator illustrated in Figure 4.8(a) and presented in [91] by Meessen *et al.* exhibits this characteristic.

Further research is necessary to investigate possibilities to integrate the passive gravity overcompensation in the actuator presented in this thesis.

- Air-bearings are applied in the actuator to support the mover and allow for the two degrees of freedom. As mentioned in the thesis, a drawback of this type of bearing is the air consumption and the requirements on the mover tolerances. Integration of a magnetic bearing in the actuator can be a suitable alternative. A preliminary investigation of such a magnetic bearing is presented in [140].

- In the P&P application a high rotational position resolution is required. In this research, an optical encoder is selected with a grid located on the mover. As a result, the mover has become a fragile and expensive part being sensitive to contamination and damage. Other measuring techniques or sensor grid locations can be further investigated to avoid the aforementioned mover properties.

- The selected stator back-iron material results in eddy current damping and significant hysteresis effects. The application of other materials has to be investigated to reduce these effects to increase the actuator efficiency and force response.

- The stiffness of the realized mover is lower than the modeled one resulting in deflection. As a result, the airgap clearance between the mover and the stator is increased to avoid contact between the two parts. Although the actuator is still able to comply with the requirements, additional research is required to understand the effect and investigate it at higher temperatures.

- Due to deflection of the mover, the accuracy of the position sensor in the rotational direction is affected. Additional measurements are required to investigate this effect.

- The specified force resolution has not been verified. Additional measurements are necessary to validate this requirement. Furthermore, a control structure has to be created to be able to detect the impact with the printed circuit board and verify the sensorless force control.

- The electromagnetic hysteresis results in an additional velocity independent damping as measured in Chapter 7. However, for small displacement, the damping characteristic is different. Further research is required to obtain a correct model of this phenomenon and investigate the effect on the sensorless force control.

- Static thermal experiments are conducted to validate the thermal behavior of the actuator. In these experiments, the total dissipation is estimated from measurements during movement according to the required motion profile. A full dynamic thermal experiment would provide a more accurate means of the total dissipation, since, for example, the effect of temperature on the iron losses is not taken into account in the conducted experiments.

Appendices

Appendix A

Vector calculus

This appendix provides the vector identities and calculus in the cylindrical coordinate system used in the analysis of Chapter 1 and Chapter 2.

$$\vec{B} = B_r\vec{e}_r + B_z\vec{e}_z + B_z\vec{e}_z, \tag{A.1}$$

$$\nabla\cdot\vec{B} = \frac{1}{r}\frac{\partial rB_r}{\partial r} + \frac{\partial B_z}{\partial z} + \frac{\partial B_\theta}{r\partial\theta}, \tag{A.2}$$

$$\nabla\times\vec{B} = \begin{bmatrix} \dfrac{\partial B_z}{r\partial\theta} - \dfrac{\partial B_\theta}{\partial z} \\[2mm] \dfrac{\partial B_r}{\partial z} - \dfrac{\partial B_z}{\partial r} \\[2mm] \dfrac{\partial rB_\theta}{r\partial r} - \dfrac{\partial B_r}{r\partial\theta} \end{bmatrix}, \tag{A.3}$$

$$\left(\nabla\times\vec{B}\right)\times\vec{B} = \begin{bmatrix} B_z\dfrac{\partial B_r}{\partial z} - B_z\dfrac{\partial B_z}{\partial r} - B_\theta\dfrac{\partial rB_\theta}{r\partial r} + B_\theta\dfrac{\partial B_r}{\partial\theta} \\[2mm] B_r\dfrac{\partial rB_\theta}{r\partial r} - B_r\dfrac{\partial B_r}{r\partial\theta} - B_z\dfrac{\partial B_z}{r\partial\theta} + B_z\dfrac{\partial B_\theta}{\partial z} \\[2mm] B_\theta\dfrac{\partial B_z}{r\partial\theta} - B_\theta\dfrac{\partial B_\theta}{\partial z} - B_r\dfrac{\partial B_r}{\partial z} + B_r\dfrac{\partial B_z}{\partial r} \end{bmatrix}, \tag{A.4}$$

$$\mathbb{T} = \begin{bmatrix} \mathbb{T}_{rr} & \mathbb{T}_{r\theta} & \mathbb{T}_{rz} \\ \mathbb{T}_{\theta r} & \mathbb{T}_{\theta\theta} & \mathbb{T}_{\theta z} \\ \mathbb{T}_{zr} & \mathbb{T}_{z\theta} & \mathbb{T}_{zz} \end{bmatrix}, \tag{A.5}$$

$$\nabla\cdot\mathbb{T} = \begin{bmatrix} \dfrac{\partial\mathbb{T}_{rr}}{\partial r} + \dfrac{\partial\mathbb{T}_{\theta r}}{r\partial\theta} + \dfrac{\mathbb{T}_{rr} - \mathbb{T}_{\theta\theta}}{r} + \dfrac{\partial\mathbb{T}_{zr}}{\partial z} \\[2mm] \dfrac{\partial\mathbb{T}_{r\theta}}{\partial r} + \dfrac{\partial\mathbb{T}_{\theta\theta}}{r\partial\theta} + \dfrac{\mathbb{T}_{r\theta} + \mathbb{T}_{\theta r}}{r} + \dfrac{\partial\mathbb{T}_{z\theta}}{\partial z} \\[2mm] \dfrac{\partial\mathbb{T}_{rz}}{\partial r} + \dfrac{\partial\mathbb{T}_{\theta z}}{r\partial\theta} + \dfrac{\mathbb{T}_{rz}}{r} + \dfrac{\partial\mathbb{T}_{zz}}{\partial z} \end{bmatrix}, \tag{A.6}$$

$$\nabla \times (\nabla \times \vec{A}) = \nabla \left(\nabla \cdot \vec{A} \right) - \nabla^2 \vec{A}, \tag{A.7}$$

$$\nabla^2 \varphi = \frac{1}{r} \frac{\partial}{\partial r} \left(r \frac{\partial \varphi}{\partial r} \right) + \frac{1}{r^2} \frac{\partial^2 \varphi}{\partial \theta^2} + \frac{\partial^2 \varphi}{\partial z^2}. \tag{A.8}$$

Appendix B

Modeling functions

B.1 Correlation functions

To solve boundary conditions between two regions with a magnetic field description based on different Fourier series, correlation functions are introduced in Section 2.7. The solutions of these functions are provided in this appendix.

$$\varsigma_s(v, n^q, n^p) = \lambda \frac{n^q \tau_v^p \tau_v^q \left[\cos\left(w^p \Delta_v\right) - \cos\left(n^q \pi\right) \cos\left(w^p \left(\Delta_v + \tau_v^q\right)\right) \right]}{\pi \left(\left(n^q \tau_v^p\right)^2 - \left(n^p \tau_v^q\right)^2 \right)} \qquad \text{for } n^p > 0, n^q > 0, \quad \text{(B.1)}$$

$$= -\lambda \frac{\sin\left(w^q \Delta_v\right) \tau_v^q}{2\tau_v^p} \qquad \text{for } n^p \tau_v^q = n^q \tau_v^p, \quad \text{(B.2)}$$

$$= \lambda \frac{\sin^2\left(\frac{n^q \pi}{2}\right)}{w^q \tau_v^p} \qquad \text{for } n^p = 0, n^q > 0, \quad \text{(B.3)}$$

$$\varsigma_c(v, n^q, n^p) = \lambda \frac{n^p \left(\tau_v^q\right)^2 \left[\sin\left(w^p \Delta_v\right) - \cos\left(n^q \pi\right) \sin\left(w^p \left(\Delta_v + \tau_v^q\right)\right) \right]}{\pi \left(\left(n^q \tau_v^p\right)^2 - \left(n^p \tau_v^q\right)^2 \right)} \qquad \text{for } n^p > 0, n^q > 0, \quad \text{(B.4)}$$

$$= \lambda \frac{\cos\left(w^q \Delta_v\right) \tau_v^q}{2\tau_v^p} \qquad \text{for } n^p \tau_v^q = n^q \tau_v^p, \quad \text{(B.5)}$$

$$= 0 \qquad \text{for } n^p = 0, n^q > 0, \quad \text{(B.6)}$$

$$\kappa_s(v, n^q, n^p) = \frac{n^q \tau_v^p}{n^p \tau_v^q} \varsigma_c(v, n^p, n^q) \qquad \text{for } n^p > 0, n^q > 0, \quad \text{(B.7)}$$

$$= \varsigma_c(v, n^p, n^q) \qquad \text{for } n^p \tau_v^q = n^q \tau_v^p, \quad \text{(B.8)}$$

$$= 0 \qquad \text{for } n^p = 0, n^q > 0, \quad \text{(B.9)}$$

$$\kappa_c(\nu, n^q, n^p) = -\frac{n^p \tau_\nu^q}{n^q \tau_\nu^p} \varsigma_s(\nu, n^p, n^q) \qquad\qquad \text{for } n^p > 0, n^q > 0, \quad \text{(B.10)}$$

$$= -\varsigma_s(\nu, n^p, n^q) \qquad\qquad \text{for } n^p \tau_\nu^q = n^q \tau_\nu^p, \quad \text{(B.11)}$$

$$= 0 \qquad\qquad \text{for } n^p = 0, n^q > 0, \quad \text{(B.12)}$$

$$\varepsilon_s(\nu, n^p, n^q) = \frac{2 n^q \left(\tau_\nu^p\right)^2 \left[\sin\left(w^p \Delta_\nu\right) - \cos\left(n^q \pi\right) \sin\left(w^p \left(\Delta_\nu + \tau_\nu^q\right)\right) \right]}{\pi \left(\left(n^q \tau_\nu^p\right)^2 - \left(n^p \tau_\nu^q\right)^2\right)} \qquad \text{for } n^p > 0, n^q > 0, \quad \text{(B.13)}$$

$$= \cos\left(w^q \Delta_\nu\right) \qquad\qquad \text{for } n^p \tau_\nu^q = n^q \tau_\nu^p, \quad \text{(B.14)}$$

$$= 0 \qquad\qquad \text{for } n^p = 0, n^q > 0, \quad \text{(B.15)}$$

$$\varepsilon_c(\nu, n^p, n^q) = \frac{2 n^q \left(\tau_\nu^p\right)^2 \left[\cos\left(w^p \Delta_\nu\right) - \cos\left(n^q \pi\right) \cos\left(w^p \left(\Delta_\nu + \tau_\nu^q\right)\right) \right]}{\pi \left(\left(n^q \tau_\nu^p\right)^2 - \left(n^p \tau_\nu^q\right)^2\right)} \qquad \text{for } n^p > 0, n^q > 0, \quad \text{(B.16)}$$

$$= \sin\left(w^q \Delta_\nu\right) \qquad\qquad \text{for } n^p \tau_\nu^q = n^q \tau_\nu^p, \quad \text{(B.17)}$$

$$= \frac{2 - 2\cos(n^q \pi)}{\pi n^q} \qquad\qquad \text{for } n^p = 0, n^q > 0, \quad \text{(B.18)}$$

where

$$w^p = \frac{n^p \pi}{\tau^p}, \tag{B.19}$$

$$w^q = \frac{n^q \pi}{\tau^q}, \tag{B.20}$$

and

$$\Delta_\nu = \Delta_\nu^q - \Delta_\nu^p. \tag{B.21}$$

Furthermore

$$\lambda = \begin{cases} 1 \text{ if region } p \text{ has periodic boundaries in the tangential direction,} \\ 2 \text{ if region } p \text{ has soft-magnetic boundaries in the tangential direction.} \end{cases} \tag{B.22}$$

B.2 Source functions

The non-homogeneous solution for the differential equation containing the magnetization is defined by

$$
\mathcal{G}^{\mathrm{x}}_{\varphi 1}(r,k,n) = \frac{B_{\mathrm{rem}}}{\mu_0 \mu_{\mathrm{r}}} \left[\left(-m_k M_{rss} + w_n m_k M_{\theta cs} \right) \mathcal{F}_1(r,k,n) + m_k^2 M_{zsc} \mathcal{F}_2(r,k,n) \right], \tag{B.23}
$$

$$
\mathcal{G}^{\mathrm{x}}_{\varphi 2}(r,k,n) = \frac{B_{\mathrm{rem}}}{\mu_0 \mu_{\mathrm{r}}} \left[\left(-m_k M_{rsc} + w_n m_k M_{\theta cc} \right) \mathcal{F}_1(r,k,n) - m_k^2 M_{zss} \mathcal{F}_2(r,k,n) \right], \tag{B.24}
$$

$$
\mathcal{G}^{\mathrm{x}}_{\varphi 3}(r,k,n) = \frac{B_{\mathrm{rem}}}{\mu_0 \mu_{\mathrm{r}}} \left[\left(-m_k M_{rcs} - w_n m_k M_{\theta ss} \right) \mathcal{F}_1(r,k,n) + m_k^2 M_{zcc} \mathcal{F}_2(r,k,n) \right], \tag{B.25}
$$

$$
\mathcal{G}^{\mathrm{x}}_{\varphi 4}(r,k,n) = \frac{B_{\mathrm{rem}}}{\mu_0 \mu_{\mathrm{r}}} \left[\left(-m_k M_{rcc} - w_n m_k M_{\theta sc} \right) \mathcal{F}_1(r,k,n) - m_k^2 M_{zcs} \mathcal{F}_2(r,k,n) \right], \tag{B.26}
$$

$$
\mathcal{G}^{\mathrm{x}}_{\varphi 5}(r,n) = \frac{B_{\mathrm{rem}}}{\mu_0 \mu_{\mathrm{r}}} \left[\left(-w_n M_{rs} + w_n^2 M_{\theta c} \right) \frac{r}{w_n^2 - 1} \right] \qquad \text{for } w_n \neq 1, \tag{B.27}
$$

$$
= \frac{B_{\mathrm{rem}}}{2\mu_0 \mu_{\mathrm{r}}} \left[\left(M_{rs} - M_{\theta c} \right) (r + r \ln(r)) \right] \qquad \text{for } w_n = 1, \tag{B.28}
$$

$$
\mathcal{G}^{\mathrm{x}}_{\varphi 6}(r,n) = \frac{B_{\mathrm{rem}}}{\mu_0 \mu_{\mathrm{r}}} \left[\left(-w_n M_{rc} - w_n^2 M_{\theta s} \right) \frac{r}{w_n^2 - 1} \right] \qquad \text{for } w_n \neq 1, \tag{B.29}
$$

$$
= \frac{B_{\mathrm{rem}}}{2\mu_0 \mu_{\mathrm{r}}} \left[\left(M_{rc} + M_{\theta s} \right) (r + r \ln(r)) \right] \qquad \text{for } w_n = 1, \tag{B.30}
$$

$$
\mathcal{G}^{\mathrm{x}}_{\varphi 7}(r) = \frac{B_{\mathrm{rem}}}{\mu_0 \mu_{\mathrm{r}}} M_{r0} r, \tag{B.31}
$$

$$
\mathcal{G}^{\mathrm{x}}_{r 1}(r,k,n) = \frac{B_{\mathrm{rem}}}{\mu_0 \mu_{\mathrm{r}}} \left[\left(-m_k M_{rss} + w_n m_k M_{\theta cs} \right) \mathcal{F}_3(r,k,n) + m_k^2 M_{zsc} \mathcal{F}_4(r,k,n) \right], \tag{B.32}
$$

$$
\mathcal{G}^{\mathrm{x}}_{r 2}(r,k,n) = \frac{B_{\mathrm{rem}}}{\mu_0 \mu_{\mathrm{r}}} \left[\left(-m_k M_{rsc} + w_n m_k M_{\theta cc} \right) \mathcal{F}_3(r,k,n) - m_k^2 M_{zss} \mathcal{F}_4(r,k,n) \right], \tag{B.33}
$$

$$
\mathcal{G}^{\mathrm{x}}_{r 3}(r,k,n) = \frac{B_{\mathrm{rem}}}{\mu_0 \mu_{\mathrm{r}}} \left[\left(-m_k M_{rcs} - w_n m_k M_{\theta ss} \right) \mathcal{F}_3(r,k,n) + m_k^2 M_{zcc} \mathcal{F}_4(r,k,n) \right], \tag{B.34}
$$

$$
\mathcal{G}^{\mathrm{x}}_{r 4}(r,k,n) = \frac{B_{\mathrm{rem}}}{\mu_0 \mu_{\mathrm{r}}} \left[\left(-m_k M_{rcc} - w_n m_k M_{\theta sc} \right) \mathcal{F}_3(r,k,n) - m_k^2 M_{zcs} \mathcal{F}_4(r,k,n) \right], \tag{B.35}
$$

$$
\mathcal{G}^{\mathrm{x}}_{r 5}(r,n) = \frac{B_{\mathrm{rem}}}{\mu_0 \mu_{\mathrm{r}}} \left[\left(-M_{rs} + w_n M_{\theta c} \right) \frac{1}{w_n^2 - 1} \right] \qquad \text{for } w_n \neq 1, \tag{B.36}
$$

$$
= \frac{B_{\mathrm{rem}}}{2\mu_0 \mu_{\mathrm{r}}} \left[\left(M_{rs} - M_{\theta c} \right) (2 + \ln(r)) \right] \qquad \text{for } w_n = 1, \tag{B.37}
$$

$$
\mathcal{G}^{\mathrm{x}}_{r 6}(r,n) = \frac{B_{\mathrm{rem}}}{\mu_0 \mu_{\mathrm{r}}} \left[\left(-M_{rc} - w_n M_{\theta s} \right) \frac{1}{w_n^2 - 1} \right] \qquad \text{for } w_n \neq 1, \tag{B.38}
$$

$$
= \frac{B_{\mathrm{rem}}}{2\mu_0 \mu_{\mathrm{r}}} \left[\left(M_{rc} + M_{\theta s} \right) (2 + \ln(r)) \right] \qquad \text{for } w_n = 1, \tag{B.39}
$$

$$
\mathcal{G}^{\mathrm{x}}_{r 7} = \frac{B_{\mathrm{rem}}}{\mu_0 \mu_{\mathrm{r}}} M_{r0}, \tag{B.40}
$$

$$\mathcal{G}^{\mathrm{x}}_{\theta 1}(r, k, n) = \mathcal{G}^{\mathrm{x}}_{z1}(r, k, n) = \mathcal{G}^{\mathrm{x}}_{\varphi 1}(r, k, n), \tag{B.41}$$

$$\mathcal{G}^{\mathrm{x}}_{\theta 2}(r, k, n) = \mathcal{G}^{\mathrm{x}}_{z2}(r, k, n) = \mathcal{G}^{\mathrm{x}}_{\varphi 2}(r, k, n), \tag{B.42}$$

$$\mathcal{G}^{\mathrm{x}}_{\theta 3}(r, k, n) = \mathcal{G}^{\mathrm{x}}_{z3}(r, k, n) = \mathcal{G}^{\mathrm{x}}_{\varphi 3}(r, k, n), \tag{B.43}$$

$$\mathcal{G}^{\mathrm{x}}_{\theta 4}(r, k, n) = \mathcal{G}^{\mathrm{x}}_{z4}(r, k, n) = \mathcal{G}^{\mathrm{x}}_{\varphi 4}(r, k, n), \tag{B.44}$$

$$\mathcal{G}^{\mathrm{x}}_{\theta 5}(r, n) = w_n \mathcal{G}^{\mathrm{x}}_{r5}(r, n), \tag{B.45}$$

$$\mathcal{G}^{\mathrm{x}}_{\theta 6}(r, n) = w_n \mathcal{G}^{\mathrm{x}}_{r6}(r, n). \tag{B.46}$$

Within these functions, $\mathcal{F}$, is an integral without an analytical solution defined as

$$\mathcal{F}_1(r, k, n) = \mathcal{I}_{w_n}\left(m_k r\right) \int_{r_0}^{r} \mathcal{K}_{w_n}\left(m_k v\right) \mathrm{d}v - \mathcal{K}_{w_n}\left(m_k r\right) \int_{r_0}^{r} \mathcal{I}_{w_n}\left(m_k v\right) \mathrm{d}v, \tag{B.47}$$

$$\mathcal{F}_2(r, k, n) = \mathcal{I}_{w_n}\left(m_k r\right) \int_{r_0}^{r_1} v\mathcal{K}_{w_n}\left(m_k v\right) \mathrm{d}v - \mathcal{K}_{w_n}\left(m_k r\right) \int_{r_0}^{r} v\mathcal{I}_{w_n}\left(m_k v\right) \mathrm{d}v, \tag{B.48}$$

$$\mathcal{F}_3(r, k, n) = \left(\mathcal{I}_{w_n-1}\left(m_k r\right) + \mathcal{I}_{w_n+1}\left(m_k r\right)\right) \int_{r_0}^{r} \mathcal{K}_{w_n}\left(m_k v\right) \mathrm{d}v$$
$$+ \left(\mathcal{K}_{w_n-1}\left(m_k r\right) + \mathcal{K}_{w_n+1}\left(m_k r\right)\right) \int_{r_0}^{r} \mathcal{I}_{w_n}\left(m_k v\right) \mathrm{d}v, \tag{B.49}$$

$$\mathcal{F}_4(r, k, n) = \left(\mathcal{I}_{w_n-1}\left(m_k r\right) + \mathcal{I}_{w_n+1}\left(m_k r\right)\right) \int_{r_0}^{r} v\mathcal{K}_{w_n}\left(m_k v\right) \mathrm{d}v$$
$$+ \left(\mathcal{K}_{w_n-1}\left(m_k r\right) + \mathcal{K}_{w_n+1}\left(m_k r\right)\right) \int_{r_0}^{r} v\mathcal{I}_{w_n}\left(m_k v\right) \mathrm{d}v, \tag{B.50}$$

where r_0 is the inner radius of the region.

B.3 Implementation

To implement the equations obtained by applying the boundary conditions, the set of equations is rewritten in matrix form which results in a single linear matrix equation to be solved, given by

$$\mathbf{EX} = \mathbf{Y}, \tag{B.51}$$

where $\mathbf{E}$ contains all known coefficients within the equation, $\mathbf{X}$ contains all unknown coefficients in the equation and $\mathbf{Y}$ contains the functions describing sources within the equations.

All equations contain infinite summations of Fourier series, hence, the problem consists of an infinite set of equations and an infinite number of unknown coefficients. To be able to implement the problem and solve the equations numerically, the infinite summation is replaced by a summation over N, K, J or L, dependent on the considered harmonic number n, k, j or l. Furthermore, the equations are rewritten such that each equation consists solely of summations for harmonic numbers starting at one, i.e.,

$$
\begin{aligned}
H_r^x(r,\theta,z) = &\sum_{k=1}^{\infty}\sum_{n=1}^{\infty} \mathcal{R}_1^x(r,k,n)\sin(w_n\theta)\sin(m_k z) + \mathcal{R}_2^x(r,k,n)\sin(w_n\theta)\cos(m_k z) \\
&+ \sum_{k=1}^{\infty}\sum_{n=0}^{\infty} \mathcal{R}_3^x(r,k,n)\cos(w_n\theta)\sin(m_k z) + \mathcal{R}_4^x(r,k,n)\cos(w_n\theta)\cos(m_k z) \\
&- \sum_{n=1}^{\infty} \mathcal{R}_5^x(r,n)\sin(w_n\theta) - \mathcal{R}_6^x(r,n)\cos(w_n\theta),
\end{aligned} \tag{B.52}
$$

is for the implementation rewritten to

$$
\begin{aligned}
H_r^x(r,\theta,z) = &\sum_{k=1}^{K}\sum_{n=1}^{N} \mathcal{R}_1^x(r,k,n)\sin(w_n\theta)\sin(m_k z) + \mathcal{R}_2^x(r,k,n)\sin(w_n\theta)\cos(m_k z) \\
&+ \sum_{k=1}^{K}\sum_{n=1}^{N} \mathcal{R}_3^x(r,k,n)\cos(w_n\theta)\sin(m_k z) + \mathcal{R}_4^x(r,k,n)\cos(w_n\theta)\cos(m_k z) \\
&+ \sum_{k=1}^{K} \mathcal{R}_3^x(r,k,0)\sin(m_k z) + \mathcal{R}_4^x(r,k,0)\cos(m_k z) \\
&- \sum_{n=1}^{N} \mathcal{R}_5^x(r,n)\sin(w_n\theta) - \mathcal{R}_6^x(r,n)\cos(w_n\theta).
\end{aligned} \tag{B.53}
$$

The same holds for the other components of the magnetic field strength and the magnetization. Consequently, all coefficients of the magnetic field within one region, consist of $\{N \times K\}, \{N \times L\}, \{J \times K\}, \{J \times L\}, N, J, K$ or L unknowns. To write the imple-

mentation in a compact manner, the following definition for the harmonics is used

$$n = 0, 1, 2, 3 \ldots N \qquad \text{harmonics in } \theta\text{-direction in region } p \qquad (B.54)$$

$$j = 1, 2, 3 \ldots J \qquad \text{harmonics in } \theta\text{-direction in region } q \qquad (B.55)$$

$$k = 0, 1, 2, 3 \ldots K \qquad \text{harmonics in } z\text{-direction in region } p \qquad (B.56)$$

$$l = 1, 2, 3 \ldots L \qquad \text{harmonics in } z\text{-direction in region } q \qquad (B.57)$$

The solution of the magnetic scalar potential for the r-dependency, e.g. $\mathcal{R}^x(r, k, n)$, consists of three parts

$$\mathcal{R}^x(r, k, n) = \begin{cases} c_6 & \text{for } n = 0, \, k = 0 \\ c_5 r^{w_n} + c_6 r^{-w_n} & \text{for } n > 0, \, k = 0 \\ c_5 \mathcal{I}_{w_n}(m_k r) + c_6 \mathcal{K}_{w_n}(m_k r) & \text{for } n \geq 0, \, k > 0, \end{cases} \qquad (B.58)$$

where c_5 and c_6 are the unknown coefficients and $r^{w_n}, r^{-w_n}, \mathcal{I}_{w_n}(m_k r)$ and $\mathcal{K}_{w_n}(m_k r)$ represent numerical values dependent on the radius. The unknown coefficients are included in $\mathbf{X}$ in (B.51) and are written as a vector. Consider a region with unknown coefficients $c^x(k, n)$, consequently, the resulting vector is defined by

$$\mathbf{c^x} = \begin{cases} [c^x(1,1), \cdots, c^x(1, N^x), , \cdots, c^x(K^x, 1), \cdots, c^x(K^x, N^x)], & \text{for } k \geq 1, n \geq 1, \\ [c^x(0,1), \cdots, c^x(0, N^x)], & \text{for } k = 0, n \geq 1, \\ [c^x(1,0), \cdots, c^x(K^x, 0)], & \text{for } k \geq 1, n = 0. \end{cases} \qquad (B.59)$$

The vector $\mathbf{X}$ is the transposed vector of a concatenation of all unknown coefficients in all regions

$$\mathbf{X} = \left[\mathbf{c_1^x}, \mathbf{c_2^x} \cdots\right]^{\mathrm{T}}. \qquad (B.60)$$

The known coefficients, $\mathcal{C}(k, n)(r)$ representing the numerical values dependent on the radius are included in $\mathbf{E}$ in (B.51) and are written in a diagonal matrix

$$\mathcal{C} = \begin{bmatrix} \mathcal{C}(1,1) \cdots & 0 & \cdots & 0 & \cdots & 0 \\ \vdots & \ddots & \vdots & \ddots & \vdots & \ddots & \vdots \\ 0 & \cdots \mathcal{C}(1,N) \cdots & 0 & \cdots & 0 \\ \vdots & \ddots & \vdots & \ddots & \vdots & \ddots & \vdots \\ 0 & \cdots & 0 & \cdots \mathcal{C}(K,1) \cdots & 0 \\ \vdots & \ddots & \vdots & \ddots & \vdots & \ddots & \vdots \\ 0 & \cdots & 0 & \cdots & 0 & \cdots \mathcal{C}(K,N) \end{bmatrix}, \qquad \text{for } k \geq 1, n \geq 1, \tag{B.61}$$

$$\mathcal{C} = \begin{bmatrix} \mathcal{C}(0,1) \cdots & 0 \\ \vdots & \ddots & \vdots \\ 0 & \cdots \mathcal{C}(0,N) \end{bmatrix}, \qquad \text{for } k = 0, n \geq 1, \tag{B.62}$$

$$\mathcal{C} = \begin{bmatrix} \mathcal{C}(1,0) \cdots & 0 \\ \vdots & \ddots & \vdots \\ 0 & \cdots \mathcal{C}(K,0) \end{bmatrix}, \qquad \text{for } k \geq 1, n = 0, \tag{B.63}$$

Correlation functions for v is θ

Consider the following equation

$$c^p(k,n) = \sum_{l=1}^{L}\sum_{j=1}^{J} \varsigma_c(\theta,j,n)\varsigma_s(z,l,k)c^q(l,j) \qquad \text{for } k \geq 0, n \geq 0. \qquad \text{(B.64)}$$

As mentioned before, the equations are implemented as summations over harmonics starting at one. Therefore, equation (B.64) has to be split in three equations

$$c^p(k,n) = \sum_{l=1}^{L}\sum_{j=1}^{J} \varsigma_c(\theta,j,n)\varsigma_s(z,l,k)c^q(l,j) \qquad \text{for } k \geq 1, n \geq 1, \qquad \text{(B.65)}$$

$$c^p(0,n) = \sum_{l=1}^{L}\sum_{j=1}^{J} \varsigma_c(\theta,j,n)\varsigma_s(z,l,0)c^q(l,j) \qquad \text{for } k = 0, n \geq 1, \qquad \text{(B.66)}$$

$$c^p(k,0) = \sum_{l=1}^{L}\sum_{j=1}^{J} \varsigma_c(\theta,j,0)\varsigma_s(z,l,k)c^q(l,j) \qquad \text{for } k \geq 1, n = 0, \qquad \text{(B.67)}$$

To write this equation as a matrix multiplication, $\varsigma_c(\theta,j,n)$ is written as a matrix $\boldsymbol{\varsigma}_{c,\theta}$ defined by

$$\boldsymbol{\varsigma}_{c,\theta} = \begin{bmatrix} \begin{bmatrix} \varsigma_c(1,1),\cdots,\varsigma_c(J,1) \\ \varsigma_c(1,2),\cdots,\varsigma_c(J,2) \\ \vdots \\ \varsigma_c(1,N),\cdots,\varsigma_c(J,N) \end{bmatrix} \cdots & & \mathbf{0} \\ \vdots & \ddots & \vdots \\ \mathbf{0} & \cdots & \begin{bmatrix} \varsigma_c(1,1),\cdots,\varsigma_c(J,1) \\ \varsigma_c(1,2),\cdots,\varsigma_c(J,2) \\ \vdots \\ \varsigma_c(1,N),\cdots,\varsigma_c(J,N) \end{bmatrix} \end{bmatrix}. \qquad \text{(B.68)}$$

The matrix $\boldsymbol{\varsigma}_{c,\theta}$ has dimensions $\{KN \times KJ\}$ to implement (B.65) hence the matrix contains K times the matrix at the top left-hand-side on the diagonal. In equation (B.65), $k = 0$ which can be interpreted as $K = 1$, therefore the matrix $\boldsymbol{\varsigma}_{c,\theta}$ should have size $\{N \times J\}$ and contains solely the top left-hand-side matrix as given in (B.68). To implement (B.67), (B.68) can be used, except that $n = 0$, and consequently $N = 1$. Hence, the resulting matrix has dimensions $\{K \times KJ\}$. The matrices $\boldsymbol{\varsigma}_{s,\theta}$, $\boldsymbol{\kappa}_{c,\theta}$ and $\boldsymbol{\kappa}_{s,\theta}$ have to be created in the same manner.

Consider the following equation

$$c^q(l,j) = \sum_{k=0}^{K}\sum_{n=0}^{N} \varepsilon_s(z,k,l)\varepsilon_c(\theta,n,j)c^p(k,n) \qquad \text{for } k \geq 1, l \geq 1, \qquad \text{(B.69)}$$

which has to be rewritten according to the implementation of solely summations starting at one

$$c^q(l,j) = \sum_{k=1}^{K}\sum_{n=1}^{N}\varepsilon_s(z,k,l)\varepsilon_c^a(\theta,n,j)c^p(k,n) + \sum_{k=1}^{K}\varepsilon_s(z,k,l)\varepsilon_c^b(\theta,0,j)c^p(k,0)$$
$$+ \sum_{n=1}^{N}\varepsilon_s(z,0,l)\varepsilon_c^c(\theta,n,j)c^p(0,n). \quad \text{(B.70)}$$

To write this equation as a matrix multiplication, $\varepsilon_c(\theta,j,n)$ is written as a matrix $\boldsymbol{\varepsilon}_{c,\theta}$ defined by

$$\boldsymbol{\varepsilon}_{c,\theta} = \begin{bmatrix} \begin{bmatrix} \varepsilon_c(1,1),\cdots,\varepsilon_c(N,1) \\ \varepsilon_c(1,2),\cdots,\varepsilon_c(N,2) \\ \vdots \\ \varepsilon_c(1,J),\cdots,\varepsilon_c(N,J) \end{bmatrix} & \cdots & \mathbf{0} \\ \vdots & \ddots & \vdots \\ \mathbf{0} & \cdots & \begin{bmatrix} \varepsilon_c(1,1),\cdots,\varepsilon_c(N,1) \\ \varepsilon_c(1,2),\cdots,\varepsilon_c(N,2) \\ \vdots \\ \varepsilon_c(1,J),\cdots,\varepsilon_c(N,J) \end{bmatrix} \end{bmatrix}. \quad \text{(B.71)}$$

The matrix $\boldsymbol{\varepsilon}_{c,\theta}$ has dimensions $\{KJ \times KN\}$ to implement $\varepsilon_c^a(\theta,j,n)$ in (B.70). To implement $\varepsilon_c^b(\theta,j,n)$, $n = 0$ and hence $N = 1$ which results in a matrix $\boldsymbol{\varepsilon}_{c,\theta}$ having size $\{KJ \times K\}$. The last term in (B.70) contains only a summation over n, hence $k = 0$ and $K = 1$. Therefore, to implement $\varepsilon_c^c(\theta,j,n)$, the dimensions of $\boldsymbol{\varepsilon}_{c,\theta}$ has to be $\{J \times N\}$ The matrix $\boldsymbol{\varepsilon}_{s,\theta}$ has to be created in the same manner.

Correlation functions for v is z

Consider the equation as given in (B.65)-(B.67). To write this equation as a matrix multiplication, $\varsigma_s(z, l, k)$ is written as a matrix $\boldsymbol{\varsigma}_{s,z}$ defined as

$$
\boldsymbol{\varsigma}_{s,z} = \begin{bmatrix}
\left[\varsigma_s(1,1)\mathbf{I_{JJ}}\right] \left[\varsigma_s(2,1)\mathbf{I_{JJ}}\right] \cdots \left[\varsigma_s(L,1)\mathbf{I_{JJ}}\right] \\
\left[\varsigma_s(1,2)\mathbf{I_{JJ}}\right] \left[\varsigma_s(2,2)\mathbf{I_{JJ}}\right] \cdots \left[\varsigma_s(L,2)\mathbf{I_{JJ}}\right] \\
\vdots \qquad\qquad \vdots \qquad \ddots \qquad \vdots \\
\left[\varsigma_s(1,K)\mathbf{I_{JJ}}\right] \left[\varsigma_s(2,K)\mathbf{I_{JJ}}\right] \cdots \left[\varsigma_s(L,K)\mathbf{I_{JJ}}\right]
\end{bmatrix} .
\tag{B.72}
$$

The resulting matrix $\boldsymbol{\varsigma}_{s,z}$ has dimension $\{KJ \times LJ\}$ to implement (B.65). For the implementation of (B.66), $\boldsymbol{\varsigma}_{s,z}$ has dimension $\{J \times LJ\}$. Equation (B.67) has to be implemented with $\boldsymbol{\varsigma}_{s,z}$ having dimensions $\{K \times L\}$. The matrices $\boldsymbol{\varsigma}_{c,z}$, $\boldsymbol{\kappa}_{c,z}$ and $\boldsymbol{\kappa}_{s,z}$ have to be created in the same manner.

Consider the equation (B.69). To solve this equation, $\varepsilon_s(z, k, l)$ has to be written as a matrix $\boldsymbol{\varepsilon}_{s,z}$, using the same transformation except that the indices are switched.

$$
\boldsymbol{\varepsilon}_{s,z} = \begin{bmatrix}
\left[\varepsilon_s(1,1)\mathbf{I_{JJ}}\right] \left[\varepsilon_s(2,1)\mathbf{I_{JJ}}\right] \cdots \left[\varepsilon_s(K,1)\mathbf{I_{JJ}}\right] \\
\left[\varepsilon_s(1,2)\mathbf{I_{JJ}}\right] \left[\varepsilon_s(2,2)\mathbf{I_{JJ}}\right] \cdots \left[\varepsilon_s(K,2)\mathbf{I_{JJ}}\right] \\
\vdots \qquad\qquad \vdots \qquad \ddots \qquad \vdots \\
\left[\varepsilon_s(1,L)\mathbf{I_{JJ}}\right] \left[\varepsilon_s(2,L)\mathbf{I_{JJ}}\right] \cdots \left[\varepsilon_s(K,L)\mathbf{I_{JJ}}\right]
\end{bmatrix} .
\tag{B.73}
$$

The matrix $\boldsymbol{\varepsilon}_{s,z}$ has dimensions $\{LJ \times KJ\}$ to implement $\varepsilon_c^a(\theta, j, n)$ and $\varepsilon_c^b(\theta, j, n)$. To implement $\varepsilon_c^c(\theta, j, n)$, $\boldsymbol{\varepsilon}_{s,z}$ has dimensions $\{LJ \times J\}$.

Note that when $\tau_\theta^p = \tau_\theta^q$, (B.64) does not contain a correlation function for θ. To simplify the analysis, the same harmonics in region p and region q can be selected in the θ-direction, i.e. $j = n$. Consequently, the identity matrix $\mathbf{I_{JJ}}$ in (B.72) and (B.73) is replaced by $\mathbf{I_{NN}}$ with dimensions $N \times N$.

Material properties

C.1 Permanent magnet
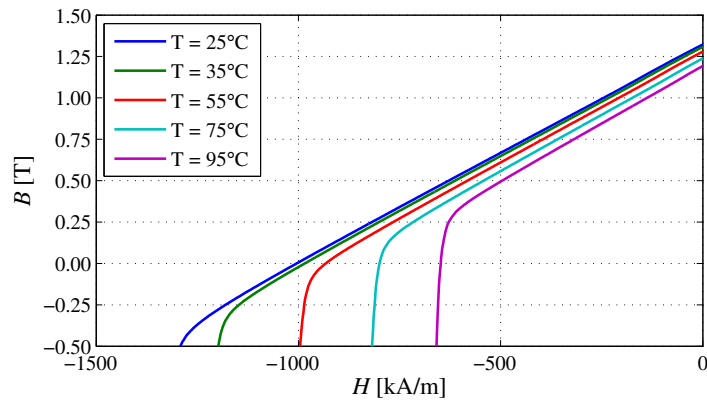
Figure C.1: Measured demagnetization curve of permanent magnet material *N45H* at different temperatures (measured using Brockhaus Hystograph).

Table C.1: Permanent magnet N45H material properties.

Parameter		Value	Description
B_{rem} @ $T = 20°\mathrm{C}$	[T]	1.34	Remanent flux density
μ_{r} @ $T = 20°\mathrm{C}$	[-]	1.05	Relative permeability
α_{rem}	[‰K^{-1}]	1.7	Temperature dependency of B_{rem}
α_{coer}	[‰K^{-1}]	2.7	Temperature dependency of H_{cb}

C.2   Soft-magnetic back-iron
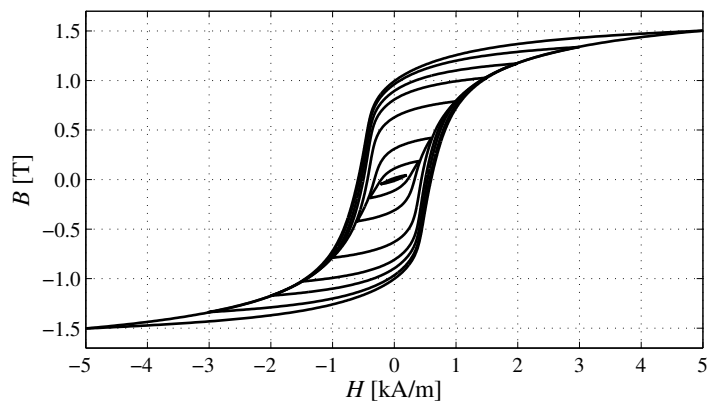
Figure C.2: BH hysteresis curves of steel *S235*, measured on a ring sample by means of DC-excitation (measured using Brockhaus Hystograph).

Table C.2: Properties of the steel *S235* sample.

Parameter		Value	Description
R_i	[mm]	20.0	Ring inner radius
R_i	[mm]	22.5	Ring outer radius
h	[mm]	5.0	Ring height
ρ	[kgm^{-3}]	7736	Mass density of steel *S235*

Experimental setup auxiliaries

To conduct measurements on the realized prototype, additional equipment is being used presented in this appendix.

D.1 Position sensor

The diameter of mover at the position of the grid is 12.681 mm, and it contains 996 lines per revolution. As such, the pitch of the grid is $\frac{12.681\cdot\pi}{996} = 39.998\,\mu$m. The analogue quadrature signal is interpolated by a factor 40 resulting in a sensor resolution of 1 μm and 0.158 mrad for translation and rotation, respectively.

D.2 Power amplifier

Each phase of the actuator is excited by means of a single axis PWM driven converter with a filtered output. Two power amplifiers each containing three individual axes are used. The specifications of the power amplifier are listed in Table D.1.

D.3 Data acquisition and control system

An *xPC target* data acquisition and control system is used for the measurements and control of the prototype. The power amplifiers are connected by means of a serial RS485 5.5 Mbits[-1] connection. The analogue encoder signals are interpolated with a Renishaw interface and digitally processed by the xPC system.

Table D.1: Power amplifier specification *(PADC 3ax)*.

Parameter		Value	Description
$\hat{I}_{\mathrm{rms}}$	[A]	2.0	Maximum continuous current
$\hat{I}_{\mathrm{peak}}$	[A]	6.0	Maximum peak current
$\hat{U}$	[V]	52.0	Maximum output voltage
$f_{\mathrm{BW},z}$	[kHz]	10.6	Bandwidth of amplifier for translation
$f_{\mathrm{BW},\theta}$	[kHz]	4.8	Bandwidth of amplifier for rotation

Nomenclature

Symbols

Symbol	Unit	Description	Chapter
$\vec{A}$	[Wb/m]	Magnetic vector potential	1
A	[m^2]	Area	5,6
a	[$\star$]	Fourier coefficient	2,3
a_z	[ms^{-2}]	Acceleration in z-direction	4,6,7
$\vec{B}$	[T]	Magnetic flux density vector	1-3,5,6
B_{rem}	[T]	Remanent flux density	1-3,5
b	[$\star$]	Fourier coefficient	2,3
C	[m]	Closed contour	1
C_{fb}	[$\star$]	Feed-back controller	7
C_{ff}	[$\star$]	Feed-forward controller	7
c	[$\star$]	Fourier coefficient	2,3
$\vec{D}$	[Cm^{-2}]	Electric flux density vector	1
d	[$\star$]	Damping constant	6,7
$\vec{E}$	[Vm^{-1}]	Electric field strength vector	1
$\vec{e}$	[$-$]	Unit vector	3
e	[$\star$]	Position error	4,7
$\vec{F}$	[N]	Force vector	1,3-7
f	[Nm^{-3}]	Force density	1,3
f	[$-$]	Function	2
f	[Hz]	Frequency	7
G	[$-$]	Function	1
G	[$\star$]	Plant	7
$\mathcal{G}$	[$\star$]	Non-homogeneous solution of the Laplace equation	2,3
$\vec{H}$	[Am^{-1}]	Magnetic field strength vector	1-3,5
H_{cb}	[Am^{-1}]	Coercivity	6
h	[m]	Height	1,5,6
h_{conv}	[Wm^{-2}K^{-1}]	Convection coefficient	6
h_{rad}	[Wm^{-2}K^{-1}]	Equivalent radiation coefficient	6
I	[kgm^2]	Moment of inertia	4,6
$\mathbf{I}$	[$-$]	Identity matrix	7

Symbol	Unit	Description	Chapter
i	$[-]$	Index or vector component	1,2
i	$[\mathrm{A}]$	Instantaneous current	5,6,7
$\mathcal{I}_o$	$[-]$	Modified Bessel function of the first kind of order o	2,3
J	$[-]$	Number of harmonics of a Fourier series	2,5
$\vec{J}$	$[\mathrm{Am^{-2}}]$	Current density vector (volume)	1
$\vec{J}_f$	$[\mathrm{Am^{-2}}]$	Free current density vector (volume)	1
$\vec{J}_m$	$[\mathrm{Am^{-2}}]$	Magnetization current density vector (volume)	1
j	$[-]$	Index or vector component	1
j	$[-]$	Harmonic number of a Fourier series	2
j_z	$[\mathrm{ms^{-3}}]$	Jerk in z-direction	4
$\vec{j}$	$[\mathrm{Am^{-1}}]$	Current density vector (surface)	1
$\vec{j}_f$	$[\mathrm{Am^{-1}}]$	Free current density vector (surface)	1
$\vec{j}_m$	$[\mathrm{Am^{-1}}]$	Magnetization current density vector (surface)	1
K	$[-]$	Number of harmonics of a Fourier series	2,5
k	$[-]$	Harmonic number of a Fourier series	2,3,5
k	$[\mathrm{Wm^{-1}K^{-1}}]$	Thermal conductivity	6
k_{ff}	$[-]$	Coil filling factor	6,7
k_d	$[-]$	Distribution factor	6
k_f	$[\star]$	Force/torque constant	7
k_l	$[-]$	Flux link factor	6
k_s	$[-]$	Skewing factor	6
k_w	$[-]$	Winding factor	6
k_p	$[-]$	Pitch factor	6
$\mathcal{K}_o$	$[-]$	Modified Bessel function of the second kind of order o	2,3
L	$[-]$	Number of harmonics of a Fourier series	2
L	$[\mathrm{H}]$	Self inductance	7
l	$[\mathrm{m}]$	Length	1,5-7
l	$[-]$	Harmonic number of a Fourier series	2
M	$[-]$	Remanent magnetization component	2,5
$\vec{M}$	$[\mathrm{Am^{-1}}]$	Magnetization vector	1
$\vec{M}_0$	$[\mathrm{Am^{-1}}]$	Remanent magnetization vector	1,2
m	$[\mathrm{m^{-1}}]$	Spatial frequency	2,3,5
m	$[\mathrm{kg}]$	Mass	4,6
N	$[-]$	Number of harmonics of a Fourier series	2,5
N	$[-]$	Number of turns	7
N_{cpp}	$[-]$	Number of coil conductors per pole	6
$\vec{n}$	$[-]$	Unit vector normal to a surface	1,3
n	$[-]$	Harmonic number of a Fourier series	2,3,5,6
O	$[-]$	Origin of coordinate system	2
P_{Cu}	$[\mathrm{W}]$	Copper loss	5-7
$\vec{P}$	$[\mathrm{Cm^{-2}}]$	Polarization vector	1
p	$[-]$	Region index	2
p	$[\mathrm{W}]$	Instantaneous power	7

Symbol	Unit	Description	Chapter
q	[C]	Electric charge	1
q	[−]	Region index	2
q	[−]	Ratio between coil pitch and pole pitch	6
q	[W]	Rate of heat transfer	6
R	[m]	Radius	2,5-7
R	[Ω]	Resistance	5-7
r	[m]	Radius	3,5,6
r	[m]	Polar or cylindrical coordinate	2,3,5,6
$\mathcal{R}$	[*]	Homogeneous solution of the Laplace equation	2,3,5
$\mathfrak{R}$	[KW^{-1}]	Thermal resistance	6
S	[m^2]	Surface	1,2,3
S	[*]	Sensitivity	7
s	[*]	Coefficient	2
T	[*]	Fundamental period of a Fourier series	2
T	[*]	Temperature	4,6,7
T_z	[Nm]	Torque around z-axis	3,4,5,7
t	[s]	Time	1,4
$\mathbb{T}$	[T^2]	Maxwell stress tensor	1,3
u	[*]	General coordinate	1,6
V	[m^3]	Volume	1
v	[*]	General coordinate	1,6
$\vec{v}$	[ms^{-1}]	Velocity	1,4,7
w	[rad^{-1}]	Spatial frequency	2,3,5
w	[m]	Width	1,6
w	[*]	General coordinate	1
$\vec{x}$	[m]	Position vector	1
x	[m]	Cartesian coordinate	2-4
x	[−]	Region index	2
y	[m]	Cartesian coordinate	2-4
z	[m]	Cartesian or cylindrical coordinate	2-7
α	[−]	Ratio	2,5,6
α	[K^{-1}]	Temperature coefficient	6
α_θ	[rads^{-2}]	Angular acceleration	4,6,7
γ	[−]	Number of regions	2
γ_θ	[rads^{-3}]	Angular jerk	4
Δ	[*]	Relative displacement or offset	2,3,5-7
δ_{ij}	[−]	Kronecker delta	1,2
ε	[−]	Correlation function	2
ε	[−]	Emissivity	6
θ	[rad]	Polar or cylindrical coordinate	2-7
κ	[−]	Correlation function	2
λ	[*]	Coefficient	2,3

Symbol	Unit	Description	Chapter
λ	[Wb]	Flux linkage	6
μ	[Hm^{-1}]	Permeability	1
μ_r	[$-$]	Relative permeability	1,2,5
ν	[*]	Tangential coordinate, z or θ	2
ρ	[Cm^{-3}]	Free electrical charge density	1
ρ	[Ωm]	Electrical resistivity	5
ρ_m	[Cm^{-3}]	Magnetic volume charge density	1
σ_m	[Cm^{-2}]	Magnetic surface charge density	1
σ	[Sm^{-1}]	Electrical conductivity	6
ς	[$-$]	Correlation function	2
τ	[*]	Pitch or tangential width	2,3,5,6
φ	[A]	Magnetic scalar potential	1,2
χ_m	[$-$]	Magnetic susceptibility	1
ω_θ	[rads^{-1}]	Angular velocity	4,7

Acronyms

Acronym	Description
2D	Two dimensional
3D	Three dimensional
ANA	Analytical
BEM	Boundary element method
DoF	Degrees of freedom
emf	Electromotive force
FEM	Finite element method
FDM	Finite difference method
MEC	Magnetic equivalent circuit
MIMO	Multi input multi output
PCB	Printed circuit board
P&P	Pick and place
TPMA	Tubular permanent magnet actuator
rms	Root mean square
SISO	Single input single output
SMD	Surface mounted device

Physical constants

Symbol	Value	Unit	Description
ϵ_0	8.85×10^{-12}	[AsV^{-1}m^{-1}]	Permittivity of vacuum
μ_0	$4\pi \times 10^{-7}$	[Hm^{-1}]	Permeability of vacuum
σ	5.67×10^{-8}	[Wm^{-1}K^{-4}]	Stefan-Boltzmann constant

---

*Unit depends on context

References

[1] Ackermann, B. and Sottek, R. [1995], 'Analytical modeling of the cogging torque in permanent magnet motors', *Electrical Engineering (Archiv fur Elektrotechnik)* **78**, 117–125. 10.1007/BF01245643. Cited on page 33.

[2] Akoun, G. and Yonnet, J. P. [1984], '3D analytical calculation of the forces exerted between two cuboidal magnets', *IEEE Transactions on Magnetics* **20**(5), 1962–1964. Cited on page 72.

[3] Alwash, J. H. H., Mohssen, A. D. and Abdi, A. S. [2003], 'Helical motion tubular induction motor', *IEEE Transactions on Energy Conversion* **18**(3), 362–369. Cited on page 97.

[4] Amara, Y., Barakat, G. and Reghem, P. [2011], 'Armature reaction magnetic field of tubular linear surface-inset permanent-magnet machines', *IEEE Transactions on Magnetics* **47**(4), 805–811. Cited on page 35.

[5] Amara, Y., Wang, J. and Howe, D. [2005], 'Analytical prediction of eddy-current loss in modular tubular permanent-magnet machines', *IEEE Transactions on Energy Conversion* **20**(4), 761–770. Cited on page 35.

[6] Atallah, K., Zhu, Z. Q. and Howe, D. [1998], 'Armature reaction field and winding inductances of slotless permanent-magnet brushless machines', *IEEE Transactions on Magnetics* **34**(5), 3737–3744. Cited on pages 35 and 73.

[7] Azzouzi, J., Barakat, G. and Dakyo, B. [2005], 'Quasi-3-D analytical modeling of the magnetic field of an axial flux permanent-magnet synchronous machine', *IEEE Transactions on Energy Conversion* **20**(4), 746–752. Cited on pages 34 and 38.

[8] Bertotti, G. [1998], *Hysteresis in Magnetism*, Academic Press. Cited on page 161.

[9] Bianchi, N. and Bolognani, S. [2002], 'Design techniques for reducing the cogging torque in surface-mounted PM motors', *IEEE Transactions on Industry Applications* **38**(5), 1259–1265. Cited on page 72.

[10] Binns, K. J., Lawrenson, P. J. and Trowbridge, C. W. [1992], *The analytical and numerical solution of electric and magnetic fields*, John Wiley & Sons, Chistester. Cited on page 22.

[11] Boldea, I. and Nasar, S. A. [1999], 'Linear electric actuators and generators', *IEEE Transactions on Energy Conversion* **14**(3), 712–717. Cited on page 37.

[12] Bolognesi, P. [2010], Structure and theoretical analysis of a novel rotary-linear isotropic brushless machine, *in* 'Electrical Machines (ICEM), 2010 XIX International Conference on', pp. 1–6. Cited on page 98.

[13] Bolte, E. [1984], 'Analytical calculation of the two-dimensional field in the air gap and the slots of electrical machines', *IEEE Transactions on Magnetics* **20**(5), 1783–1785. Cited on pages 32 and 33.

[14] Boules, N. [1984], 'Two-dimensional field analysis of cylindrical machines with permanent magnet excitation', *IEEE Transactions on Industry Applications* **IA-20**(5), 1267–1277. Cited on page 32.

[15] Boules, N. [1985], 'Prediction of no-load flux density distribution in permanent magnet machines', *IEEE Transactions on Industry Applications* **IA-21**(3), 633–643. Cited on page 32.

[16] Cain, G. and Meyer, G. [2006], *Seperation of variables for partial differential equations : an eigenfunction approach*, Chapman & Hall/CRC, UK. Cited on pages 22 and 47.

[17] Carpenter, C. J. [1960], 'Surface-integral methods of calculating forces on magnetized iron parts', *Proceedings of the IEE - Part C: Monographs* **107**(11), 19–28. Cited on page 72.

[18] Chen, L. and Hofmann, W. [2007], Design of one rotary-linear permanent magnet motor with two independently energized three phase windings, *in* 'Power Electronics and Drive Systems, 2007. PEDS '07. 7th International Conference on', pp. 1372–1376. Cited on page 99.

[19] Chitayat, A. [1998], 'Rotary-linear actuator', U.S. Patent 5,982,053, Anorad Corporation. Cited on pages 99 and 100.

[20] Cho, H.-S., Im, C.-H. and Jung, H.-K. [2001], 'Magnetic field analysis of 2-D permanent magnet array for planar motor', *IEEE Transactions on Magnetics* **37**(5), 3762–3766. Cited on page 34.

[21] Coleman, Conrad, W. and Whittier [1986], 'Linear and rotary actuator', U.S. Patent 4,607,197, IMC Magnetics Corporation. Cited on page 96.

[22] Coulomb, J. [1983], 'A methodology for the determination of global electromechanical quantities from a finite element analysis and its application to the evaluation of magnetic forces, torques and stiffness', *IEEE Transactions on Magnetics* **19**(6), 2514–2519. Cited on page 72.

[23] Coulomb, J. and Meunier, G. [1984], 'Finite element implementation of virtual work principle for magnetic or electric force and torque computation', *IEEE Transactions on Magnetics* **20**(5), 1894–1896. Cited on page 72.

[24] de Boeij, J. [2009], Multi-Level Contactless Motion Systems, PhD thesis, Eindhoven University of Technology. Cited on page 90.

[25] De La Ree, J. and Boules, N. [1989], 'Torque production in permanent-magnet synchronous motors', *IEEE Transactions on Industry Applications* **25**(1), 107–112. Cited on page 73.

[26] De Medeiros, L. H., Reyne, G. and Meunier, G. [1998], 'Comparison of global force calculations on permanent magnets', *IEEE Transactions on Magnetics* **34**(5), 3560–3563. Cited on page 73.

[27] de Medeiros, L. H., Reyne, G. and Meunier, G. [1999], 'About the distribution of forces in permanent magnets', *IEEE Transactions on Magnetics* **35**(3), 1215–1218. Cited on page 73.

[28] de Wit, P., van Dijk, J., Blomer, T. and Rutgers, P. [1997], Mechatronic design of a z-phi; induction actuator, *in* 'International Conference on Electrical Machines and Drives', pp. 279 –283. Cited on page 97.

[29] Deodhar, R. P., Staton, D. A., Jahns, T. M. and Miller, T. J. E. [1996], 'Prediction of cogging torque using the flux-mmf diagram technique', *IEEE Transactions on Industry Applications* **32**(3), 569–576. Cited on page 73.

[30] Dubas, F. and Espanet, C. [2009], 'Analytical solution of the magnetic field in permanent-magnet motors taking into account slotting effect: No-load vector potential and flux density calculation', *IEEE Transactions on Magnetics* **45**(5), 2097–2109. Cited on page 34.

[31] Encica, L., Paulides, J. J. H. and Lomonova, E. A. [2009], 'Space-mapping optimization in electromechanics: an overview of algorithms and applications', *COMPEL: The International Journal for Computation and Mathematics in Electrical and Electronic Engineering* **28**, 1216–1226. Cited on page 24.

[32] Fleszar, J. and Mendrela, E. A. [1983], 'Twin-armature rotary-linear induction motor', *Electric Power Applications, IEE Proceedings B* **130**(3), 186–192. Cited on page 97.

[33] Furlani, E. P. [1993], 'Formulas for the force and torque of axial couplings', *IEEE Transactions on Magnetics* **29**(5), 2295–2301. Cited on page 72.

[34] Furlani, E. P. [2001], *Permanent Magnet and Electromechanical Devices*, Academic Press. Cited on pages 12, 21, 22, 46, and 47.

[35] Gieras, J. F. [2004], 'Analytical approach to cogging torque calculation of PM brushless motors', *IEEE Transactions on Industry Applications* **40**(5), 1310–1316. Cited on page 73.

[36] Gieras, J. F., Wang, R.-J. and Kamper, M. J. [2008], *Axial Flux Permanent Magnet Brushless Machines*, 2nd edn, Springer. Cited on page 38.

[37] Griffiths, D. J. [1999], *Introduction to electrodynamics*, 3rd edn, Prentice Hall. Cited on page 15.

[38] Gysen, B. L. J. [2011], Generalized Harmonic Modeling Technique for 2D Electromagnetic Problems, PhD thesis, Eindhoven University of Technology. Cited on pages 19 and 35.

[39] Gysen, B. L. J., Janssen, J. L. G., Paulides, J. J. H. and Lomonova, E. A. [2009], 'Design aspects of an active electromagnetic suspension system for automotive applications', *IEEE Transactions on Industry Applications* **45**(5), 1589–1597. Cited on pages 35 and 106.

[40] Gysen, B. L. J., Meessen, K. J., Paulides, J. J. H. and Lomonova, E. A. [2008], 'Semi-analytical calculation of the armature reaction in slotted tubular permanent magnet actuators', *IEEE Transactions on Magnetics* **44**(11), 3213–3216. Cited on pages 35 and 73.

[41] Gysen, B. L. J., Meessen, K. J., Paulides, J. J. H. and Lomonova, E. A. [2010], 'General formulation of the electromagnetic field distribution in machines and devices using Fourier analysis', *IEEE Transactions on Magnetics* **46**(1), 39–52. Cited on pages 23, 34, 40, 69, and 128.

[42] Gysen, B. L. J., Meessen, K. J., Paulides, J. J. H. and Lomonova, E. A. [2011], '3D analytical and numerical modeling of tubular actuators with skewed permanent magnets', *IEEE Transactions on Magnetics* **47**(9), 2200–2212. Cited on page 73.

[43] Hague, B. [1929], *Electromagnetic Problems in Electrical Engineering*, Oxford University Press, London. Cited on pages 12, 21, 22, 32, and 45.

[44] Halbach, K. [1980], 'Design of permanent multipole magnets with oriented rare earth cobalt material', *Nuclear Instruments and Methods* **69**(1), 1–10. Cited on page 108.

[45] Hanselman, D. [2003], *Brushless permanent magnet motor design*, The Writer's Collective, USA. Cited on page 139.

[46] Hendershot, J. R. and Miller, T. J. E. [2010], *Design Of Brushless Permanent-Magnet Motors*, Motor Design Books LLC. Cited on page 139.

[47] Hewitt, E. and Hewitt, R. [1979], 'The Gibbs-Wibraham phenomenon: An episode in Fourier analysis', *Archive for History of Exact Sciences* **21**, 129–160. Cited on page 69.

[48] Higuchi Toshiro, H. A. [1987], 'Non-contact double-acting type actuator', JP Patent 62141950, Higuchi Toshiro. Cited on page 96.

[49] Howe, D. and Zhu, Z. Q. [1992], 'The influence of finite element discretisation on the prediction of cogging torque in permanent magnet excited motors', *IEEE Transactions on Magnetics* **28**(2), 1080–1083. Cited on page 72.

[50] Hwang, S.-M., Eom, J.-B., Hwang, G.-B., Jeong, W.-B. and Jung, Y.-H. [2000], 'Cogging torque and acoustic noise reduction in permanent magnet motors by teeth pairing', *IEEE Transactions on Magnetics* **36**(5), 3144–3146. Cited on page 72.

[51] Ilhan, E., Gysen, B. L. J., Paulides, J. J. H. and Lomonova, E. A. [2010], 'Analytical hybrid model for flux switching permanent magnet machines', *IEEE Transactions on Magnetics* **46**(6), 1762–1765. Cited on page 24.

[52] Incropera, F. P. and DeWitt, D. P. [2007], *Fundamentals of heat and mass transfer*, John Wiley. Cited on pages 146 and 147.

[53] Jackson, J. D. [1999], *Classical electrodynamics*, 3rd edn, Wiley. Cited on pages 16, 20, 21, 22, and 163.

[54] Jahns, T. M. and Soong, W. L. [1996], 'Pulsating torque minimization techniques for permanent magnet ac motor drives-a review', *IEEE Transactions on Industrial Electronics* **43**(2), 321–330. Cited on page 72.

[55] Jang, S. M., Choi, J. Y., Lee, S. H., Cho, S. K. and Jang, W. B. [2003], Analysis of the tubular motor with Halbach and radial magnet array, *in* 'International Conference on Electrical Machines and Systems', Vol. 1, pp. 250–252. Cited on page 99.

[56] Jansen, J. W. [2007], Magnetically Levitated Planar Actuator with Moving Magnets, PhD thesis, Eindhoven University of Technology. Cited on pages 90 and 101.

[57] Jansen, J. W., van Lierop, C. M. M., Lomonova, E. A. and Vandenput, A. J. A. [2007], 'Modeling of magnetically levitated planar actuators with moving magnets', *IEEE Transactions on Magnetics* **43**(1), 15–25. Cited on page 35.

[58] Jansen, J. W., van Lierop, C. M. M., Lomonova, E. A. and Vandenput, A. J. A. [2008], 'Ironless magnetically levitated planar actuator', *Journal of Applied Physics* **103**(7), 07E905–07E905–3. Cited on page 19.

[59] Janssen, J. L. G. [2011], Extended Analytical Charge Modeling for Permanent-Magnet Based Devices, PhD thesis, Eindhoven University of Technology. Cited on pages 22 and 25.

[60] Janssen, J. L. G., Paulides, J. J. H., Encica, L. and Lomonova, E. A. [2008], Analytical modeling of permanent magnets on a soft magnetic support for a suspension system, *in* 'International Conference on Electrical Machines and Systems', pp. 3825–3830. Cited on page 22.

[61] Janssen, J. L. G., Paulides, J. J. H. and Lomonova, E. A. [2009], 'Passive limitations for a magnetic gravity compensator', *Journal of System Design and Dynamics* **3**(4), 671–680. Cited on page 72.

[62] Janssen, J. L. G., Paulides, J. J. H. and Lomonova, E. A. [2011], '3-D analytical calculation of the torque between perpendicular magnetized magnets in magnetic suspensions', *IEEE Transactions on Magnetics* **47**(10), 4286–4289. Cited on page 72.

[63] Jeon, W. J., Tanabiki, M., Onuki, T. and Yoo, J. Y. [1997], Rotary-linear induction motor composed of four primaries with independently energized ring-windings, *in* 'Industry Applications Conference, 1997. Thirty-Second IAS Annual Meeting, IAS '97., IEEE', Vol. 1, pp. 365–372. Cited on page 97.

[64] Jiao, G. and Rahn, C. D. [2004], 'Field weakening for radial force reduction in brushless permanent-magnet dc motors', *IEEE Transactions on Magnetics* **40**(5), 3286–3292. Cited on pages 73 and 77.

[65] Jin, M. J. [2002], *The Finite Element Method in Electromagnetics*, 2 edn, Wiley. Cited on page 19.

[66] Kamerbeek, E. M. H. [1970], On the theoretical and experimental determination of the electromagnetic torque in electrical machines, PhD thesis, Technische Hogeschool Eindhoven. Cited on pages 14 and 16.

[67] Kim, D.-H., Lowther, D. A. and Sykulski, J. K. [2005], 'Efficient force calculations based on continuum sensitivity analysis', *IEEE Transactions on Magnetics* **41**(5), 1404–1407. Cited on page 72.

[68] Kim, D.-H., Lowther, D. A. and Sykulski, J. K. [2007], 'Efficient global and local force calculations based on continuum sensitivity analysis', *IEEE Transactions on Magnetics* **43**(4), 1177–1180. Cited on page 72.

[69] Kim, U. and Lieu, D. K. [1998], 'Magnetic field calculation in permanent magnet motors with rotor eccentricity: without slotting effect', *IEEE Transactions on Magnetics* **34**(4), 2243–2252. Cited on page 33.

[70] Kim, W., Trumper, D. L. and Lang, J. H. [1997], Modeling and vector control of a planar magnetic levitator, *in* 'Industry Applications Conference, 1997. Thirty-Second IAS Annual Meeting, IAS '97., Conference Record of the 1997 IEEE', Vol. 1, pp. 349–356. Cited on page 90.

[71] Krebs, G., Tounzi, A., Pauwels, B. and Willemot, D. [2008], General overview of integrated linear rotary actuators, *in* 'Electrical Machines, 2008. ICEM 2008. 18th International Conference on', pp. 1–6. Cited on page 96.

[72] Krebs, G., Tounzi, A., Pauwels, B., Willemot, D. and Piriou, F. [2008], 'Design of a permanent magnet actuator for linear and rotary movements', *European Physical Journal Applied Physics* **44**, 77–85. Cited on pages 99 and 101.

[73] Krop, D. C. J., Lomonova, E. A. and Vandenput, A. J. A. [2008], 'Application of Schwarz-Christoffel mapping to permanent-magnet linear motor analysis', *IEEE Transactions on Magnetics* **44**(3), 352–359. Cited on page 73.

[74] Lee, K., DeBortoli, M. J., Lee, M. J. and Salon, S. J. [1991], 'Coupling finite elements and analytical solution in the airgap of electric machines', *IEEE Transactions on Magnetics* **27**(5), 3955–3957. Cited on page 24.

[75] Lee, S., Jones, W. and Campbell, J. [1970], Convergence of numerical solutions of iris-type discontinuity problems, *in* 'Antennas and Propagation Society International Symposium, 1970', Vol. 8, pp. 384–392. Cited on page 69.

[76] Liebman, M. K. [2001], Rotary-Linear Axes for High Speed Machining, PhD thesis, Massachusetts Institute of Technology. Cited on page 98.

[77] Liu, Z. J., Bi, C., Zhang, Q. D., Jabbar, M. A. and Low, T. S. [1996], 'Electromagnetic design for hard disk drive spindle motors with fluid film lubricated bearings', *IEEE Transactions on Magnetics* **32**(5), 3893–3895. Cited on pages 73 and 77.

[78] Liu, Z. J. and Li, J. T. [2007], 'Analytical solution of air-gap field in permanent-magnet motors taking into account the effect of pole transition over slots', *IEEE Transactions on Magnetics* **43**(10), 3872–3883. Cited on page 33.

[79] Magnussen, F. and Sadarangani, C. [2003], Winding factors and joule losses of permanent magnet machines with concentrated windings, *in* 'Electric Machines and Drives Conference, 2003. IEMDC'03. IEEE International', Vol. 1, pp. 333–339. Cited on page 140.

[80] Mallinson, J. [1973], 'One-sided fluxes – a magnetic curiosity?', *IEEE Transactions on Magnetics* **9**(4), 678–682. Cited on page 108.

[81] Marinescu, M. and Marinescu, N. [1988], 'Numerical computation of torques in permanent magnet motors by Maxwell stresses and energy method', *IEEE Transactions on Magnetics* **24**(1), 463–466. Cited on page 72.

[82] Marinescu, M. and Marinescu, N. [1992], 'New concept of permanent magnet excitation for electrical machines: analytical and numerical computation', *IEEE Transactions on Magnetics* **28**(2), 1390–1393. Cited on page 33.

[83] Markovic, M. and Perriard, Y. [2009], 'Optimization design of a segmented Halbach permanent-magnet motor using an analytical model', *IEEE Transactions on Magnetics* **45**(7), 2955–2960. Cited on page 35.

[84] Maxwell, J. C. [1904], *A treatise on electricity and magnetism*, Vol. 1-2, 3rd edn, Oxford : Clarendon. Cited on page 12.

[85] Meessen, K. J., Gysen, B. L. J., Paulides, J. J. H. and Lomonova, E. A. [2008], 'Halbach permanent magnet shape selection for slotless tubular actuators', *IEEE Transactions on Magnetics* **44**(11), 4305–4308. Cited on pages 43 and 128.

[86] Meessen, K. J., Gysen, B. L. J., Paulides, J. J. H. and Lomonova, E. A. [2010], 'Three-dimensional magnetic field modeling of a cylindrical Halbach array', *IEEE Transactions on Magnetics* **46**(6), 1733–1736. Cited on pages 26 and 108.

[87] Meessen, K. J., Gysen, B. L. J., Paulides, J. J. H. and Lomonova, E. A. [2012], 'General formulation of fringing fields in 3D cylindrical structures using Fourier analysis', *IEEE Transactions on Magnetics* **48**(8), 2307–2323. Cited on page 26.

[88] Meessen, K. J., Paulides, J. J. H. and Lomonova, E. A. [2009*a*], 'Analysis and design of a slotless tubular permanent magnet actuator for high acceleration applications', *Journal of Applied Physics* **105**(7), 07F110–3. Cited on pages 106, 107, 113, and 157.

[89] Meessen, K. J., Paulides, J. J. H. and Lomonova, E. A. [2009*b*], Novel moving coil tubular actuator with double sided PM array, *in* 'Proceedings IEEE International Magnetics Conference, INTERMAG', pp. 80–80. Cited on page 106.

[90] Meessen, K. J., Paulides, J. J. H. and Lomonova, E. A. [2010], 'Modeling and experimental verification of a tubular actuator for 20-g acceleration in a pick-and-place application', *IEEE Transactions on Industry Applications* **46**(5), 1891–1898. Cited on pages 37, 106, 107, 113, 128, and 148.

[91] Meessen, K. J., Paulides, J. J. H. and Lomonova, E. A. [2011*a*], Analysis and design considerations of a 2-DoF rotary-linear actuator, *in* 'Electric Machines Drives Conference (IEMDC), 2011 IEEE International', pp. 336–341. Cited on pages 27, 98, 99, and 194.

[92] Meessen, K. J., Paulides, J. J. H. and Lomonova, E. A. [2011*b*], 'Analysis of 3D effects in segmented cylindrical quasi-Halbach magnet arrays', *IEEE Transactions on Magnetics* **47**(4), 727–733. Cited on pages 26, 106, and 108.

[93] Meessen, K. J., Paulides, J. J. H. and Lomonova, E. A. [2011*c*], Modeling of magnetization patterns for 2-DoF rotary-linear actuators., *in* 'Proceedings of XV International Symposium on Electromagnetic Fields in Mechatronics, Electrical and Electronic Engineering, Madeira.', pp. 1–8. Cited on page 105.

[94] Meessen, K. J., Paulides, J. J. H. and Lomonova, E. A. [2012], 'Modeling of magnetization patterns for 2-DoF rotary-linear actuators.', *COMPEL: The International Journal for Computation and Mathematics in Electrical and Electronic Engineering* **31**(5), 1428–1440. Cited on page 26.

[95] Meessen, K. J., Paulides, J. J. H. and Lomonova, E. A. [2012, accepted for publication*a*], 'Analysis of a novel magnetization pattern for 2-DoF rotary-linear actuators', *IEEE Transactions on Magnetics* . Cited on pages 26, 27, and 108.

[96] Meessen, K. J., Paulides, J. J. H. and Lomonova, E. A. [accepted for publication*b*], 'Force calculations in 3D cylindrical structures using fourier analysis and the Maxwell stress tensor', *IEEE Transactions on Magnetics* . Cited on page 26.

[97] Mendrela, E. A. and Gierczak, E. [1987], 'Double-winding rotary-linear induction motor', *IEEE Transactions on Energy Conversion* **EC-2**(1), 47–54. Cited on page 97.

[98] Miskin, E. [1954], 'Theory of squirrel-cagee induction machine derived directly from Maxwell's field equations', *Quarterly Journal of Mechanics and Applied Mathematics* **7**, 472–487. Cited on page 32.

[99] Mizia, J., Adamiak, K., Eastham, A. R. and Dawson, G. E. [1988], 'Finite element force calculation: comparison of methods for electric machines', *IEEE Transactions on Magnetics* **24**(1), 447–450. Cited on page 72.

[100] Muller, W. [1990], 'Comparison of different methods of force calculation', *IEEE Transactions on Magnetics* **26**(2), 1058–1061. Cited on page 72.

[101] Onuki, T., Jeon, W. J. and Tanabiki, M. [1997], 'Induction motor with helical motion by phase control', *IEEE Transactions on Magnetics* **33**(5), 4218–4220. Cited on page 97.

[102] Ostovic, V. [1989], *Dynamics of Saturated Electric Machines*, Springer-Verlag. Cited on page 23.

[103] Overboom, T. T., Jansen, J. W., Lomonova, E. A. and Tacken, F. J. F. [2010], 'Design and optimization of a rotary actuator for a two-degree-of-freedom z-ϕ-module', *IEEE Transactions on Industry Applications* **46**(6), 2401–2409. Cited on pages 98 and 99.

[104] Panofsky, W. K. H. and Phillips, M. [1962], *Classical Electricity and Magnetism*, Addison-Wesley. Cited on page 14.

[105] Parviainen, A., Niemela, M. and Pyrhönen, J. [2004], 'Modeling of axial flux permanent-magnet machines', *IEEE Transactions on Industry Applications* **40**(5), 1333–1340. Cited on page 38.

[106] Qishan, G. and Hongzhan, G. [1985*a*], 'Air gap field for PM electric machines', *Electric Machines & Power Systems* **10**(5-6), 459–470. Cited on page 32.

[107] Qishan, G. and Hongzhan, G. [1985*b*], 'Effect of slotting in PM electric machines', *Electric Machines & Power Systems* **10**(4), 273–284. Cited on page 32.

[108] Qishan, G. and Hongzhan, G. [1986], 'The fringing effect in PM electric machines', *Electric Machines & Power Systems* **11**(2), 159–169. Cited on pages 33 and 34.

[109] Rabiee, M. and Cathey, J. J. [1988], 'Verification of a field theory analysis applied to a helical motion induction motor', *IEEE Transactions on Magnetics* **24**(4), 2125–2132. Cited on page 97.

[110] Ravaud, R. and Lemarquand, G. [2009], 'Comparison of the coulombian and amperian current models for calculating the magnetic field produced by radially magnetized arc-shaped permanent magnets', *Progress In Electromagnetics Research* **95**, 309–327. Cited on page 22.

[111] Reece, A. B. J. and Preston, T. [2000], *Finite element methods in electrical power engineering*, 1st edn, Oxford University Press. Cited on page 19.

[112] Ren, Z. [1994], 'Comparison of different force calculation methods in 3D finite element modelling', *IEEE Transactions on Magnetics* **30**(5), 3471–3474. Cited on page 72.

[113] Roters, H. C. [1955], *Electromagnetic Devices*, 6th edn, Wiley, Chichester. Cited on page 23.

[114] Rovers, J. M. M., Stöck, M., Jansen, J. W., van Lierop, C. M. M., Lomonova, E. A. and Perriard, Y. [2012], 'Real-time 3D thermal modeling of a magnetically levitated planar actuator', *Mechatronics* **in press**. Cited on page 147.

[115] Sato, Y. [2007], 'Development of a 2-degree-of-freedom rotational/linear switched reluctance motor', *IEEE Transactions on Magnetics* **43**(6), 2564–2566. Cited on page 96.

[116] Satomi Hirobumi, I. T. [1996], 'Linear-rotary composite type stepping motor', JP Patent 8275484, Oriental Motor. Cited on page 96.

[117] Shute, H. A., Wilton, D. T., McKirdy, D. M. A., Jermey, P. M. and Mallinson, J. C. [2006], 'Analytic three-dimensional response function of a double-shielded magnetoresistive or giant magnetoresistive perpendicular head', *IEEE Transactions on Magnetics* **42**(5), 1611–1619. Cited on page 194.

[118] Skogestad, S. and Postlethwaite, I. [2007], *Multivariable feedback control, Analysis and design*, 2nd edn, Wiley. Cited on page 176.

[119] Smythe, W. R. [1939], *Static and dynamic electricity*, 3rd edn, McGraw-Hill, New York. Cited on pages 13, 21, 22, and 72.

[120] Sogard, M. R. [2002], 'Two-dimensional electric motor', U.S. Patent 6,455,956, Nikon Corporation. Cited on pages 99 and 100.

[121] Stratton, J. A. [1941], *Electromagnetic Theory*, McGraw-Hill. Cited on page 14.

[122] Swift, G. L. [2004], 'Rotary-linear actuator system method of manufacturing and method of using a rotary-linear actuator', U.S. Patent 6,798,087, Anorad Corporation. Cited on page 98.

[123] Trumper, D., Kim, W.-J. and Williams, M. [1996], 'Design and analysis framework for linear permanent-magnet machines', *IEEE Transactions on Industry Applications* **32**(2), 371–379. Cited on page 33.

[124] Turner, A., Ramsay, K., Clark, R. and Howe, D. [2007], Direct-drive rotary-linear electromechanical actuation system for control of gearshifts in automated transmissions, *in* 'Vehicle Power and Propulsion Conference, 2007. VPPC 2007. IEEE', pp. 267–272. Cited on page 98.

[125] Urankar, L. [1984], 'Vector potential and magnetic field of current-carrying finite arc segment in analytical form, part iv: General three-dimensional current density', *IEEE Transactions on Magnetics* **20**(6), 2145–2150. Cited on page 21.

[126] van der Burg, R. A. J., Lomonova, E. A., Meessen, K. J. and Paulides, J. J. H. [2011], 'Moving device as well as a component placement device provided with such a moving device', U.S. Patent 2011/0194923, Assembleon B.V. Cited on pages 26 and 105.

[127] Wang, J. and Howe, D. [2005], 'Tubular modular permanent-magnet machines equipped with quasi-Halbach magnetized magnets - part I: Magnetic field distribution, emf, and thrust force', *IEEE Transactions on Magnetics* **41**(9), 2470–2478. Cited on page 35.

[128] Wang, J., Howe, D. and Jewell, G. W. [2003*a*], 'Fringing in tubular permanent-magnet machines: Part I. magnetic field distribution, flux linkage, and thrust force', *IEEE Transactions on Magnetics* **39**(6), 3507–3516. Cited on pages 23, 33, 35, 37, and 73.

[129] Wang, J., Howe, D. and Jewell, G. W. [2003*b*], 'Fringing in tubular permanent-magnet machines: Part II. cogging force and its minimization', *IEEE Transactions on Magnetics* **39**(6), 3517–3522. Cited on pages 33 and 35.

[130] Wang, J., Howe, D. and Jewell, G. W. [2004], 'Analysis and design optimization of an improved axially magnetized tubular permanent-magnet machine', *IEEE Transactions on Energy Conversion* **19**(2), 289–295. Cited on page 33.

[131] Wang, J., Inoue, M., Amara, Y. and Howe, D. [2005], 'Cogging-force-reduction techniques for linear permanent-magnet machines', *Electric Power Applications, IEE Proceedings -* **152**(3), 731–738. Cited on page 159.

[132] Wang, J., Jewell, G. W. and Howe, D. [1999], 'A general framework for the analysis and design of tubular linear permanent magnet machines', *IEEE Transactions on Magnetics* **35**(3), 1986–2000. Cited on pages 33 and 37.

[133] Wang, J., Wang, W., Jewell, G. W. and Howe, D. [1998], 'A novel spherical permanent magnet actuator with three degrees-of-freedom', *IEEE Transactions on Magnetics* **34**(4), 2078–2080. Cited on pages 34 and 90.

[134] Williamson, S., Flack, T. J. and Volschenk, A. F. [1995], 'Representation of skew in time-stepped two-dimensional finite-element models of electrical machines', *IEEE Transactions on Industry Applications* **31**(5), 1009–1015. Cited on page 38.

[135] Woodson, H. H. and Melcher, J. R. [1968*a*], *Electromechanical Dynamics, Part I : Discrete Systems*, John Wiley & Sons. Cited on pages 13 and 14.

[136] Woodson, H. H. and Melcher, J. R. [1968*b*], *Electromechanical Dynamics, Part II : Fields, Forces, and Motion*, John Wiley & Sons. Cited on page 15.

[137] Yan, L., Chen, I.-M., Yang, G. and Lee, K.-M. [2006], 'Analytical and experimental investigation on the magnetic field and torque of a permanent magnet spherical actuator', *Mechatronics, IEEE/ASME Transactions on* **11**(4), 409–419. Cited on page 90.

[138] Yonnet, J. P. and Allag, H. [2011], 'Three-dimensional analytical calculation of permanent magnet interactions by "magnetic node" representation', *IEEE Transactions on Magnetics* **47**(8), 2050–2055. Cited on page 72.

[139] Youmssi, A. [2006], 'A three-dimensional semi-analytical study of the magnetic field excitation in a radial surface permanent-magnet synchronous motor', *IEEE Transactions on Magnetics* **42**(12), 3832–3841. Cited on page 34.

[140] Zanis, R., Meessen, K. J., Compter, J. C. and Lomonova, E. A. [2011], Design and control of magnetic bearings for rotary-linear motion applications, *in* 'Proceedings of The 8th International Symposium on Linear Drives for Industry Applications', pp. 1–6. Cited on page 195.

[141] Zarko, D., Ban, D. and Lipo, T. A. [2006], 'Analytical calculation of magnetic field distribution in the slotted air gap of a surface permanent-magnet motor using complex relative air-gap permeance', *IEEE Transactions on Magnetics* **42**(7), 1828–1837. Cited on page 73.

[142] Zarko, D., Ban, D. and Lipo, T. A. [2008], 'Analytical solution for cogging torque in surface permanent-magnet motors using conformal mapping', *IEEE Transactions on Magnetics* **44**(1), 52–65. Cited on page 35.

[143] Zhilichev, Y. [1998], 'Three-dimensional analytic model of permanent magnet axial flux machine', *IEEE Transactions on Magnetics* **34**(6), 3897–3901. Cited on page 34.

[144] Zhilichev, Y. [2000*a*], 'Analysis of permanent magnet machines using crossing macro-elements', *IEEE Transactions on Magnetics* **36**(5), 3122–3124. Cited on page 24.

[145] Zhilichev, Y. [2000*b*], 'Analytic solutions of magnetic field problems in slotless permanent magnet machines', *COMPEL: The International Journal for Computation and Mathematics in Electrical and Electronic Engineering* **19**(4), 940–955. Cited on page 34.

[146] Zhilichev, Y. [2007], 'Calculation of magnetic field of tubular permanent-magnet assemblies in cylindrical bipolar coordinates', *IEEE Transactions on Magnetics* **43**(7), 3189 –3196. Cited on page 33.

[147] Zhu, W., Pekarek, S., Fahimi, B. and Deken, B. J. [2007], 'Investigation of force generation in a permanent magnet synchronous machine', *IEEE Transactions on Energy Conversion* **22**(3), 557–565. Cited on page 35.

[148] Zhu, Z. Q. and Howe, D. [1992], 'Analytical prediction of the cogging torque in radial-field permanent magnet brushless motors', *IEEE Transactions on Magnetics* **28**(2), 1371–1374. Cited on page 73.

[149] Zhu, Z. Q. and Howe, D. [1993*a*], 'Instantaneous magnetic field distribution in brushless permanent magnet DC motors. II: Armature-reaction field', *IEEE Transactions on Magnetics* **29**(1), 136–142. Cited on pages 33 and 73.

[150] Zhu, Z. Q. and Howe, D. [1993*b*], 'Instantaneous magnetic field distribution in brushless permanent magnet DC motors. III: Effect of stator slotting', *IEEE Transactions on Magnetics* **29**(1), 143–151. Cited on page 33.

[151] Zhu, Z. Q. and Howe, D. [1993*c*], 'Instantaneous magnetic field distribution in permanent magnet brushless DC motors. IV: Magnetic field on load', *IEEE Transactions on Magnetics* **29**(1), 152 –158. Cited on page 33.

[152] Zhu, Z. Q., Howe, D., Bolte, E. and Ackermann, B. [1993], 'Instantaneous magnetic field distribution in brushless permanent magnet DC motors, part I: Open-circuit field', *IEEE Transactions on Magnetics* **29**(1), 124–135. Cited on pages 33 and 36.

[153] Zhu, Z. Q., Ishak, D., Howe, D. and Jintao, C. [2007], 'Unbalanced magnetic forces in permanent-magnet brushless machines with diametrically asymmetric phase windings', *IEEE Transactions on Industry Applications* **43**(6), 1544–1553. Cited on pages 35, 73, and 77.

[154] Zhu, Z. Q., Wu, L. J. and Xia, Z. P. [2010], 'An accurate subdomain model for magnetic field computation in slotted surface-mounted permanent-magnet machines', *IEEE Transactions on Magnetics* **46**(4), 1100–1115. Cited on page 23.

Samenvatting

**Electromagnetic Fields and Interactions in 3D Cylindrical Structures:
Modeling and Application**

De toenemende vraag naar efficiënte en compacte actuatiesystemen resulteert in een zoektocht naar nieuwe elektromagnetische actuatorconfiguraties. Nauwkeurige modellering van de elektromagnetische velden in deze actuatoren is in veel gevallen een vereiste om tot een ontwerp te komen dat aan de vaak uitdagende eisen voldoet. Bestaande analytische modelleringstechnieken zijn vaak toegespitst op het berekenen van deze velden in conventionele roterende en lineair bewegende motoren, gerepresenteerd in 2D coördinatensystemen. Dit proefschrift beschrijft een uitbreiding van een analytische harmonische modelleringstechniek om de 3D elektromagnetische veldverdeling snel en nauwkeurig te kunnen voorspellen in cilindrische actuatoren.

De harmonische modelleringstechniek is gebaseerd op Fourierreeksen om de magnetische velden te beschrijven. De in dit proefschrift beschreven uitbreiding van deze techniek biedt de mogelijkheid om de veldverdeling ten gevolge van permanente magneten in zowel uniforme als getande cilindrische structuren te beschrijven. Deze cilinders dienen in de lengterichting periodiciteit ofwel een ijzeren afsluiting te hebben. Verder kan vertanding in de lengterichting of de omwentelingsrichting mee worden genomen alsmede vierkante holtes of gaten. De methode om het model op te stellen en op te lossen is op een generieke manier beschreven zodat deze toepasbaar is voor vele cilindrische structuren. De magnetische veldvergelijkingen en de implementatie van het model in een matrixformulering zijn gegeven. Een model is opgesteld van een voorbeeldstructuur die bestaat uit een alternerend magneet patroon omsloten door een cilinder met daarin een vierkant gat. De resultaten hiervan zijn gevalideerd met een eindige-elementenmodel.

Om de elektromagnetische interacties in de structuur, in de vorm van passieve aantrekkingskrachten, te kunnen bepalen, is de Maxwell-stress-tensor analytisch uitgewerkt. De harmonische veldvergelijkingen uit het afgeleide model zijn hiervoor gebruikt, resulterend in compacte vergelijkingen die de verschillende krachtcomponenten beschrijven.

233

De beschreven 3D harmonische modelleringstechniek is toegepast in de analyse en het ontwerp van een twee vrijheidsgraden, rotatie-translatie actuator. Deze actuator vervangt gestapelde actuatorconfiguraties en is specifiek ontworpen als plaatsingskop voor een componentplaatsingsmachine voor het positioneren van componenten op printplaten. Een nieuw magnetisatiepatroon voor een elektromagnetische actuator is voorgesteld. Dit magnetisatiepatroon is geschikt om de hoge kracht en het relatief lage koppel te kunnen leveren. Dit patroon kan gerealiseerd worden door gebruik te maken van parasitaire veldeffecten in het magneetpatroon van een cilindrische lineaire actuator. Verschillende stator- en spoelconfiguraties zijn onderzocht om een actuator te kunnen realiseren met een hoge krachtdichtheid. Bij de selectie van de configuratie is rekening gehouden met onder andere de maakbaarheid van het uiteindelijke ontwerp. Elektromagnetische en thermische analyses zijn uitgevoerd om inzicht te krijgen in de relatie tussen de afmetingen van de verschillende actuatoronderdelen en de prestaties om vervolgens tot een optimaal actuatorontwerp te kunnen komen.

De ontworpen actuator is gerealiseerd ter validatie van de gebruikte modellen en methodes. Zowel de realisatie als de experimentele verificatie is beschreven. De metingen laten zien dat de ontworpen en gerealiseerde actuator de uitdagende specificaties van de componentplaatsingsmachine kan volbrengen. Dit houdt in: Een versnelling in de verticale richting van $a_z = 150\,\text{ms}^{-2}$ bij een slag van 30 mm, een taakcyclus van 34%, en een statische positioneringfout van minder dan 5 μm. De vereiste versnelling in de rotatierichting is $\alpha_\theta = 3500\,\text{rads}^{-2}$ bij een taakcyclus van 47% en een statische positioneringfout van maximaal 0.35 mrad. Verder volgt uit de metingen dat de gespecificeerde gecombineerde rotatie-translatie beweging resulteert in een constante dissipatie van 13.5 W hetgeen resulteert in een opwarming van de actuator van 30°C ten opzichte van de omgeving. De meetresultaten van de gerealiseerde actuator komen goed overeen met de resultaten van de ontwikkelde harmonische modellen. Hiermee is aangetoond dat deze modelleringstechniek geschikt is voor de analyse van cilindrische structuren met permanente magneten.

Dankwoord

Nu ik dit dankwoord aan het schrijven ben, realiseer ik me dat ik hierbij echt een streep onder mijn promotieonderzoek en proefschrift zet, ook al is het eigenlijk nooit af. Tijdens de afgelopen vier jaar hebben vele personen bijgedragen aan dit onderzoek die ik graag wil bedanken.

Allereerst wil ik Elena en Johan bedanken voor het geven van de mogelijkheid om deze promotie te doorlopen in de EPE-groep. Elena, bedankt voor je vertrouwen, enthousiasme en steun tijdens het hele traject. Met jouw "helikopterview" zorgde je ervoor dat ik met de vele aspecten van de elektromechanica in contact ben gekomen. Johan, bedankt voor je begeleiding, de vele discussies, en de projectvergaderingen die we samen hebben gehad. Jouw positieve kijk hielp mij vaak aan hernieuwde motivatie en je kritische blik op mijn werk deed mij inzien dat er vaak meer uit te halen viel dan ik in eerste instantie inzag.

Tijdens het (INEMA) project is er veel samenwerking geweest met industriële partners: Assembléon, TNO, Tecnotion, en Prodrive. Rik, bedankt voor de ondersteuning vanuit Assembléon, Maarten, Jeroen en Jeroen bedankt voor jullie bijdrage in het mechanische ontwerp en realisatie van de actuator. Erwin bedankt voor je geduld en de pogingen die je hebt besteed aan het realiseren van de spoelen en statordelen die in theorie makkelijk in elkaar pasten! Heren van het EPC/GTD, Erwin, Jeroen en Jovita, bedankt voor de discussies en de fijne samenwerking bij het realiseren van de prototypes. Ik vond het erg prettig dat ik op ieder moment kon binnenlopen met aanvullingen of vragen.

Furthermore, I would like to thank my (core) committee members; prof. Maarten Steinbuch, prof. Sykulski, prof. Barakat, and dr. Bart Gysen for reading my thesis and providing comments on the content to improve the thesis. With your fresh opinions I was able to dot the i's and cross the t's of my thesis. Additionally I would like to thank prof. Canders for being part of my committee.

Graag wil ik ook alle collega's binnen de EPE-groep bedanken voor de leuke en open sfeer. In het bijzonder wil ik Jeroen (het is gelukt!) en Bart bedanken voor de eindeloze

discussies en conversaties over technische en niet-technische onderwerpen. Ik heb het erg gezellig gehad in ons kantoor de afgelopen vier jaar. Bart, naast de gezelligheid wil ik je bedanken voor onze samenwerking, met name op het gebied van het uitbreiden van de harmonische modelleringstechniek. Hans, Dave en Kevin, jullie hebben de laatste maanden het stokje overgenomen van Jeroen en Bart, bedankt voor jullie ideeën die ik nog wel eens heb gebruikt tijdens het schrijven van mijn proefschrift. Marijn, bedankt voor alle assistentie in het lab en bij andere praktische uitdagingen.

Speciale dank gaat uit naar het RoboCup team Tech United dat me veel tijd heeft gekost tijdens mijn promotieonderzoek, maar ook zo enorm veel heeft opgeleverd. Erg gaaf dat ik met jullie in dit geweldige team heb kunnen werken en acht onvergetelijke toernooien heb mee mogen maken. Vier jaar geleden had ik niet het idee dat ik ooit wereldkampioen zou zijn, maar na vier ongelooflijk spannende finales hebben we het dit jaar toch nog voor elkaar gekregen. Bedankt voor de enorm gave ervaringen en lol die we hebben gehad, en nog zullen hebben! Jeroen, bedankt voor de spoedcursus regeltechniek, het heeft me enorm geholpen bij het in regeling brengen van mijn actuator. Ook Elena wil ik hier nog een keer bedanken voor de steun die je me altijd voor mijn RoboCup activiteiten hebt gegeven.

Ten slotte wil ik pap, mam, zus, zusjes en schoonfamilie bedanken voor hun steun en begrip voor de afwezigheid door reisjes en drukte, vooral richting het einde. En als laatste degene die ik misschien wel het meest moet bedanken, Marleen. Lieveling, je hebt altijd voor me klaar gestaan en me gesteund waar nodig. Bedankt voor alles!

<div style="text-align: right;">

Koen Meessen
juli 2012

</div>

Curriculum Vitae

Koen Meessen was born on March 28th 1983 in Warnsveld, the Netherlands. After finishing his pre-university education at the Etty Hillesum College in Deventer, he started his study of Electrical Engineering at the Eindhoven University of Technology in 2001. During his traineeship at the Royal Institute of Technology Stockholm, he worked on "Finite element analysis of a permanent magnet synchronous machine". He received his Master's degree in February 2008. His graduation project was performed in cooperation with Assembléon on the topic of "Analysis and design of a rotary and a linear actuator for 2-DoF applications". From February 2008 until August 2012 he worked as a PhD student in the group of Electromechanics and Power Electronics at the department of Electrical Engineering of the Eindhoven University of Technology. His research topic comprised the analytical modeling of electromagnetic fields in three dimensional cylindrical structures applied to the analysis and design of a two degrees of freedom electromagnetic actuator. He is first author of ten journal publications and eleven conference publications and inventor of one patent. During his PhD project he was a member of the Tech United Mid-size league Robocup team, which became world champion in 2012. For this professional activity he was granted a contract extension of six months.